SIEMENS Healthineers

MAGNETOM Flash

The Magazine of MRI

Issue Number 3/2016 | RSNA Edition

Not for distribution in the US

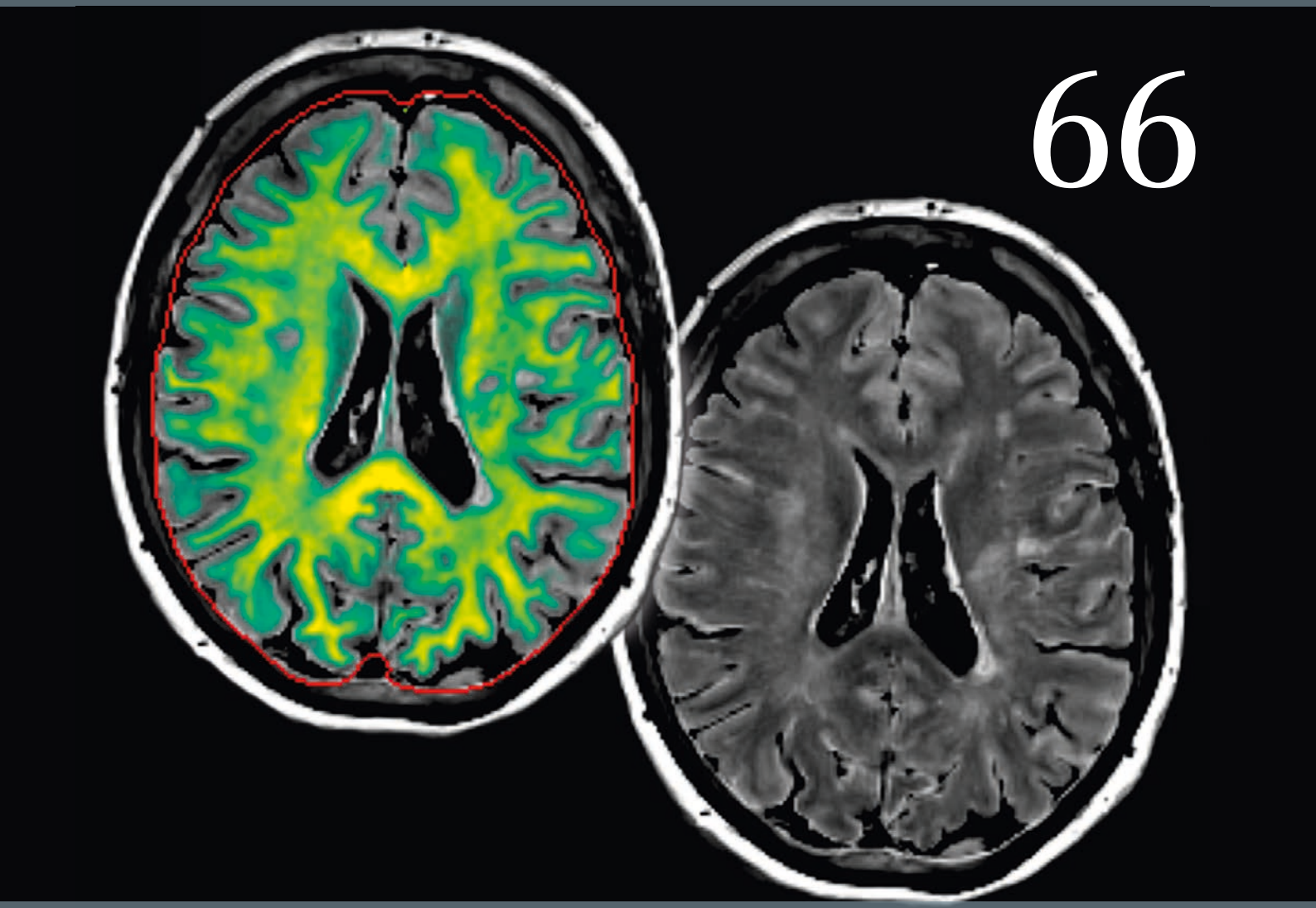

66

Editorial Comment
Modern Radiology from a Private Practice Perspective
Henrik Michaely
Page 2

Long-term Experience with MR Upgrades
Christos Loupatatzis
Page 12

Rapid Estimation of Myelin
Tobias Granberg
Page 112

SMS Accelerated DWI Throughout the Body
Valentin Tissot
Page 116

Professor Dr. Henrik Michaely obtained his M.D. and Ph.D. from medical school in Heidelberg in 2003 and 2004 respectively. In the same year, he commenced his residency in Diagnostic Radiology at the Institute of Clinical Radiology at Munich University (Prof. M. Reiser). During this period, he spent four months as a research fellow at the University of California, Los Angeles (Prof. P. Finn) to gain expertise in cardiovascular and high-field body MR-imaging. He passed his radiology boards in 2008 and was immediately afterwards appointed section chief for MR-imaging and associate professor for radiology at the University Medical Center Mannheim (Prof. S. Schoenberg) where he remained for seven years. During this time, he was responsible for the entire spectrum of clinical MR-imaging and headed the research group for abdominal and vascular imaging. After a three-month position as visiting professor at the Martinos Center for Biomedical Imaging in Boston (Prof. A. Guimaraes), in 2011/12 he was appointed Vice Chair of the Institute of Clinical Radiology and Nuclear Medicine of the University Center Mannheim. In 2013 he joined a large private practice in Karlsruhe, Germany, where he is now executive associate. His main focus is on the implementation of new imaging techniques that allow for higher patient throughput and optimized patient care in a non-academic outpatient setting.

Modern Radiology from a Private Practice Perspective

It is an honor to write an editorial for MAGNETOM Flash – yet the perspective of a German radiologist from private practice may be unfamiliar to most readers. Therefore, I will briefly describe my work setting and the German medical system to which we belong.

The "Diagnostische Gemeinschaftspraxis Karlstrasse" is a large physician-owned private practice in the heart of Karlsruhe, Germany. With a team of ten board-certified radiologists and physicians for nuclear medicine and over 60 radiology technicians and medical assistants, we are the largest private radiology group of the upper Rhine region surrounding Karlsruhe with approximately one million inhabitants. Our medical equipment comprises five 1.5T MR-scanners (MAGNETOM Aera, MAGNETOM Avanto, MAGNETOM Espree, Achieva ds, Achieva) a dual-energy 128-row MDCT (SOMATOM Definition AS+), digital X-ray, digital mammography, fluoroscopy, DEXA, ultrasound and two gamma cameras that are run in corporation with a neighboring hospital. The entire workflow from patient registration to reporting and image distribution to referring physicians is paperless. We perform almost 100,000 diagnostic studies per year with a focus on orthopedic, neurologic and oncologic abdominal studies. Our policy is for radiologists to present the images and the report to all patients immediately after the exam – which is the most time-consuming and demanding part of daily work. Yet, the direct contact with patients often allows a further narrowing of the diagnosis and provides a better visibility of radiology and its capabilities to all patients.

Reimbursement for diagnostic procedures varies according to the insurance status of the patients. For all patients with private medical insurance there is a linear relationship between performed studies and payment (i.e. if an MRI and a CT are performed, both can be billed separately). These patients make up 5-15% of all patients. Roughly 90% of the patients are within the statutory health insurance. For these patients reimbursement is not linear, and if, for example, an MRI study of the brain and a CT study of the chest are performed after bronchial carcinoma resection only a flat fee of 70-90 EUR will be paid per annual quarter for all performed studies. On the plus side, an easy and quick exam such as a chest X-ray will be reimbursed by the same amount. In addition, each physician has an allowed number of studies that can be billed per quarter of the year: if this number is exceeded, any study above this limit will only be partly reimbursed or if significantly exceeded not reimbursed at all.

Despite those legal restrictions the need for imaging is high and continuously increasing as modern radiology is a pivotal medical specialty that helps to detect and stage diseases, and allows us to define and monitor therapy and to set up further steps in patient management. In addition, patients actively demand from their referring physicians that imaging studies be performed before a specific therapy is initiated. In

	# CT exams per 1000 inhabitants	# MR exams per 1000 inhabitants	Ratio CT : MR	Total cost per inhabitant [€]
Germany	114	97	1 : 0.85	22
France	130	49	1 : 0.38	28
USA	228	91	1 : 0.40	53

Table 1: There is a clear shift towards MR-imaging in Germany while the costs per inhabitant in Germany are minimal.
Source: Barmer GEK-Arztreport 2011.

Germany particularly MR exams are requested as many patients are afraid of X-rays (see Table 1). This overall picture leads to an increase in the number of MR exams while easy/cheap CT-exams and even X-ray exams decrease in number. The reimbursement – as stated above – is the same for both imaging modalities putting private practices under a high economic pressure. Of course, every radiology practice strives to provide optimal equipment and state-of-the-art exams such as low-dose CT, new MRI equipment, multiparametric prostate MRI, whole-body diffusion imaging or dual-energy CT. Unfortunately, technical advances and improved diagnostic approaches are not reflected in higher reimbursement. For example, reimbursement for PET-CT in Germany is still limited to two indications.

These premises lead to an extremely high workload in private practice with productivity being the most important economic aspect thereof in Germany. As a consequence, cutting or strictly controlling your fixed cost is key for success. As the overall quality of the studies performed does not change reimbursement, some private practices might try to minimize the costs by saving on equipment investments. While this might work in rural areas with no other competitor, radiology practices in urban areas have taken another approach and tried to improve their patient experience and referring physician experience. Patient acquisition can be achieved by offering wide-bore MRIs, silent scan modes such as Quiet Suite, described in recent editions of MAGNETOM Flash [1-4], and low-dose CT.

The look-and-feel of the scanners and the entire practice is more important to patients, since the majority is unable to assess the medical quality. After each exam the report is discussed with patients for three reasons: firstly, talking to the patients allows us to double check the exam results with the patient's symptoms and often improves the quality of our reports. Secondly, the radiologist's visibility

"As the external economic pressure from increasing staff costs, increasing amount of regulation and competing practices is gradually but steadily increasing, a market adjustment is already underway."

Prof. Dr. Henrik Michaely

vis-a-vis the patient is significantly increased. And thirdly, patients appreciate the direct contact and interaction which will give us an edge over competing institutions/ practices in which no direct contact between patients and radiologist takes place.

The referring physicians request high-quality studies using new techniques such as CAIPIRINHA, TWIST, Dixon fat-saturation or quantitative evaluations such as liver reporting. Quite a few of these techniques are reflected in the current issue of MAGNETOM Flash, such as fast, motion insensitive imaging (see Marco Ravanelli et al. on the strength of FREEZEit in head and neck imaging in uncooperative patients; Jan Fritz et al. on 3D CAIPIRINHA SPACE[1] as a new technique to enable the isotropic acquisition of high-quality 3D data sets for efficient and comprehensive MRI of joints; Advanced and accelerated diffusion-weighted imaging throughout the body with Simultaneous Multi-Slice as shown by Valentin Tissot et al., or Robert Sellers' How-I-do-it on LiverLab for non-invasive, quantitative liver imaging). But also standardization of exam protocols and structured reports play a role. In this issue streamlined workflow is shown by Christos Loupatatzis on the advantages of DotGO and the various Dot engines; or by Bac Nguyen on fast and robust workflow with the Pediatric 16 coil.

Yet another important aspect is the electronic transmission of reports and images. At our practice for example, images and written reports in pdf-format are available online to the referring physician 10-20 minutes after the end of the exam. Any help from manufacturers in further pursuing those aims is highly appreciated and a major selling point for new equipment. Quantitative assessment of liver fat content in MRI or automatic labelling of vertebral bodies in MRI – as provided by the Spine Dot Engine (see Loupatatzis on page 12) – or in CT are highly welcomed steps in this direction, particularly as they occur 'inline', meaning no further user interference and hence no additional personnel is required.

Other key selling points include the robustness of the equipment and ease of use of the equipment (see Loupatatzis on the benefits of SlideConnect coils, or Nancy Talbot on the Tim Dockable Table).

The robustness is important in two ways: firstly, with a high hourly throughput and long working times in private practice, equipment down times can barely be tolerated. Protocols need to provide good image quality within minimal exam time: one of the reasons CAIPIRINHA and Dixon-techniques are used at our practice. Secondly, patients tend to have higher BMI's which increases the wear and tear of the equipment and requires adequate equipment (e.g. increased table load capacity or larger joint coils). Not being able to provide high-quality knee exams in obese patients is an obvious flaw that all referring physicians and even most patients will notice. Beyond

[1] WIP, CAIPIRINHA SPACE is currently under development and is not for sale in the US and in other countries. Its future availability cannot be ensured.

Editorial Board

We appreciate your comments.
Please contact us at magnetomworld.med@siemens.com

Antje Hellwich
Editor-in-chief

Reto Merges
Head of Scientific Markting

Sunil Kumar S.L., Ph.D.
Senior Manager Applications, Canada

Wellesley Were
MR Business Development Manager Australia and New Zealand

Gary R. McNeal, MS (BME)
Advanced Application Specialist, Cardiovascular MR Imaging Hoffman Estates, IL, USA

Review Board

Lisa Chuah, Ph.D.
Global Segment Manager Neurology, Pediatrics, and Orthopedics

Christoph Forman
Cardiovascular Application Development

Berthold Kiefer, Ph.D.
Head of Oncological and Interventional Applications

Heiko Meyer, Ph.D.
Head of Neuro Applications

Edgar Müller
Head of Cardiovascular Applications

Michaela Schmidt
Cardiovascular Application Development

Gregor Thörmer, Ph.D.
Global Segment Manager Men's and Women's Health

these hardware requirements, support from the scanners' software is required to facilitate the quick and consistent planning of the exams.

These advantages in medical technology allow us to streamline the workflow and hereby increase the number of examinations. As the external economic pressure from increasing staff costs, increasing amount of regulation and competing practices is gradually but steadily increasing, a market adjustment is already underway. Private radiology practices in larger cities in Germany are consolidating to create larger groups that can use their equipment and their employees to the greatest economic benefit. Similar developments could be observed in the dialysis market which resembles radiology in its technical character and the ability to precisely plan patient throughput. In dialysis there is meanwhile an oligopoly with only four major countrywide groups partly dominated by Germany's largest stock corporations.

The future of radiology in private practice in Germany is being shaped right now. If we can adjust to the economic pressure whilst also meeting patients' wishes and the referring physicians' needs, consolidated physician-owned private practices will prevail. Failure to make this adjustment will most likely lead to corporate practices. In the meantime, however, we will keep focusing on our patients and providing the best image quality and medical care for them.

I hope you enjoy reading about the many new advances in MR imaging that we present to you in this RSNA-issue.

Prof. Dr. Henrik Michaely

References

1 Pierre EY et al. Making MRI Scanning Quieter. MAGNETOM Flash 55 (5) 2013; 30-34.
2 Ida M et al. Quiet T1-weighted 3D Imaging of the Central Nervous System Using PETRA. MAGNETOM Flash 55 (5) 2013; 35-43.
3 Aida N. Quiet Sequences for Pediatric Patients: T1-PETRA and Quiet SWI. MAGNETOM Flash 57 (2)2014; 14-18.
4 Reiss-Zimmermann M. syngo MR E11 on a MAGNETOM Aera: First Impressions. MAGNETOM Flash 62 (2)2015; 20-22.

Content

MAGNETOM Sempra.* Daily success with 1.5T

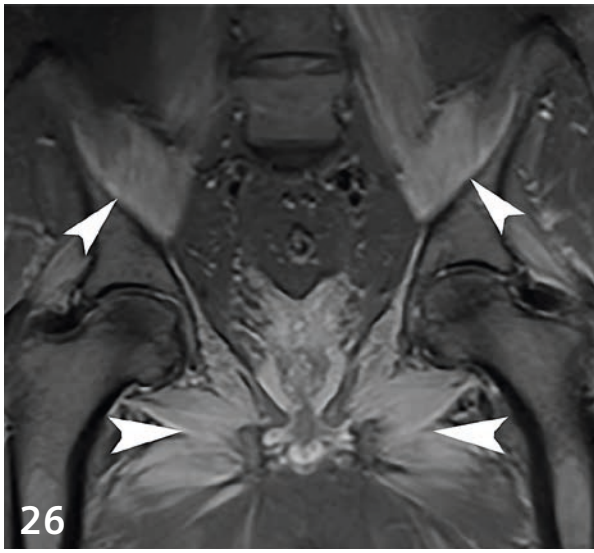

MRI in Inflammatory Myopathies

Image Gallery

8 MAGNETOM Sempra.*
Daily success with 1.5T

Business

12 Long-term Experience with MR Upgrades
Christos Loupatatzis, MRI AG Spital Maennedorf, Switzerland

18 The fit Experience in Canada
Nancy Talbot, Princess Margaret Cancer Center, Toronto, Canada

Musculoskeletal MRI

22 Review: MRI of Muscle Denervation Syndromes
Gustav Andreisek, et al., University of Zurich, Switzerland

26 Utility of MRI Findings in Inflammatory Myopathies
Christopher J. Hanrahan, et al., University of Utah School of Medicine, Salt Lake City, UT, USA

30 High Resolution Isotropic 3D CAIPIRINHA SPACE[1] MRI of the Musculoskeletal System
Jan Fritz, et al., Johns Hopkins University School of Medicine, Baltimore, MD, USA

Abdominal Imaging

39 How-I-do-it: MR LiverLab
Robert Sellers, Siemens Healthineers, Cary, NC, USA

44 Iron quantification with LiverLab
Stephan Kannengiesser, Siemens Healthineers, Erlangen, Germany

48 Motion Correction of ^{90}Y Dose Maps with MR/PET Imaging
Zahi A. Fayad, et al., Mount Sinai, New York, NY, USA

Cardio-pulmonary Imaging

52 Motion Correction in PET/MR Using the Biograph mMR
Thomas Vahle, et al., New York University, Langone Medical Center, New York, NY, USA

60 Cardio-Pulmonary MRI for Diagnosis and Monitoring of Chronic Thromboembolic Pulmonary Hypertension (CTEPH)
Jens Vogel-Claussen, et al., Hannover Medical School, Hannover, Germany

Cardiovascular Imaging

65 Free-breathing Late Enhancement Imaging: Phase Sensitive Inversion Recovery (PSIR) with Respiratory Motion Corrected (MOCO)[1] Averaging
Peter Kellman, et al., National Heart, Lung, and Blood Institute, National Institutes of Health, Bethesda, MD, USA

74 4D Flow MRI[1] – an Update
Michael Markl, et al., Feinberg School of Medicine, Northwestern University, Chicago, IL, USA

80 How-I-do-it: Imaging of Vascular Calcification Using PETRA and StarVIBE
Marcos P. Botelho, et al., Northwestern Memorial Hospital, Chicago, IL, USA

*510(k) pending. MAGNETOM Sempra is not commercially available. Future availability cannot be guaranteed.

[1] WIP, the product is currently under development and is not for sale in the US and in other countries. Its future availability cannot be ensured.

[2] MR scanning has not been established as safe for imaging fetuses and infants less than two years of age. The responsible physician must evaluate the benefits of the MR examination compared to those of other imaging procedures.

[3] MAGNETOM 7T is ongoing research. All data shown are acquired using a non-commercial system under institutional review board permission. MAGNETOM 7T is still under development and not commercially available yet. Its future availability cannot be ensured.

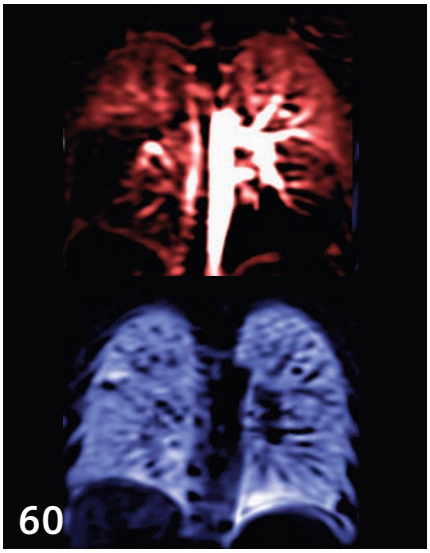

Fourier Decomposition for Monitoring of CTEPH

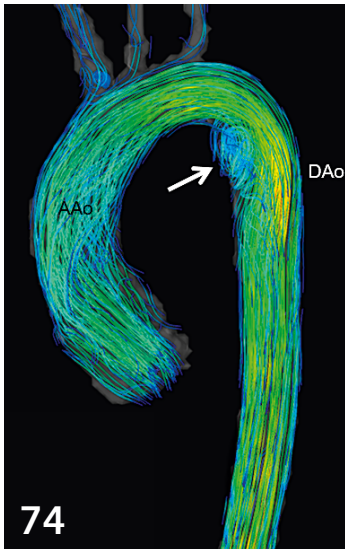

4D Flow MRI[1]

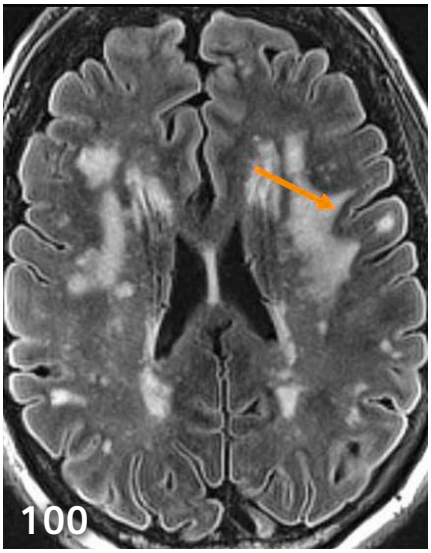

Clinical Neuroimaging at 7T[3]

Pediatric Imaging

82 Case Report: Hypertrophic Cardiomyopathy in a Pediatric Patient;[2] Usefulness of T1 Mapping Synthetic Inversion Recovery Imaging
Giuseppe Muscogiuri, et al., Bambino Gesù – Children's Hospital IRCCS, Rome, Italy

84 Case Series:[2] Utilization of the Pediatric 16 Coil for 1.5T and 3T Systems
Bac Nguyen, Oslo University Hospital, Rikshospitalet, Oslo, Norway

Head and Neck Imaging

92 FREEZEit StarVIBE: Freezing the Moving Head and Neck at a Sub-Millimetric Scale
Marco Ravanelli, et al., Università degli Studi di Brescia, Italy

Neurology

95 New Protocol for the MR Imaging of Pituitary Adenomas
Denis Gardeur, Centre RMX, Paris, France

100 Case Study: Magnetic Resonance Fingerprinting (MRF)[1] Imaging of the Brain
Siegfried Trattnig, et al., Medical University Vienna, Austria

100 Clinical Neuroimaging at 7T[3] Compared to Lower Field: a Photo Essay
Stephen E. Jones, et al., Cleveland Clinic, Cleveland, OH, USA

112 Rapid Estimation of Myelin for Diagnostic Imaging (REMyDI)[1]
Tobias Granberg, et al., Karolinska Institutet, Stockholm, Sweden

Oncological Imaging

116 First Clinical Experiences with Simultaneous Multi-Slice Accelerated DWI Throughout the Body
Valentin Tissot, et al., Morvan Hospital, Brest, France

Women's and Men's Health

122 Pelvic Congestion Syndrome: The Role of MRI
Rahel A. Kubik-Huch, et al., Kantonsspital Baden, Switzerland

126 Simultaneous Multi-Slice RESOLVE[1] for Optimized DWI of the Breast at 3 Tesla
Lukas Filli, et al., University Hospital Zurich, Switzerland

130 Transurethral MR-Thermometry Guided Ultrasound Ablation[1] of the Prostate
David Bonekamp, et al., German Cancer Research Center (DKFZ), Heidelberg, Germany

The information presented in MAGNETOM Flash is for illustration only and is not intended to be relied upon by the reader for instruction as to the practice of medicine. Any healthcare practitioner reading this information is reminded that they must use their own learning, training and expertise in dealing with their individual patients. This material does not substitute for that duty and is not intended by Siemens Healthcare to be used for any purpose in that regard. The treating physician bears the sole responsibility for the diagnosis and treatment of patients, including drugs and doses prescribed in connection with such use. The Operating Instructions must always be strictly followed when operating the MR System. The source for the technical data is the corresponding data sheets.

MAGNETOM Sempra. Daily success with 1.5T

MAGNETOM Sempra[1] is the latest addition to the MAGNETOM family of 1.5T MRI systems with Tim 4G and Dot technolgy. It is designed to provide solutions to the key challenges that you are facing on a daily basis. Besides delivering consistent imaging quality especially in core exams, it is also packed with features to ensure lower operating cost and total cost of ownership.

[1] 510(k) pending. MAGNETOM Sempra is not commercially available. Future availability cannot be guaranteed.

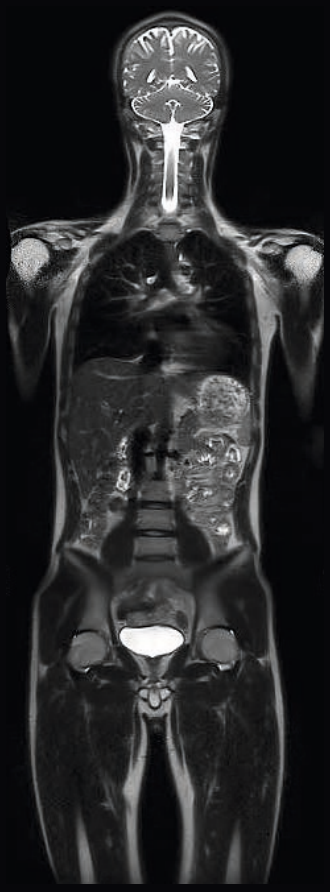

HASTE T2 in 3 steps

REVEAL b800 in 4 steps

TSE sag whole-spine in 2 steps

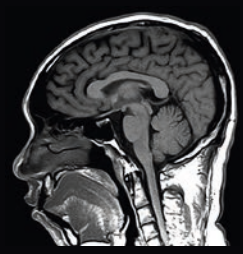

SE T1 sag

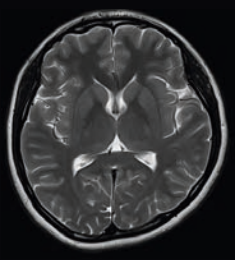

TSE T2

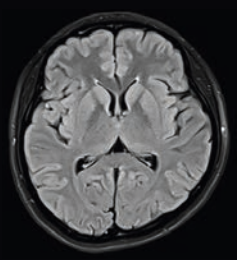

TIRM T2 Dark Fluid

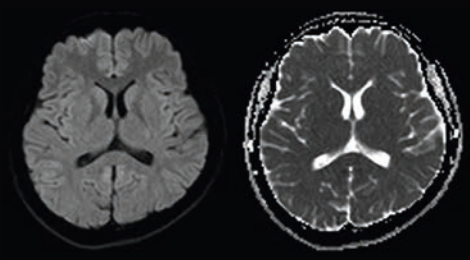

RESOLVE b1000, ADC

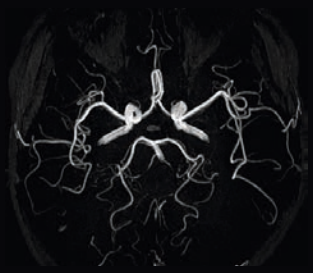

TOF MRA

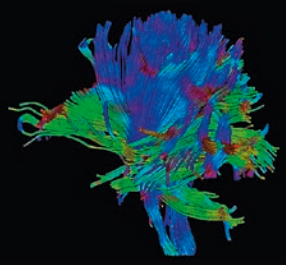

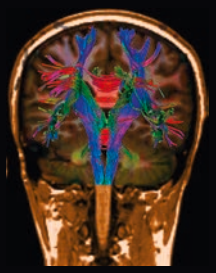

DTI fibre tracking

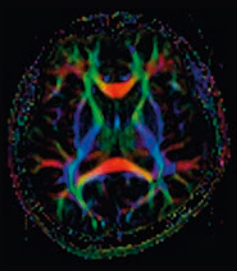

Color FA

TSE T2 sag

TSE T1 sag

TSE T2 sag

TSE T1 sag

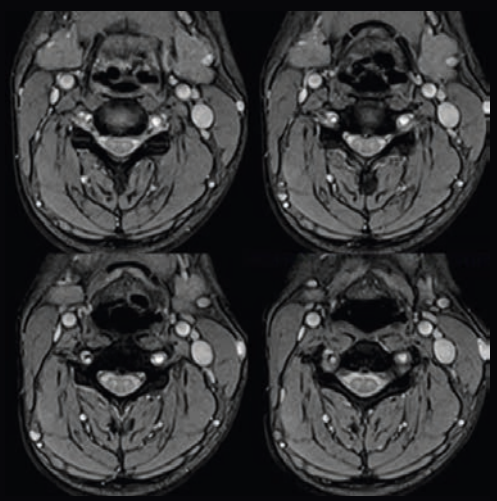

MEDIC T2 tra

TSE T2 tra

HASTE T2 cor

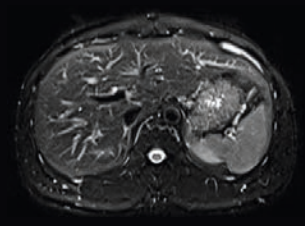

TSE T2 fat sat free-breathing

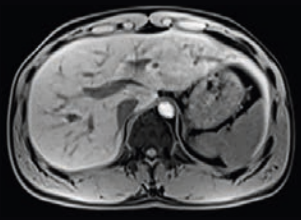

CAIPIRINHA 4 VIBE

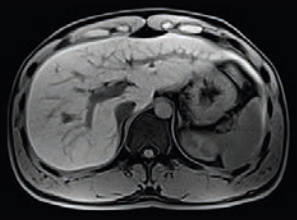

StarVIBE

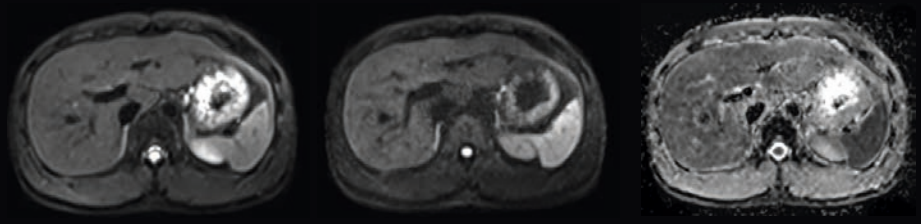

DWI b50, 800 and ADC

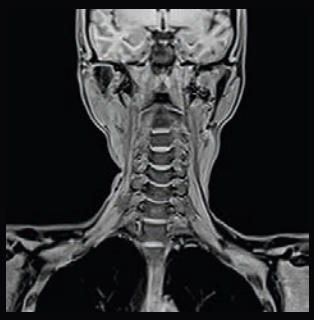

VIBE Dixon water cor

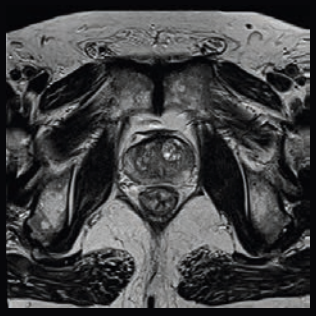

TSE T2 tra

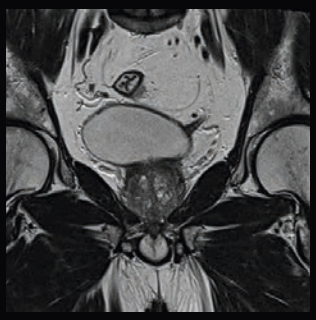

TSE T2 cor

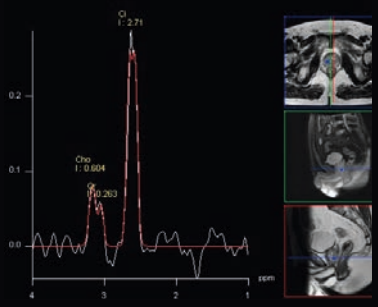

3D CSI

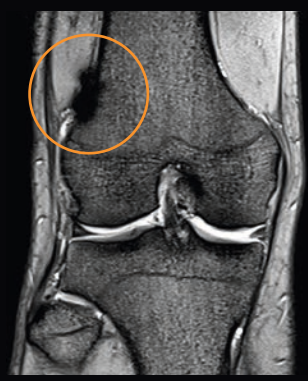

MEDIC

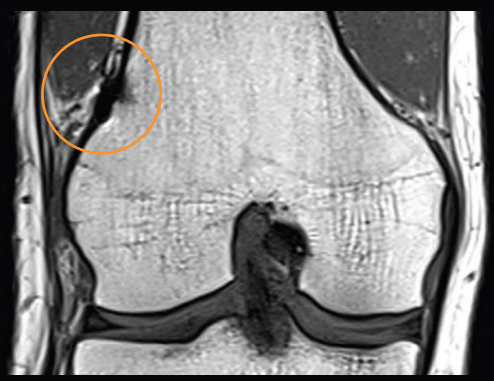

TSE with WARP

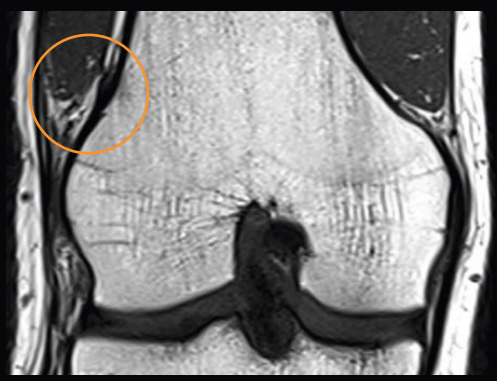

TSE with Advanced WARP

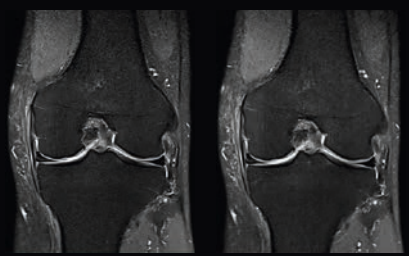

TSE PD fat sat cor

Quiet X

TSE PD fat sat cor

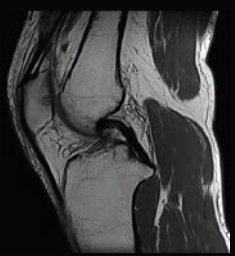

TSE PD sag

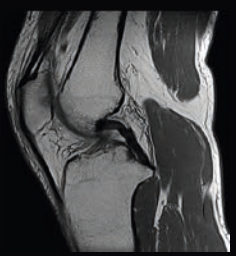

Quiet X

TSE PD sag

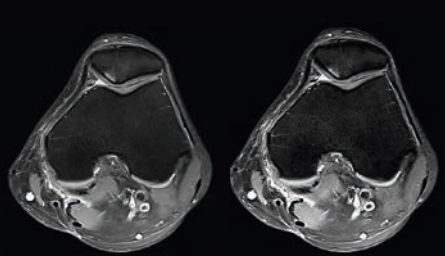

TSE PD fat sat tra

Quiet X

TSE PD fat sat tra

SIEMENS Healthineers

Relevant clinical information

www.siemens.com/magnetom-world

From technology to clinical applications, you will find all the latest news on Siemens MR at www.siemens.com/magnetom-world.

Don't miss the talks of international experts on all aspects of Magnetic Resonance Imaging.

Go to
Clinical Corner > Clinical Talks

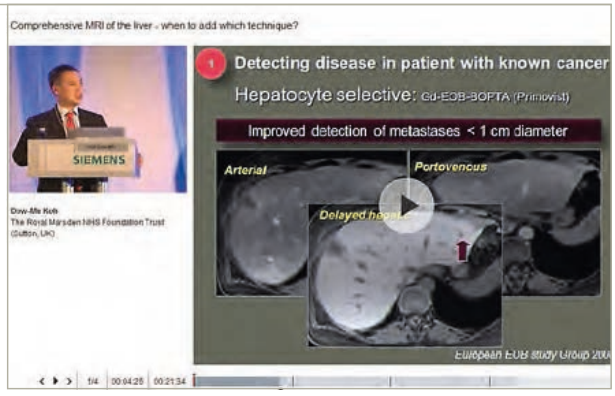

The centerpiece of the MAGNETOM World Internet platform consists of our users' clinical results. Here you will find case reports and clinical methods.

Go to
Clinical Corner > Case Studies

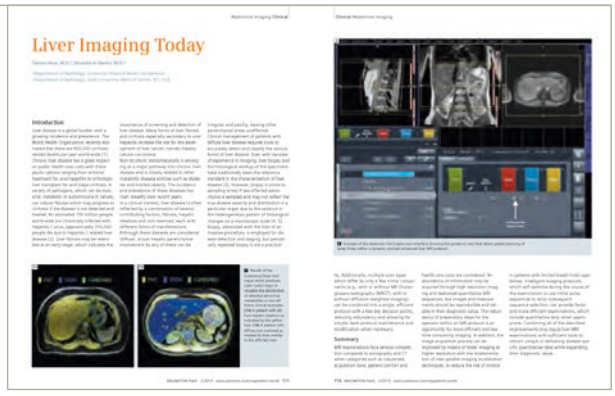

Just a mouse click away you will find application videos and useful tips allowing you to optimize your daily MR examinations.

Go to
Clinical Corner > Application Tips

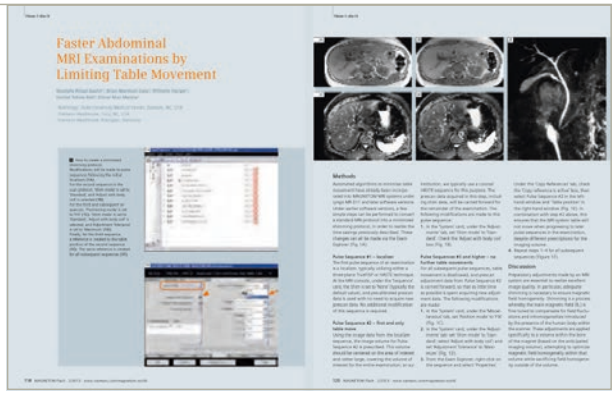

Long-term Experience with MR Upgrades

Christos Loupatatzis, M.D; Christoforos Stoupis, M.D.

MRI AG Spital Maennedorf, Switzerland

In this article we share some of our experiences over the last few years with MR upgrades.

The MRI AG Spital Maennedorf is located beside Lake Zurich in Switzerland and is one of the leading MR-centers in the region. With its close relationship to the academic hospital Maennedorf and to specialized practitioners with a variety of subspecialties including Orthopedics, Trauma-/General-/Hand- and Neuro-Surgery, Neurology, Psychiatry, Gastroenterology, Urology, Gynecology and Angiology we receive requests for MR examinations all over the body ("from head to toe"). We therefore need an MRI scanner able to perform all kinds of examinations at a very high level. Our referring physicians recognize the high quality of our work and our participation in radiology boards and meetings (e.g. European School of Radiology). Without the proper technical equipment it would not be possible to sustain this high level.

In 2007 the decision was made to acquire a MAGNETOM Avanto 1.5T MRI system (Siemens Healthcare, Erlangen, Germany). This scanner worked consistently over the years to provide very good image quality. Nevertheless, always aiming to optimize our image quality and performance, in 2013 we became one of the first MRI centers in Switzerland to perform a fit upgrade, accompanied by a Dot upgrade. Notwithstanding the acquisition of additional diagnostic tools during the first years (such as spectroscopy,

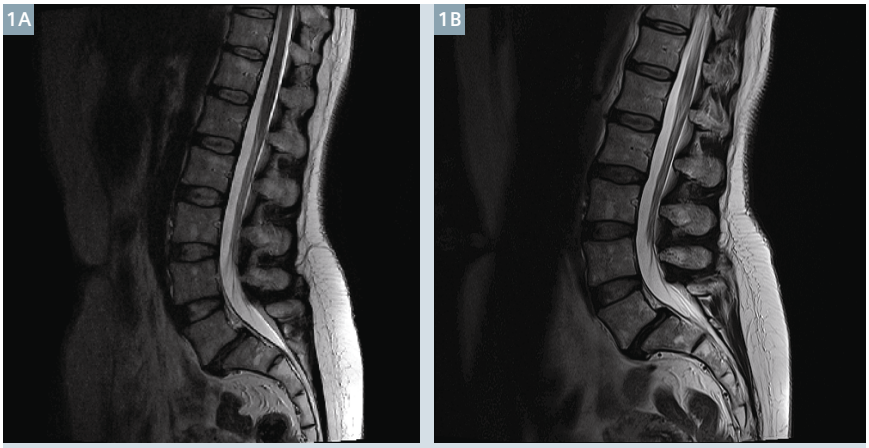

TR 4000 ms, TE 122 ms, TA 3 min, 12 slices, FOV 317 x 320, matrix 754 x 896, SL 4.0 mm

TR 3250 ms, TE 91 ms, TA 3:31 min, 15 slices, FOV 300 x 300, matrix 307 x 512, SL 4.0 mm

1 46-year-old female patient. T2w sagittal images of the lumbar spine, before **(1A)** and after **(1B)** MAGNETOM Avanto^{fit} upgrade. Note the improved image quality in 1B (i.e. better delineation of the nerve roots).

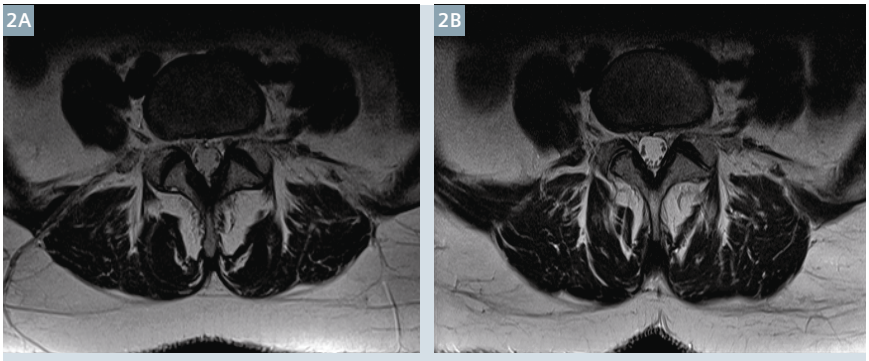

TR 3100 ms, TE 108 ms, TA 3:03 min, 15 slices, FOV 248 x 250, matrix 311 x 448, SL 4.0 mm

TR 3800 ms, TE 108 ms, TA 2:58 min, 16 slices, FOV 200 x 200, matrix 269 x 448, SL 4.0 mm

2 Same patient as in Figure 1. T2w axial images of the lumbar spine, before **(2A)** and after **(2B)** MAGNETOM Avanto^{fit} upgrade. In 2B note the possibility to reduce the FOV and therefore improved image resolution, in shorter acquisition time (i.e. the nerve roots).

perfusion imaging and susceptibility-weighted imaging), this fit upgrade was our first major MR upgrade.
A second major step has been our update to software version *syngo* MR E11C. A milestone in this context was our participation as a CPF ("Customer Preference Feedback") reference center for the *syngo* MR E11C software version in 2015/2016.

Avanto^{fit} and first Dot engine experiences

Despite the high image quality of the MAGNETOM Avanto system, we needed firstly to respond to our referring physicians' demands for the best image quality, and secondly to stay competitive as a leading MRI center amongst the increasing number of 3T systems available in the Zurich area. We decided on the Avanto^{fit} upgrade instead of buying a new scanner, a solution we thought would be more cost efficient and less time consuming. Since we have only one MRI scanner, we could not afford the time required for the de-installation and a new installation, whereas an upgrade would reduce the downtime of the system to a couple of days.

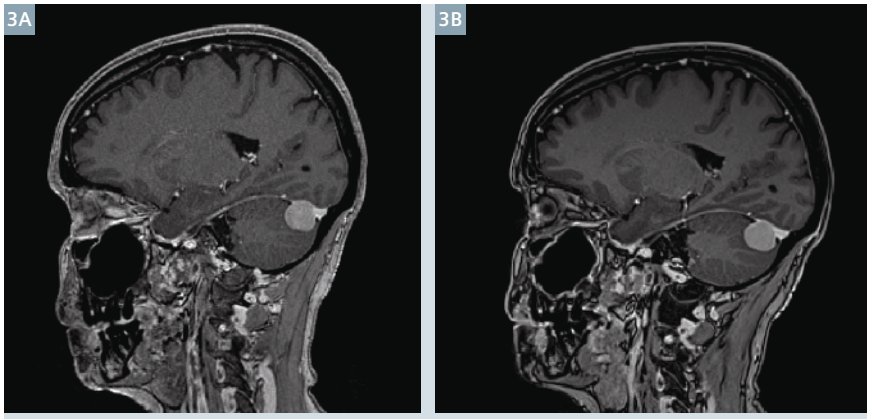

TR 2060 ms, TE 3.4 ms, TI 1100 ms, TA 5:11 min, 208 slices, FOV 250 x 250, matrix 320 x 320, SL 0.9 mm

TR 2000 ms, TE 2.5 ms, TI 900 ms, TA 5:01 min, 208 slices, FOV 250 x 250, matrix 288 x 288, SL 0.9 mm

3 54-year-old female patient. 3D-MPRAGE-sequence of the brain after contrast administration before **(3A)** and after **(3B)** MAGNETOM Avanto^{fit} upgrade showing a meningeoma of the cerebellar tentorium. Note the much better image quality in less acquisition time in 3B (i.e. the delineation of the cortical matter).

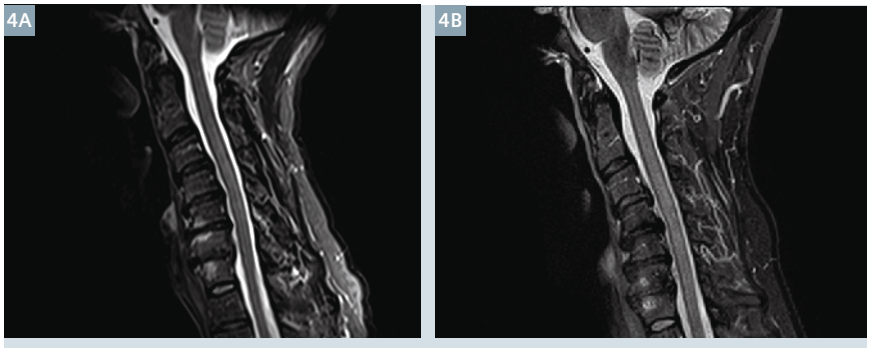

TR 3500 ms, TE 91 ms, TA 3:27 min, 12 slices, FOV 280 x 280, matrix 384 x 512, SL 3.5 mm

TR 3500 ms, TE 29 ms, TA 3:47 min, 12 slices, FOV 220 x 220, matrix 515 x 512, SL 3.0 mm

4 45-year-old male patient. STIR sagittal images of the cervical spine, before **(4A)** and after **(4B)** MAGNETOM Avanto^{fit} upgrade. Note the possibility to reduce both the FOV and the slice-thickness with minimal increase in acquisition time, and with a superior image quality in 4B (i.e. the subtle signal intensity changes of the spinal cord).

We decided to carry out this fit upgrade during the summer holiday season, when most of our referring physicians were on holiday. Following the fit upgrade installation we received one week's intensive support from our Siemens MR Application Specialist, since obviously an adjustment of all our sequence protocols was necessary. This intensive and time-consuming period after installation was followed by a two-month period of further protocol optimization, with the help of the application specialist, adapting the initial protocols after gaining some experience with the new system. In retrospect, all of our efforts were worthwhile.

The improvement of the image quality was obvious in all examinations over the whole body. External neurologists and orthopedic surgeons mentioned that our image quality was so good that they thought we bought a 3T-system (Figs. 1, 2).
This fit upgrade had two benefits of a 1.5T over a 3T system: Less susceptibility artifacts, specifically in abdominal imaging, as well as patient security and fewer limitations in case of intracorporeal medical devices such as prosthetic cardiac valves etc. This was definitively the right choice for our institution.

In brain-imaging specifically the 3D-MPRAGE-sequence became much crispier and clearer (Fig. 3) and the RESOLVE-diffusion showed significantly less artifacts in comparison to the standard EPI diffusion.
In spine-imaging we were able to reduce the field-of-view (FOV) and therefore increase the resolution with even higher signal-to-noise ratio (SNR) (Fig. 4). In shoulder-imaging, the new Shoulder 16-channel coil not only gave better image quality, but also increased patient comfort when positioned. In knee-imaging, the new 15-channel Tx/Rx Knee coil produced images of a quality superior to the previous system (Fig. 5). The only disadvantage is that obese patients and patients after trauma unable to stretch-out their knee do not fit into this coil: For those cases we still use the previous Extremity coil with an additional adapter in order to enable

the link with the new system. Special mention should go to the Hand/Wrist 16 coil and Foot/Ankle 16 coil for their convenience for the patient and for enabling the scan of very small structures (such as a finger joint) or the whole hand, and the foot without moving the target area within the coil (for example imaging a distal joint or a proximal joint; Fig. 6).

Feedback from our technologists tells us that one of the advantages of the fit upgrade is the much easier handling of the coils with the new innovative SlideConnect system and the new in-room display at the scanner, which enables the technologist to get information about the coils before leaving the scanner room. Additionally the display provides patient-data-information, ECG-waves, etc.

Definitely one of the biggest steps of evolution and advantage of the new system is the standardization of the exam protocols using the Dot engines in routine examinations. The first Dot engines we used were the Brain and the Spine Dot Engines. The Brain Dot Engine, with AutoAlign, its automatic anatomic orientation, not only helps less experienced technologists to reliably find the anatomic landmarks for an optimal examination, but also guides the radiologist in the comparison of the image-planes in follow-up brain studies such as in multiple sclerosis patients, because of the identical slice orientation and slice-positioning.

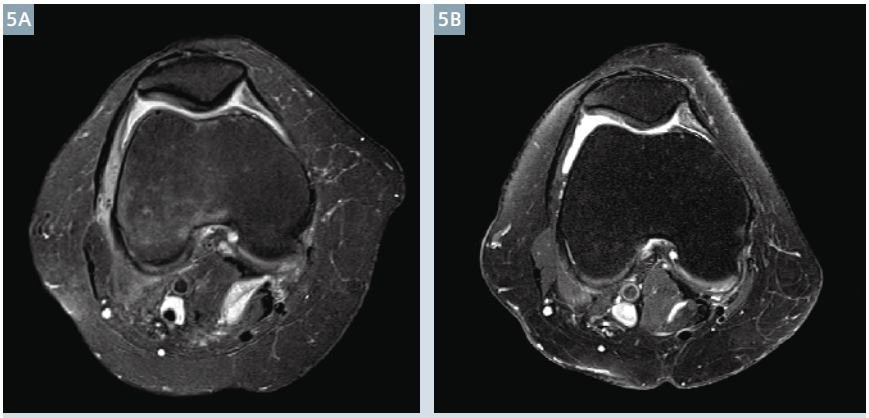

TR 2120 ms, TE 41 ms, TA 2:14:2 min, 32 slices, FOV 160 x 160, matrix 240 x 320, SL 3 mm

TR 3600, TE 45 ms, TA 3:10 min, 30 slices, FOV 160 x 160, matrix 269 x 448, SL 3 mm

5 75-year-old female patient. Proton Density-weighted fat sat (PDfs) axial images of the knee before **(5A)** and after **(5B)** MAGNETOM Avanto^{fit} upgrade, using the new 15 channel knee coil. Note the much better image quality in 5B (i.e. in the retropatellar cartilage).

TR 3010 ms, TE 26 ms, TA 2:09 min, 20 slices, FOV 186 x 220, matrix 345 x 512, SL 2 mm

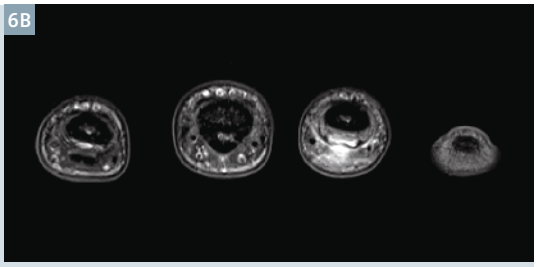

TR 4200 ms, TE 28 ms, TA 3:31 min, 25 slices, FOV 96 x 110, matrix 353 x 448, SL 3 mm

6 15-year-old male patient with rupture of the flexor digitorum profundus tendon (4th finger). Note the high quality images: **(6A)** Coronal PDfs image showing the rectracted tendon and **(6B)** axial PDfs image showing the empty space, where the tendon should be.

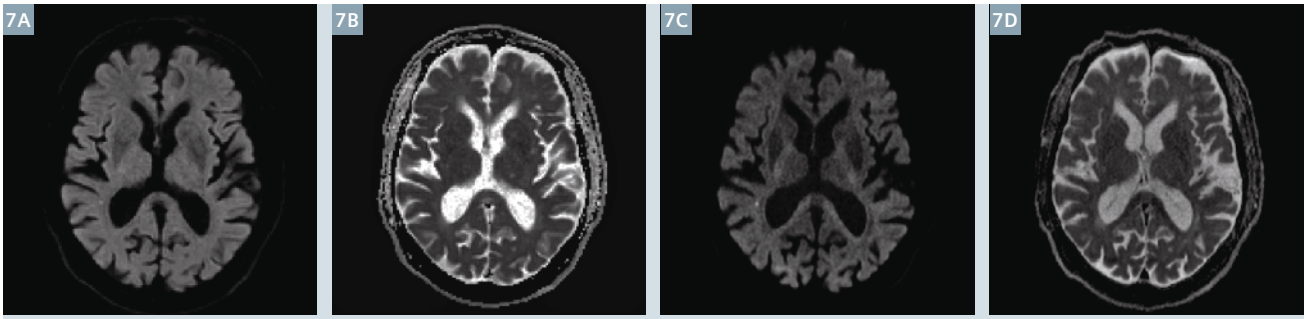

TR 4000 ms, TE 64 ms, SL 5 mm, TA 1:34 ms, 25 slices, b-value 1000

TR 3000 ms, TE 83 ms, SL 2.5 mm, TA 2:40 ms, 40 slices, b-value 2000

7 71-year-old male patient with focal acute embolic ischemia within the Meyer's loop on the right hemisphere (standard RESOLVE Diffusion **(7A)** b1000 image, **(7B)** ADC map). Note the much better visibility of the pathology using thinner slices and higher b-value (modified SMS-Diffusion **(7C)** b2000 image, **(7D)** ADC map). Because of the Simultaneous Multi-Slice acquisition, the image quality is very good **(7C, D)**, even with a b-value of 2000. (Also see Table 1.)

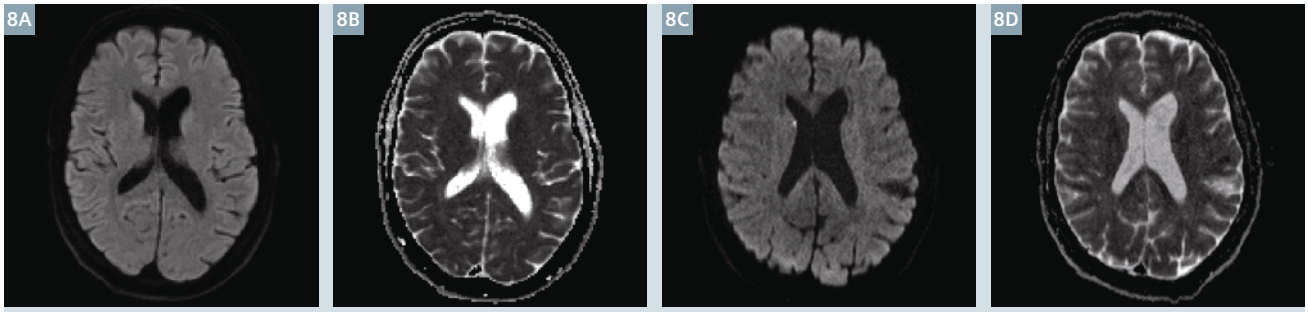

TR 4000 ms, TE 64 ms, SL 5 mm, TA 1:34 ms, 25 slices, b-value 1000

TR 3200 ms, TE 83 ms, SL 2.5 mm, TA 2:51 ms, 40 slices, b-value 2000

8 56-year-old male patient with focal acute lacunar infarct in the head of the right caudate nucleus, only visible in the modified SMS-Diffusion sequence **(8C, D)**. No visibility of the pathology at all in the standard 5 mm RESOLVE diffusion **(8A, B)**. Standard RESOLVE Diffusion **(8A)** b1000 image, **(8B)** ADC map; modified SMS-Diffusion **(8C)** b2000 image, **(8D)** ADC map. (Also see Table 1.)

The Spine Dot Engine was very useful in ensuring a complete coverage of the spine, even for patients with scoliosis. The automatic labelling of the axial slices is very much appreciated by our referring spine-surgeons, helping them to look quickly through the images even as hard-copy films, which many of them still share and discuss with their patients, rather than the primary images taken from CD.

Update to *syngo* MR E11C

The update to the new software version *syngo* MR E11C has had profound benefits for our team. Whilst we faced major software layout changes, we also benefited from new possibilities and opportunities by using the new workflow and a number of new Dot engines.

Perhaps the most important improvement in image quality due to *syngo* MR E11C is simultaneous multi-slice (SMS) diffusion-imaging. Realizing the possibilities of high SNR and time-efficiency of this sequence, one of our first modifications for brain imaging was to create a 2.5 mm thin sliced sequence with a b-value of 2000 s/mm². This modification was initially scrutinized by the Siemens-developers, who were quickly convinced of the advantages of this modification. With such a high b-value the conspicuity of acute ischemic lesions increased dramatically. Using the very robust RESOLVE diffusion (b-value 1000 s/mm², 5 mm slice thickness) as a standard sequence, we sometimes doubted the interpretation of our findings as to whether or not there was an ischemic lesion. However, using the modified SMS-diffusion, we were able to eliminate these doubts in all cases. Therefore this sequence found its way into our standard stroke protocol (Figs. 7, 8, Tab. 1).

	Original parameters	Parameters for SMS Diffusion in stroke protocol
Voxel size (mm)	0.6 x 0.6 x 4.0	0.6 x 0.6 x 2.5
PAT	4	4
Accelerator factor slice	2	2
Slices	28	40
Position	Isocenter	L2.8 A26.4 H21.7 mm
Orientation	Transversal	T > C-4.1 > S-2.1
FOV (mm)	220	230
Slices (mm)	4	2.5
TR (ms)	4000	3200
TE (ms)	97	83
Coil elements	HE 1-4	HE 1-4; NE1,2
AutoAlign	–	Head > Brain
Initial position (L x P x H) (mm)	Isocenter	0 x 17 x 2.8
System adjustments		
B1 Shim mode	TrueForm	None
Diffusion mode	4-scan trace	4-scan trace
Diffusion scheme	bipolar	monopolar
Diffusion-weightings		
b-value 1	0 s/mm²	0 s/mm²
b-value 2	1000 s/mm²	2000 s/mm²
Sequence part 1		
Echo spacing (ms)	1.04	0.91
Bandwidth (Hz/Px)	1042	1240
TA (min)	1:17	2:51

Table 1: Modified parameters of Simultaneous Multi-Slice (SMS) Diffusion for standard stroke protocol.

A substantial improvement of the new *syngo* MR E11 software has been the new ability with the Dot Cockpit to create and combine Dot protocols in a definitively easier way than in prior software versions. With a basic instruction we were able to create our own new Dot-protocols, according to our local needs, without reliance on an application specialist.

Initially, the acceptance of the Abdomen Dot Engine was suboptimal: being used to manually adapting the positioning of various parameters (e.g. slice, slab, FOV etc.) to the patients' anatomy and cooperation, we had to learn a more passive role during the acquisition of the examination. Nevertheless, the vast advantages of a guided workflow and automatic adaption of field-of-view and number of slices to the individual anatomy with AutoCoverage soon convinced us – especially for the liver. Less experienced technologists in particular appreciated the automatism for the more challenging abdominal studies. The automatic breathing commands in the Dot Engine allowed us to standardize the timing of our arterial phase in liver imaging by using the bolus-tracking technique with automatic bolus detection, thereby enabling us to acquire a consistent arterial phase, independent of patients' cardiac output. This contrast phase stability has been particularly useful in the follow-up of patients with liver cirrhosis and screening for hepatocellular carcinoma. As to time-efficiency, the new fast BLADE technique allowed a much quicker T2 acquisition of the liver, especially when using a gated technique (Fig. 9), and the coronal T1 3D acquisition became much faster by using FREEZEit and the StarVIBE (T1 VIBE CAIPIRINHA) technique. The DynaVIBE offers the possibility of multi-arterial phase acquisition, although some institutions prefer only one well-timed arterial phase with bolus-tracking. The StarVIBE technique minimizes breathing artefacts, and is especially useful with patients who are not able to hold their breath, or deaf patients. This was also one of the sequences we modified with the assistance of Siemens creating a test-version[1] of a dynamic StarVIBE sequence, which enabled dynamic liver imaging with decent image quality even with totally uncooperative patients (Fig. 10, Tab. 2). Liver-evaluation techniques with quantification of fat and iron-deposition within the liver are completing an advanced evaluation of liver pathologies.

A new innovative technique with the potential to revolutionize MR-Angiography is the Quiescent-Interval Single-Shot (QISS) sequence. This is the first reasonable alternative to contrast-enhanced angiography, in particular peripheral angiography

[1] WIP, the product is currently under development and is not for sale in the US and in other countries. Its future availability cannot be ensured.

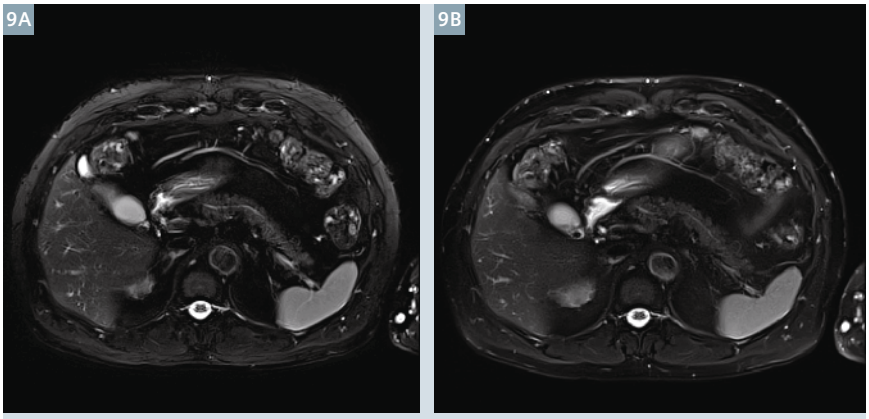

TR 5325.3 ms, TE 96 ms, TA 46.06 x 5, FOV 380 x 380, matrix 320 x 320, SL 6 mm

TR 5274.1, TE 83 ms, TA 22.77 x 5, FOV 380 x 380, matrix 320 x 320, SL 6 mm

9 Abdominal imaging of a 64-year-old male patient. Comparison between T2w fs-acquisition of the liver with gated T2 BLADE **(9A)** and T2w fast BLADE technique **(9B)**. Note the sharper image contrast and better visibility of the gallbladder stone in less than half of the time in T2w fast BLADE in **9B**.

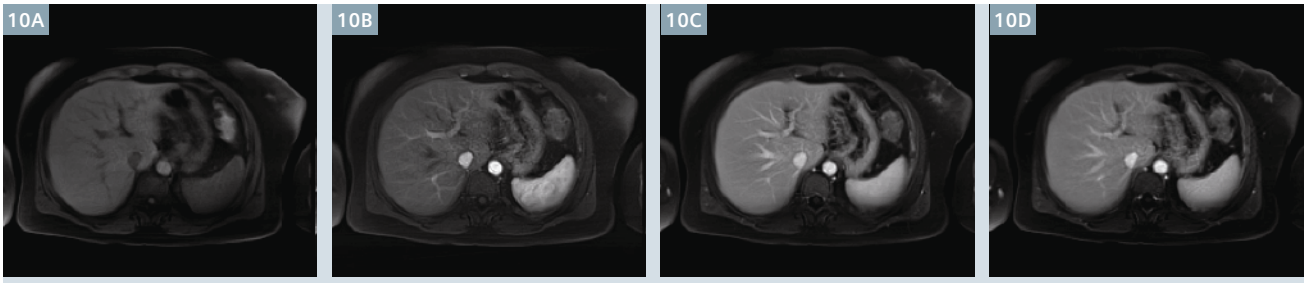

TR 3.3 ms, TE 1.4 ms, TA 21.35 sec, SL 4 mm, FOV 380 x 380

10 46-year-old female patient, immigrant, unable to understand the language in which the breathing commands were spoken. Modified StarVIBE sequence was used to acquire dynamic imaging before and after contrast-enhancement: **(10A)** without contrast medium, **(10B)** late arterial phase, **(10C)** first hepatovenous phase, **(10D)** second hepatovenous phase. Note the sharp organ contours and the well delineated anatomic structures without breath-hold imaging in different phases (each phase less than 22 seconds). (Also see table 2)

	Original parameters	Parameters for T1 StarVIBE dynamic liver imaging
Voxel size (mm)	1.2 x 1.2 x 3.0	1.7 x 1.7 x 4.0
Slab group		
Position	Isocenter	Isocenter
Orientation	Transversal	Transversal
Rotation	0.00 deg	90 deg
Phase directions	A - P	R - L
Slice oversampling	44.5%	0.0%
Slices per slab	72	52
FOV (mm)	380	380
Slice thickness (mm)	3	4
TR (ms)	2.83	3.26
TE (ms)	1.48	1.44
Flip angle	9 deg	10 deg
Lines per shot	56	18
Coil elements	BO1-3;SP2,3	BO1-3;SP2-4
Contrast – Dynamic		
Multiple series	Each measurement	Off
Resolution		
Base resolution	320	224
Radial views	680	220
System adjustments		
B1 Shim mode	TrueForm	Off
Sequence part 1		
Bandwidth (Hz/Px)	820	600
Sequence Assistant		
Allowed delay	60 s	–
TA (min)	2:53	0:21

Table 2: Modified parameters for dynamic liver imaging for totally uncooperative patients.

of lower extremity arteries (Fig. 11). Furthermore the QISS sequence can visualize arterial vessels in the lower leg each time without any overlay of venous vessels, which may happen in contrast-enhanced angiography. Knowing the adverse effects of contrast-media discussed in recent years, such as nephrogenic systemic fibrosis (NSF) and gadolinium accumulation in the brain, and having recently had the personal experience of a very rare life-threatening anaphylactic shock due to gadolinium administration, we do appreciate any development in this direction.

Summary

Our long-term experience with MR upgrades is a real success story. Technical innovations lead to better image quality and faster examination protocols, help improve the comfort and safety of the patients through the MR-examination, and especially help increase the radiologists' confidence in the final diagnosis. Therefore, an increased image quality that convinces the referring physician is an improvement in the quality of our product that we hope will lead to a better patient outcome.

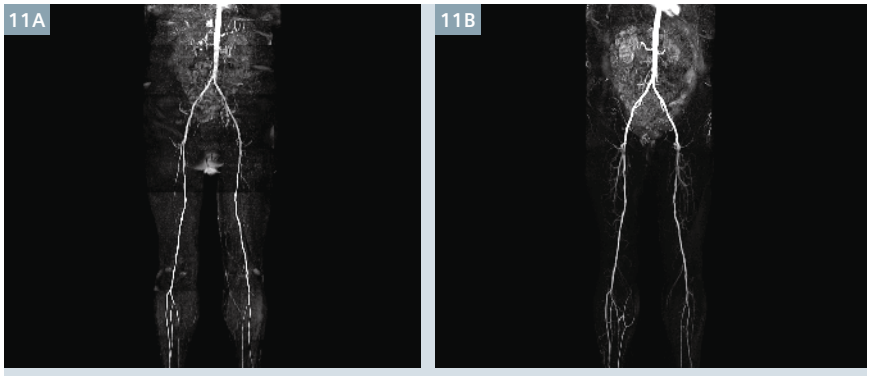

TR 544.4, TE 1.7, TT 475.0, TI 345.0 **TR 3.0, TE 1.0**

11 71-year-old female patient. Comparison between MR Angiography (MRA) with QISS technique without intravenous contrast administration **(11A)** and MRA with intravenous contrast administration (gadobenate dimeglumine) **(11B)**. Note the comparable image quality in **(11A)** without intravenous contrast. One of the additional benefits of the QISS technique is the lack of overlapping venous artifacts as seen sometimes in contrast-enhanced MRA.

Contact

Christos Loupatatzis, M.D.
Spital Maennedorf
Department of Radiology
Asylstrasse 10
8708 Maennedorf
Switzerland
Phone: +44 922 20 10
c.loupatatzis@spitalmaennedorf.ch

The fit Experience in Canada

Nancy Talbot, MAppSc, M.R.T.(R.)(M.R.)

Princess Margaret Cancer Center, University Health Network, Toronto, Canada

Introduction

Canada has a large number of MAGNETOM Avanto 1.5T scanners, and a growing number of MAGNETOM Avanto^{fit} 1.5T scanners.

Due to the funding models in Canada, currently and in the foreseeable future, there is the mentality of having to do more with less. Canada has a low number of MRI systems per capita compared to many other countries, and a scanner runs on average 18 to 24 hours per day.

The Siemens Avanto^{fit} upgrade program allows radiologists and technologists to bring their existing systems up to the cutting edge of MRI technology, at a significantly lower cost than a new high end clinical system, all within a very short three weeks of downtime. A new system installation is normally ten to fourteen weeks of downtime due to construction, possible damage/ replacement of the radio frequency cage etc.

The upgrades

The Toronto General Hospital (TGH) and the Princess Margaret Cancer Center (PM) MRI departments, both part of the University Health Network (UHN) and the Joint Department of Medical Imaging (JDMI), upgraded to the MAGNETOM Avanto^{fit} and MAGNETOM Skyra^{fit} systems in late 2013.

These included two MAGNETOM Avanto 1.5T scanners to Avanto^{fit}, and two MAGNETOM Verio 3T scanners to the Skrya^{fit} system. As the first fit upgrades in North America for Siemens, each scanner had a planned downtime of 4 weeks to anticipate a learning curve on the install process. The upgrade process, which included mechanics, Siemens commissioning and applications training spanned approximately four months for the two hospital sites. Back to back upgrades took place at Toronto General followed by Princess Margaret.

1 Liver imaging.

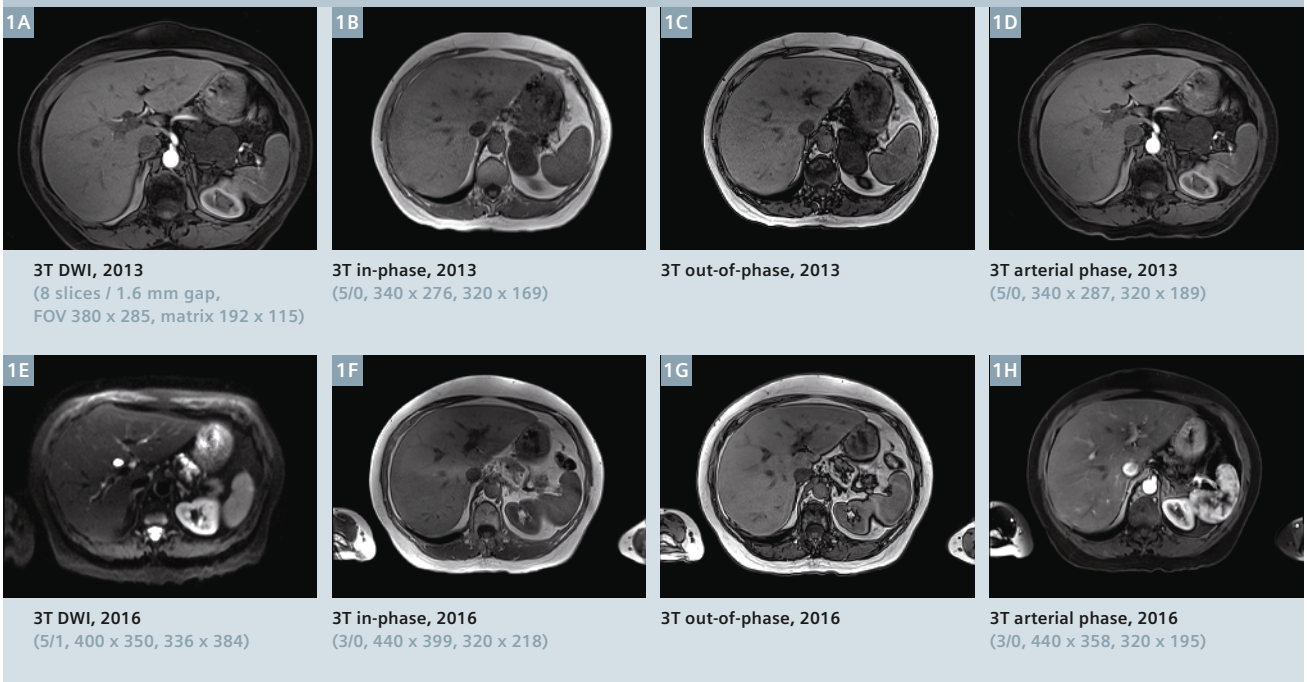

1A 3T DWI, 2013 (8 slices / 1.6 mm gap, FOV 380 x 285, matrix 192 x 115)

1B 3T in-phase, 2013 (5/0, 340 x 276, 320 x 169)

1C 3T out-of-phase, 2013

1D 3T arterial phase, 2013 (5/0, 340 x 287, 320 x 189)

1E 3T DWI, 2016 (5/1, 400 x 350, 336 x 384)

1F 3T in-phase, 2016 (3/0, 440 x 399, 320 x 218)

1G 3T out-of-phase, 2016

1H 3T arterial phase, 2016 (3/0, 440 x 358, 320 x 195)

The upgrade itself included all components except the gradient coil and the magnet for all four of the systems. Each scanner was already equipped with the SQ gradients 45/200. Systems that were equipped with the Q gradient 33/125 would be upgraded to the SQ gradient. Coil and software upgrades were dependant on the configurations of the existing systems and discussions with Siemens during the purchase. The upgraded 1.5T systems are essentially now a MAGNETOM Aera scanner with a 60 cm bore, and the 3T upgraded system is now a MAGNETOM Skyra scanner, bringing them up to the current standards of the top systems in the fleet. The fit systems also offer the option of upgrading to the Tim Dockable Table.

First experience

Once the upgraded systems were in operation, from an imaging perspective, users immediately saw an improvement in signal-to-noise ratio (SNR) for neuro exams. For exams requiring greater resolution, users were able to drop the field-of-view (FOV) and still see better SNR than on the previous system. This was also evident with the 3T system where pelvic and abdominal imaging was greatly improved both by the 18-channel body matrix coil, but also with the use of the FREEZEit CAIPIRINHA-Dixon-TWIST-VIBE sequence. In our cardiac imaging at the Toronto General site, scan times were shortened on many exams by the implementation of the Cardiac Dot Engine.

If the technologists were to list their favorite features of the upgrade, they would name: the Tim Dockable Table, the ability to reset the patient alarm in the room, faster table movement when the align light is on, and the ability to start the scan from inside the room.

From an exam quality perspective, there were improvements in imaging across the entire body. Time is needed to work through site protocols to optimize to radiologists preferences, however, there is no doubt that the upgrade has been well worth it. Some examples following will show improvements to the imaging. In drastic cases, we were able to eliminate the use of the endorectal coil for 3T prostate imaging for most indications, while in subtle cases, there is simply improved SNR while utilizing the same parameters.

Imaging examples

All images shown are of the same patient and on the same scanner before and after the upgrade.

The sequence details provided are (slice/gap, FOV, matrix).

2 Prostate imaging. After the 3T system upgrade (2016) we gained equivalent image quality as previous exams done with the endorectal (ER) coil (2010).

2010 Scan done with endorectal coil	2016 Scan done with 18-channel Body coil
2A 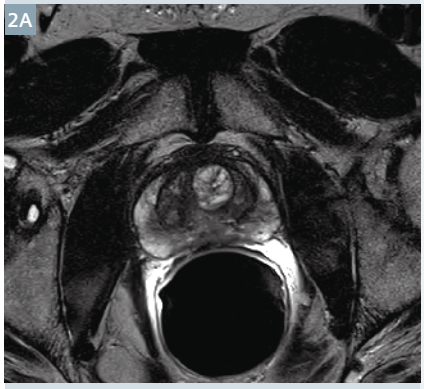	2B 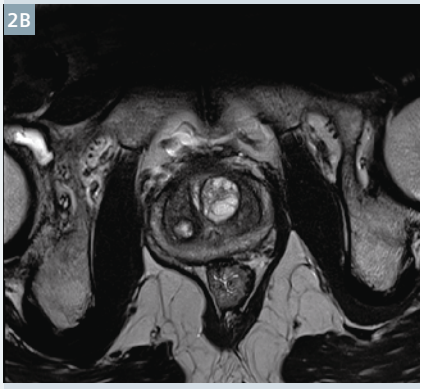
3T axial T2w, 2010 (3/0, 140 x 140, 320 x 256)	**3T axial T2w, 2016** (3/0.6, 160 x 160, 320 x 310)
2C 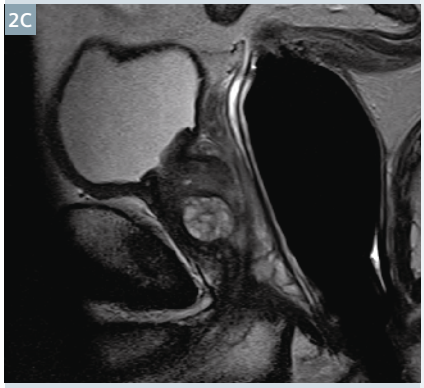	2D 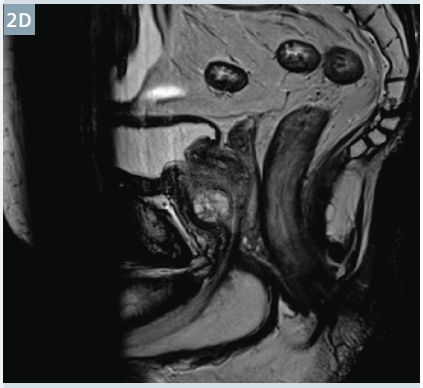
3T sagittal T2w, 2010 (4/0, 140 x 140, 320 x 192)	**3T sagittal T2w, 2016** (3/0.6, 200 x 200, 320 x 310)
2E 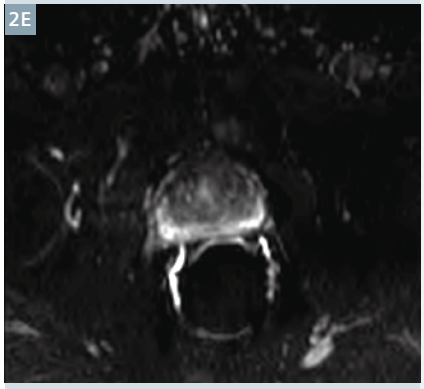	2F 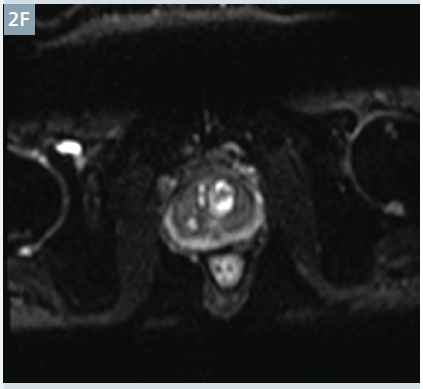
3T DWI, 2010 (3/0, 184 x 184, 128 x 128)	**3T DWI, 2016** (3/0, 200 x 200, 128 x 128)

3 Brain imaging at 1.5T shows improved SNR (note: the resolution for FLAIR is decreased).

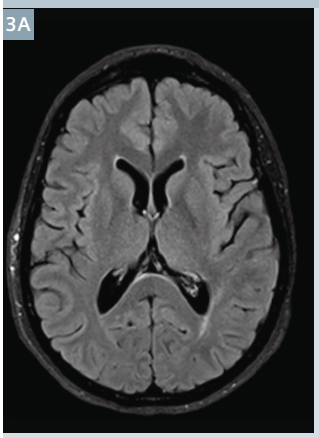

1.5T axial FLAIR, 2011
(4/1, 230 x 183, 512 x 408)

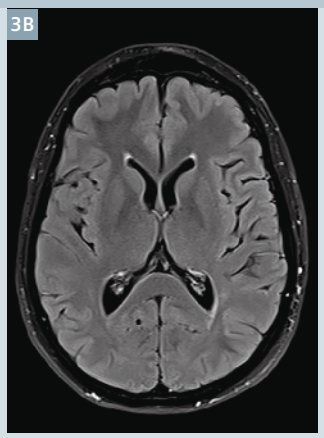

1.5T axial FLAIR, 2016
(4/1, 230 x 180, 320 x 175)

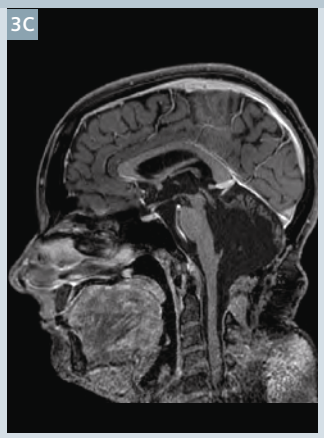

1.5T sagittal MPRAGE, 2011
(1 mm, 250 x 250, 256 x 256)

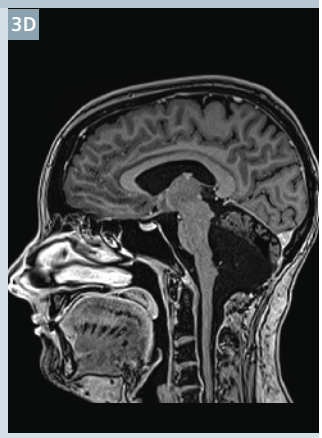

1.5T sagittal MPRAGE, 2016
(1 mm, 250 x 250, 256 x 256)

4 Sella imaging at 3T.
The parameters are the same but note the significant increase in SNR throughout the images with the Skyra^{fit} upgrade.

3T sagittal T1w, 2012
(2/0, 180 x 180, 384 x 384)

3T coronal T1w, 2012
(2/0, 180 x 180, 320 x 320)

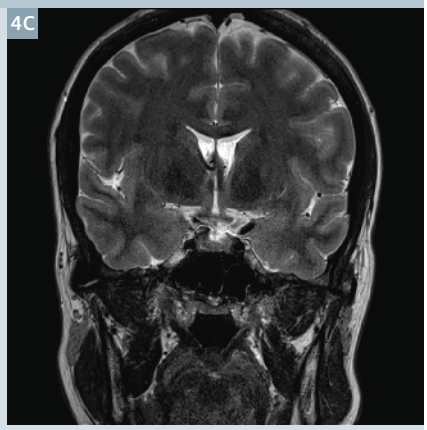

3T coronal T2w, 2012

3T coronal T1w, 2016
(2/0, 180 x 180, 320 x 320)

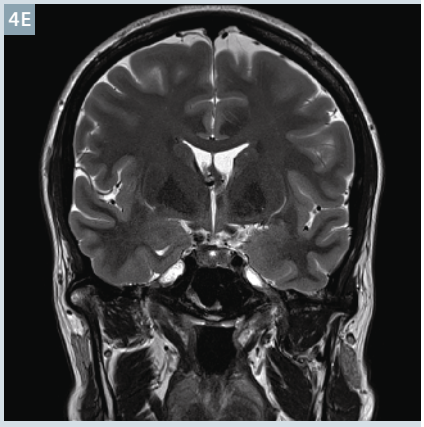

3T coronal T2w, 2016

5 After the 3T system upgrade (2016) we increased resolution on T2 imaging in pelvic exams.

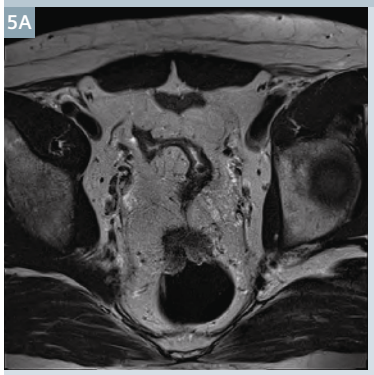

3T axial T2w, 2012
(4/1, 220 x 220, 320 x 320)

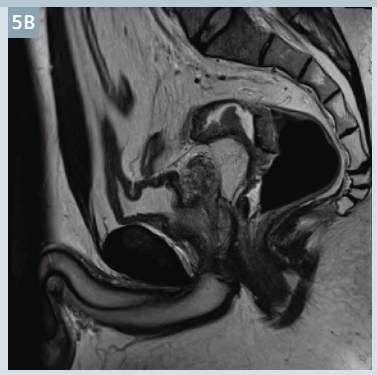

3T sagittal T2w, 2012
(4/1, 220 x 220, 320 x 320)

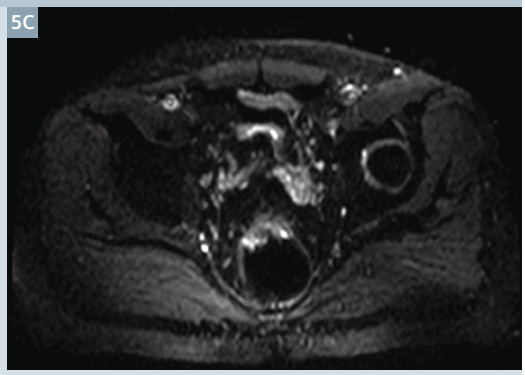

3T axial DWI, 2012
(4/0.8, 278 x 370, 384 x 230)

3T axial T2w, 2016
(4/1, 200 x 200, 320 x 320)

3T sagittal, T2w, 2016
(3/0.5, 220 x 220, 320 x 320)

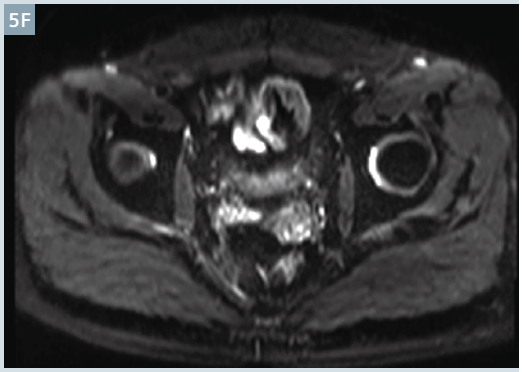

3T axial DWI, 2016
(4/1, 144 x 192, 340 x 340)

"The fit upgrade option is of an amazing value. If you have a system with a stable magnet, you will end up with the equivalent to a new system at approximately a third of the cost, as well as decreased downtime.

We are happy to keep our Avanto magnet, with the 50 cm z-axis FOV and excellent homogeneity, and yet have all the features and software of the Aera system."

Nancy Talbot, MRI Supervisor,
Princess Margaret Cancer Centre

The statements by Siemens' customers described herein are based on results that were achieved in the customer's unique setting. Since there is no 'typical' setting and many variables exist there can be no guarantee that other customers will achieve the same results.

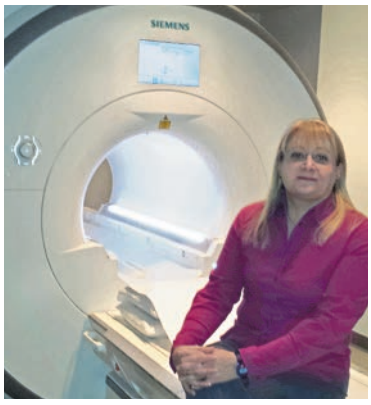

Contact

Nancy Talbot, MAppSc, M.R.T.(R.)(M.R.)
MRI Supervisor
Princess Margaret Cancer Center
3-970
610 University Avenue
Toronto, ON M5G 2M9
Canada
Phone: +1 416-946-4501 ext. 5369
nancy.talbot@uhn.on.ca

Review: Magnetic Resonance Imaging of Muscle Denervation Syndromes

Gustav Andreisek, M.D., MBA[1,2]; Avneesh Chhabra, M.D.[3]

[1] Radiology, Spital Thurgau, Münsterlingen, Switzerland
[2] University of Zurich, Zurich, Switzerland
[3] Musculoskeletal Radiology, University of Texas Southwestern Medical Center, Dallas, TX, USA

Introduction

Muscles can be affected by a broad variety of pathologies, one of which is muscle denervation syndrome. As the term indicates, muscular denervation syndrome is caused by an underlying neurogenic disorder. There are a broad variety of neurogenic disorders that can cause these muscle abnormalities clinically and on imaging. The list of pathologies includes, but is not exclusively limited to [1]:

1. **Systemic nerve diseases**
   e.g. ischemia, vasculitis, toxic, endocrine and metabolic disorders [2], hereditary motor-sensory neuropathies, amyloidosis, hyperlipidemia, acute and chronic demyelinating inflammatory neuropathies, etc.
2. **Local conditions**
   e.g. plexopathy, nerve injury, perineural or intraneural compressive lesions, adhesive neuropathy after surgery, infections and nerve sheath tumors, etc.
3. **Neuropathies related to functional anatomical changes**
   e.g. habitual leg crossing, repeated typing, obesity and repetitive exercise, which may cause traction mononeuritis or compressive neuropathy in functional compartment syndromes.

Muscle abnormalities as depicted on magnetic resonance imaging

Neurogenic magnetic resonance (MR) imaging abnormalities of skeletal muscles are related to time course of development. In the early phase, increased muscle signal on fat-suppressed T2-weighted or STIR images is the main imaging finding. It is hypothesized to be related to increased intramuscular fluid, congestion and/or relative shift of intra- and extra-compartmental fluid due to factors, such as altered muscle activity or inactivity. Subsequently, over time, it progresses to muscle atrophy and fatty infiltration with associated increased signal on T1-weighted images (Fig. 1).

In late stages, there might or might not be an increased signal on fat-suppressed T2-weighted or STIR images, and the predominant imaging finding is muscle atrophy characterized by increased signal on T1-weighted images associated with loss of muscle volume. MR imaging has a high sensitivity for the detection of increased muscle signal on fat-suppressed T2-weighted or STIR images and the changes appear earlier than on US or CT imaging.

Increased signal on fat-suppressed T2-weighted or STIR images of muscles is also seen with a number of other muscle disorders. The list of possible pathologies causing increased T2 signal is broad and includes trauma, early myositis ossificans, inflammatory myopathies such as dermatomyositis, polymyositis, eosinophilic myositis, proliferative myositis, or myositis associated with connecting connective tissue diseases, infectious myositis, infiltrating neoplasm, rhabdomyolysis, muscle infarction, sickle cell disease, or overuse syndromes. Whereas some differential diagnosis can be excluded based on clinical examination or labo-

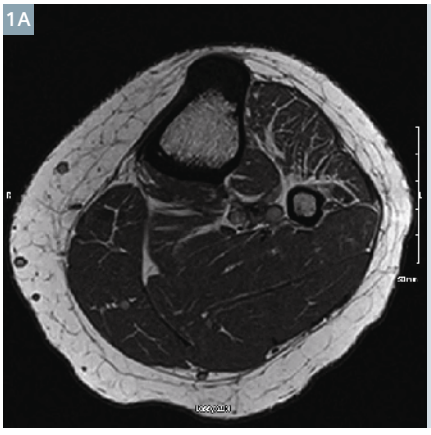

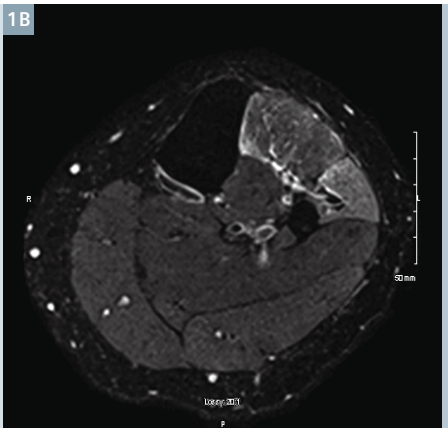

1 Axial images of a 36-year-old man with traumatic common peroneal nerve injury. MR images show a typical muscle denervation pattern in the subacute phase with increased signal and mild loss of bulk on T1-weighted (**1A**) and fat saturated T2-weighted (**1B**) images affecting the tibialis anterior, extensor digitorum and peroneal muscles.

ratory data, many of them may remain on the list of possible differential diagnosis. MR imaging is also highly sensitive but specificity may vary due to factors such as reader skill, technique and unavailable clinical history and findings at the time of interpretation. Therefore, it is important to understand the role of MR imaging in these conditions, as MRI cannot be the 100% problem-solving tool in all cases [3]. However, its real value is in excluding many other differential diagnoses, therefore supporting establishment of the main diagnosis [4]. This role is important as it can help in lowering healthcare costs by avoiding unnecessary exams or assessments as well as reducing the risk of a delayed diagnosis. In fact, this might become even more important in healthcare systems where ideology and planning exits to reimburse procedures based on their value (value-based healthcare model).

The role of MR imaging in neurogenic muscle disorders includes, but is not exclusively limited to [1]:

1. **Systemic nerve diseases**
   MR imaging is not expected to make these diagnoses alone. However, MRI may be used to confirm the clinical suspicion (based on symptoms, clinical exam, electrodiagnostic tests and laboratory findings) by demonstrating abnormality of the innervating and regional muscle denervation changes or, exclude any structural cause for neuropathies in these cases. The muscle denervation changes are limited to the territory of neuropathic nerves, are diffuse without intramuscular hemorrhage and there is no associated perimuscular or perifascial edema as could be conspicuous in myopathy cases.

2. **Local conditions**
   MR imaging has a major role in these cases as it supplements information gained from the clinical exam and electrodiagnostic tests or provides information, which may not be possible to attain from other (imaging) modalities. Not only the muscle denervation change is visible but also the offending lesion, such as an intra- or perineural lesion (Fig. 2) or other tumors (Fig. 3), can be identified.

2 35-year-old man with physical signs of a winged scapula after motor vehicle accident. Coronal T1-weighted MR image shows atrophy of the right serratus anterior muscle compared to the normal contralateral left side (**2A**, arrows). The muscle is innervated by the long thoracic nerve which appears both, thickened on T1-weighted MR images (**2B**, arrow), and with increased signal intensity on fat suppressed T2-weighted MR images (**2C**). For comparison, corresponding MR images of the left normal long thoracic nerve are shown (**2D, E**). Please note that the long thoracic nerve directly arises from C5-7 without entering the brachial plexus. It does not innervate other muscles.

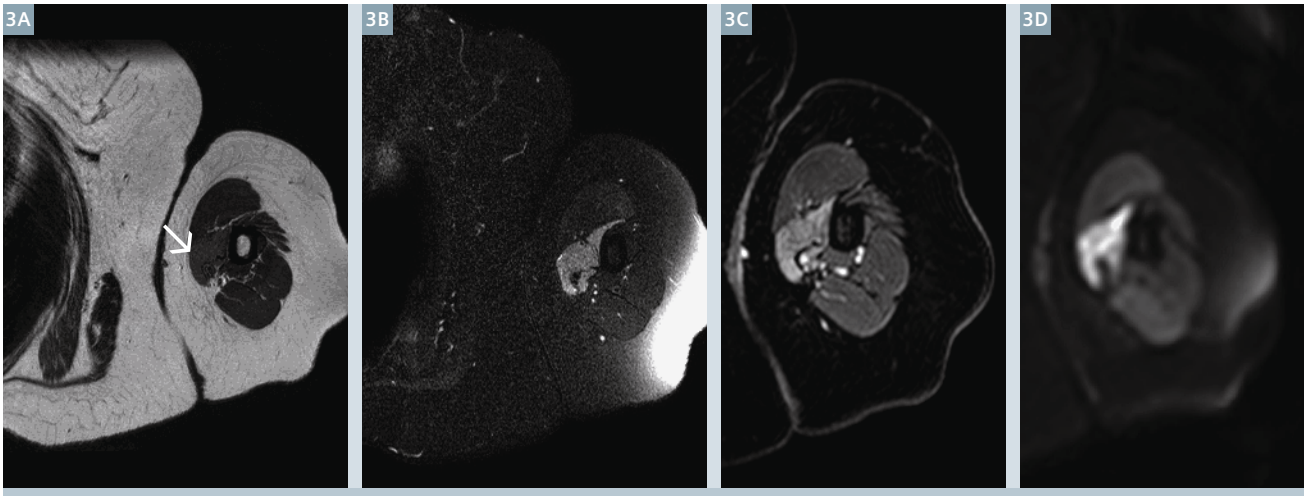

3 Axial MR images of a 46-year-old woman with clinical weakness of the coracobrachialis muscle (arrow). MR images show increased signal on T1-weighted (**3A**) and fat saturated T2-weighted (**3B**) MR images. However, there is also enhancement on postcontrast fat suppressed T1-weighted MR images as well as diffusion restriction on b=800 diffusion-weighted images raising the suspicion of a non-neurogenic disorder. In this case, MR-targeted muscle biopsy revealed muscle lymphoma.

3. Neuropathies related to functional anatomical changes
The role of MR imaging is limited in these circumstances. These disorders are mostly diagnosed on the basis of clinical and pressure catheter studies. Sometimes, ultrasound examinations are used to unveil dynamic nerve compression or dislocation. However, rarely, MRI may be used in clinically confounding cases with imaging performed before and after the exercise/effort in question. Indirect signs such as significant prolongation of T2 signal intensity within the affected muscle compartment may aid in the diagnosis of compartment syndrome.

Nerve disorders

The underlying cause for muscle denervation syndrome includes a broad variety of neurogenic diseases that can be divided according to the anatomic site of affliction (neuromuscular junction or nerve cell body, axon and myelin sheath) or functional involvement (sensory, motor or autonomic) [5].

Neuromuscular junction (NMJ) disorders are primarily related to acetylcholine receptor abnormalities. They can be familial/congenital, such as myasthenia gravis, or acquired, such as drug induced, botulism or paraneoplastic (Eaton-Lambert syndrome). Whereas many neuromuscular disorders show predominant involvement of lower extremities, NMJ disorders present with facial and extraocular muscle weakness, however, with normal tendon reflexes and normal sensation. The latter is usually confirmed by electrodiagnostic tests showing normal electromyograms and normal nerve conduction velocities. By contrast, nerve diseases distal to the NMJ may present with motor weakness, sensory symptoms and autonomic symptoms depending upon the affected nerve and its functional role. In these cases, electrodiagnostic studies usually show pathologic electromyograms as well as delayed nerve conduction [1].

With predominant axonal involvement, distribution of involvement and clinical presentation are usually distal > proximal, and legs > arms. Nerve biopsy may be useful in axonal and myelin disorders. The pathologist usually classifies the histologic alterations as axonal neuropathy, demyelinating neuropathy, inflammatory neuropathy, or as a process of the supporting and/or vascular tissues, such as vasculitis, storage disease, and infectious or neoplastic infiltration. However, MR imaging findings of muscle denervation can be very similar and should be correlated with clinical, available electrodiagnostic, and other clinical and/or laboratory information to establish the final diagnosis [6]. MR imaging, especially MR neurography, is particularly helpful in demonstrating the nerve lesions and localization of the pathology. The affected nerve shows most signal, fascicular and/or caliber alteration, at or immediately proximal to the site of compression or injury. The affected muscles often show enhancement on post gadolinium imaging but there is no significant restriction on diffusion-weighted imaging (DWI). MR neurography is also helpful in grading the nerve injury into stretch injury, neuroma in continuity and complete nerve discontinuity (Fig. 4).

The differential diagnosis of myopathies (muscular dystrophy/myositis) may result from infectious, endocrine, metabolic, autoimmune, myoglobinuria or familial causes, such as limb-girdle syndrome. Myopathies present with isolated motor symptoms and the distribution is usually proximal and symmetric with absent tendon reflexes in the involved muscles. Electrodiagnostic testing is usually pathologic with respect to the motor unit potential analysis (e.g. abnormal amplitude, duration, number of phases, and firing rate). In addition, serologic exams might show high creatine kinase levels

in myopathies. Muscle biopsy is often used to make the final diagnosis and the role of MR imaging is to show one or a combination of edema like signal intensity changes on fat suppressed T2-weighted MR images, fatty infiltration or atrophy depending upon the stage of the disease, similar to denervation muscle changes. However, the involved muscles may not correspond to single nerve territory and regional nerves will show normal signal intensity, thereby excluding neuropathy as the cause of muscle findings. Patchy involvement, multicompartment affliction, perimuscular fascial edema and patchy intramuscular and or fascial enhancement may be seen with myositis, which is absent with muscle denervation changes. On DWI, the presence of a mass lesion can show diffusion restriction (Fig. 3). In myopathy cases, the nerves show normal signal and MR imaging appearance.

In conclusion, MR imaging in muscle denervation syndromes is very valuable in either establishing the diagnosis, ruling out related pathologies, or a combination of both.

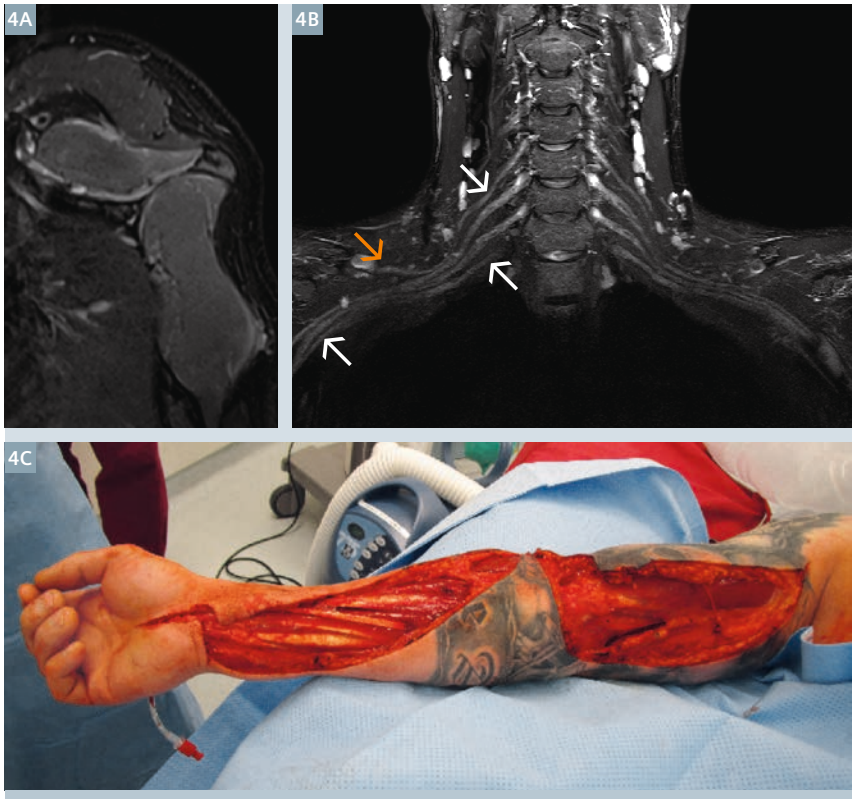

4 MR image of a 32-year-old man after a high-voltage accident and with palsy of the right arm. MR neurography shows increased T2-signal of supraspinatus and infraspinatus muscles of the right shoulder (**4A**) as well as mild thickening and hyperintensity of the right brachial plexus (white arrows) and suprascapular nerve (orange arrow) on coronal STIR SPACE image (**4B**) in keeping with traction injury with possible ischemia. Subsequently, muscle compartment arm and forearm decompression surgery was performed (**4C**).

References

1 Chabbra A, Andreisek G. Magnetic Resonance Neurography. London: Jaypee, 2012.

2 Thakkar RS, Del Grande F, Thawait GK, Andreisek G, Carrino JA, Chhabra A. Spectrum of high-resolution MRI findings in diabetic neuropathy. AJR American journal of roentgenology. 2012;199(2):407-12.

3 Wessig C, Bendszus M, Reiners K, Pham M. [Lesions of the peripheral nerves: MR neurography as an innovative supplement to electrodiagnostics]. Handchirurgie, Mikrochirurgie, plastische Chirurgie: Organ der Deutschsprachigen Arbeitsgemeinschaft für Handchirurgie: Organ der Deutschsprachigen Arbeitsgemeinschaft für Mikrochirurgie der Peripheren Nerven und Gefasse 2012;44(3):155-62.

4 Chhabra A, Andreisek G, Soldatos T, et al. MR neurography: past, present, and future. AJR American journal of roentgenology. 2011;197(3):583-91.

5 Chhabra A. Peripheral MR neurography: approach to interpretation. Neuroimaging Clin N Am. 2014;24(1):79-89.

6 Chhabra A, Zhao L, Carrino JA, et al. MR Neurography: Advances. Radiology research and practice. 2013;2013:809568.

Avneesh Chhabra

Gustav Andreisek

Contact

PD Dr. Gustav Andreisek, M.D., SCMR
Executive MBA HSG
Head of Radiology
Kantonsspital Münsterlingen
Spitalcampus 1
8596 Münsterlingen
Switzerland
Phone: +41 71 686 23 30
Fax +41 71 686 26 74
gustav@andreisek.de

Utility of MRI Findings in Inflammatory Myopathies

Christopher J. Hanrahan; Barry G. Hansford

Department of Radiology and Imaging Sciences, University of Utah School of Medicine, Salt Lake City, UT, USA

Introduction

MR imaging can provide important information for establishing a diagnosis in inflammatory myopathies, and routine MRI sequences can help exclude alternative diagnoses. With MRI, muscle pathologic findings typically fall into three categories: mass lesions, fatty atrophy, and edema [1]. Masses can include muscle injury with hematoma or myositis ossificans, sarcoma or pseudosarcoma, abscess, parasitic infection, or sarcoidosis. Fatty infiltration and atrophy is the end-stage result of many muscle pathologies, including disuse, myopathy, tendon injury, or denervation. Muscle edema is the third muscle pathology commonly encountered with clinical MR imaging. Muscular edema can be caused by muscle injury, denervation, drug-induced myopathy, or inflammatory myopathies including paraneoplastic syndromes. The focus of this article is to present several cases of muscle edema to demonstrate the utility of MR imaging in simplifying the differential diagnosis based on the distribution of findings and clinical history.

Case 1

A 37-year-old male rancher developed pain, weakness, and slight stiffness in his left thigh one month previously and noticed a mass. He denied any injury or constitutional symptoms. On his initial examination, he was afebrile with mild swelling of his left thigh with tenderness and a palpable mass. There was no redness or warmth to touch. He showed 4/5 strength with extension, but there was no atrophy of the left thigh. His initial radiographs were negative. His initial MRI showed extensive edema within the vastus medialis and intermedius muscles with a central mass with low intensity rim (Fig. 1A-C). Follow-up MRI three months later, showed decreased muscular edema and development of a discreet mass with low signal intensity rim (Fig. 1D-F).

Diagnosis: Myositis Ossificans

Myositis ossificans is a benign, self-limited condition that presents following an injury to muscle [2]. The presenting clinical scenario may mimic muscle denervation or myopathy and since patients frequently do not recall an inciting event. The initial imaging may also be confusing, especially on MRI, given the intramuscular inflammatory mass-like appearance and lack of zonal peripheral mineralization. In this particular case, there is no initial muscle abnormality visible on the T1 sequence (Fig. 1A), but rim of low signal intensity on the fluid sensitive sequence indicates an underlying mass (Fig. 1C), which in some cases is only appreciated after subsequent imaging [2]. A mass usually develops within 6-8 weeks and extensive edema has been described in lesions that are imaged within 8 weeks of the inciting event [2]. Clinical and imaging follow-up can confirm the diagnosis (Figure 1D-F). The ossific rim usually appears after 4-6 weeks, but early in its formation may only be visible by CT [2]. Post-contrast imaging will demonstrate enhancement due to its extensive vascularity [2]. Biopsy should be avoided, especially early (within 1-2 weeks) when the mass could potentially be confused upon histology with extraskeletal osteosarcoma resulting in aggressive therapies for an inherently benign condition [3].

Case 2

A 56-year-old female with renal cell carcinoma developed right lower extremity weakness, primarily with extension following radical right nephrectomy, retroperitoneal lymph

Key Points

Inflammatory myopathies encompass several rare diseases that affect the lower extremities greater than the upper extremities and include inclusion body myositis, polymyositis, and dermatomyositis. The presence of inflammatory myopathy must be distinguished from other potential causes of muscle pathology, including muscle injury, nerve injury, rhabdomyolysis, tumor and diabetic ischemic myopathy. MR imaging can help to exclude other pathologies and can provide important information about the location and extent of inflammation. For cases in which a specific diagnosis by MRI alone may not always be possible, MRI may provide value in localizing the greatest areas of inflammation to focus muscle biopsy, since treatments may differ depending on the underlying etiology.

node dissection, and inferior vena cava thrombectomy, which was complicated by iliopsoas and paraspinal hematoma. Five months following surgery she was evaluated and found to have 0 out of 5 right quadriceps muscle strength compared to 5 out of 5 strength within the extensor hallucis longus, tibialis anterior, gastrocnemius, and soleus muscles. Pelvic MR imaging was performed and demonstrates unilateral muscle edema within the quadriceps musculature, specifically the rectus femoris and vastus lateralis muscles (Fig. 2).

Diagnosis: Femoral Nerve Injury
MR imaging can help distinguish a nerve injury edema pattern from myopathy. Most commonly, MR imaging of denervation is unilateral and demonstrates edema and possibly atrophy of the musculature within a specific and typical distribution of the affected nerve. Although electromyography (EMG), nerve conduction studies, or ultrasound can be used to localize nerve injury, MR imaging has the advantage of greater sensitivity, non-invasiveness compared to EMG, superior anatomic resolution, and in some cases allows identification of aberrant nerve supply [4].

Case 3

A 58-year-old female who presented with a 12-day rash that initially started on her chest and back and spread to her neck, face and forehead. She revealed progressive muscle weakness over the course of the past year primarily within her shoulders and hips manifest by increasing difficulty brushing her teeth and climbing stairs. She had been treated with a steroid taper without significant improvement of her rash or her muscle weakness. On examination, she was afebrile with an erythematous rash over her upper, back, chest, and neck with macules and papules over her lateral thighs and elbows, but no rash over her eyelids. She was unable to lift her arms off the bed and had 3 out of 5 muscle strength with knee extension and mild decreased grip strength. She had an elevated creatine kinase at 678 (units/liter; reference range 20-180 U/l) with a normal erythrocyte sedimentation rate and C-reactive protein. Tests for anti-nuclear antibody, lyme disease, and coccidiomycosis were negative. An MRI of her thighs demonstrated relatively symmetric muscle edema within her knee extensors (Fig. 3). Initial muscle biopsy of her left vastus lateralis was negative, while subsequent biopsy of her right semitendinosus muscle revealed perivascular inflammation.

Diagnosis: Dematomyositis
Dermatomyositis is an autoimmune inflammatory myopathy that results in subacute symmetric proximal muscle weakness. There is a predilection for women and age can vary, but has a peak between 30 and 50 years of age [5]. The differential diagnosis of muscle weakness includes other inflammatory myopathies, such as polymyositis and inclusion body myositis. In this particular patient the presence of a rash favors dermatomyositis over polymyositis and inclusion body myositis, however it is important to exclude inclusion body myositis, as this disease does not respond to most therapies, including steroids [6, 7], as reportedly occurred in the short term with this patient. The disease is characterized by an erythematous rash and often has Gottron's papules over extensor surfaces as in this patient over the elbows. They frequently also have a heliotrope rash characterized by erythematous eyelids, which this patient did not have.

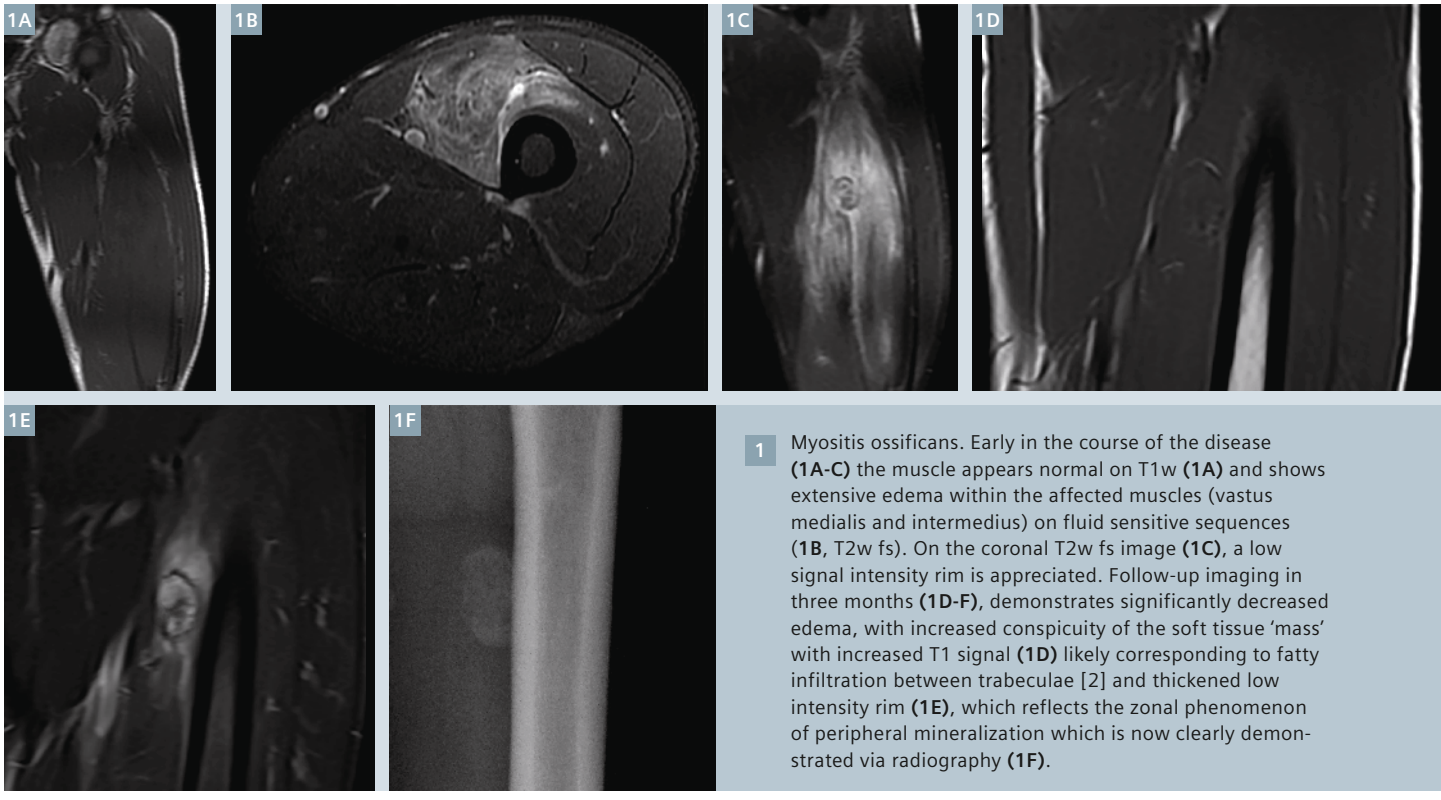

1 Myositis ossificans. Early in the course of the disease **(1A-C)** the muscle appears normal on T1w **(1A)** and shows extensive edema within the affected muscles (vastus medialis and intermedius) on fluid sensitive sequences (**1B**, T2w fs). On the coronal T2w fs image **(1C)**, a low signal intensity rim is appreciated. Follow-up imaging in three months **(1D-F)**, demonstrates significantly decreased edema, with increased conspicuity of the soft tissue 'mass' with increased T1 signal **(1D)** likely corresponding to fatty infiltration between trabeculae [2] and thickened low intensity rim **(1E)**, which reflects the zonal phenomenon of peripheral mineralization which is now clearly demonstrated via radiography **(1F)**.

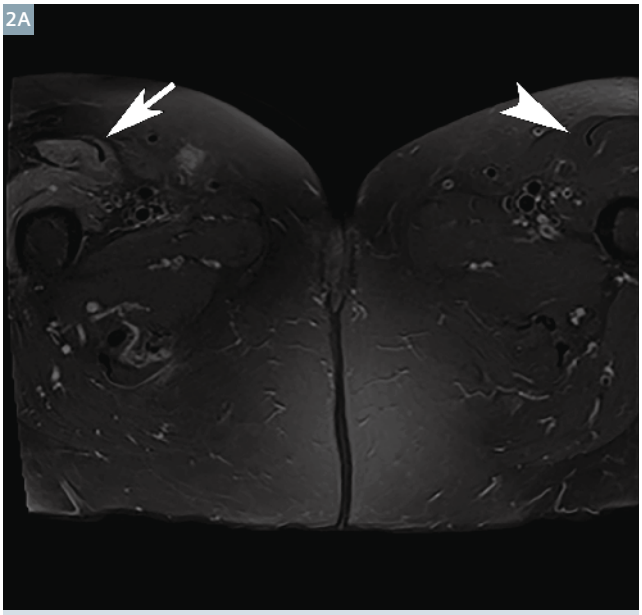

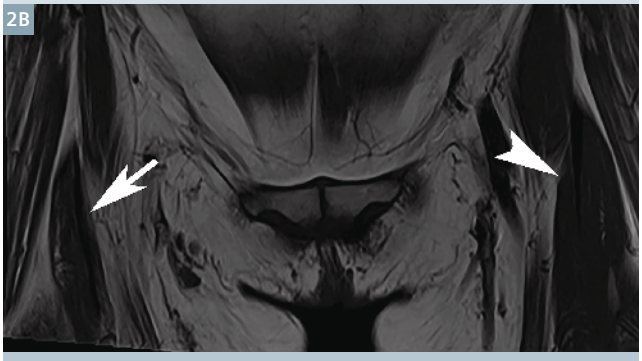

2 Right femoral distribution denervation. Five months following right nephrectomy for renal cell carcinoma, the patient has edema within the rectus femoris and vastus lateralis muscles (arrow in **2A**; T2w fat suppressed axial image) as well as mild atrophy (arrow in **2B**; T1w coronal image).

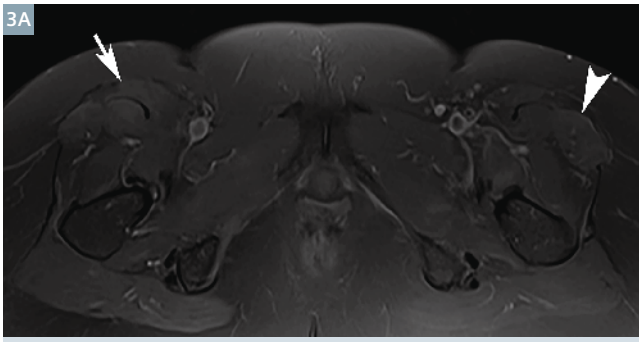

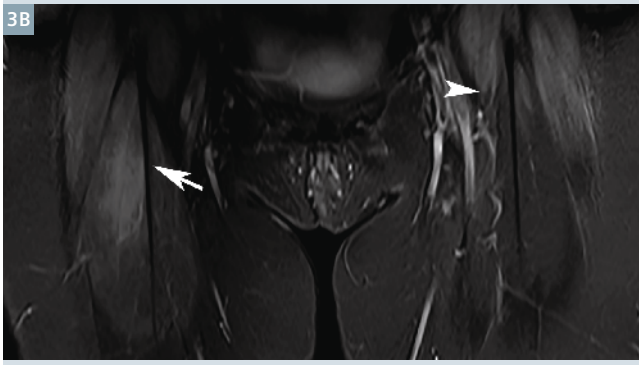

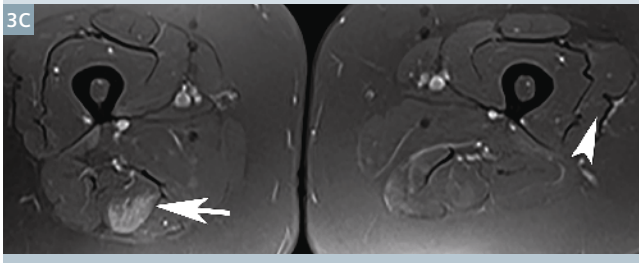

3 Dermatomyositis. Axial proton density with fat suppression **(3A)** and coronal STIR **(3B)** images demonstrate bilateral muscle edema in the rectus femoris and tensor fascia lata muscles (arrow on right side and arrowhead left side). Distal axial proton density-weighted image with fat suppression demonstrates asymmetric involvement of the right greater than left semitendinosus muscle (arrow) and no involvement of the left vastus lateralis muscle (arrowhead), which is consistent with the negative biopsy result performed at this location.

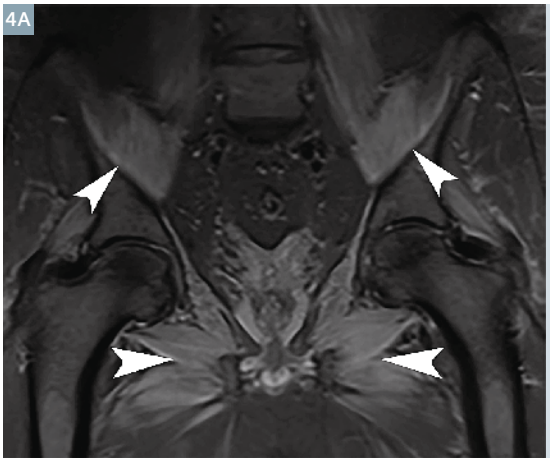

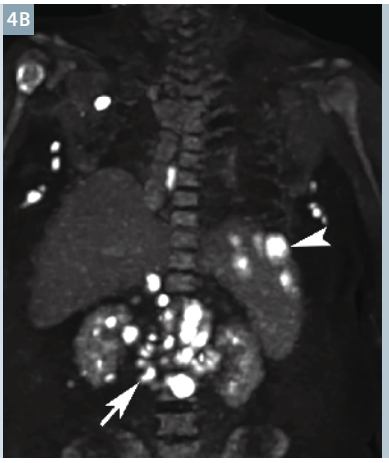

4 Polymyositis with lymphoma. Coronal STIR image **(4A)** of the pelvis demonstrates symmetric edema in multiple muscle groups (arrowheads). Maximum intensity projection (MIP) image from subsequent PET/CT scan **(4B)** demonstrates FDG uptake in extensive retroperitoneal lymphadenopathy (arrow) and splenic uptake (arrowhead) from lymphomatous infiltration.

MR imaging

MRI can be helpful in confirming the presence of myopathy, excluding non-inflammatory causes of muscle disease and, in some cases, differentiation between inflammatory myopathies. Ultimately, the definitive diagnosis is made through muscle biopsy. The distinguishing features of the inflammatory myopathies by histology include perivascular inflammation with dermatomyositis, endomysial inflammation with polymyositis, and both the presence of inclusion bodies and endomysial inflammation in inclusion body myositis [5, 7-10]. Theoretically, this would translate into differences in MR imaging, but in practice the edema and enhancement patterns in individual muscles overlap, especially between dermatomyositis and polymyositis. Dermatomyositis, with its perivascular inflammation, tends to have more perifascial muscle edema than polymyositis, which occurs more frequently in the juvenile form of the disease, but nevertheless is not diagnostic [11-13]. However, one distinguishing feature of inclusion body myositis by MR imaging is the relative sparing of the rectus femoris muscle early in the disease process and the predominant involvement of flexor digitorum profundus in the forearm [14, 15]. In this case, which is relatively early in the disease process based on the relative paucity of muscle atrophy, there is involvement of the rectus femoris muscle suggesting that this is not inclusion body myositis, despite a history of lack of response to steroids.

Case 4

A 59-year-old male presented with a one-month history of proximal muscle weakness, arthralgia, fevers, weight loss, and truncal rash, along with progressive shortness of breath. He underwent a laboratory workup and was found to be anemic with elevated c-reactive protein and ESR and a positive ANA. His SPEP was negative. He was initially put on steroids with a presumed lupus diagnosis, which helped his weakness. A subsequent elevated LDH and lymphadenopathy by computed tomography as well as a negative bone marrow biopsy prompted a referral to an oncologist. He then underwent a lymph node biopsy and MRI of the pelvis for muscle weakness (Fig. 4).

Diagnosis: Polymyositis with lymphoma

MR imaging revealed a highly symmetrical myopathy without significant perifascial edema, which was confirmed polymyositis by biopsy. Whenever the diagnosis of polymyositis or dermatomyositis is made, an occult malignancy should be considered [10, 16]. Malignancy associated with these inflammatory myopathies is defined as a malignancy diagnosed within 3 months of the diagnosis of inflammatory myopathy and occurs in 3-6% of polymyostis and 13-29% of dermatomyositis [10, 16]. Despite the relatively high association with underlying malignancy and likely paraneoplastic etiology, there is no current consensus regarding a standard malignancy workup for this patient population.

Barry G. Hansford

Christopher J. Hanrahan

Contact

Christopher J. Hanrahan, M.D., Ph.D.
Associate Professor and Section Chief, Musculoskeletal Imaging
Department of Radiology and Imaging Sciences
University of Utah School of Medicine
30 North 1900 East
Salt Lake City, UT, 84132, USA
Chris.hanrahan@hsc.utah.edu

References

1 May, D.A., et al., Abnormal signal intensity in skeletal muscle at MR imaging: patterns, pearls, and pitfalls. Radiographics, 2000. 20 Spec No: p. S295-315.
2 Kransdorf, M.J., J.M. Meis, and J.S. Jelinek, Myositis ossificans: MR appearance with radiologic-pathologic correlation. American Journal of Roentgenology, 1991. 157(6): p. 1243-1248.
3 Hoch, B. and A. Montag, Reactive bone lesions mimicking neoplasms. Semin Diagn Pathol, 2011. 28(1): p. 102-12.
4 Kim, S.-J., et al., MR Imaging Mapping of Skeletal Muscle Denervation in Entrapment and Compressive Neuropathies. RadioGraphics, 2011. 31(2): p. 319-332.
5 Mammen, A.L., Dermatomyositis and polymyositis: Clinical presentation, autoantibodies, and pathogenesis. Ann N Y Acad Sci, 2010. 1184: p. 134-53.
6 Greenberg, S.A., Inclusion body myositis. Curr Opin Rheumatol, 2011. 23(6): p. 574-8.
7 Greenberg, S.A., Pathogenesis and therapy of inclusion body myositis. Curr Opin Neurol, 2012. 25(5): p. 630-9.
8 Needham, M. and F.L. Mastaglia, Sporadic inclusion body myositis: A review of recent clinical advances and current approaches to diagnosis and treatment. Clin Neurophysiol, 2015.
9 Iaccarino, L., et al., The clinical features, diagnosis and classification of dermatomyositis. J Autoimmun, 2014. 48-49: p. 122-7.
10 Milisenda, J.C., A. Selva-O'Callaghan, and J.M. Grau, The diagnosis and classification of polymyositis. J Autoimmun, 2014. 48-49: p. 118-21.
11 Ladd, P.E., et al., Juvenile dermatomyositis: correlation of MRI at presentation with clinical outcome. AJR Am J Roentgenol, 2011. 197(1): p. W153-8.
12 Tomasova Studynkova, J., et al., The role of MRI in the assessment of polymyositis and dermatomyositis. Rheumatology (Oxford), 2007. 46(7): p. 1174-9.
13 Hernandez, R.J., et al., MR imaging in children with dermatomyositis: musculoskeletal findings and correlation with clinical and laboratory findings. AJR Am J Roentgenol, 1993. 161(2): p. 359-66.
14 Adams, E.M., et al., The idiopathic inflammatory myopathies: spectrum of MR imaging findings. Radiographics, 1995. 15(3): p. 563-74.
15 Cox, F.M., et al., Magnetic resonance imaging of skeletal muscles in sporadic inclusion body myositis. Rheumatology, 2011. 50(6): p. 1153-1161.
16 Andras, C., et al., Dermatomyositis and polymyositis associated with malignancy: a 21-year retrospective study. J Rheumatol, 2008. 35(3): p. 438-44.

High Resolution Isotropic 3D CAIPIRINHA SPACE MRI of the Musculoskeletal System

Gaurav K. Thawait, M.D.; Rushyuan J. Lee, M.D.; Derek F. Papp, M.D.; Jan Fritz, M.D.

Johns Hopkins University School of Medicine, Baltimore, MD, USA

Introduction

Magnetic resonance imaging (MRI) has an important role in the diagnosis, characterization and surveillance of many conditions affecting the musculoskeletal system, including trauma, degeneration, inflammation and infection of bone, joints, ligaments, tendons, and muscles.

The high-contrast resolution of native and contrast-enhanced MRI enables multiparameteric characterization of a multitude of conditions. The morphological analysis of musculoskeletal structures and fine detail are crucial for the detection and characterization of abnormalities, such as ligamentous tears, cartilage defects, muscle-tendon unit injuries, fractures as well as bone marrow abnormalities, collections, and neoplastic disease.

Technical considerations

Many abnormalities are accurately characterized by a combination of intermediate-weighted MR images without fat suppression and STIR (Short Tau Inversion Recovery) or T2-weighted MR images with fat suppression. In current practice, this is frequently achieved with the use of two-dimensional (2D) turbo spin echo (TSE) pulse sequences. 2D MR images can be acquired with a high in-plane spatial resolution, e.g. with a pixel size of 0.5 x 0.5 mm^2; however, in order to achieve a sufficient amount of MR signal, a slice thickness of 2-4 mm is required, which together with slice gaps generates partial volume effects. Owing to the inability for multiplanar reformations due to anisotropic voxel size, images in axial, sagittal and coronal orientation have to be acquired separately, which can be a time consuming process.

In contrast to 2D TSE, three-dimensional (3D) TSE using Sampling Perfection with Application optimized Contrast using different flip angle Evolutions (SPACE) is based on volume excitation and therefore yields markedly more MR signal. Using 3D SPACE with a high number of phase-encoding steps in z-direction enables the calculation of substantially thinner slice partitions and the generation of 3D MRI data sets with isotropic voxels size.

Such isotropic data sets with sufficiently small voxel size virtually eliminate partial volume effects and provide an opportunity for improved display of small anatomic detail. In addition, virtually any imaging plane can be reformatted from single parent data sets (Fig. 1), including standard axial, sagittal and coronal MR images, as well as oblique and curved planar reformations and 3D volume rendered MR images.

While this concept has been proven to be feasible with a diagnostic accuracy equal to or better than 2D TSE MRI [1-3], current 3D TSE techniques may be limited by low contrast-to-noise ratios (CNR), which could lead to limited conspicuity of cartilage and fluid [4], and image blur related to T2-decay during long echo trains and overall long acquisition times [5].

In order to increase the speed of 3D TSE image acquisition, one-dimensional parallel imaging techniques have been successfully applied, which reduces imaging time by undersampling in one phase encoding direction. Acceleration of 3D TSE, however, has typically been limited to a factor of 2, as higher unidirectional acceleration factors cause degradation of image

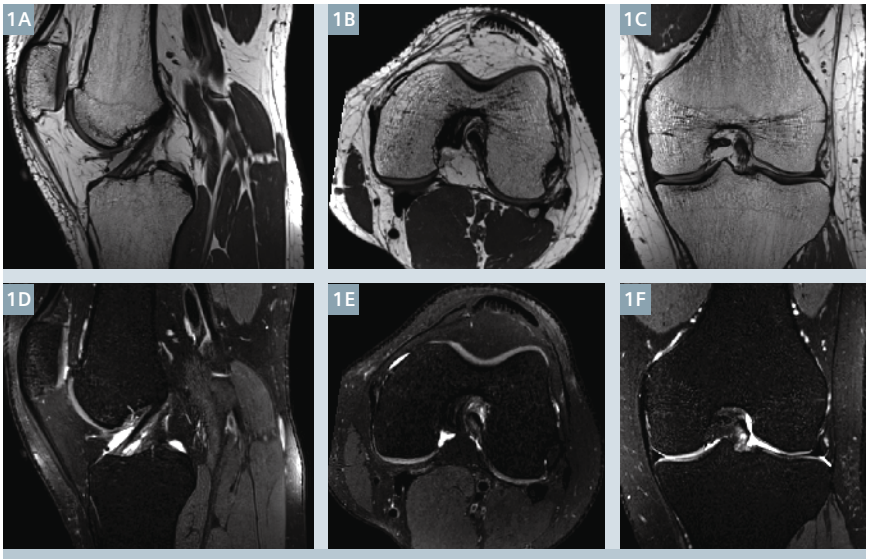

1 Normal left knee of a 37-year-old healthy man. Sagittal isotropic 0.5 mm intermediate-weighted and 0.6 mm T2 SPAIR-weighted 3D CAIPIRINHA SPACE source MR images **(1A and D)** with standard axial **(1B and E)** and coronal **(1C and F)** reformats.

quality through the occurrence of aliasing artifacts [6].

The CAIPIRINHA (Controlled Aliasing In Parallel Imaging Results IN Higher Acceleration) sampling pattern enables two-dimensional parallel imaging acceleration in both phase and partition encoding directions which substantially reduces aliasing artifacts and image noise through an optimized use of coil sensitivities [7, 8]. Multiple studies have shown the improved image quality and higher signal-to-noise ratios of gradient echo MR imaging techniques utilizing CAIPIRINHA when compared to standard parallel imaging technique such as GRAPPA [9].

CAIPIRINHA SPACE[1] is a new generation 3D TSE pulse sequence that enables high quality 3D TSE data acquisition with acceleration factors of 4 and similar or better image quality than conventional 3D SPACE and conventional 2D TSE sequences [10]. The high parallel imaging acceleration afforded by CAIPIRINHA enables the acquisition of high-resolution isotropic data sets with high signal and contrast-to-noise ratios that permit T1-, intermediate- and T2-weighted image contrasts without or with homogenous SPAIR (SPectrally Adiabatic Inversion Recovery) fat suppression. The 4-fold acceleration substantially reduces the time required for data acquisition and enables isotropic, high spatial resolution 3D MRI protocols for comprehensive evaluation of a multitude of musculoskeletal applications.

[1] WIP, CAIPIRINHA SPACE is currently under development and is not for sale in the US and in other countries. Its future availability cannot be ensured.

Clinical applications

The following clinical cases illustrate the application of a rapid high-resolution 3D CAIPIRINHA SPACE pulse sequence protocol for the evaluation of a variety of musculoskeletal conditions in adult and pediatric[2] patients. The 10-minute isotropic 3D CAIPIRINHA SPACE protocol consisted of intermediate-weighted MR images without fat suppression and T2-weighted MR images with fat suppression with parameter details given in Table 1. All studies were performed on a state-of-the-art 3-Tesla MR imaging system (MAGNETOM Skyra, Siemens Healthcare, Erlangen, Germany) with multi-channel surface coils, such as a 15-channel transmit/receive knee coil (QED, Mayfield Village, OH, USA), 18-channel body matrix and 16-channel ankle and foot receive-only coil (Siemens Healthcare).

Physeal bars

Physeal bars are due to a premature focal physeal arrest and cause interruptions of normal growth plate due to formation of a bony or fibrous bridge between the epiphysis and metaphysis. They can occur when there is contact between epiphysis and metaphysis due to damage to the physeal cartilage layers or displacement through a fracture. Physeal bars appear more commonly in the lower extremity than upper extremity and are common in the proximal tibia [11].

MRI is the method of choice for evaluation of physeal bars. MR imaging can accurately define the size and location and differentiate cartilaginous, fibrous and osseous components. Early fibrous bars appear as low signal intensity structures on intermediate-weighted MR images, while osseous physeal bars contain bone marrow and thus appear as hyperintense bridges between the epiphyseal and metaphyseal marrow on intermediate-weighted MR images that shows signal drop-out with fat suppression. Cartilaginous contents follow the characteristics of physeal cartilage and present with intermediate signal intensity on intermediate-weighted MR images and high signal intensity on fat-suppressed T2-weighted MR images.

Treatment strategies vary by site and type of growth arrest. For example, if at least 2 years or 2 cm of growth is predicted and the bar is <50% of the physeal area, then bar excision is recommended. If the bar involves more than 50% of physeal surface, completion of the arrest with an epiphysiodesis may be indicated [12].

[2] MR scanning has not been established as safe for imaging fetuses and infants less than two years of age. The responsible physician must evaluate the benefits of the MR examination compared to those of other imaging procedures.

Parameters	Intermediate-weighted 3D CAIPIRINHA SPACE	T2-SPAIR 3D CAIPIRINHA SPACE
Orientation	Sagittal	Sagittal
Repetition time (ms)	900	1100
Echo time (ms)	28	110
Echo train length	52	44
Receiver bandwidth (Hz/pixel)	422	399
Field-of-view (mm)	160 x 160	160 x 160
Voxel dimensions (mm)	0.5 x 0.5 x 0.5	0.63 x 0.63 x 0.63
Number of slices	240	190
In-plane frequency encoding direction	Anterior to posterior	Anterior to posterior
Acquisition time	5 min	5 min

Table 1: 10-minute 3D CAIPIRINHA SPACE isotropic orthopedic MR imaging protocol.

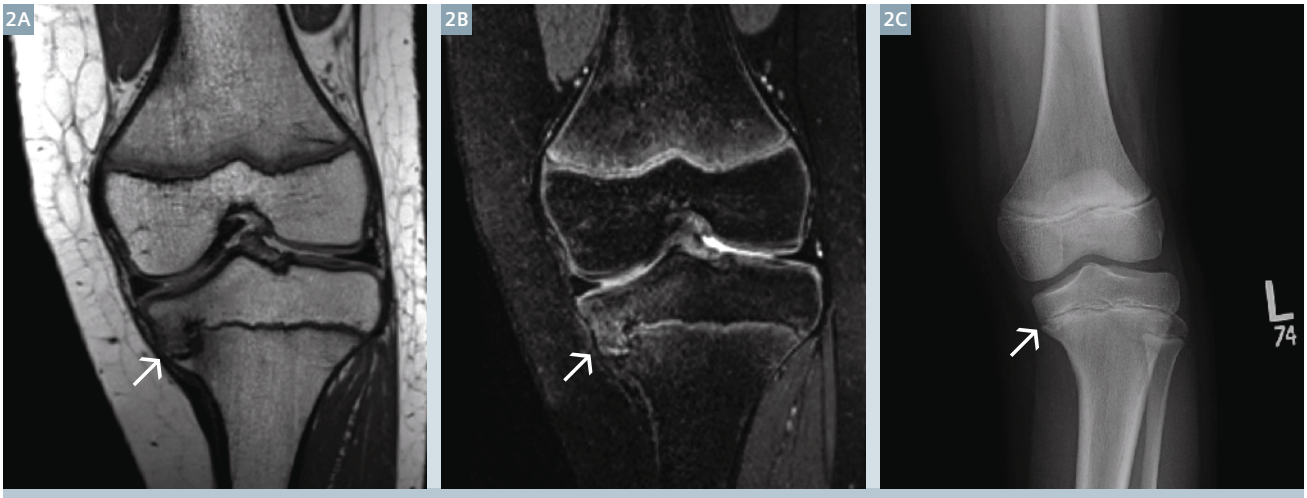

2 9-year-old girl with left knee pain and subtle deformity of the left proximal tibia. Coronal reformats of isotropic 0.5 mm intermediate-weighted **(2A)** and 0.6 mm T2 SPAIR-weighted **(2B)** 3D CAIPIRINHA SPACE MR images show a physeal bar (white arrows) across the medial aspect of the proximal tibial physis with mature bone marrow signal and mild edema pattern. Larger field-of-view antero-posterior radiograph **(2C)** shows mild left tibia vara deformity (Blount disease).

Bucket handle-type meniscal tear

Bucket handle meniscal tears are uncommon but characteristic vertical longitudinal tears that typically occur after a traumatic event; and in 80% of cases, involve the medial meniscus. The torn central meniscal fragment is often displaced towards the center of the joint, which can cause pain and locking symptoms. Bucket handle meniscal tears are frequently associated with anterior cruciate ligament (ACL) injuries [13].

On MR imaging, the double posterior cruciate ligament (PCL) sign is highly specific (98-100%) for the diagnosis of a displaced bucket handle tear [14]. A double PCL sign appears on sagittally oriented MR images when the medial meniscal tear displaces centrally so that it comes to locate anteroinferior to the PCL mimicking a second, smaller PCL. Rarely, a displaced lateral meniscus bucket handle tear may create a double PCL sign, which is often associated with a torn ACL. Careful MR imaging evaluation allows to differentiate the double PCL sign from accessory meniscofemoral and medial oblique meniscomeniscal ligaments. Other MR imaging signs can also be used to identify a bucket handle tear, such as absent bow tie, fragment within intercondylar notch, double anterior horn or flipped meniscus and disproportionally small posterior horn [15].

Historically, several treatments for bucket handle tears have been proposed such as arthroscopic subtotal meniscectomy and thermal shrinkage of posterolateral capsule. Current

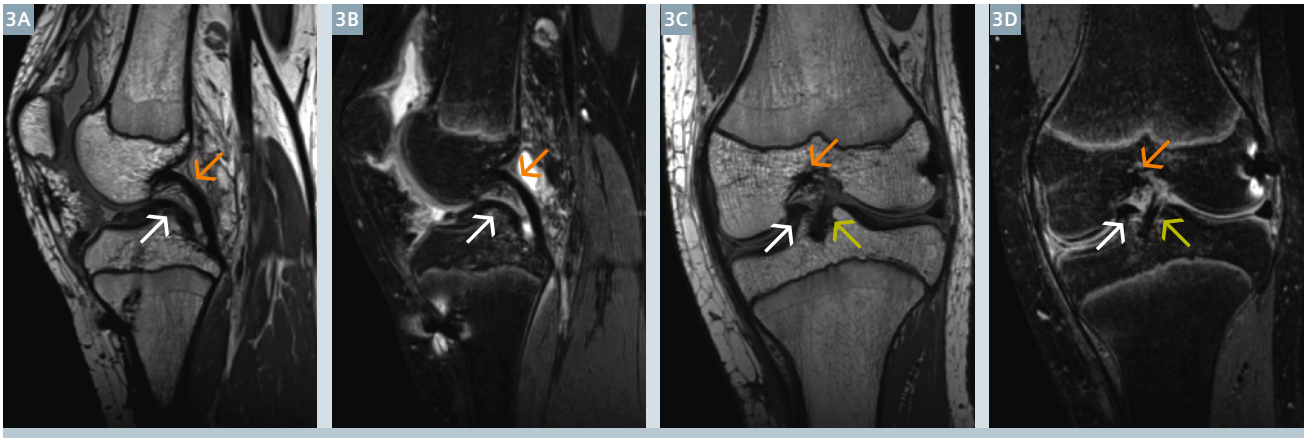

3 14-year-old teenager with left knee pain following healed anterior cruciate ligament reconstruction. Sagittal oblique isotropic 0.5 mm intermediate-weighted **(3A)** and 0.6 mm T2 SPAIR-weighted **(3B)** 3D CAIPIRINHA SPACE MR images with corresponding coronal reformats show a double PCL sign (3A and B, white arrows) of a bucket handle tear of the medial meniscus, created by displacement of the central meniscal fragment into the intercondylar notch. The posterior cruciate ligament (orange arrows) and the partially visualized anterior cruciate ligament graft (green arrows) are intact.

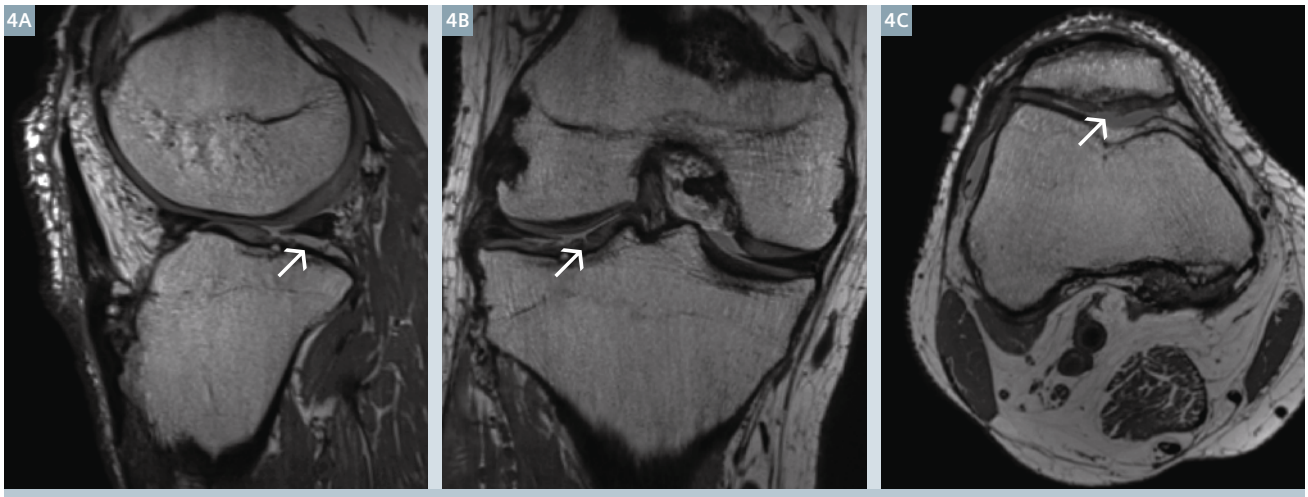

4 58-year-old man with right knee pain. Sagittal, coronal and axial reformats of an isotropic 0.5 mm intermediate-weighted 3D CAIPIRINHA SPACE MRI data set show full thickness cartilage loss over the posterior tibia plateau subjacent to the posterior third of the lateral meniscus (**4A**, arrow) as well as partial thickness cartilage defects and fissures of the articular cartilage of the central lateral tibia plateau (**4B**, arrow) and patella (**4C**, arrow). There is also a horizontal tear of the lateral meniscus.

treatment recommendations include meniscal preservation whenever possible with arthroscopic repair [16].

Cartilage defects

Loss of articular hyaline cartilage is the hallmark of degenerative osteoarthrosis and detectable by MR imaging before joint space narrowing occurs on radiographs. In clinical practice, cartilage defects may be graded with a modified Noyes or Outerbridge classification scheme [17]. The original Noyes score was based on arthroscopic findings, which was then modified for MR imaging findings. Modified Noyes score divides cartilage defect into 4 grades (Table 2).

Grades	Characteristics
Grade 0	Normal cartilage
Grade 1	Increased T2 signal intensity without loss of cartilage substance
Grade 2A	Superficial partial thickness cartilage loss of less than 50% of the total articular surface thickness
Grade 2B	Deep partial thickness cartilage loss equal to or more than 50% of total articular surface thickness
Grade 3	Full thickness cartilage loss with exposure of subchondral bone

Table 2: Modified Noyes classification for MR imaging grading of articular cartilage defects.

MRI is the modality of choice for assessment of cartilage damage. MR imaging techniques can evaluate both morphologic and compositional characteristics of articular cartilage. Morphological assessment of cartilage provides information about early cartilage degeneration as indicated by low or high signal intensity alterations, as well as substance defects such as fissuring, delamination, shear injuries and focal or diffuse partial and full thickness cartilage defects. Intermediate-weighted turbo spin echo pulse sequences with sufficiently high spatial resolution provide versatile and accurate morphological cartilage assessment due to their T2 sensitivity with good contrast between cartilage surface and the synovial fluid. Similar to 2D sequences, 3D sequences such as SPACE and Dual-Echo Steady State (DESS) provide high-contrast resolution between cartilage and synovial fluid for accurate assessment of cartilage integrity. Compositional MR imaging methods such as T2 mapping can be useful to identify early-stage degeneration [18]. Other compositional MR imaging methods include dGEMRIC, T1ρ, Sodium imaging and diffusion-weighted imaging.

Osteochondritis dissecans

Osteochondritis dissecans (OCD) describes the process of aseptic separation of the osseous component of an osteochondral fragment with gradual fragmentation of the articular surface. The condition typically occurs in active male teenagers and young adults. Patients may be asymptomatic, however, pain, joint locking and synovitis are common symptoms at the time of presentation. While the exact etiology is unknown, repetitive trauma and ischemia are suspected to play a major role. Approximately 75% of all cases occur in the femoral condyle, followed by the talus and the capitellum.

MRI is the diagnostic modality of choice for the characterization of osteochondritis dissecans, whereas radiography received a weak recommendation for the diagnosis of OCD by the American Academy of Orthopedic Surgeons (AAOS) due to the inability to visualize unossified

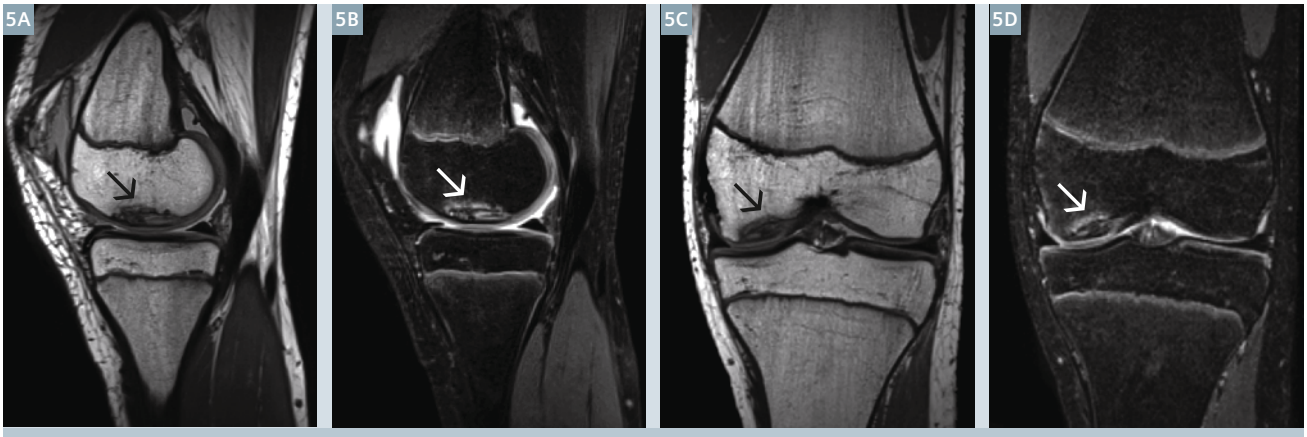

5 13-year-old teenager with left knee pain. Sagittal and coronal reformats of isotropic 0.5 mm intermediate-weighted **(5A and B)** and 0.6 mm T2 SPAIR-weighted **(5C and D)** 3D CAIPIRINHA SPACE MR images show a non-displaced osteochondritis dissecans lesion (arrows) along the inner margin of the medial femoral condyle. There are small cysts and a hyperintense rim along the host bone – fragment interface and a linear cartilage defect along the posterior margin.

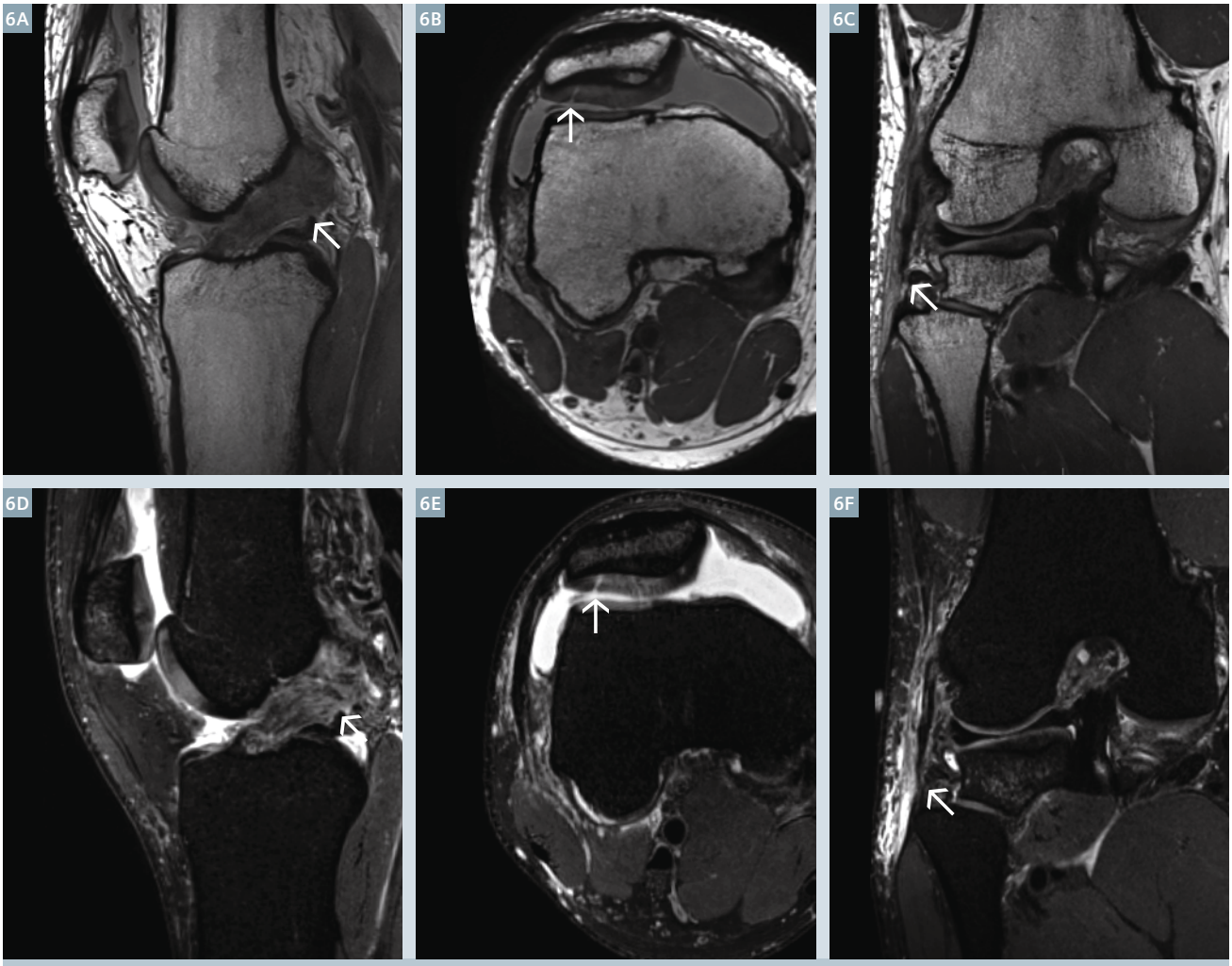

6 29-year-old man with history of recent American Football injury of the right knee. Sagittal oblique **(6A and D)**, axial **(6B and E)** and coronal oblique **(6C and F)** reformats of isotropic 0.5 mm intermediate-weighted and 0.6 mm T2 SPAIR-weighted 3D CAIPIRINHA SPACE MR images show a high-grade partial thickness tear of the anterior cruciate (arrows, 6A and D), a full-thickness fissure of the patellar cartilage (arrows, 6B and E) and a partial thickness tear of the lateral collateral ligament near the insertion (arrows, 6C and F).

elements and inability to assess for signs of mechanical instability [19].

Several MR imaging findings may be used to predict the stability of an OCD lesion [20, 21]. In adults with OCD of the knee, a high T2 signal intensity rim and cysts along the host bone – fragment interface, a high T2 signal intensity fracture line extending through the articular cartilage overlying an OCD lesion, and a fluid-filled osteochondral defect are signs of instability. In the pediatric population, a high T2 signal intensity rim or cysts surrounding the OCD lesion may be present in surgically stable OCD lesions; however, multiple cysts and a single cyst with a diameter greater than 5 mm have a high specificity for instability.

Anterior cruciate ligament tears

The anterior cruciate ligament (ACL) is the major restraint to anterior translation of the tibia relative to femur. It also provides restraint to rotatory forces. While one might assume that these injuries occur from contact mechanisms, ACL tears are more commonly non-contact injuries. Authors have described the pivot shift mechanism, which occurs when a combined valgus and axial force is exerted on the flexed knee with quadriceps loading, anterior tibial translation and external rotation of femur [22]. The combination of varus force with internal rotation of tibia and hyperextension of the knee joint may also cause ACL tears.

MRI is the reference standard for the imaging diagnosis of anterior cruciate ligament tears with sensitivity of 83%-95% and specificity of 95%-100% [23]. Depending on the extent of injury, MRI might show a focal discontinuity of the ACL, diffuse or focally abnormal signal intensity, abnormal bowing or non-visualization of the ligament. A major indication of MRI in the presence of an ACL injury is the evaluation for concomitant injuries, such as the collateral ligaments, menisci or articular cartilage. Fat suppressed, fluid sensitive MR images often show a pivot-shift-type osseous bone marrow edema contusion pattern at the posterolateral tibial plateau or condylopatellar sulcus at the lateral femoral condyle [23]. Chronically remodeled, complete ACL tears may demonstrate different patterns of scarring of the torn ligament remnants [24]. The most common injury pattern of partial ACL tears is a complete tear of anteromedial bundle with either an intact or partially torn posterolateral bundle [25].

Surgical treatment depends on the grade of injury and joint stability. Single bundle or double bundle ACL reconstructions may be performed with auto- or allografts. MRI has been shown to be accurate in identifying complete graft tears [26].

Medial collateral ligament tears

The superficial medial collateral ligament (MCL) provides the primary restraint to valgus loads, external rotation of the tibia, and anterior tibial translation when the anterior cruciate ligament is injured. The deep medial collateral ligament and the posterior oblique ligament provide additional stability to the medial knee joint and posteromedial corner. The medial collateral ligament is among the most frequently injured ligamentous structures of the knee with an annual incidence for injury between 0.24 and 7.3 per 1000 individuals [27].

Causes of medial collateral ligament injuries include direct valgus forces aimed at the knee, non-contact, or overuse injuries. The degree of injury and stability may be graded by the degree of medial joint line opening into grade 1 (<5 mm of medial joint line opening), grade 2 (5 to 10 mm) and grade 3 (>10 mm). MR imaging may be used to additionally grade the tear similar to the O'Donoghue classification (Table 3); however, it

Grading	Ligamentous Integrity	O'Donoghue classification	MRI classification
Grade 1	Interstitial injury	Structurally intact	Signal hyperintensity of the ligament without visualization of disrupted fibers
Grade 2	Partial thickness tear	Incomplete ligament tear, no valgus laxity	Disrupted and intact fibers
Grade 3	Full thickness tear	Complete ligament tear, valgus laxity	Disruption of all fibers

Table 3: MR grading of MCL tears.

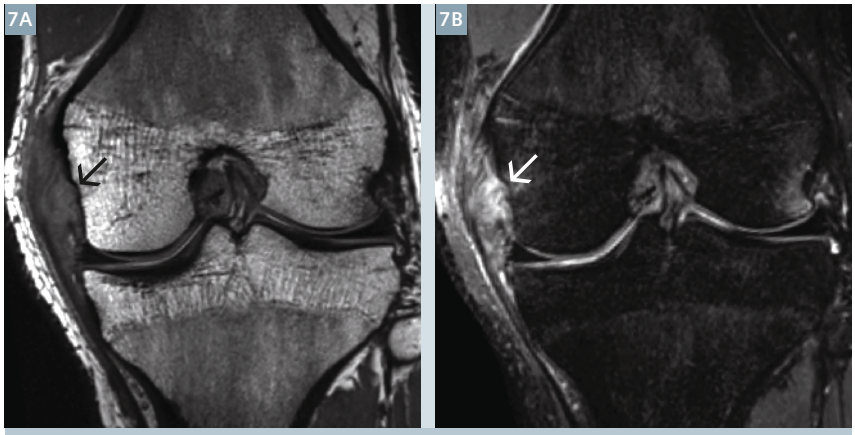

7 16-year-old teenager with recent trauma to the left knee during a soccer game. Coronal reformats of isotropic 0.5 mm intermediate-weighted **(7A)** and 0.6 mm T2 SPAIR-weighted **(7B)** 3D CAIPIRINHA SPACE MR images show a high-grade partial thickness tear (arrows) of the femoral origins of the superficial and deep medial collateral ligament.

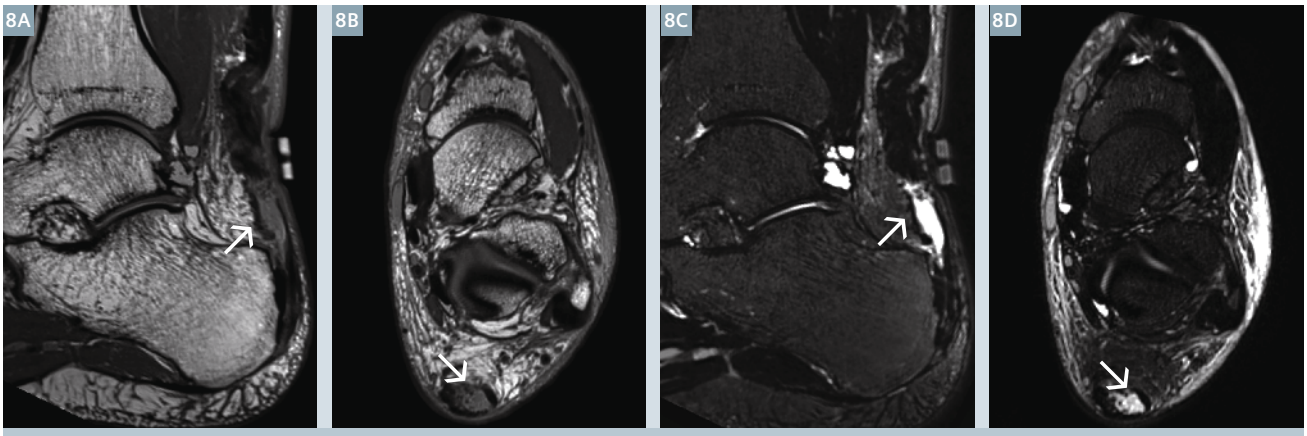

8 43-year-old man with recent ankle trauma and limited plantar flexion. Sagittal **(8A and C)** and axial **(8B and D)** reformats of isotropic 0.5 mm intermediate-weighted and 0.6 mm T2 SPAIR-weighted 3D CAIPIRINHA SPACE MR images show a complete distal midsubstance tear (arrows) of the degenerated Achilles tendon with retraction and gap formation.

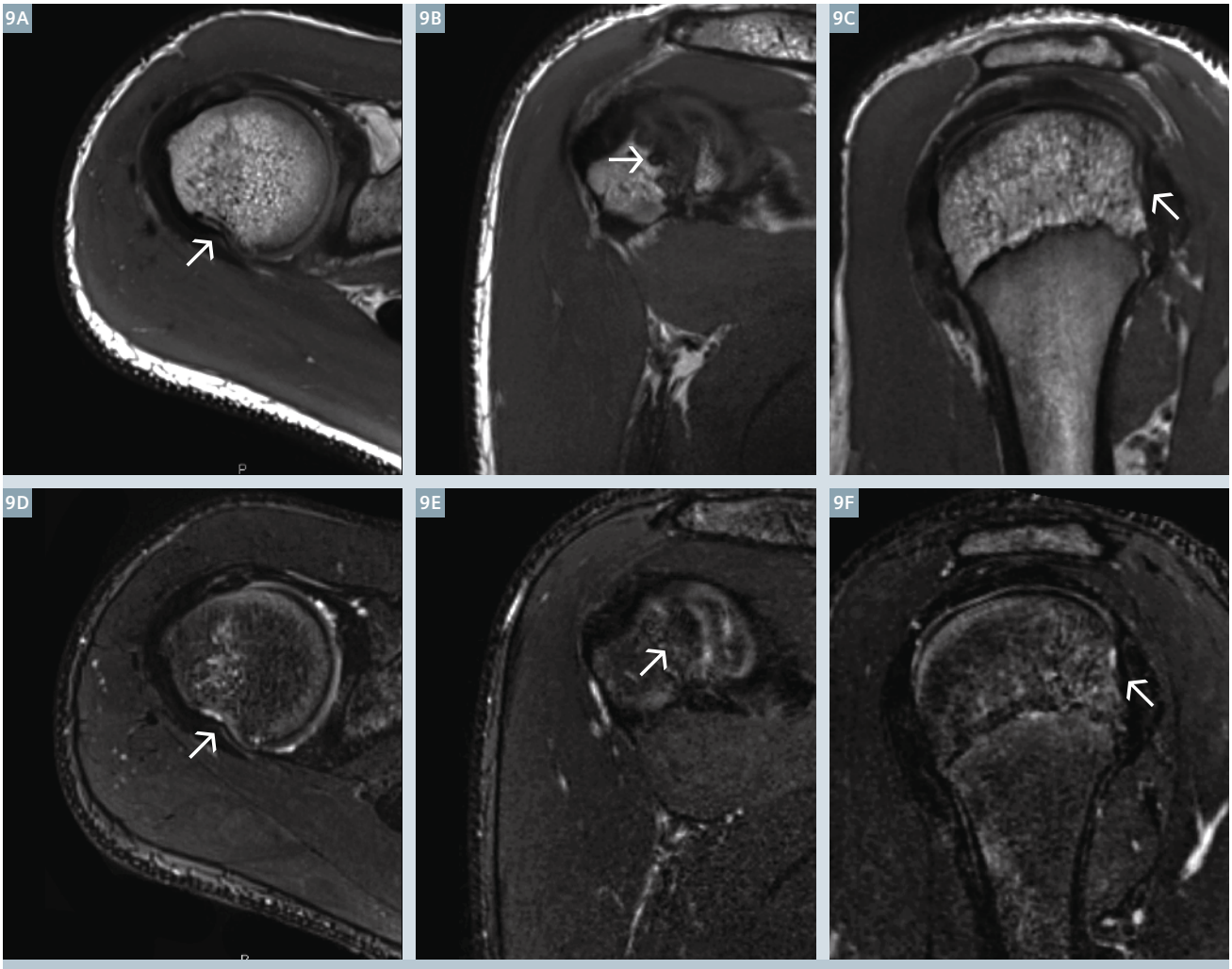

9 17-year-old boy with recent glenohumeral translation event during a Lacrosse game. Axial **(9A and D)**, coronal oblique **(9B and E)** and sagittal oblique **(9C and F)** reformats of isotropic 0.6 mm intermediate-weighted and 0.7 mm T2 SPAIR-weighted 3D CAIPIRINHA SPACE MR images show an acute Hill-Sachs fracture deformity (arrows) along the posterosuperior humeral head.

may be most helpful in the evaluation of tears associated with additional internal knee injuries. Depending on the severity, anterior cruciate ligament tears may be present in 20-78% of cases, medial meniscus tear in up to 55%, and extensor mechanism tears in up to 21%.

Conservative management and bracing has been advocated as primary method of treatment for low-grade injuries due to intrinsic healing capacity of the MCL, while surgical repair was reserved for grade III injuries, especially in athletes. However, recent studies have shown that a repair of the MCL might improve valgus stability in general population and thus, should be evaluated based on chronicity and extent of MCL injury along with appropriate patient selection [28].

Achilles tendon tears

The Achilles tendon is the most frequently injured tendon of the body. This tendon rupture occurs mostly in younger patients, predominantly male, and is typically sports-related. Physical activities that impart intermittent, but repetitive stress to the tendon without time given to adapt may lead to spontaneous rupture [29]. Other predisposing factors include intratendinous steroid injections, diabetes mellitus, use of fluoroquinolones and gout. Achilles tendon tears are often non-insertional, mid-substance ruptures, which is a region of relative hypovascularity located 2-6 cm proximal to insertion site.

MR imaging is highly accurate for the diagnosis of Achilles tendon rupture, which can be partial or complete. MR imaging shows a full thickness tear as a complete tendinous gap filled with edema or blood along with retraction ends, whereas a partial tear may be shown as longitudinal and transversal tendon substance defects that are hyperintense on intermediate-weighted and T2-weighted MR images. Timely diagnosis is important for optimal treatment outcome as delays are associated with poor outcomes such as weak plantar flexion and inability to run [30].

Glenohumeral translation

The Hill-Sachs lesion was first described by Hill and Sachs in 1940 as a "groove defect of the posterolateral humeral head" [31]. The Hill-Sachs lesion represents an impaction fracture of the posterosuperior or posterolateral humeral head and typically occurs when the humeral head impacts against the anteroinferior glenoid rim during an anteroinferior glenohumeral translation event [32, 33]. The lesion is acutely painful and may trigger recurring dislocation or subluxation as the groove defect serves as a lever, facilitating dislocation when the joint is extended and externally rotated. Hill-Sachs lesions are often associated with Bankart and Bankart-variant lesions of the anteroinferior glenoid labrum. MRI often shows a region of typically wedge shaped Hill-Sachs defect in the posterosuperior humeral head, which is accompanied with bone marrow edema pattern in the acute phase.

Developmental dysplasia of the hip

Developmental dysplasia of the hip (DDH) describes a range of deformities of the femoral head and acetabulum that are associated with dysfunction and pain and may lead to subluxation, instability and frank dislocation. Early detection is important, as treatment is more effective in infancy and becomes increasingly difficult at later stages with increasing risk of long term disability [34].

The condition may be diagnosed by physical examination using a variety of tests, such as the Barlow or Ortolani procedures. Ultrasound is considered a good diagnostic tool but, lately, its role in screening has been debated [35]. While MRI does not play a major role in screening for DDH [36], its major utility lies in the evaluation of the degree of cartilage loss as well as the assessment of joint congruity and condition of growth cartilage and ossification centers [37]. MR imaging is also useful for the assessment following surgical joint relocation and application of spica cast.

In summary, 3D CAIPIRINHA SPACE is a new technique that enables the isotropic acquisition of high-quality 3D data sets for efficient and comprehensive MRI of joints.

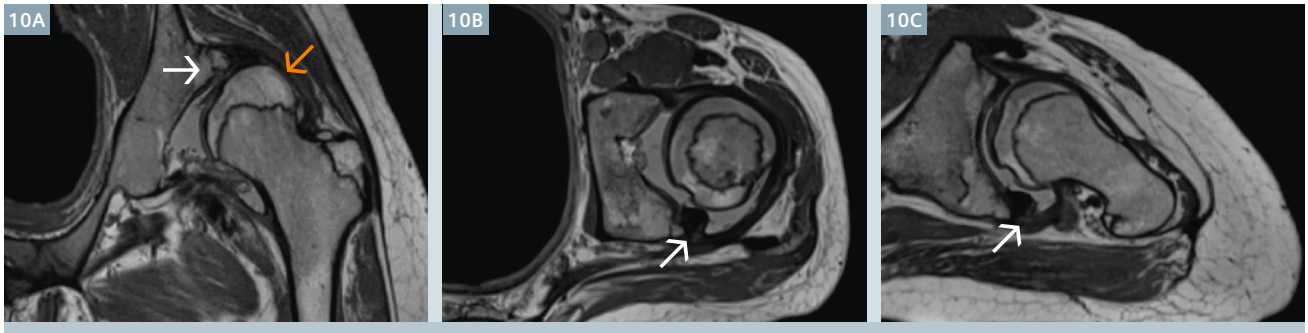

10 28-year-old woman with history of developmental dysplasia of the left hip. Coronal oblique **(10A)**, axial **(10B)** and axial oblique **(10C)** reformats of isotropic 0.7 mm intermediate-weighted 3D CAIPIRINHA SPACE MR images show a dysplastic acetabulum with deficient lateral femoral head coverage (10A, white arrow) as well as lateral subluxation of the deformed femoral head (10A, orange arrow). There is moderate synovitis and hypertrophy of the degenerated acetabular labrum (10B and C, arrows).

References

1 M. Notohamiprodjo, A. Horng, M.F. Pietschmann, et al. MRI of the knee at 3 T: first clinical results with an isotropic PDfs-weighted 3D-FSE-sequence Investigative Radiology, 44 (9) (2009), pp. 585–597.

2 Notohamiprodjo M, Horng A, Kuschel B, Paul D, Li G, Raya JG, Reiser MF, Glaser C. 3D-imaging of the knee with an optimized 3D-FSE-sequence and a 15-channel knee-coil. Eur J Radiol. 2012 Nov;81(11):3441-9.

3 Notohamiprodjo M, Kuschel B, Horng A, Paul D, Baer P, Li G, Garcia del Olmo JM, Reiser MF, Glaser C. 3D-MRI of the ankle with optimized 3D-SPACE. Invest Radiol. 2012 Apr;47(4):231-9.

4 K.J. Stevens, R.F. Busse, E. Han, et al. Ankle: isotropic MR imaging with 3D-FSE-cube—initial experience in healthy volunteers Radiology, 249 (3) (2008), pp. 1026–1033.

5 R. Kijowski, K.W. Davis, M.A. Woods, et al. Knee joint: comprehensive assessment with 3D isotropic resolution fast spin-echo MR imaging—diagnostic performance compared with that of conventional MR imaging at 3.0 T Radiology, 252 (2) (2009), pp. 486–495.

6 Breuer FA, Blaimer M, Mueller MF, Griswold MA, Jakob PM. CAIPIRINHA-Revisited. MAGNETOM Flash 2015;3(63):8-15.

7 Breuer FA, Blaimer M, Mueller MF, et al. Controlled aliasing in volumetric parallel imaging (2D CAIPIRINHA). Magn Reson Med 2006; 55:549-556.

8 Horger W, Kiefer B. Fat Suppression Techniques –a Short Overview. MAGNETOM Flash 2011;1(46):56-59.

9 Wright KL, Harrell MW, Jesberger JA, et al. Clinical evaluation of CAIPIRINHA: comparison against a GRAPPA standard. J Magn Reson Imaging 2014; 39:189-194.

10 Fritz J, Fritz B, Thawait GG, Meyer H, Gilson WD, Raithel E. Three-Dimensional CAIPIRINHA SPACE TSE for 5-Minute High-Resolution MRI of the Knee. Invest Radiol. 2016 Oct;51(10):609-17.

11 Khoshhal KI, Kiefer GN. Physeal bridge resection. J Am Acad Orthop Surg. 2005 Jan-Feb;13(1):47-58.

12 Gauger EM, Casnovsky LL, Gauger EJ, Bohn DC, Van Heest AE. Acquired Upper Extremity Growth Arrest. Orthopedics. 2016 Sep 29:1-9.

13 Boody BS, Omar IM, Hill JA. Displaced Medial and Lateral Bucket Handle Meniscal Tears With Intact ACL and PCL. Orthopedics. 2015 Aug;38(8):e738-41.

14 Camacho MA. The double posterior cruciate ligament sign. Radiology. 2004 Nov;233(2):503-4.

15 Nguyen JC, De Smet AA, Graf BK, Rosas HG. MR imaging-based diagnosis and classification of meniscal tears. Radiographics. 2014 Jul-Aug;34(4):981-99.

16 Ahn JH, Kim KI, Wang JH, Kyung BS, Seo MC, Lee SH. Arthroscopic repair of bucket-handle tears of the lateral meniscus. Knee Surg Sports Traumatol Arthrosc. 2015 Jan;23(1):205-10.

17 Crema MD, Roemer FW, Marra MD, Burstein D, Gold GE, Eckstein F, Baum T, Mosher TJ, Carrino JA, Guermazi A. Articular cartilage in the knee: current MR imaging techniques and applications in clinical practice and research. Radiographics. 2011 Jan-Feb;31(1):37-61.

18 Dunn TC, Lu Y, Jin H, Ries MD, Majumdar S. T2 relaxation time of cartilage at MR imaging: comparison with severity of knee osteoarthritis. Radiology. 2004 Aug;232(2):592-8.

19 Zbojniewicz AM, Laor T. Imaging of osteochondritis dissecans. Clin Sports Med. 2014 Apr;33(2):221-50.

20 Kijowski R, Blankenbaker DG, Shinki K, Fine JP, Graf BK, De Smet AA. Juvenile versus adult osteochondritis dissecans of the knee: appropriate MR imaging criteria for instability. Radiology. 2008 Aug;248(2):571-8.

21 Samora WP, Chevillet J, Adler B, Young GS, Klingele KE. Juvenile osteochondritis dissecans of the knee: predictors of lesion stability. J Pediatr Orthop. 2012 Jan-Feb;32(1):1-4.

22 Quatman CE, Quatman-Yates CC, Hewett TE. A 'plane' explanation of anterior cruciate ligament injury mechanisms: a systematic review. Sports Med. 2010 Sep 1;40(9):729-46.

23 Naraghi A, White LM. MR imaging of cruciate ligaments. Magn Reson Imaging Clin N Am. 2014 Nov;22(4):557-80.

24 Nakase J, Toratani T, Kosaka M, Ohashi Y, Tsuchiya H. Roles of ACL remnants in knee stability. Knee Surg Sports Traumatol Arthrosc. 2013 Sep;21(9):2101-6.

25 Ng AW, Griffith JF, Hung EH, Law KY, Yung PS. MRI diagnosis of ACL bundle tears: value of oblique axial imaging. Skeletal Radiol. 2013 Feb;42(2):209-17.

26 Horton LK, Jacobson JA, Lin J, Hayes CW. MR imaging of anterior cruciate ligament reconstruction graft. AJR Am J Roentgenol. 2000 Oct;175(4):1091-7.

27 Roach CJ, Haley CA, Cameron KL, Pallis M, Svoboda SJ, Owens BD. The epidemiology of medial collateral ligament sprains in young athletes. Am J Sports Med. 2014 May;42(5):1103-9.

28 Long JM, Waterman BR. Surgical Repair of Medial Collateral Ligament and Posteromedial Corner Injuries of the Knee: A Systematic Review. Arthroscopy. 2015 Nov;31(11):2249-55.

29 Schweitzer ME, Karasick D. MR imaging of disorders of the Achilles tendon. AJR Am J Roentgenol. 2000 Sep;175(3):613-25.

30 Singh D. Acute Achilles tendon rupture. BMJ. 2015 Oct 22;351:h4722.

31 Hill HA, Sachs MD. The grooved defect of the humeral head: a frequently unrecognized complication of dislocations of the shoulder joint. Radiology. 1940;35: 690–700.

32 Richards RD, Sartoris DJ, Pathria MN, Resnick D. Hill-Sachs lesion and normal humeral groove: MR imaging features allowing their differentiation. Radiology. 1994 Mar;190(3):665-8.

33 Demehri S, Hafezi-Nejad N, Fishman EK. Advanced imaging of glenohumeral instability: the role of MRI and MDCT in providing what clinicians need to know. Emerg Radiol. 2016 Aug 13. [Epub ahead of print].

34 Kotlarsky P, Haber R, Bialik V, Eidelman M. Developmental dysplasia of the hip: What has changed in the last 20 years? World J Orthop. 2015 Dec 18;6(11):886-901.

35 US Preventive Services Task Force. "Screening for Developmental Dysplasia of the Hip: Recommendation Statement." PEDIATRICS 117, no. 3 (3, 2006): 898-902. doi:10.1542/peds.2005-1995.

36 Karmazyn BK, Gunderman RB, Coley BD, et al. ACR Appropriateness Criteria on developmental dysplasia of the hip: child. J Am Coll Radiol 2009;6(8):551–557.

37 Rosenbaum DG, Servaes S, Bogner EA, Jaramillo D, Mintz DN. MR Imaging in Postreduction Assessment of Developmental Dysplasia of the Hip: Goals and Obstacles. Radiographics. 2016 May-Jun;36(3):840-54.

Contact

Jan Fritz, M.D., P.D., D.A.B.R.
Director of Interventional MR Imaging
Associate Director MSK Fellowship
Assistant Professor of Radiology and Radiological Sciences
Johns Hopkins University School of Medicine
Russell H. Morgan Department of Radiology and Radiological Science
Musculoskeletal Radiology
601 N. Caroline Street, JHOC 3140A
Baltimore, MD 21287, USA
jfritz9@jhmi.edu

MR LiverLab

Robert Sellers, RT(R)(MR)(CT)

Siemens Healthineers, Cary, NC, USA

Liver disease is any disturbance of liver function that causes illness. In the US up to 20% of adult liver patients have non-alcoholic fatty liver disease (NAFLD) or non-alcoholic steatohepatitis (NASH) [1]. The current monitoring of these patients is liver biopsy. MR is offering some promising techniques for fat and iron evaluation in routine clinical liver diagnostics. Siemens' LiverLab offers a comprehensive package for liver fat evaluation. LiverLab provides clinically relevant biomarkers: Fat signal fraction, which correlates with hepatic steatosis, and R2* of water, which correlates with iron content. The purpose of this article is to share the knowledge of implementing LiverLab at my sites.

LiverLab consists of three sequences incorporated into the Abdomen Dot Engine protocol. The t1 vibe e-Dixon (First look Dixon), vibe q-Dixon (Multi-echo Dixon), and the HISTO (breath-hold spectroscopy) sequences are usually performed in conjunction with routine liver examination. LiverLab must be performed as a Dot Engine.

The t1 vibe e-Dixon (or First look Dixon) is a single breath-hold 3D acquisition that provides whole-liver coverage and generates opposed and in-phase images as well as fat and water images. It is a two-point Dixon technique. After image acquisition the system performs Inline Liver Segmentation and suggests a region-of-interest (ROI) placement for the subsequent evaluation protocol. It is important to check the Liver Segmentation for quality since it cannot be corrected. This segmentation is used again for the q- or Multi-echo Dixon sequence. It is not repeated for the q-Dixon, and therefore the patient must follow the same breath-hold instructions very carefully. Based on a dual ratio analysis, the system performs and assigns a voxel classification of either normal liver tissue, fat deposition, iron deposition or combined deposition. Based on these findings the system determines an evaluation recommendation for

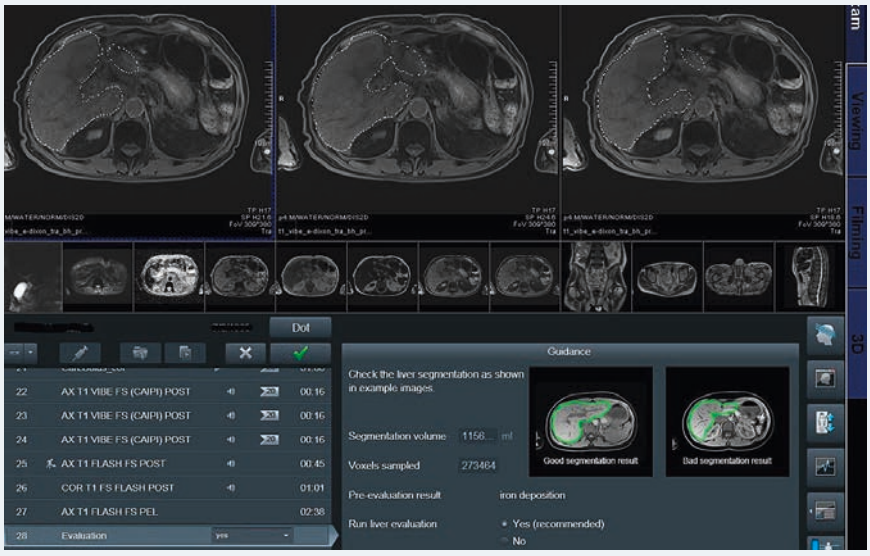

further evaluation. It is important to note this is not a diagnosis. If the recommendation comes back as normal, it only means that if further evaluation were to be performed it would very likely come back with normal MR values.

It has been my experience that if the patient is being referred for fat/iron evaluation we will proceed with further evaluation (q-Dixon and HISTO) even if the system comes back with a normal tissue classification.

e- or First look Dixon generates six series in the patient browser: the in-phase, opposed-phase, fat, water, water with segmentation, and the report. In some cases to display the segmentation on the PACS system I have saved them as RGB images.

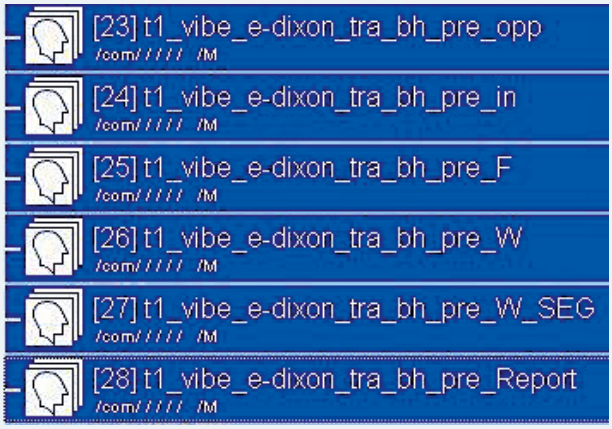

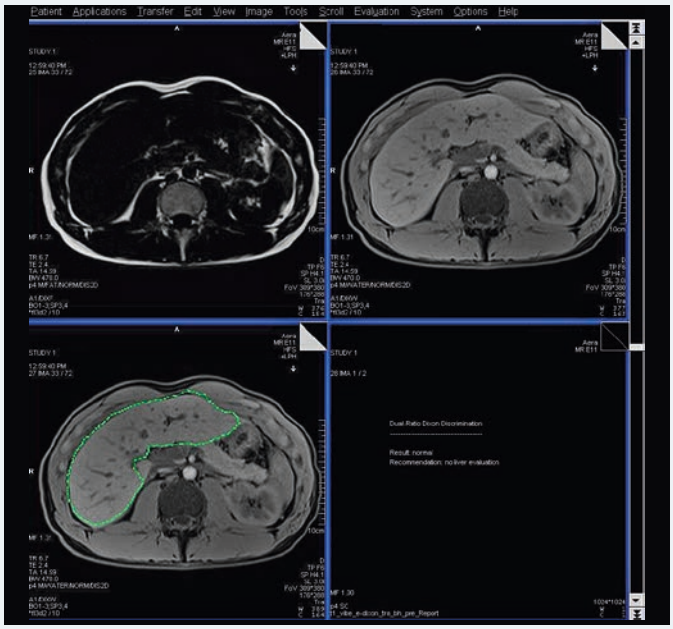

The q-Dixon (or Multi-echo Dixon) is a single breath-hold VIBE Dixon with multiple, typically six echoes that provides whole-liver coverage. The q-Dixon should be performed with the same breath-hold instructions as the e-Dixon sequence to properly project the liver segmentation from e-Dixon to q-Dixon. The system opens the sequence with a suggested position for the ROI, but you can reposition it. The ROI should be positioned in liver tissue not over vessels or the gallbladder. q-Dixon provides mean fat signal fraction and R2* values for both a region-of-interest and the segmented liver volume. The liver segmentation must be checked for quality. If liver segmentation fails the segmentation Fat Fraction and R2* values will not be accurate, since they may include non-liver tissue; in those cases, a properly placed ROI will provide better results. In addition multi-echo VIBE Dixon provides volumetric fat fraction, R2* maps, T2* maps, water fraction, and a goodness-of-fit map. R2* values are corrected for fat effects and the fat percentage is corrected for the T2* effects. R2* is the inverse of T2*. A higher R2* value correlates with a higher iron content whereas a lower T2* value correlates with a higher iron content. q-Dixon will generate eight series in the patient browser: water, fat, fat percentage, goodness-of-fit,

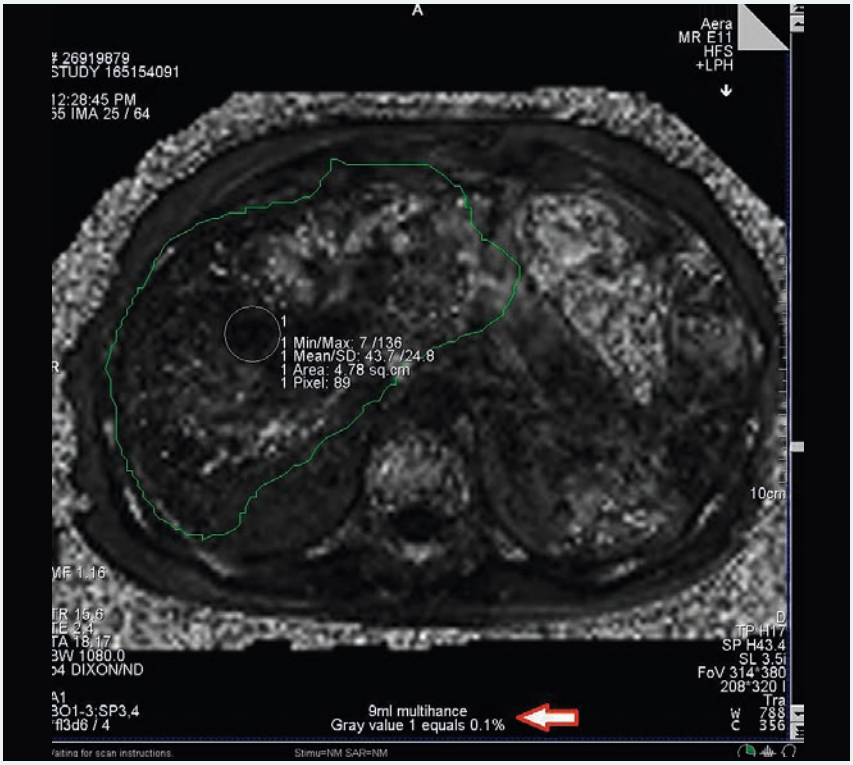

R2* map, T2* map, and water percentage. The fat fraction, R2* and goodness-of-fit datasets will show the segmentation and the ROI position. The goodness-of-fit is an indication of fitting residual errors of the fat percentage and the R2* results. The smaller the value, the better and more reliable the results. To check the goodness-of-fit, draw a ROI over liver tissue on the goodness-of-fit map to get a mean value. The fit error values are also part of the DICOM report, on top of the fat fraction and R2* values. The goodness-of-fit percentage is the mean value multiplied by 0.1. Goodness-of-fit should be 5% or less. For example a mean value of 43.7 would be a fit of 4.37%.

The q-Dixon Evaluation Report will have two color bars. The top color bar is for fat fraction and the bottom is for R2* (iron). Each bar will provide a segmentation value (whole-liver volume from segmentation of liver) and a ROI value. For fat it will show a percent and for R2* it will show a value of seconds to the inverse of 1 (sec^{-1}). R2* is sensitive to iron deposition and is the preferred clinical biomarker. However, if there is too much iron then the signal of the gradient echo sequence can be very low or even zero (below the noise floor) and then the R2* value will not be reliable. In rare instances the fat and water images provided by Dixon can swap, thereby giving an inaccurate value for fat percentage. The system will make a note on the report that the fat percentage is unusually high and the arrows on the top color bar will not be seen.

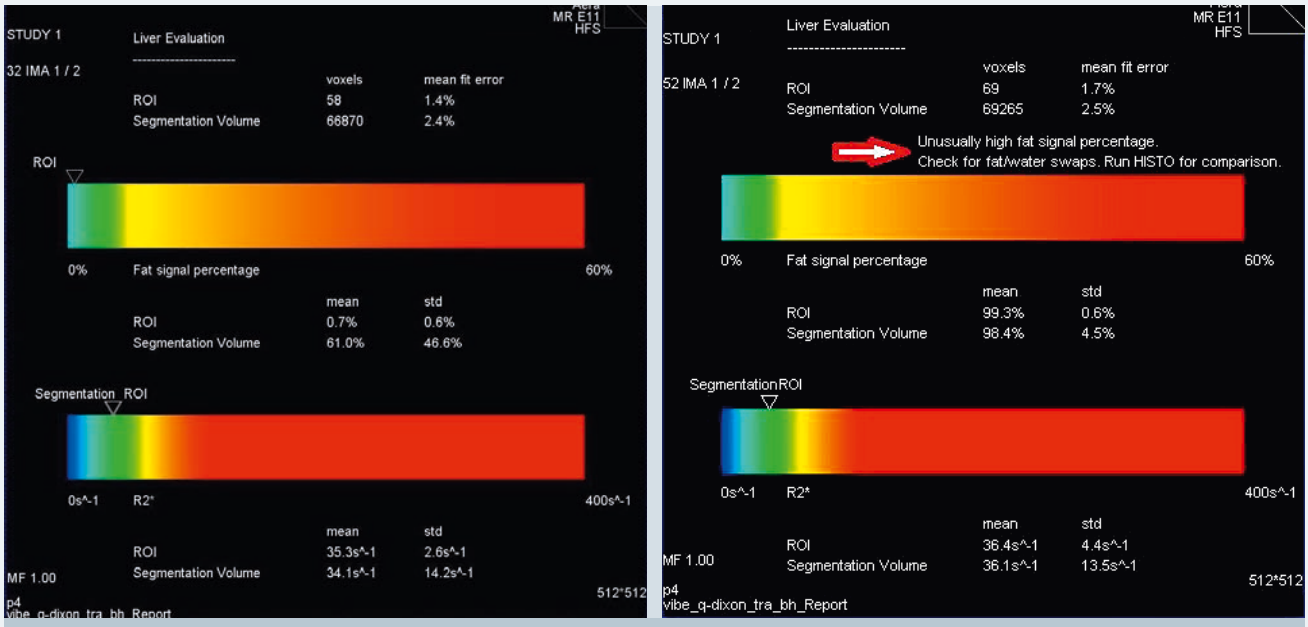

Note: The normal fat percentage result and the result where fat and water are swapped. The fat and water images will also give a clear indication that a fat and water swap has occurred. If fat and water swap does occur the HISTO sequence will provide accurate fat fraction. A FOV that is too small might cause this. Use a slightly larger FOV for signal. Avoid changing the TEs of the optimized multi echo sequence as delivered, as Dixon relies on specific TE values to calculate fat and water.

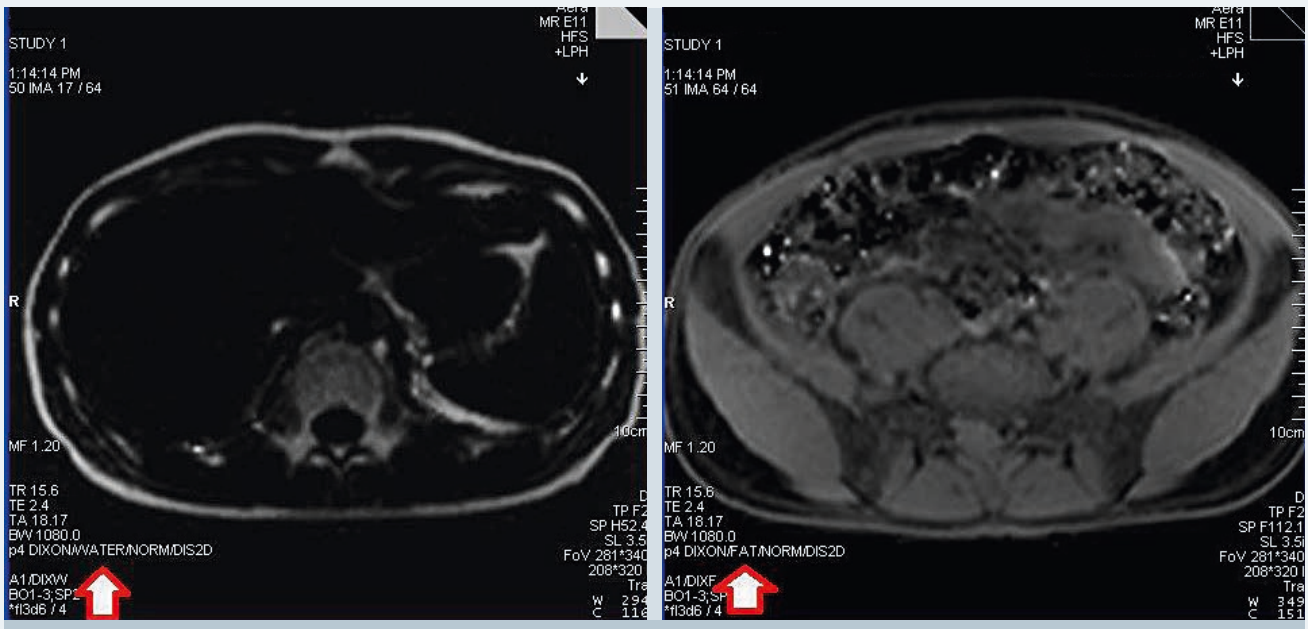

Note: The image labeled water is fat and the image labeled fat is water.

If liver segmentation fails or if the physician desires, the fat fraction or R2* map can be loaded into viewing and additional ROIs or manual segmentation can be drawn using the ROI tool or the Freehand ROI Tool. Multiply the mean value by 1 to get the seconds to the inverse of 1 (sec^{-1}). For manual segmentation the ROI would have to be drawn out for each slice and then the value averaged together. This is very useful as even if the ROI had not been placed in a desired location there is no need to repeat the series; the ROI can be drawn as post processing on the R2* map. LiverLab does not provide an iron quant value (liver iron concentration or LIC usually obtained from the liver biopsy). There are studies that support taking the R2* value and converting to iron quant value. These differ in acquisition and parameter fitting, and hence the calibration equations are slightly different. To date, there is no published iron calibration specifically for R2* from multi-echo VIBE Dixon, so if previously published calibrations are used, care must be taken. See 'Iron quantification with LiverLab' (page 44).

Note: The mean value and the notation at the bottom for what factor to multiply the mean value by.

The HISTO sequence is a 15 second breath-hold (STEAM) spectroscopy sequence. It is a single voxel spectroscopy with typically a 3 x 3 x 3 cm^3 voxel size. The system will recommend a location for the voxel size but it can be repositioned in liver tissue not over vessels or the gallbladder. When the HISTO sequence is opened the system will take the sequence in the active graphic segment and create a new series without distortion correction. I recommend you ensure that the e-dixon vibe (Screening Dixon) sequence is in the active box prior to opening the sequence. From there I right click and select series and load that non-distortion corrected series into Applications 3D MPR, and then generate coronal and sagittal reformats which can be dragged into the graphic segments from the browser for positioning the voxel in all 3 planes. With the axial image active, the scroll nearest tool will select the coronal and sagittal image closest to the voxel position on the axial much the same as normal spectroscopy

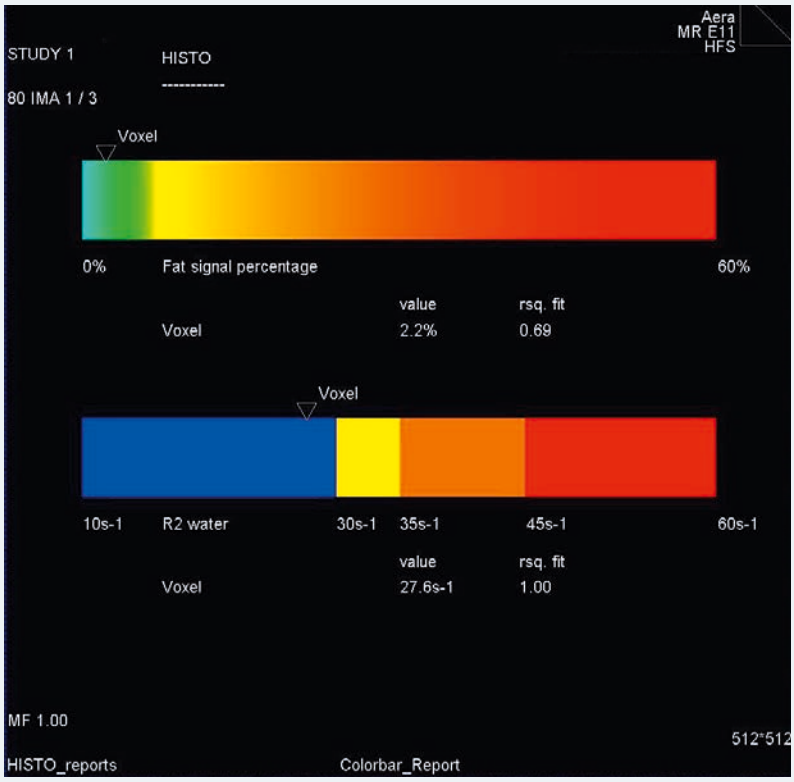

positioning. HISTO provides Proton Density Fat Fraction (PDFF) that has been corrected for fat and water transverse relaxation. Since this is a spin echo sequence R2 values are provided rather than R2* values (R2* is calculated from GRE sequences). The color bar map will show fat at the top in percent and R2 water with a value in seconds inverted over 1. The fit value (rsq fit "R-squared") should be as close to 1 as possible, preferably >0.95. For additional Quality Control there is a T2 relaxation curve for water and fat with the lowest TE value scanned showing a spectral peak above it showing fat at 1.3 ppm (red) and water at 4.7 ppm (blue).

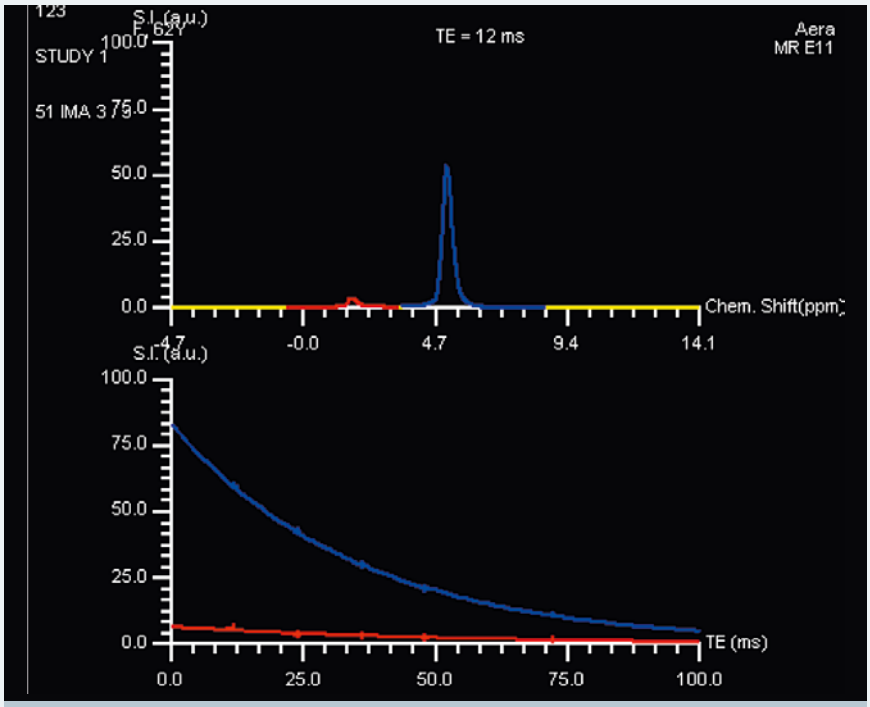

Note: I find the 'shift to image plane' context menu entry very useful.

For patients with very high iron content there is a second HISTO sequence in the Siemens library with shorter TE values. Under Siemens-Abdomen-library-3d you will find two HISTO sequences. The primary sequence has echo times of 12, 24, 36, 48, and 72. The secondary sequence is for patients that have higher iron content where the TEs are shorter 12, 15, 18, 21, and 24 so that the signal is not destroyed by the higher TEs due to the higher iron content.

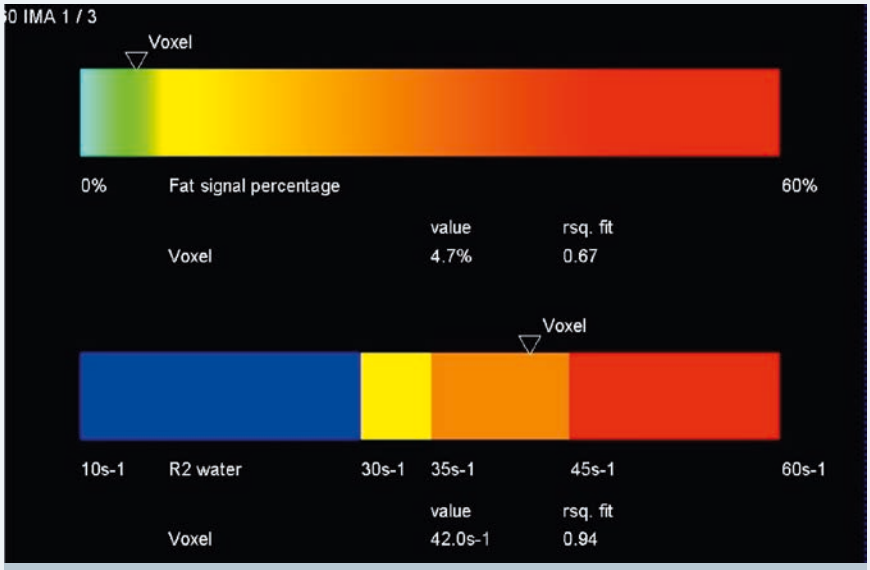

Note: The high R2 value and the arrow on the lower color bar indicating high iron content.

References

1 Lazo et al. BMJ. 2011;343:d6891.
2 Jie Deng et al. Hepatic Fat Quantification in Pediatric Patients using Multi-echo Dixon VIBE. MAGNETOM Flash 2(62) 2015, p. 23-25.
3 Puneet Sharma et al. An Efficient Workflow for Quantifying Hepatic Lipid and Iron Deposition using LiverLab. MAGNETOM Flash 3(58) 2014, p. 12-17.
4 Stephan Kannengiesser et al. Case Study LiverLab. MAGNETOM Flash 3(58) 2014, p. 18f.

Contact

Robert Sellers
Siemens Medical Solutions, Inc.
HC NAM USA SV CS EDU MR
221 Gregson Drive
27511 Cary, NC
USA

Iron Quantification with LiverLab

Stephan Kannengiesser, Ph.D.

Siemens Healthineers, MR Oncology Applications, Erlangen, Germany

Multi-echo Dixon VIBE contained in LiverLab provides liver fat fraction values which are corrected for the effects of transversal relaxation. By doing this, it also provides a simultaneous estimation of that transversal relaxation time T2*, which is corrected for fat signal effects, herefafter called $T2_c$*. The reciprocal value of this estimate, fat-corrected $R2_c$* = 1/ $T2_c$*, can be used, within limits, to assess liver iron concentration (LIC). This note provides some guidelines for doing that.

MR liver iron quantification

Liver iron content is an important clinical biomarker. It can be assessed by various methods, including biopsy, which is still considered to be the gold standard but potentially harmful for the patient and suffering from a large sampling variability. It is also possible to use biomagnetic susceptibility measured with SQUID devices, but these are few and far between.

Alternatively, the effect of iron on the MR signal can be exploited. One such technique uses the transverse relaxation rate R2 = 1/T2 from spin-echo images, calibrated against biopsy [1], and this has been cast into a commercial product with regulatory approval: FerriScan (Resonance Health, Claremont, WA, Australia). Another, larger group of published techniques uses the transverse relaxation rate R2* = 1/T2* from 2D gradient-echo images, also calibrated against biopsy [2-5]. Unfortunately, these calibrations vary, if not by very much. Potential reasons for these variations are differences in the reference histology procedure [6], but also in data acquisition, and probably most importantly, in the R2* evaluation procedures, and there mainly in how they deal with noise. Some techniques use a constant noise offset as model parameter, others subtract a measured noise level, or truncate the number of echoes used. Fortunately, it seems that different techniques, despite different calibrations, lead to comparable LIC values [7]. However, the previously published methods do not take fat signal effects into account.

In order for the $R2_c$* to be truly quantitative, the data fitting procedure needs to correct for confounding effects, in particular image noise and signal modulations from fat [8]. A disadvantage of taking the fat signal into account is that any erroneous swaps of fat and water not only lead to errors in the estimation of the fat fraction (in that case, it is *not* equal to one minus the water fraction), but also to a confounded estimation of $R2_c$*. An important additional effect to consider is that liver R2* scales almost linearly with field strength [9, 10].

R2* from multi-echo Dixon VIBE

The multi-step adaptive fitting approach in [11] was originally designed for fat quantification, and its signal model contains terms for water and fat, as well as R2*; the inner fitting step uses magnitude data; appropriate protocols have to be used so that the later echo images still have sufficient signal-to-noise ratio (SNR).

Protocol design

In general, measurement protocols for R2* estimation need echo times which are as short as possible to capture rapid signal decay [5]. On the other hand, the initial water/fat separation step in multi-echo Dixon VIBE works best when the first two echo times are at or near opposed- and in-phase. At 3T, these two requirements are not in conflict (the first opposed-phase echo time is 1.23 ms), but at 1.5T, echo times near opposed- and in-phase are preferred. To reduce noise bias, the SNR of the acquisition should be as high as possible, so smaller image matrices and moderate parallel imaging (iPAT) acceleration factors are helpful. Asymmetric data acquisition should be avoided [12]. Finally, since the later echoes will always be dominated by noise if R2* is very high, it may be advantageous to use only 4 instead of the standard number of 6 echoes. Recommended protocols are listed in Table 1.

	1.5T	3T
TE [ms]	1.1, 2.2, 3.3, 4.4 (5.5, 9.5)[1]	min, typ. 1.1, 2.2, 3.3, ...
Matrix	160	
Bandwidth [Hz/pixel]	typ. 1100 for minimum first TE	
Flip angle [°]	6[2]	5[2]
TR [ms]	min, typ. 11	
Asymmetric echo	off	
Partial Fourier	off	
Parallel imaging	CAIPIRINHA x3 (abdomen preset: PE x1, 3D x3, reordering shift 2)	

Table 1: Recommended protocol values for iron estimation with multi-echo Dixon VIBE.

[1] At very high R2*, leaving out the later echoes will help to avoid noise bias.
[2] Depending on TR. Higher flip angles will improve SNR, but introduce a T1 bias in the fat fraction values.

Data interpretation

A mean $R2_c^*$ can be measured from the corresponding parameter maps via a region-of-interest (ROI) using any viewing software. In multi-echo Dixon VIBE, one grey scale unit corresponds to 1 s^{-1}, as it is also noted in the DICOM image comment. This value can then be multiplied with the iron calibration conversion factor of choice (see below). Several ROIs in different slices can be used to assess spatial heterogeneity of liver iron overload, or to average results. As long as the inline liver segmentation contained in LiverLab was successful, the average R2* across the entire liver can also be used, but it has to be noted that structures inside the liver which are not liver parenchyma, e.g. large vessels, are not automatically excluded.

Iron calibration

So far, no direct iron calibration for fat-corrected $R2_c^*$ against biopsy has been published. However, initial comparisons between $R2_c^*$ and LIC from FerriScan come to similar conclusions [13, 14]. Figure 1 lists a number of iron calibration curves.

Noise bias on magnitude images will in general lead to under-estimation of R2*, and requires an increased calibration factor. Depending on the noise level, this effect sets in when T2* approaches twice the first TE, which is typically ~1 ms. Consequently, R2* values above 500 s^{-1} should always be assumed to be under-estimated; this means that currently severe iron overload cannot be reliably detected at 3T using LiverLab. It can, however, be assumed that R2* estimates are reproducible up to ~1000 s^{-1} as long as the protocol is held constant, the setup of patient and receive coils is comparable, and that there are no fat/water swaps, which would make follow-up examinations possible.

Trying to summarize the current state of knowledge, and taking into account the tendencies of the individual original techniques to under- or over-estimate R2*, a tentative working value for converting $R2_c^*$ from multi-echo Dixon VIBE in units of s^{-1} into LIC in units of mg/g dry weight (dw) at 1.5T seems to be approximately 0.032 mg/g Fe_{dw}/s^{-1}, e.g.

Examplary calculation for 1.5T

$R2_c^* = 200\ s^{-1}$

$\rightarrow LIC = 0.032 \cdot 200\ mg/g\ Fe_{dw}$
$= 6.4\ mg/g\ Fe_{dw}$

Most iron calibrations contain, beside the proportionality factor, an offset in mg/g Fe_{dw}, which is positive for some calibrations, and negative for others. In the absence of further evidence, we suggest to assume this offset to be zero, which seems to be supported by simulations [15]. Using the field-strength dependence as reported in [9], and typical Larmor frequency values of Siemens MR scanners, this translates into a conversion factor at 3T of approximately 0.017 mg/g Fe_{dw}/s^{-1}. Table 2 summarizes values which take into account an assumed under-estimation towards high R2* values.

However, for now, the LIC values calculated using LiverLab always have to be interpreted with care by an experienced user.

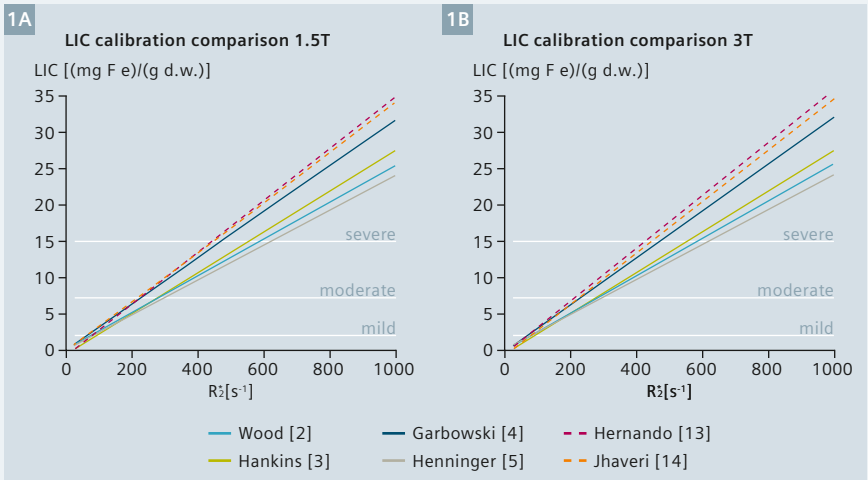

1 Existing iron calibrations. **(1A)** 1.5T; solid lines are calibrated against biopsy results, dashed lines are calibrated against FerriScan. **(1B)** 3T; there are no biopsy-based calibrations; results projected from 1.5T using [9], except Hernando [8].

	1.5T	3T[3]
mild (LIC ≥ 2 mg/g Fe_{dw})	65 s^{-1}	115 s^{-1}
moderate (LIC ≥ 7 mg/g Fe_{dw})	215 s^{-1}	400 s^{-1}
severe (LIC ≥ 15 mg/g Fe_{dw})	440 s^{-1}	n/a

Values in this table are a tentative and preliminary projection from existing studies, taking into account some expected under-estimation of R2* given the current limits of implementation in LiverLab.

Results will vary depending on protocol settings and image SNR, as well as on future changes in the algorithm.

Data interpretation and diagnostic conclusions are solely in the responsibility of the user.

Table 2: Tentative cut-off values of $R2_c^*$ from multi-echo Dixon VIBE for different grades of liver iron overload.

[3] 3T values are projected from 1.5T values using [9].

Offline processing of individual echoes

Multi-echo Dixon VIBE allows exporting the individual echoes in addition to the parameter maps. In challenging cases, or when an external cross-calibration is desired, these can be processed manually with custom software, see for example [16].

Likewise, the data acquisition protocols of existing iron calibrations, e.g. [3], or the signal-intensity ratio method described in [17], can easily be reproduced using the product 2D GRE sequence, and the results compared to those of LiverLab as long as the appropriate post-processing is used.

Conclusion and outlook

Although multi-echo Dixon VIBE from LiverLab was originally designed for liver fat evaluation, the $R2_c$* values, used with care, allow estimating liver iron concentration within limits.

There are predevelopment activities and ongoing studies to extend multi-echo Dixon VIBE to properly calibrated iron quantification in a future software version. We encourage all users of LiverLab to share their experience using the current product version.

Contact

Stephan Kannengiesser
Siemens Healthcare GmbH
MR PI TIO ONCO
Postbox 32 60
91050 Erlangen
Germany
Phone: +49 (1525) 4689516
stephan.kannengiesser@siemens.com

References

1 St Pierre TG, Clark PR, Chua-anusorn W, et al. Noninvasive measurement and imaging of liver iron concentrations using proton magnetic resonance. Blood 2005;105:855-861.

2 Wood JC, Enriquez C, Ghugre N, et al. MRI R2 and R2* mapping accurately estimates hepatic iron concentration in transfusion-dependent thalassemia and sickle cell disease patients. Blood 2005;106:1460-1465.

3 Hankins JS, McCarville MB, Loeffler RB, et al. R2* magnetic resonance imaging of the liver in patients with iron overload. Blood 2009;113:4853-4855.

4 Garbowski MW, Carpenter JP, Smith G, et al. Biopsy-based calibration of T2* magnetic resonance for estimation of liver iron concentration and comparison with R2 Ferriscan. J Cardiovasc Magn Reson 2014;16:40-50.

5 Henninger B, Zoller H, Rauch s, et al. R2* relaxometry for the quantification of hepatic iron overload: Biopsy-based calibration and comparison with the literature. RöFo 2015;187:472-479.

6 Butensky E, Fischer R, Hudes M, et al. Variability in hepatic iron concentration in percutaneous needle biopsy specimens from patients with transfusional hemosiderosis. Am J Clin Pathol 2005;123:146-152.

7 Meloni A, Rienhoff HY, Jones A, et al. The use of appropriate calibration curves corrects for systematic differences in liver R2* values measured using different software packages. Br J Haematol 2013.

8 Hernando D, Levin YS, Sirlin CB, et al. Quantification of liver iron with MRI: state of the art and remaining challenges. J Magn Reson Imaging 2014;40:1003-1021.

9 Storey P, Thompson AA, Carqueville CL, et al. R2* imaging of transfusional iron burden at 3T and comparison with 1.5T. J Magn Reson Imaging 2007;25:540-547.

10 Meloni A, Positano V, Keilberg P, et al. Feasibility, reproducibility, and reliability for the T2* iron evaluation at 3T in comparison with 1.5T. Magn Reson Med 2012;68:543-551.

11 Zhong X, Nickel MD, Kannengiesser S, et al. Liver fat quantification using a multi-step adaptive fitting approach with multi-echo GRE imaging. Magn Reson Med 2014;72:1353-1365.

12 Storey P, Liu YW, and Novikov DS. Artifact-free T2* mapping without post hoc corrections. Proc ISMRM 2015;23:442.

13 Hernando D, Quazi N, and Reeder SB. Calibration of confounder-corrected R2* for liver iron quantification at 1.5T and 3T: preliminary results. Proc ISMRM 2013;21:4194.

14 Jhaveri K, Kannengiesser S, Sadougi N, et al. A prospective study comparing R2* derived liver iron concentration (LIC) with noise-corrected post processing of data against FerriScan reported LIC in patients with liver iron overload. Proc ISMRM 2016;24:3854.

15 Ghugre NR, Doyle EK, Storey P, et al. Relaxivity-iron calibration in hepatic iron overload: Predictions of a Monte Carlo model. Magn Reson Med 2015;74:879-883.

16 Fernandes JL, and Kalaf JM. Increasing productivity in myocardial and liver T2* acquisition and analysis. MAGNETOM Flash 2015;1:28-32 (www.ironcalculator.com).

17 Gandon Y, Olivié D, Guyader D, et al. Non-invasive assessment of hepatic iron stores by MRI. Lancet 2004; 363:357-362 (www.ironbymr.fr).

Further Reading

An Efficient Workflow for Quantifying Hepatic Lipid and Iron Deposition using LiverLab

Puneet Sharma, Diego Martin (University of Arizona, Tucson, AZ, USA), MAGNETOM Flash #58 (3/2014)

Case Study LiverLab

Stephan Kannengiesser et al. (Siemens Healthcare, Erlangen, Germany), MAGNETOM Flash #58 (3/2014)

The articles are online at

www.siemens.com/magnetom-world

Try them on your system

Trial licenses for many of the applications featured in this issue of MAGNETOM Flash are available free of charge for a period of 90 days.

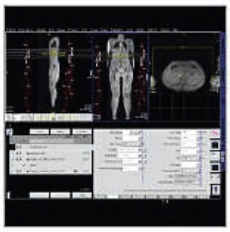

Tim Planning Suite
Allows planning of several stations at once, e.g. on composed localizer images. >

Tim Planning Suite

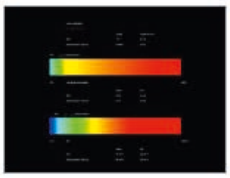

LiverLab
Evaluating the iron and fat content of the liver is an important step in monitoring early stages of liver diseases. >

LiverLab

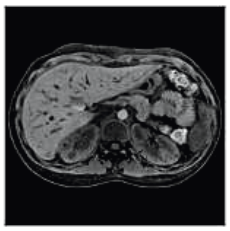

FREEZEit
Embrace motion in liver imaging. >

FREEZEit

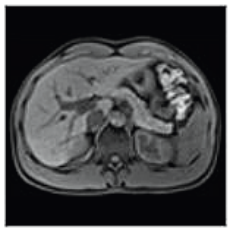

CAIPIRINHA
High-resolution 3D imaging with reduced breath-hold times. >

CAIPIRINHA

Brain Dot Engine
The Brain Dot Engine increaes productivity and standardization with guided and automated workflows. >

Brain Dot Engine

Abdomen Dot Engine
The Abdomen Dot Engine is customized for dynamic liver examinations and cosistent contrast timing. >

Abdomen Dot Engine

Spine Dot Engine
The Spine Dot Engine optimizes cervical, thoracic, and lumbar spine imaging for a wide range of patients and conditions. >

Spine Dot Engine

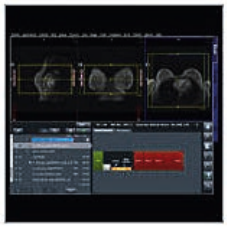

Breast Dot Engine
The Breast Dot Engine supports consistent frequency selection for fat, water, saline or silicone. >

Breast Dot Engine

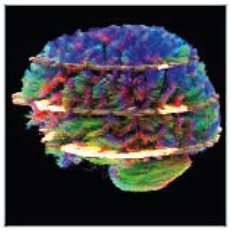

Simultaneous Multi-Slice
Accelerate advanced neuro applications for clinical routine. >

Simultaneous Multi-Slice

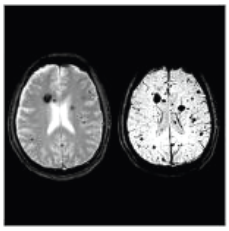

SWI
SWI is a new type of contrast technique in MRI that detects blood and iron deposits better than conventinal methods. >

Susceptibility-weighted Imaging

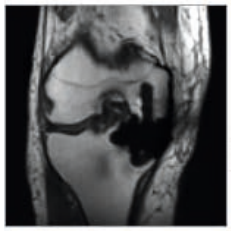

Advanced WARP
Advanced WARP corrects in- and through-plane distortions for more accurate diagnosis of tissue surrounding orthopedic implants. >

Advanced WARP

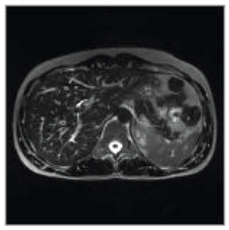

SPACE
SPACE enables the acquisition of high resolution 3D datasets. >

SPACE

For further details, product overviews, image galleries, step-by-step videos and general requirements visit us at:

www.siemens.com/mri-options-overview

Motion Correction of ^{90}Y Dose Maps with MR/PET Imaging

Nicolas A. Karakatsanis, Ph.D., MEng[1]; Mootaz Eldib, Ph.D.[1]; Niels Oesingmann, Ph.D.[2]; David D. Faul, Ph.D.[2]; Lale Kostakoglu, M.D., MPH[3]; Karin Knesaurek, Ph.D.[3]; Zahi A. Fayad, Ph.D.[1,4]

[1] Translational and Molecular Imaging Institute, Icahn School of Medicine at Mount Sinai, New York, NY, USA
[2] Siemens Healthineers, New York, NY, USA
[3] Department of Radiology, Icahn School of Medicine at Mount Sinai, New York, NY, USA
[4] Cardiovascular Institute, Icahn School of Medicine at Mount Sinai, New York, NY, USA

Introduction

Yttrium-90 (^{90}Y)[1] radioembolization is a therapeutic procedure that delivers local radiation to hepatic tumors [1]. Clinically, patients undergo a ^{90}Y Bremsstrahlung SPECT scan to determine if there was any extrahepatic deposition and, most importantly, to predict if the tumor is likely to respond to therapy based on the level of the delivered dose [2]. In addition, it is also possible to image and quantify the delivered ^{90}Y dose by PET, which was shown in this study to be superior to Bremsstrahlung SPECT in terms of spatial resolution and quantification accuracy [3]. Clinical SPECT and PET scanners are currently integrated with CT systems to enable localization as well as attenuation correction of the detected emission activity signal from the CT anatomical transmission signal [4]. However, clinical PET/CT studies have shown that the relative difference in dose between responding and non-responding lesions may be as low as 25%, thus demonstrating the importance of precise anatomical localization and high quantitative accuracy when assessing dose deposition [5]. Localization of the ^{90}Y signal distribution in the liver can be challenging with PET/CT, mainly due to the poor soft tissue discrimination and limited motion tracking capabilities offered by CT.

However, the recent advent of integrated MR/PET systems in clinic, supporting the simultaneous acquisition of PET and MR data, has enabled the automatic and highly accurate spatiotemporal co-registration of metabolic PET with anatomical and functional MR images [6]. The novel hybrid MR/PET technology may thus offer significant clinical benefits in ^{90}Y dose imaging assessments over PET/CT. First, MRI is associated with considerably better soft tissue constant therefore permitting the more accurate drawing of ROIs on the MR image when evaluating ^{90}Y PET regional assessments (Fig. 1). Second, the superior soft tissue resolution and absence of radiation exposure of MRI allows for more accurate tracking of the respiratory motion for improved PET motion correction. Thus, MR/PET could considerably enhance quantification in ^{90}Y dose imaging and therefore potentially improve therapeutic efficiency in clinic. Indeed, recent MR/PET studies have indicated a stronger relationship between tumor response and delivered dose even in the absence of motion correction [7].
In this study we are targeting the optimization of clinical ^{90}Y MR/PET imaging with a particular focus on MR-based motion correction of the ^{90}Y dose maps using the Biograph mMR integrated MR/PET system [8].

[1] Availability subject to restrictions. Agent referenced herein is not currently recognized by the US FDA as being safe and effective, and Siemens does not make any claims regarding their use.

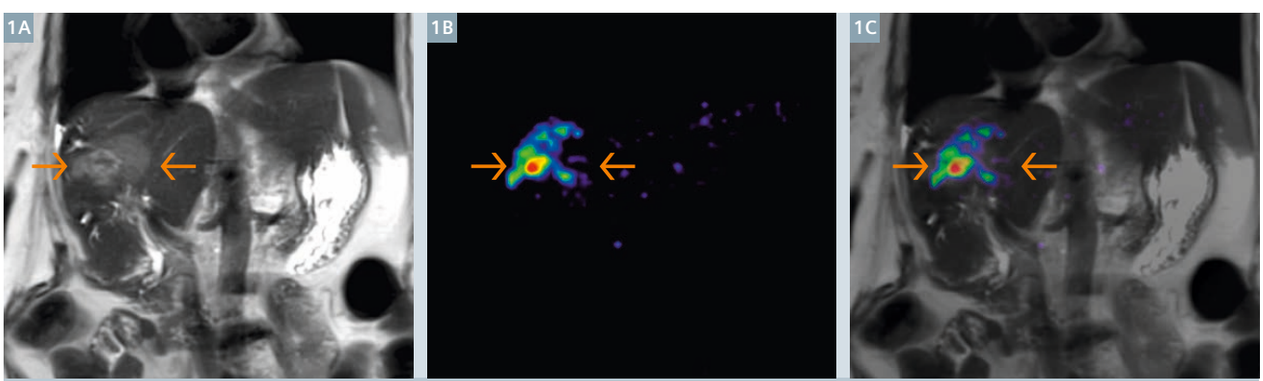

1 MRI **(1A)**, PET **(1B)**, and fused MRI/PET **(1C)** images of a subject who underwent ^{90}Y radioembolization. Arrows point to the lesion in the MR image (COR-HASTE) and the PET image.

3933_MR_Flash_66_RSNA_Inhalt.indd 48 09.11.16 09:51

Motion tracking and correction strategy for simultaneous ^{90}Y MR/PET imaging

The acquisition of anatomical MR signal of high spatial and temporal resolution allows for high temporal sampling rates of detailed 3D respiratory 3D cartesian motion vector field (MVF) estimates. In addition, the simultaneous acquisition of ^{90}Y PET data permits their synchronization with the MR-based respiratory motion phase for the accurate respiratory gating of the PET data. Finally, the gated PET data and the MVF are imported into a 4D PET motion-compensated image reconstruction (MCIR) algorithm to directly generate the motion-corrected ^{90}Y PET dose maps.

In this study, we exploit MR-based motion correction capabilities of the Biograph mMR system to assess the improvement in the quantitative accuracy of the ^{90}Y dose distribution assessments by reducing the respiratory motion blurring effect in the final PET reconstructed images. The lesions are often in the top region of the liver, which could move up to 2 cm due to respiration [9]. Therefore, our main goals are to:

1) Develop an optimal data acquisition and reconstruction scheme specially tuned for ^{90}Y imaging post radioembolization on the Siemens Biograph mMR; and
2) Evaluate the Biograph mMR motion correction algorithm (software version *syngo* MR E11p).

2

2 Sketch of the current data acquisition protocol on the mMR at Mount Sinai. Total scan time on the horizontal direction is about 30 minutes and includes patient positioning in the scanner.

Previously, we conducted a preliminary evaluation of the MCIR algorithm performance on ^{90}Y phantom studies [10, 11]. Currently, we expand our validation on patient data to optimize the motion-compensated reconstruction parameters in the clinic.

Our current protocol at Mount Sinai is outlined in Figure 2. The total scan time ranges between 30 and 35 minutes. Currently we run a prototype motion tracking sequence (Siemens BodyCOMPASS) during the acquisition of the PET scan. The sequence permits the generation of a set of high resolution 3D MR gated images, namely a 4D MR image, each corresponding to a different phase of the respiratory cycle, from end-expiration to end-inspiration. Subsequently, standard image registration methods are used to calculate from the gated MR images the 3D non-rigid motion transformation maps, which constitute the estimated motion model. In addition, the same MR data can be utilized to track the trace of the respiratory motion throughout the PET acquisition. This trace can be later employed to sort the synchronized PET data into the same set of respiratory gates. After the completion of the MR tracking sequence, we acquire additional MRI data with sequences designed for high-resolution anatomical static imaging to facilitate the accurate MR-based region-of-interest (ROI) localization in the ^{90}Y PET dose maps. Current MRI sequences in the exam are: 1) Axial HASTE, 2) Coronal HASTE, 3) 3D Dixon, 4) Axial T1w. We find HASTE images to be best for that purpose; however, contrast-enhanced MRI is used by other groups and its use should be investigated in the future. It is important to note that for ^{90}Y imaging it would be ideal to find only one sequence to be used for ROI definition in order to minimize scan time as much as possible. As a consequence, it would then be feasible to dedicate the entire PET scan for motion tracking if needed.

Figure 3 shows sample sagittal images showing the various phases. The sequence as well as the data sorting algorithm seems to perform well in resolving motion.

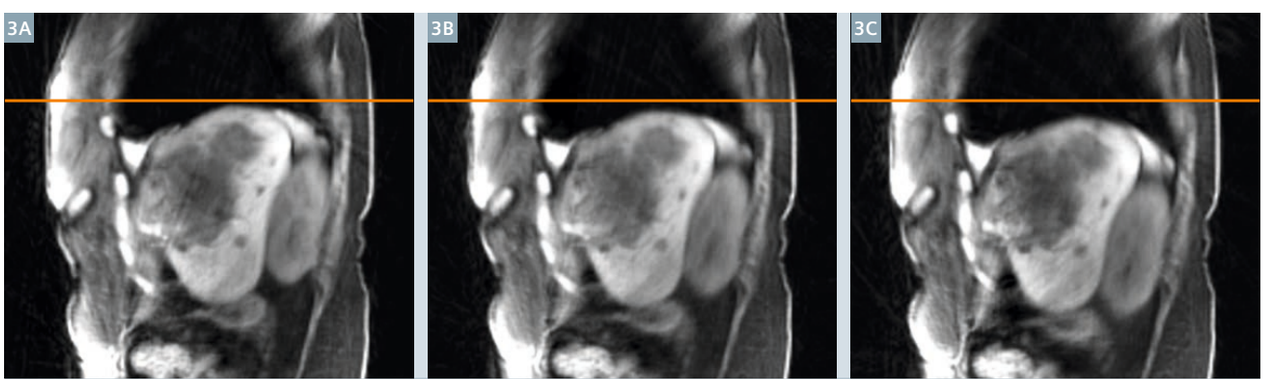

3 Examples of 3 different MR gated images corresponding to respective phases of the respiratory motion cycle, as generated with MR motion tracking sequence included in Biograph mMR *syngo* MR E11p software.

3933_MR_Flash_66_RSNA_Inhalt.indd 49 09.11.16 09:51

Enhancing ^{90}Y dose maps quantification with motion-compensated MR/PET imaging

Figure 4A illustrates a clear visual improvement in resolution and contrast of ^{90}Y dose maps after application of motion correction within the PET reconstruction. Motion corrected ^{90}Y PET images (right) are characterized by higher signal contrast recovery compared to the respective images without motion correction, i.e. static images (left). Moreover, the motion-corrected ^{90}Y images are associated with superior signal-to-noise ratio (SNR) compared to the gated ^{90}Y image (middle). The line plot in Figure 4B quantitatively confirms the improved contrast recovery for ^{90}Y dose maps when motion correction is applied. The degree of ^{90}Y contrast enhancement in the liver would be expected to reach maximum score levels for lesions located in the top of the liver, at the liver-lung interface. This is attributed to the strongest resolution degradation effects often observed in the liver-lung interface due to respiratory motion-induced contamination of the liver ^{90}Y uptake signal with the considerably smaller background signal from the lung. Indeed, the alignment of the ^{90}Y dose with the MR anatomical map before and after motion correction in Figure 5 illustrates the automatic correction of the position of the ^{90}Y deposited dose distribution within the liver after motion correction. This is of high importance in clinical practice, as occasionally a percentage of ^{90}Y activity may be observed in lungs due to air embolization [12].

Furthermore, in Figure 6 more clinical cases are presented where reconstructed ^{90}Y dose maps have benefited from MR-based PET motion correction. The contrast recovery enhancement of motion-corrected versus static PET images is visually evident in focal ^{90}Y uptake regions.

Moreover, in some clinical cases, no attachment to the target was observed for the delivered ^{90}Y dose thus resulting in diffused ^{90}Y distribution as shown in Figure 7.

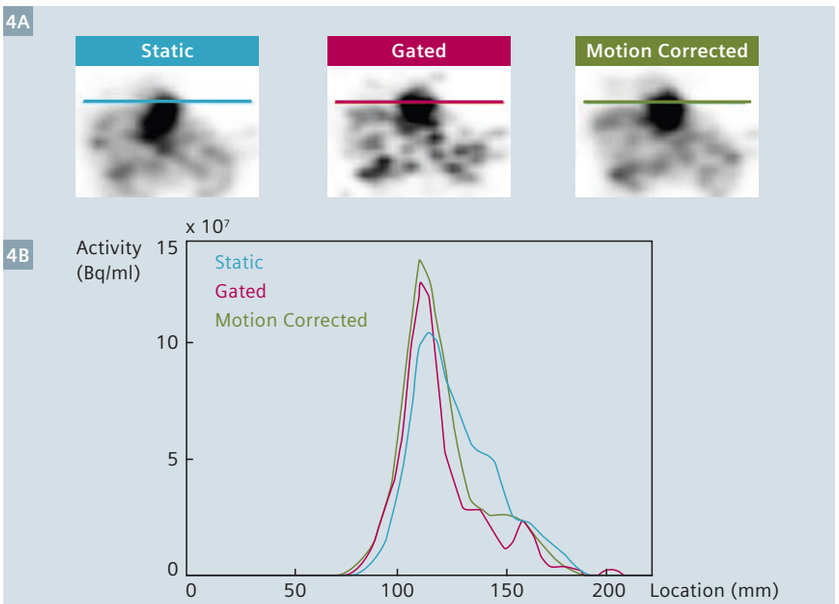

4 **(4A)** ^{90}Y PET images reconstructed without motion correction (static), gated (i.e. using the acquired data from only one respiratory phase), or motion corrected. Motion correction clearly improves activity signal recovery as shown visually in PET images **(4A)** and quantitatively in the respective line profiles **(4B).**

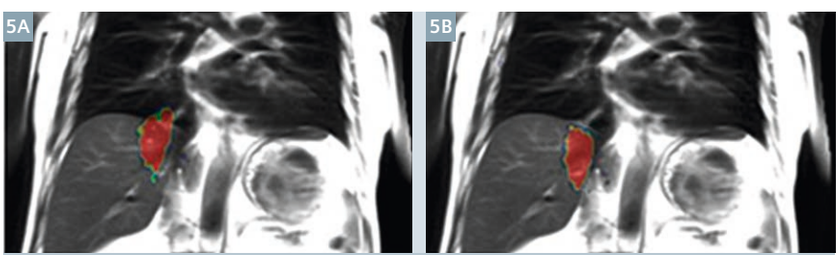

5 Automatic co-registration of MR with ^{90}Y before **(5A)** and after **(5B)** PET motion correction demonstrating the significantly improved accuracy in localizing the ^{90}Y signal distribution after motion correction.

Nevertheless, the Biograph mMR *syngo* MR E11p motion correction algorithm did not induce any artifacts or false positives.

Clinical prospects in motion-compensated ^{90}Y MR/PET imaging

Our preliminary findings in a few patients show that MR based motion correction for ^{90}Y could improve the quantitative accuracy of the data. As mentioned above, the literature indicates a difference between responding and non-responding lesions of 25%, and thus the margin for error is quite small. The effect of motion, especially at the top of the liver, could be higher than that margin and thus its use could be significant. To accurately measure the improvement, a cohort of about 20-30 subjects is desirable to show the potential benefits of motion correction. There are some attenuation correction issues including lack of a lung segment (i.e. LAC = 0) in some of our cases which require further evaluation. We have been using the motion correction sequence using the default parameters and this might require some optimization. Moreover, optimization, streamlining, and integration of motion correction into routine reconstruction are needed. Finally, the best number of gates and the navigator signal from the belt should be further investigated.

3933_MR_Flash_66_RSNA_Inhalt.indd 50 09.11.16 09:51

6

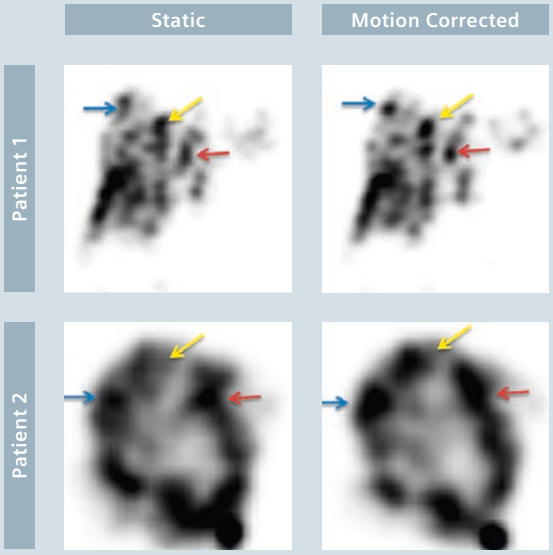

6 Clinical ^{90}Y PET images without (static) and with motion correction for 2 clinical cases with specific binding of ^{90}Y to the liver tissue.

7

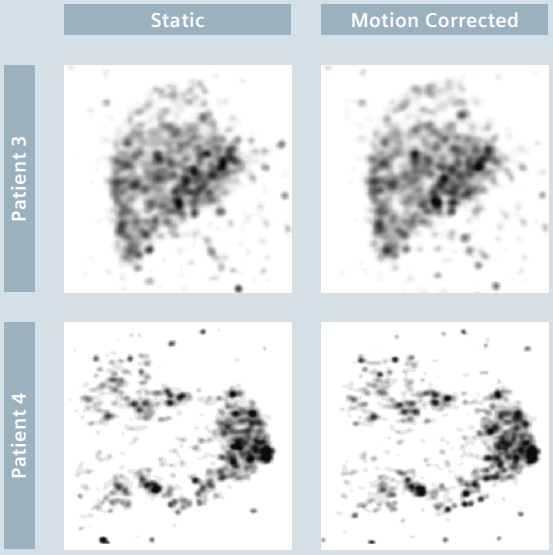

7 Clinical ^{90}Y PET images without (static) and with motion correction for 2 clinical cases characterized by absence of specific binding of ^{90}Y to the liver tissue.

References

1 Salem R and Thurston KG. Radioembolization with 90 Yttrium microspheres: a state-of-the-art brachytherapy treatment for primary and secondary liver malignancies: part 1: Technical and methodologic considerations. Journal of vascular and interventional radiology 2006; 17: 1251-1278.

2 Sarfaraz M, Kennedy AS, Lodge MA, Li XA, Wu X and Cedric XY. Radiation absorbed dose distribution in a patient treated with yttrium-90 microspheres for hepatocellular carcinoma. Medical physics 2004; 31: 2449-2453.

3 Elschot M, Vermolen BJ, Lam MG, de Keizer B, van den Bosch MA and de Jong HW. Quantitative comparison of PET and Bremsstrahlung SPECT for imaging the in vivo yttrium-90 microsphere distribution after liver radioembolization. PLoS One 2013; 8: e55742.

4 Townsend DW, Carney JP, Yap JT and Hall NC. PET/CT today and tomorrow. Journal of Nuclear Medicine 2004; 45: 4S-14S.

5 Srinivas SM, Natarajan N, Kuroiwa J, Gallagher S, Nasr E, Shah SN, DiFilippo FP, Obuchowski N, Bazerbashi B, Yu N and McLennan G. Determination of Radiation Absorbed Dose to Primary Liver Tumors and Normal Liver Tissue Using Post-Radioembolization (90)Y PET. Front Oncol 2014; 4: 255.

6 Judenhofer MS, Wehrl HF, Newport DF, Catana C, Siegel SB, Becker M, Thielscher A, Kneilling M, Lichy MP and Eichner M. Simultaneous PET-MRI: a new approach for functional and morphological imaging. Nature medicine 2008; 14: 459-465.

7 Fowler KJ, Maughan NM, Laforest R, Saad NE, Sharma A, Olsen J, Speirs CK and Parikh PJ. PET/MRI of hepatic 90Y microsphere deposition determines individual tumor response. Cardiovascular and interventional radiology 2016; 39: 855-864.

8 Delso G, Fürst S, Jakoby B, Ladebeck R, Ganter C, Nekolla SG, Schwaiger M and Ziegler SI. Performance measurements of the Siemens mMR integrated whole-body PET/MR scanner. Journal of nuclear medicine 2011; 52: 1914-1922.

9 Osman MM, Cohade C, Nakamoto Y and Wahl RL. Respiratory motion artifacts on PET emission images obtained using CT attenuation correction on PET-CT. European journal of nuclear medicine and molecular imaging 2003; 30: 603-606.

10 Maughan NM, Eldib M, Conti M, Knešaurek K, Faul D, Parikh PJ, Fayad ZA and Laforest R. Phantom study to determine optimal PET reconstruction parameters for PET/MR imaging of 90Y microspheres following radioembolization. Biomedical Physics & Engineering Express 2016; 2: 015009.

11 Eldib M, Oesingmann N, Faul DD, Kostakoglu L, Knešaurek K and Fayad ZA. Optimization of yttrium-90 PET for simultaneous PET/MR imaging: A phantom study. Medical Physics 2016; 43: 4768-4774.

12 Herba M, Illescas F, Thirlwell M, Boos G, Rosenthall L, Atri M and Bret P. Hepatic malignancies: improved treatment with intraarterial Y-90. Radiology 1988; 169: 311-314.

Contact

Zahi A. Fayad, Ph.D, FAHA, FACC, FISMRM
Icahn School of Medicine at Mount Sinai
Mount Sinai Endowed Chair in Medical Imaging and Bioengineering
Professor of Radiology and Medicine (Cardiology)
Director, Translational and Molecular Imaging Institute
Director, Cardiovascular Imaging Research
Vice-Chair for Research, Department of Radiology
One Gustave L. Levy Place
Box 1234
New York, NY 10029-6574, USA
Phone: +1 212 824 8452
Fax: +1 240 368 8096
zahi.fayad@mssm.edu

Motion Correction in PET/MR Using the Biograph mMR

Thomas Vahle, Ph.D.[1]; Michael Fieseler, Ph.D.[2]; Fernando E. Boada, Ph.D.[1]

[1] New York University, Langone Medical Center, Center for Advanced Imaging Innovation and Research (CAI²R), New York, NY, USA
[2] European Institute for Molecular Imaging (EIMI), Münster, Germany

Introduction

Respiratory motion affects quantitative and qualitative evaluation of PET data. As an example, there are concerns about the accuracy of PET/CT in the detection and characterization of small pulmonary lesions. It has been reported that sub-centimeter nodules have a high (40%) false negatives rate [1]. This appears to be related to respiratory and cardiac motion combined with the inherently sequential acquisition of PET and CT images when using a conventional PET/CT scanner [2].

For PET/CT several approaches have been presented to reduce the motion blur and to improve the PET reconstructions. Here, motion information can be taken from either CT or PET images. Using CT images usually comes with a higher dose delivery to the patient due to the additional CT acquisitions required for the motion estimation. Even if high-resolution CT images can be used to provide sufficient characterization of the motion, this approach is still limited due to the sequential nature of the acquisition in PET and CT.

Several approaches have been discussed to estimate the motion directly from PET images representing different motion states during a respiratory cycle. Although encouraging results have been presented, this might still not be sufficient for all applications. PET gives functional information, thus only structures with sufficient tracer uptake are visible. The quality of motion estimation from PET data may depend on which structures are actually depicted. For example, in PET using ^{18}F-FDG[1], structures like the liver and the heart are visible and may give sufficient information to estimate motion, while a tracer very specific for small structures, e.g., atherosclerotic plaques, might pose a problem for motion estimation from PET data alone.

Modern PET/MR systems allow acquiring MR and PET data simultaneously [3]. Since spatial and temporal alignment is intrinsically ensured, the MR data can directly be used to correct the PET data for motion. MRI gives morphological information with good soft tissue contrast, thus structure visibility is independent of tracer uptake.

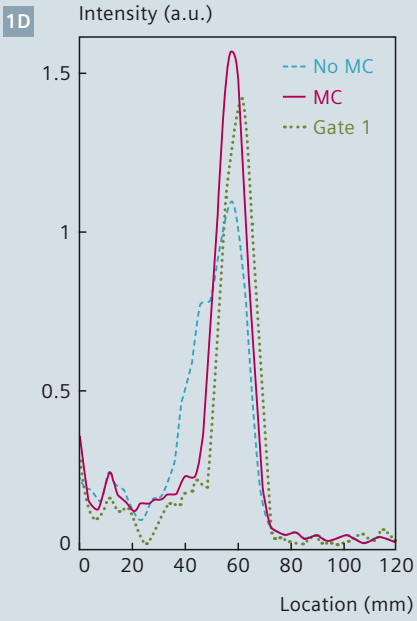

1 Overlay of PET and MR data for **(1A)** reference motion state (single PET gate), **(1B)** reconstruction without motion correction, **(1C)** reconstruction with motion correction. **(1D)** Line profiles in feet-head direction through the lesion for **(1A–C)**, showing higher signal intensity and less blurring after motion correction.

[1] The full prescribing information for the Fludeoxyglucose F18 injection can be found at page 57.

Additionally, MRI has the potential for better spatial resolution, compared to PET. In motion correction for PET/MR, four basic MRI acquisition strategies are used:

1) Fast acquisition of 3D data
2) 2D acquisitions with subsequent sorting into 3D data
3) Gating of *k*-space data with subsequent reconstruction
4) Simultaneous reconstruction of motion and image data

In the first strategy, data are acquired that may be directly used for motion estimation, while in the second and third strategy data for motion estimation are derived from the collected data.

A possible problem with strategy 1 is that image quality and acquisition time are inversely related in MRI. To achieve a sufficient temporal resolution, i.e., to cover the respiratory cycle with a sufficient number of 3D volumes, very fast acquisitions have to be employed, thus image quality has to be sacrificed. In strategies 2 and 3, data is collected over the course of several respirations and sorted afterwards. A possible problem to consider with strategies 2 and 3 might be that datasets constructed from several respiratory cycles may not cover variation between respiration cycles (inter-cycle variation, see [4]).

Fast 3D acquisitions have been investigated, e.g., in [5-7], achieving temporal resolutions of 0.6-0.7 seconds per 3D volume.

In [5], fast 3D acquisitions are compared to retrospectively sorted 2D acquisitions. In comparison the authors state that motion estimation is rendered difficult in low quality 3D acquisitions. King *et al.* proposed the creation of a motion model derived from fast 3D data, which is then parameterized by a 2D navigator [6]. 3D data is acquired over several respiration cycles. Subjects were instructed to perform different breathing patterns during acquisition, with the aim to be able to account for variable breathing during application of the model.

Acquisition of 2D slices in sagittal orientation with subsequent sorting into 3D volumes has been investigated [8-11]. Sagittal slice orientation is chosen since respiratory motion has only a small left-right component, so sagittal slice orientation covers the dominant directions head-feet (HF) and anterior-posterior (AP). The signal used for sorting is a 1D navigator crossing the diaphragm during the PET acquisition. Also, image similarity metrics like mutual information (MI) have been investigated for sorting [5]. Gradient echo sequences (GRE) are used [8-10], as well as a TrueFISP sequence [11].

Continuous acquisition of MRI data with subsequent sorting of *k*-space data has been demonstrated in [12-15]. In this work, MRI data are acquired continuously as T1-weighted radial stack of stars spoiled 3-dimensional GRE with fat suppression and sagittal slab orientation.

Due to the acquisition type presented in [12-15], the center of *k*-space is sampled with a high temporal frequency.

The signal at the center of *k*-space gives a measure of the total amount of (transverse) magnetization as detected by the receiver coils in each coil element. As sensitivity of the coils differs spatially, respiratory motion leads to variations in the amount of magnetization measured [16]. This allows for the extraction of a gating signal (self-gating). Variable amplitude-based gating is used for both MRI and PET data.

In [17], tagged MRI is acquired synchronized to an ECG. A navigator is additionally acquired to keep track of the respiratory phase. All acquired MRI raw data are sorted according to respiratory and cardiac phase and subsequently reconstructed. As acquisition of tagged data can be time consuming, the possibility of accelerated acquisition using parallel imaging and compressed sensing were demonstrated [18].

Simultaneous reconstruction of MRI data and estimation of motion has been proposed in [19, 20]. Here, image reconstruction and motion estimation are solved as a coupled inverse problem. The motion model used is parameterized by an additionally acquired respiratory signal using a pressure-sensitive bellow.

As mentioned above, MRI itself offers additional ways to extract respiratory signals. 1D navigators may serve as a gating signal or to parameterize a derived motion model. Also, a 2D navigator has been used in [5] to parameterize a motion model.

In self-gated MRI sequences, a signal derived from the center of *k*-space may be used for gating of MRI [12-15].

In [12], the signal of the pressure-sensitive bellows shipped with the scanner is compared to a self-gating signal derived from MRI and several signals derived from PET data. Though the study is somewhat limited due to a clipped bellows signal and comparatively low activity, the authors conclude that gating signals derived from either PET or MRI are comparable to those from external sensors.

Often, 4-5 gates are chosen for respiratory motion correction [9, 12, 20]. In [15] the average binning error is determined for MRI data. The authors find that with five gates or more the binning error falls below the PET pixel size of 2 mm. In [8], 10 gates are chosen to cover a full respiration cycle (instead of the full range of excursion) to account for differences between motion during inspiration and expiration (hysteresis).

In this work we demonstrate applications of motion correction for lung and cardiac imaging using a self-navigated, three-dimensional, T1-weighted MRI sequence[2] on the Biograph mMR.

Materials and methods

Study population

Patients were recruited using an IRB-approved protocol and written informed consent was obtained

[2] WIP, the product is currently under development and is not for sale in the US and in other countries. Its future availability cannot be ensured.

for the 3 patients. All patients (64, 67, 75 y) first underwent a PET/CT examination (Biograph mCT, Siemens Medical Solutions USA, Inc. Knoxville TN, USA). Afterwards, additional PET/MR data were acquired (Biograph mMR, Siemens Healthcare, Erlangen, Germany). All data were collected at the NYU Langone Medical Center.

An average activity of 539.46 ± 8.11 MBq was injected and the PET/MR acquisitions were performed 218.3 ± 43 min post injection. No additional radiotracer was injected for the PET/MR acquisition. At the mMR, PET list mode was acquired simultaneously with the Siemens work-in-progress (WIP) sequence. For attenuation correction the routine MR-based segmentation AC was performed.

For the MRI based motion correction data were acquired using a three-dimensional, T1-weighted VIBE sequence. This sequence allows deriving a respiratory signal from the acquired *k*-space data (self-navigation), and also provides the ability to sort the acquired samples according to their position in the respiratory cycle. Retrospective gating was performed resulting in 5 datasets representing different motion states. Images were reconstructed using a non-uniform Fourier transformation. Motion vectors were calculated using an adapted demons algorithm [26] with local cross correlation as a similarity measure and a spatial regularization that was optimized for inferring respiratory motion in the given protocol. Motion fields are computed directly inline after the gated acquisition and are made persistent in the *syngo* database for later usage in motion correction.

Data processing

In order to ensure temporal synchronization between both modalities, the binning information from the gating signal was used to sort the PET raw data accordingly. The missing arms in the μ-maps due to the limited field of view were recovered using the maximum likelihood reconstruction of attenuation and activity (MLAA). For this step as well as for the calculation of the scatter estimates, the offline reconstruction tools were used. All PET images were reconstructed iteratively with a 3D ordered-subsets expectation maximization (OSEM) algorithm using 3 iterations and 21 subsets implemented in the reconstruction framework. Further parameters used for the OSEM algorithm were a matrix size of 172 x 172, pixel size 4.17 mm^2, slice thickness 2.03 mm, and Gaussian filtering with an FWHM of 4 mm. For the reconstruction with motion correction, the OSEM

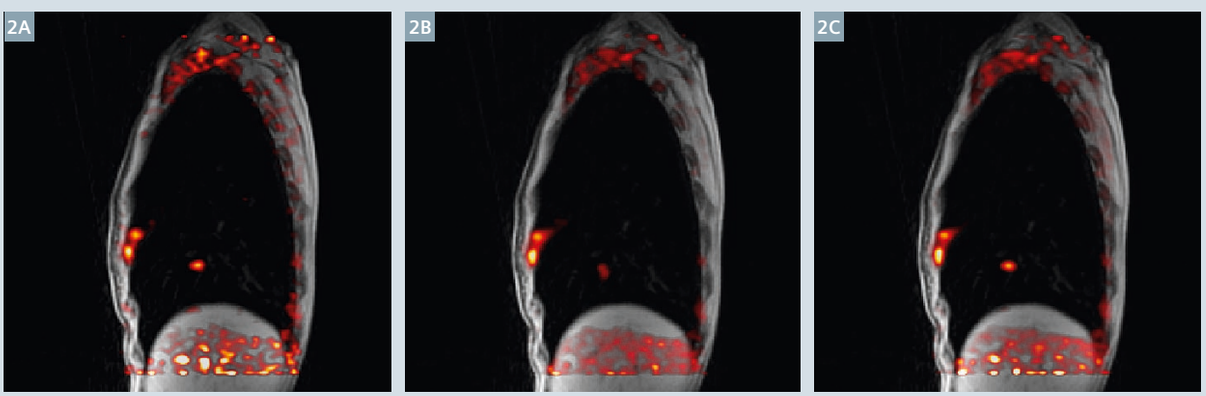

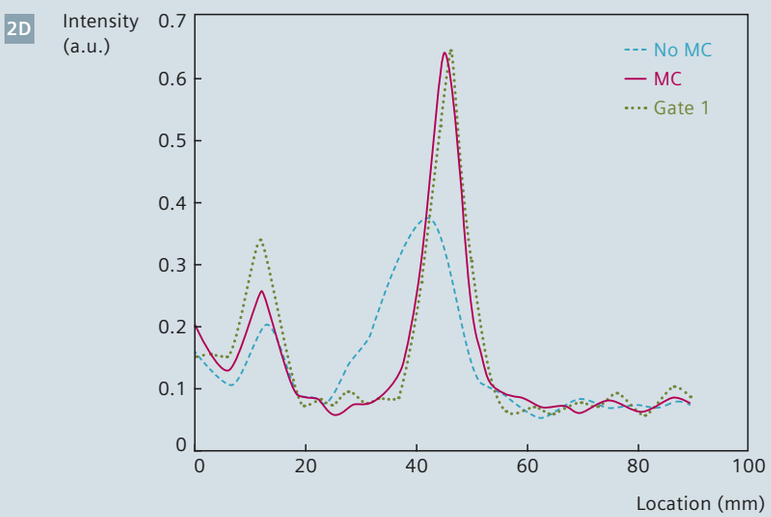

2 Overlay of PET and MR data for **(2A)** reference motion state (single PET gate), **(2B)** reconstruction without motion correction, **(2C)** reconstruction with motion correction. **(2D)** Line profiles through the lesion for **(2A–C)** in feet-head direction. The signal for motion corrected data matches the signal for the reference motion state closely.

3933_MR_Flash_66_RSNA_Inhalt.indd 54 09.11.16 09:54

algorithm was extended by two operators handling the motion between the different states of the respiratory cycle. The motion vectors provided by the WIP sequence were used to warp the current image estimate to the corresponding motion state before the forward projection and back to the reference state after the back projection step. Hence all PET data can be used within a motion-compensating OSEM extension to compute a single motion-free PET image.

Results

Benefits of the motion correction algorithm can be prominently observed in anatomical regions or structures which are strongly affected by respiratory motion like the lung or the abdomen.

Lung nodule detection could be considerably improved by the use of the combined MR/PET platform. This is illustrated in Figure 1. Respiratory motion leads to significant blurring of the lesion signal. Upon motion correction (Fig. 1C), the blurring is significantly reduced leading to both improved lesion localization as well as improved quantitative assessment of the tracer uptake.

Figure 2 presents another example of improved small lesion detection using MR/PET based motion correction. As can be appreciated in the line plot (Fig. 2D), the peak intensity over background of the lesion in uncorrected PET data is only about half of the peak intensity in motion corrected PET data.

Figure 3 shows an example for motion correction of the heart. After motion correction (Fig. 3C), the structure of the heart is more clearly resolved than in the uncorrected data (Fig. 3B) or gated data (Fig. 3A).

In addition to the blur reduction and increase in peak intensity, the noise characteristic of the motion corrected image is comparable to a regular static non-motion corrected acquisition and greatly exceeds regular gated acquisitions. Hence, small lesions affected by respiratory motion will benefit from better detectability with a boost in signal to noise after motion correction as demonstrated in these examples, which is not achievable with common respiratory gating techniques.

Discussion

Self-navigated imaging sequences provide a straightforward way to include motion correction into a PET/MR scanner. The simultaneous acquisition of data for both modalities allows an easy transfer of temporal and spatial information from one modality to the other one. The MR based respiratory gating signal extracted from acquired *k*-space data can thereby also be used to sort the PET data accordingly.

In this initial evaluation of three patient cases, the potential of the motion correction based on the Siemens WIP sequence was shown. After motion correction, quantitative and qualitative evaluation of the PET images is improved. This improvement is mainly visible for the two cases with lung nodules, but respiratory motion correction also has an impact on cardiac datasets despite the remaining contractile motion of the beating heart.

Conclusion

Respiratory motion correction could become an important application for combined PET/MR systems. The presented Siemens WIP sequence combined with motion corrected PET reconstruction improved the PET quantification in these three cases significantly compared to standard (non-motion corrected) PET. Validation of this motion correction approach using a larger patient cohort is ongoing. The initial results presented here make this approach a promising tool for clinical applications.

Acknowledgments

This work was performed in collaboration with the European Institute for Molecular Imaging (EIMI) and Siemens Healthcare GmbH. The authors would like to thank Matthias Fenchel and Robert Grimm (both Siemens Healthcare GmbH) for their valuable participation and support.

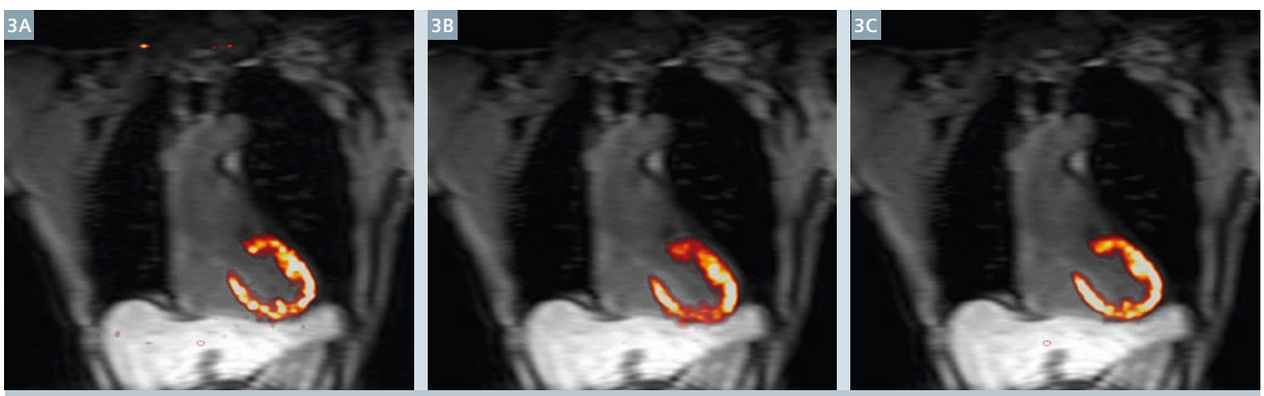

3 Overlay of PET and MR data for **(3A)** reference motion state, **(3B)** reconstruction without motion correction, **(3C)** reconstruction with motion correction. Motion correction reduces the blurring visible in uncorrected data **(3B)** and shows less noise than gated data **(3A)**.

3933_MR_Flash_66_RSNA_Inhalt.indd 55 09.11.16 09:54

References

1 Girvin F, Ko JP. Pulmonary nodules: detection, assessment, and CAD. AJR Am J Roentgenol. 2008;191(4):1057-69.

2 Benjamin MS, Drucker EA, McLoud TC, Shepard JA. Small pulmonary nodules: detection at chest CT and outcome. Radiology. 2003;226(2):489-93.

3 Quick HH, von Gall C, Zeilinger M, Wiesmüller M, Braun H, Ziegler S, Kuwert T, Uder M, Dörfler A, Kalender WA, Lell M. Integrated whole-body PET/MR hybrid imaging: clinical experience. Invest Radiol. 2013 May;48(5):280-9.

4 McClelland, Jamie R et al. "Respiratory motion models: a review." Medical image analysis 17.1 (2013): 19-42.

5 Dikaios, Nikolaos et al. "MRI-based motion correction of thoracic PET: initial comparison of acquisition protocols and correction strategies suitable for simultaneous PET/MRI systems." European radiology 22.2 (2012): 439-446.

6 King, Andrew P et al. "Thoracic respiratory motion estimation from MRI using a statistical model and a 2-D image navigator." Medical image analysis 16.1 (2012): 252-264.

7 Fieseler, Michael et al. "A dynamic thorax phantom for the assessment of cardiac and respiratory motion correction in PET/MRI: a preliminary evaluation." Nuclear Instruments and Methods in Physics Research Section A: Accelerators, Spectrometers, Detectors and Associated Equipment 702 (2013): 59-63.

8 Manber, Richard et al. "Practical PET respiratory motion correction in clinical PET/MR." Journal of Nuclear Medicine 56.6 (2015): 890-896.

9 Würslin, Christian et al. "Respiratory motion correction in oncologic PET using T1-weighted MR imaging on a simultaneous whole-body PET/MR system." Journal of Nuclear Medicine 54.3 (2013): 464-471.

10 Fayad, Hadi et al. "Reconstruction-incorporated respiratory motion correction in clinical simultaneous PET/MR imaging for oncology applications." Journal of Nuclear Medicine 56.6 (2015): 884-889.

11 Petibon, Yoann et al. "MR-based motion correction in simultaneous PET/MR liver imaging." Journal of Nuclear Medicine 54.supplement 2 (2013): 68-68.

12 Fürst, Sebastian et al. "Motion correction strategies for integrated PET/MR." Journal of Nuclear Medicine 56.2 (2015): 261-269.

13 Feng, Li et al. "Golden-angle radial sparse parallel MRI: Combination of compressed sensing, parallel imaging, and golden-angle radial sampling for fast and flexible dynamic volumetric MRI." Magnetic resonance in medicine 72.3 (2014): 707-717.

14 Feng, Li et al. "XD-GRASP: Golden-angle radial MRI with reconstruction of extra motion-state dimensions using compressed sensing." Magnetic resonance in medicine 75.2 (2016): 775-788.

15 Grimm, Robert et al. "Self-gated MRI motion modeling for respiratory motion compensation in integrated PET/MRI." Medical image analysis 19.1 (2015): 110-120.

16 Lin, Wei et al. "Respiratory motion-compensated radial dynamic contrast-enhanced (DCE)-MRI of chest and abdominal lesions." Magnetic resonance in medicine 60.5 (2008): 1135-1146.

17 Ouyang, Jinsong, Quanzheng Li, and Georges El Fakhri. "Magnetic resonance-based motion correction for positron emission tomography imaging." Seminars in nuclear medicine 31 Jan. 2013: 60-67.

18 Huang, Chuan et al. "Accelerated acquisition of tagged MRI for cardiac motion correction in simultaneous PET-MR: Phantom and patient studies." Medical physics 42.2 (2015): 1087-1097.

19 Odille, Freddy et al. "Generalized Reconstruction by Inversion of Coupled Systems (GRICS) applied to free-breathing MRI." Magnetic Resonance in Medicine 60.1 (2008): 146-157.

20 Fayad, Hadi J et al. "A generic PET/MRI respiratory motion correction using a generalized reconstruction by inversion of coupled systems (GRICS) approach." Nuclear Science Symposium and Medical Imaging Conference (NSS/MIC), 2012 IEEE 27 Oct. 2012: 2813-2816.

21 Belaroussi, Boubakeur et al. "Intensity non-uniformity correction in MRI: existing methods and their validation." Medical Image Analysis 10.2 (2006): 234-246.

22 Myronenko, Andriy, and Xubo Song. "Intensity-based image registration by minimizing residual complexity." IEEE Transactions on Medical Imaging 29.11 (2010): 1882-1891.

23 Dutta, Joyita et al. "Respiratory motion compensation in simultaneous PET/MR using a maximum a posteriori approach." 2013 IEEE 10th International Symposium on Biomedical Imaging 7 Apr. 2013: 800-803.

24 Heinrich, Mattias P et al. "Globally optimal deformable registration on a minimum spanning tree using dense displacement sampling." International Conference on Medical Image Computing and Computer-Assisted Intervention 1 Oct. 2012: 115-122.

25 Dawood, Mohammad et al. "A mass conservation-based optical flow method for cardiac motion correction in 3D-PET." Medical physics 40.1 (2013): 012505.

26 Thirion JP. Image matching as a diffusion process: an analogy with Maxwell's demons. Medical image analysis. 1998 Sep 30;2(3):243-60.

The statements by Siemens' customers described herein are based on results that were achieved in the customer's unique setting. Since there is no 'typical' setting and many variables exist there can be no guarantee that other customers will achieve the same results.

Contact

Thomas Vahle, Ph.D.
New York University
Langone Medical Center
Center for Advanced Imaging Innovation and Research (CAI²R)
4th Floor 660 First Avenue
New York, NY, 10016, USA
Thomas.Vahle@nyumc.org

3933_MR_Flash_66_RSNA_Inhalt.indd 56 09.11.16 09:54

HIGHLIGHTS OF PRESCRIBING INFORMATION

These highlights do not include all the information needed to use Fludeoxyglucose F 18 Injection safely and effectively. See full prescribing information for Fludeoxyglucose F 18 Injection.
Fludeoxyglucose F 18 Injection, USP
For intravenous use
Initial U.S. Approval: 2005

RECENT MAJOR CHANGES

Warnings and Precautions (5.1, 5.2)	7/2010
Adverse Reactions (6)	7/2010

INDICATIONS AND USAGE

Fludeoxyglucose F18 Injection is indicated for positron emission tomography (PET) imaging in the following settings:

- Oncology: For assessment of abnormal glucose metabolism to assist in the evaluation of malignancy in patients with known or suspected abnormalities found by other testing modalities, or in patients with an existing diagnosis of cancer.
- Cardiology: For the identification of left ventricular myocardium with residual glucose metabolism and reversible loss of systolic function in patients with coronary artery disease and left ventricular dysfunction, when used together with myocardial perfusion imaging.
- Neurology: For the identification of regions of abnormal glucose metabolism associated with foci of epileptic seizures (1).

DOSAGE AND ADMINISTRATION

Fludeoxyglucose F 18 Injection emits radiation. Use procedures to minimize radiation exposure. Screen for blood glucose abnormalities.

- In the oncology and neurology settings, instruct patients to fast for 4 to 6 hours prior to the drug's injection. Consider medical therapy and laboratory testing to assure at least two days of normoglycemia prior to the drug's administration (5.2).
- In the cardiology setting, administration of glucose-containing food or liquids (e.g., 50 to 75 grams) prior to the drug's injection facilitates localization of cardiac ischemia (2.3).

Aseptically withdraw Fludeoxyglucose F 18 Injection from its container and administer by intravenous injection (2).

The recommended dose:

- for adults is 5 to 10 mCi (185 to 370 MBq), in all indicated clinical settings (2.1).
- for pediatric patients is 2.6 mCi in the neurology setting (2.2).

Initiate imaging within 40 minutes following drug injection; acquire static emission images 30 to 100 minutes from time of injection (2).

DOSAGE FORMS AND STRENGTHS

Multi-dose 30mL and 50mL glass vial containing 0.74 to 7.40 GBq/mL (20 to 200 mCi/mL) Fludeoxyglucose F 18 Injection and 4.5mg of sodium chloride with 0.1 to 0.5% w/w ethanol as a stabilizer (approximately 15 to 50 mL volume) for intravenous administration (3).

CONTRAINDICATIONS

None

WARNINGS AND PRECAUTIONS

- Radiation risks: use smallest dose necessary for imaging (5.1).
- Blood glucose adnormalities: may cause suboptimal imaging (5.2).

ADVERSE REACTIONS

Hypersensitivity reactions have occurred; have emergency resuscitation equipment and personnel immediately available (6).
To report SUSPECTED ADVERSE REACTIONS, contact PETNET Solutions, Inc. at 877-473-8638 or FDA at 1-800-FDA-1088 or www.fda.gov/medwatch.

USE IN SPECIFIC POPULATIONS

Pregnancy Category C: No human or animal data. Consider alternative diagnostics; use only if clearly needed (8.1).

- Nursing mothers: Use alternatives to breast feeding (e.g., stored breast milk or infant formula) for at least 10 half-lives of radioactive decay, if Fludeoxyglucose F 18 Injection is administered to a woman who is breast-feeding (8.3).
- Pediatric Use: Safety and effectiveness in pediatric patients have not been established in the oncology and cardiology settings (8.4).

See 17 for PATIENT COUNSELING INFORMATION

Revised: 1/2011

FULL PRESCRIBING INFORMATION: CONTENTS*

1 INDICATIONS AND USAGE
1.1 Oncology
1.2 Cardiology
1.3 Neurology
2 DOSAGE AND ADMINISTRATION
2.1 Recommended Dose for Adults
2.2 Recommended Dose for Pediatric Patients
2.3 Patient Preparation
2.4 Radiation Dosimetry
2.5 Radiation Safety – Drug Handling
2.6 Drug Preparation and Administration
2.7 Imaging Guidelines
3 DOSAGE FORMS AND STRENGTHS
4 CONTRAINDICATIONS
5 WARNINGS AND PRECAUTIONS
5.1 Radiation Risks
5.2 Blood Glucose Abnormalities
6 ADVERSE REACTIONS
7 DRUG INTERACTIONS
8 USE IN SPECIFIC POPULATIONS
8.1 Pregnancy
8.3 Nursing Mothers
8.4 Pediatric Use
11 DESCRIPTION
11.1 Chemical Characteristics
11.2 Physical Characteristics
12 CLINICAL PHARMACOLOGY
12.1 Mechanism of Action
12.2 Pharmacodynamics
12.3 Pharmacokinetics
13 NONCLINICAL TOXICOLOGY
13.1 Carcinogenesis, Muta-genesis, Impairment of Fertility
14 CLINICAL STUDIES
14.1 Oncology
14.2 Cardiology
14.3 Neurology
15 REFERENCES
16 HOW SUPPLIED/STORAGE AND DRUG HANDLING
17 PATIENT COUNSELING INFORMATION

* Sections or subsections omitted from the full prescribing information are not listed.

FULL PRESCRIBING INFORMATION

1 INDICATIONS AND USAGE

Fludeoxyglucose F 18 Injection is indicated for positron emission tomography (PET) imaging in the following settings:

1.1 Oncology

For assessment of abnormal glucose metabolism to assist in the evaluation of malignancy in patients with known or suspected abnormalities found by other testing modalities, or in patients with an existing diagnosis of cancer.

1.2 Cardiology

For the identification of left ventricular myocardium with residual glucose metabolism and reversible loss of systolic function in patients with coronary artery disease and left ventricular dysfunction, when used together with myocardial perfusion imaging.

1.3 Neurology

For the identification of regions of abnormal glucose metabolism associated with foci of epileptic seizures.

2 DOSAGE AND ADMINISTRATION

Fludeoxyglucose F 18 Injection emits radiation. Use procedures to minimize radiation exposure. Calculate the final dose from the end of synthesis (EOS) time using proper radioactive decay factors. Assay the final dose in a properly calibrated dose calibrator before administration to the patient [see Description (11.2)].

2.1 Recommended Dose for Adults

Within the oncology, cardiology and neurology settings, the recommended dose for adults is 5 to 10 mCi (185 to 370 MBq) as an intravenous injection.

2.2 Recommended Dose for Pediatric Patients

Within the neurology setting, the recommended dose for pediatric patients is 2.6 mCi, as an intravenous injection. The optimal dose adjustment on the basis of body size or weight has not been determined [see Use in Special Populations (8.4)].

2.3 Patient Preparation

- To minimize the radiation absorbed dose to the bladder, encourage adequate hydration. Encourage the patient to drink water or other fluids (as tolerated) in the 4 hours before their PET study.
- Encourage the patient to void as soon as the imaging study is completed and as often as possible thereafter for at least one hour.
- Screen patients for clinically significant blood glucose abnormalities by obtaining a history and/or laboratory tests [see Warnings and Precautions (5.2)]. Prior to Fludeoxyglucose F 18 PET imaging in the oncology and neurology settings, instruct patient to fast for 4 to 6 hours prior to the drug's injection.
- In the cardiology setting, administration of glucose-containing food or liquids (e.g., 50 to 75 grams) prior to Fludeoxyglucose F18 Injection facilitates localization of cardiac ischemia

2.4 Radiation Dosimetry

The estimated human absorbed radiation doses (rem/mCi) to a newborn (3.4 kg), 1-year old (9.8 kg), 5-year old (19 kg), 10-year old (32 kg), 15-year old (57 kg), and adult (70 kg) from intravenous administration of Fludeoxyglucose F 18 Injection are shown in Table 1. These estimates were calculated based on human[2] data and using the data published by the International Commission on Radiological Protection[4] for Fludeoxyglucose ^{18} F. The dosimetry data show that there are slight variations in absorbed radiation dose for various organs in each of the age groups. These dissimilarities in absorbed radiation dose are due to developmental age variations (e.g., organ size, location, and overall metabolic rate for each age group). The identified critical organs (in descending order) across all age groups evaluated are the urinary bladder, heart, pancreas, spleen, and lungs.

Table 1. Estimated Absorbed Radiation Doses (rem/mCi) After Intravenous Administration of Fludeoxyglucose F-18 Injection[a]

Organ	Newborn (3.4 kg)	1-year old (9.8 kg)	5-year old (19 kg)	10-year old (32 kg)	15-year old (57 kg)	Adult (70 kg)
Bladder wall[b]	4.3	1.7	0.93	0.60	0.40	0.32
Heart wall	2.4	1.2	0.70	0.44	0.29	0.22
Pancreas	2.2	0.68	0.33	0.25	0.13	0.096
Spleen	2.2	0.84	0.46	0.29	0.19	0.14
Lungs	0.96	0.38	0.20	0.13	0.092	0.064
Kidneys	0.81	0.34	0.19	0.13	0.089	0.074
Ovaries	0.80	0.8	0.19	0.11	0.058	0.053
Uterus	0.79	0.35	0.19	0.12	0.076	0.062
LLI wall *	0.69	0.28	0.15	0.097	0.060	0.051
Liver	0.69	0.31	0.17	0.11	0.076	0.058
Gallbladder wall	0.69	0.26	0.14	0.093	0.059	0.049
Small intestine	0.68	0.29	0.15	0.096	0.060	0.047
ULI wall **	0.67	0.27	0.15	0.090	0.057	0.046
Stomach wall	0.65	0.27	0.14	0.089	0.057	0.047
Adrenals	0.65	0.28	0.15	0.095	0.061	0.048
Testes	0.64	0.27	0.14	0.085	0.052	0.041
Red marrow	0.62	0.26	0.14	0.089	0.057	0.047
Thymus	0.61	0.26	0.14	0.086	0.056	0.044
Thyroid	0.61	0.26	0.13	0.080	0.049	0.039
Muscle	0.58	0.25	0.13	0.078	0.049	0.039
Bone surface	0.57	0.24	0.12	0.079	0.052	0.041
Breast	0.54	0.22	0.11	0.068	0.043	0.034
Skin	0.49	0.20	0.10	0.060	0.037	0.030
Brain	0.29	0.13	0.09	0.078	0.072	0.070
Other tissues	0.59	0.25	0.13	0.083	0.052	0.042

[a] MIRDOSE 2 software was used to calculate the radiation absorbed dose. Assumptions on the biodistribution based on data from Gallagher et al.1 and Jones et al.2

[b] The dynamic bladder model with a uniform voiding frequency of 1.5 hours was used. *LLI = lower large intestine; **ULI = upper large intestine

2.5 Radiation Safety – Drug Handling

- Use waterproof gloves, effective radiation shielding, and appropriate safety measures when handling Fludeoxyglucose F 18 Injection to avoid unnecessary radiation exposure to the patient, occupational workers, clinical personnel and other persons.
- Radiopharmaceuticals should be used by or under the control of physicians who are qualified by specific training and experience in the safe use and handling of radionuclides, and whose experience and training have been approved by the appropriate governmental agency authorized to license the use of radionuclides.
- Calculate the final dose from the end of synthesis (EOS) time using proper radioactive decay factors. Assay the final dose in a properly calibrated dose calibrator before administration to the patient [see Description (11.2)].
- The dose of Fludeoxyglucose F 18 used in a given patient should be minimized consistent with the objectives of the procedure, and the nature of the radiation detection devices employed.

2.6 Drug Preparation and Administration

- Calculate the necessary volume to administer based on calibration time and dose.
- Aseptically withdraw Fludeoxyglucose F 18 Injection from its container.
- Inspect Fludeoxyglucose F 18 Injection visually for particulate matter and discoloration before administration, whenever solution and container permit.
- Do not administer the drug if it contains particulate matter or discoloration; dispose of these unacceptable or unused preparations in a safe manner, in compliance with applicable regulations.
- Use Fludeoxyglucose F 18 Injection within 12 hours from the EOS.

2.7 Imaging Guidelines

- Initiate imaging within 40 minutes following Fludeoxyglucose F 18 Injection administration.
- Acquire static emission images 30 to 100 minutes from the time of injection.

3 DOSAGE FORMS AND STRENGTHS

Multiple-dose 30 mL and 50 mL glass vial containing 0.74 to 7.40 GBq/mL (20 to 200 mCi/mL) of Fludeoxyglucose F 18 Injection and 4.5 mg of sodium chloride with 0.1 to 0.5% w/w ethanol as a stabilizer (approximately 15 to 50 mL volume) for intravenous administration.

4 CONTRAINDICATIONS

None

5 WARNINGS AND PRECAUTIONS

5.1 Radiation Risks

Radiation-emitting products, including Fludeoxyglucose F 18 Injection, may increase the risk for cancer, especially in pediatric patients. Use the smallest dose necessary for imaging and ensure safe handling to protect the patient and health care worker [see Dosage and Administration (2.5)].

5.2 Blood Glucose Abnormalities

In the oncology and neurology setting, suboptimal imaging may occur in patients with inadequately regulated blood glucose levels. In these patients, consider medical therapy and laboratory testing to assure at least two days of normoglycemia prior to Fludeoxyglucose F 18 Injection administration.

6 ADVERSE REACTIONS

Hypersensitivity reactions with pruritus, edema and rash have been reported in the postmarketing setting. Have emergency resuscitation equipment and personnel immediately available.

7 DRUG INTERACTIONS

The possibility of interactions of Fludeoxyglucose F 18 Injection with other drugs taken by patients undergoing PET imaging has not been studied.

8 USE IN SPECIFIC POPULATIONS

8.1 Pregnancy

Pregnancy Category C

Animal reproduction studies have not been conducted with Fludeoxyglucose F 18 Injection. It is also not known whether Fludeoxyglucose F 18 Injection can cause fetal harm when administered to a pregnant woman or can affect reproduction capacity. Consider alternative diagnostic tests in a pregnant woman; administer Fludeoxyglucose F 18 Injection only if clearly needed.

8.3 Nursing Mothers

It is not known whether Fludeoxyglucose F 18 Injection is excreted in human milk. Consider alternative diagnostic tests in women who are breast-feeding. Use alternatives to breast feeding (e.g., stored breast milk or infant formula) for at least 10 half-lives of radioactive decay, if Fludeoxyglucose F 18 Injection is administered to a woman who is breast-feeding.

8.4 Pediatric Use

The safety and effectiveness of Fludeoxyglucose F 18 Injection in pediatric patients with epilepsy is established on the basis of studies in adult and pediatric patients. In pediatric patients with epilepsy, the recommended dose is 2.6 mCi. The optimal dose adjustment on the basis of body size or weight has not been determined. In the oncology or cardiology settings, the safety and effectiveness of Fludeoxyglucose F 18 Injection have not been established in pediatric patients.

11 DESCRIPTION

11.1 Chemical Characteristics

Fludeoxyglucose F 18 Injection is a positron emitting radiopharmaceutical that is used for diagnostic purposes in conjunction with positron emission tomography (PET) imaging. The active ingredient 2-deoxy-2-[^{18}F]fluoro-D-glucose has the molecular formula of $C_6H_{11}{}^{18}FO_5$ with a molecular weight of 181.26, and has the following chemical structure:

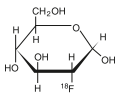

Fludeoxyglucose F 18 Injection is provided as a ready to use sterile, pyrogen free, clear, colorless solution. Each mL contains between 0.740 to 7.40GBq (20.0 to 200 mCi) of 2-deoxy-2-[^{18}F]fluoro-D-glucose at the EOS, 4.5 mg of sodium chloride and 0.1 to 0.5% w/w ethanol as a stabilizer. The pH of the solution is between 4.5 and 7.5. The solution is packaged in a multiple-dose glass vial and does not contain any preservative.

11.2 Physical Characteristics

Fluorine F 18 decays by emitting positron to Oxygen O 16 (stable) and has a physical half-life of 109.7 minutes. The principal photons useful for imaging are the dual 511 keV gamma photons, that are produced and emitted simultaneously in opposite direction when the positron interacts with an electron (Table 2).

Table 2. Pricipal Radiation Emission Data for Fluorine F18

Radiation/Emission	% Per Disintegration	Mean Energy
Positron (b+)	96.73	249.8 keV
Gamma (±)*	193.46	511.0 keV

*Produced by positron annihilation

From: Kocher, D.C. Radioactive Decay Tables DOE/TIC-I 1026, 89 (1981)

The specific gamma ray constant (point source air kerma coefficient) for fluorine F 18 is 5.7 R/hr/mCi (1.35 x 10-6 Gy/hr/kBq) at 1 cm. The half-value layer (HVL) for the 511 keV photons is 4 mm lead (Pb). The range of attenuation coefficients for this radionuclide as a function of lead shield thickness is shown in Table 3. For example, the interposition of an 8 mm thickness of Pb, with a coefficient of attenuation of 0.25, will decrease the external radiation by 75%.

Table 3. Radiation Attenuation of 511 keV Photons by lead (Pb) shielding

Shield thickness (Pb) mm	Coefficient of attenuation
0	0.00
4	0.50
8	0.25
13	0.10
26	0.01
39	0.001
52	0.0001

For use in correcting for physical decay of this radionuclide, the fractions remaining at selected intervals after calibration are shown in Table 4.

Table 4. Physical Decay Chart for Fluorine F18

Minutes	Fraction Remaining
0*	1.000
15	0.909
30	0.826
60	0.683
110	0.500
220	0.250

*calibration time

12 CLINICAL PHARMACOLOGY

12.1 Mechanism of Action

Fludeoxyglucose F 18 is a glucose analog that concentrates in cells that rely upon glucose as an energy source, or in cells whose dependence on glucose increases under pathophysiological conditions. Fludeoxyglucose F 18 is transported through the cell membrane by facilitative glucose transporter proteins and is phosphorylated within the cell to [18F] FDG-6-phosphate by the enzyme hexokinase. Once phosphorylated it cannot exit until it is dephosphorylated by glucose-6-phosphatase. Therefore, within a given tissue or pathophysiological process, the retention and clearance of Fludeoxyglucose F 18 reflect a balance involving glucose transporter, hexokinase and glucose-6-phosphatase activities. When allowance is made for the kinetic differences between glucose and Fludeoxyglucose F 18 transport and phosphorylation (expressed as the ‚lumped constant" ratio), Fludeoxyglucose F 18 is used to assess glucose metabolism. In comparison to background activity of the specific organ or tissue type, regions of decreased or absent uptake of Fludeoxyglucose F 18 reflect the decrease or absence of glucose metabolism. Regions of increased uptake of Fludeoxyglucose F 18 reflect greater than normal rates of glucose metabolism.

12.2 Pharmacodynamics

Fludeoxyglucose F 18 Injection is rapidly distributed to all organs of the body after intravenous administration. After background clearance of Fludeoxyglucose F 18 Injection, optimal PET imaging is generally achieved between 30 to 40 minutes after administration.

In cancer, the cells are generally characterized by enhanced glucose metabolism partially due to (1) an increase in activity of glucose transporters, (2) an increased rate of phosphorylation activity, (3) a reduction of phosphatase activity or, (4) a dynamic alteration in the balance among all these processes. However, glucose metabolism of cancer as reflected by Fludeoxyglucose F 18 accumulation shows considerable variability. Depending on tumor type, stage, and location, Fludeoxyglucose F 18 accumulation may be increased, normal, or decreased. Also, inflammatory cells can have the same variability of uptake of Fludeoxyglucose F 18.

In the heart, under normal aerobic conditions, the myocardium meets the bulk of its energy requirements by oxidizing free fatty acids. Most of the exogenous glucose taken up by the myocyte is converted into glycogen. However, under ischemic conditions, the oxidation of free fatty acids decreases, exogenous glucose becomes the preferred myocardial sub strate, glycolysis is stimulated, and glucose taken up by the myocyte i s metabolized immediately instead of being converted into glycogen. Under these conditions, phosphorylated Fludeoxyglucose F 18 accumulates in the myocyte and can be detected with PET imaging.

In the brain, cells normally rely on aerobic metabolism. In epilepsy, the glucose metabolism varies. Generally, during a seizure, glucose metabolism increases. Interictally, the seizure focus tends to be hypometabolic.

12.3 Pharmacokinetics

Distribution: In four healthy male volunteers, receiving an intravenous administration of 30 seconds in duration, the arterial blood level profile for Fludeoxyglucose F 18 decayed triexponentially. The effective half-life ranges of the three phases were 0.2 to 0.3 minutes, 10 to 13 minutes with a mean and standard deviation (STD) of 11.6 (±) 1.1 min, and 80 to 95 minutes with a mean and STD of 88 (±) 4 min.

Plasma protein binding of Fludeoxyglucose F 18 has not been studied.

Metabolism: Fludeoxyglucose F 18 is transported into cells and phosphorylated to [^{18}F]-FDG-6- phosphate at a rate proportional to the rate of glucose utilization within that tissue. [F18]-FDG-6-phosphate presumably is metabolized to 2-deoxy-2-[F18]fluoro-6-phospho-D-mannose([F 18]FDM-6-phosphate).

Fludeoxyglucose F 18 Injection may contain several impurities (e.g., 2-deoxy-2-chloro-D-glucose (ClDG)). Biodistribution and metabolism of ClDG are presumed to be similar to Fludeoxyglucose F 18 and would be expected to result in intracellular formation of 2-deoxy-2-chloro-6-phospho-D-glucose (ClDG-6-phosphate) and 2-deoxy-2-chloro-6-phospho-D-mannose (ClDM-6-phosphate). The phosphorylated deoxyglucose compounds are dephosphorylated and the resulting compounds (FDG, FDM, ClDG, and ClDM) presumably leave cells by passive diffusion. Fludeoxyglucose F 18 and related compounds are cleared from non-cardiac tissues within 3 to 24 hours after administration. Clearance from the cardiac tissue may require more than 96 hours. Fludeoxyglucose F 18 that is not involved in glucose metabolism in any tissue is then excreted in the urine.

Elimination: Fludeoxyglucose F 18 is cleared from most tissues within 24 hours and can be eliminated from the body unchanged in the urine. Three elimination phases have been identified in the reviewed literature. Within 33 minutes, a mean of 3.9% of the administrated radioactive dose was measured in the urine. The amount of radiation exposure of the urinary bladder at two hours post-administration suggests that 20.6% (mean) of the radioactive dose was present in the bladder.

Special Populations:

The pharmacokinetics of Fludeoxyglucose F 18 Injection have not been studied in renally-impaired, hepatically impaired or pediatric patients. Fludeoxyglucose F 18 is eliminated through the renal system. Avoid excessive radiation exposure to this organ system and adjacent tissues.

The effects of fasting, varying blood sugar levels, conditions of glucose intolerance, and diabetes mellitus on Fludeoxyglucose F 18 distribution in humans have not been ascertained [see Warnings and Precautions (5.2)].

13 NONCLINICAL TOXICOLOGY

13.1 Carcinogenesis, Mutagenesis, Impairment of Fertility

Animal studies have not been performed to evaluate the Fludeoxyglucose F 18 Injection carcinogenic potential, mutagenic potential or effects on fertility.

14 CLINICAL STUDIES

14.1 Oncology

The efficacy of Fludeoxyglucose F 18 Injection in positron emission tomography cancer imaging was demonstrated in 16 independent studies. These studies prospectively evaluated the use of Fludeoxyglucose F 18 in patients with suspected or known malignancies, including non-small cell lung cancer, colo-rectal, pancreatic, breast, thyroid, melanoma, Hodgkin's and non-Hodgkin's lymphoma, and various types of metastatic cancers to lung, liver, bone, and axillary nodes. All these studies had at least 50 patients and used pathology as a standard of truth. The Fludeoxyglucose F 18 Injection doses in the studies ranged from 200 MBq to 740 MBq with a median and mean dose of 370 MBq.

In the studies, the diagnostic performance of Fludeoxyglucose F 18 Injection varied with the type of cancer, size of cancer, and other clinical conditions. False negative and false positive scans were observed. Negative Fludeoxyglucose F 18 Injection PET scans do not exclude the diagnosis of cancer. Positive Fludeoxyglucose F 18 Injection PET scans can not replace pathology to establish a diagnosis of cancer. Non-malignant conditions such as fungal infections, inflammatory processes and benign tumors have patterns of increased glucose metabolism that may give rise to false-positive scans. The efficacy of Fludeoxyglucose F 18 Injection PET imaging in cancer screening was not studied.

14.2 Cardiology

The efficacy of Fludeoxyglucose F 18 Injection for cardiac use was demonstrated in ten independent, prospective studies of patients with coronary artery disease and chronic left ventricular systolic dysfunction who were scheduled to undergo coronary revascularization. Before revascularization, patients underwent PET imaging with Fludeoxyglucose F 18 Injection (74 to 370 MBq, 2 to 10 mCi) and perfusion imaging with other diagnostic radiopharmaceuticals. Doses of Fludeoxyglucose F 18 Injection ranged from 74 to 370 MBq (2 to 10 mCi). Segmental, left ventricular, wall-motion assessments of asynergic areas made before revascularization were compared in a blinded manner to assessments made after successful revascularization to identify myocardial segments with functional recovery.

Left ventricular myocardial segments were predicted to have reversible loss of systolic function if they showed Fludeoxyglucose F 18 accumulation and reduced perfusion (i.e., flow-metabolism mismatch). Conversely, myocardial segments were predicted to have irreversible loss of systolic function if they showed reductions in both Fludeoxyglucose F 18 accumulation and perfusion (i.e., matched defects).

Findings of flow-metabolism mismatch in a myocardial segment may suggest that successful revascularization will restore myocardial function in that segment. However, false-positive tests occur regularly, and the decision to have a patient undergo revascularization should not be based on PET findings alone. Similarly, findings of a matched defect in a myocardial segment may suggest that myocardial function will not recover in that segment, even if it is successfully revascularized. However, false-negative tests occur regularly, and the decision to recommend against coronary revascularization, or to recommend a cardiac transplant, should not be based on PET findings alone. The reversibility of segmental dysfunction as predicted with Fludeoxyglucose F 18 PET imaging

depends on successful coronary revascularization. Therefore, in patients with a low likelihood of successful revascularization, the diagnostic usefulness of PET imaging with Fludeoxyglucose F 18 Injection is more limited.

14.3 Neurology

In a prospective, open label trial, Fludeoxyglucose F 18 Injection was evaluated in 86 patients with epilepsy. Each patient received a dose of Fludeoxyglucose F 18 Injection in the range of 185 to 370 MBq (5 to 10 mCi). The mean age was 16.4 years (range: 4 months to 58 years; of these, 42 patients were less than 12 years and 16 patients were less than 2 years old). Patients had a known diagnosis of complex partial epilepsy and were under evaluation for surgical treatment of their seizure disorder. Seizure foci had been previously identified on ictal EEGs and sphenoidal EEGs. Fludeoxyglucose F 18 Injection PET imaging confirmed previous diagnostic findings in 16% (14/87) of the patients; in 34% (30/87) of the patients, Fludeoxyglucose F 18 Injection PET images provided new findings. In 32% (27/87), imaging with Fludeoxyglucose F 18 Injection was inconclusive. The impact of these imaging findings on clinical outcomes is not known.

Several other studies comparing imaging with Fludeoxyglucose F 18 Injection results to subsphenoidal EEG, MRI and/or surgical findings supported the concept that the degree of hypometabolism corresponds to areas of confirmed epileptogenic foci. The safety and effectiveness of Fludeoxyglucose F 18 Injection to distinguish idiopathic epileptogenic foci from tumors or other brain lesions that may cause seizures have not been established.

15 REFERENCES

1. Gallagher B.M., Ansari A., Atkins H., Casella V., Christman D.R., Fowler J.S., Ido T., MacGregor R.R., Som P., Wan C.N., Wolf A.P., Kuhl D.E., and Reivich M. "Radiopharmaceuticals XXVII. 18F-labeled 2-deoxy-2-fluoro-d-glucose as a radiopharmaceutical for measuring regional myocardial glucose metabolism in vivo: tissue distribution and imaging studies in animals," J Nucl Med, 1977; 18, 990-6.
2. Jones S.C., Alavi, A., Christman D., Montanez, I., Wolf, A.P., and Reivich M. "The radiation dosimetry of 2 [F-18] fluoro-2-deoxy-D-glucose in man," J Nucl Med, 1982; 23, 613-617.
3. Kocher, D.C. "Radioactive Decay Tables: A handbook of decay data for application to radiation dosimetry and radiological assessments," 1981, DOE/TIC-I 1026, 89.
4. ICRP Publication 53, Volume 18, No. I-4,1987, pages 75-76.

16 HOW SUPPLIED/STORAGE AND DRUG HANDLING

Fludeoxyglucose F 18 Injection is supplied in a multi-dose, capped 30 mL and 50 mL glass vial containing between 0.740 to 7.40 GBq/mL (20 to 200 mCi/mL), of no carrier added 2-deoxy-2-[F 18] fluoro-D-glucose, at end of synthesis, in approximately 15 to 50 mL. The contents of each vial are sterile, pyrogen-free and preservative-free.

NDC 40028-511-30; 40028-511-50

Receipt, transfer, handling, possession, or use of this product is subject to the radioactive material regulations and licensing requirements of the U.S. Nuclear Regulatory Commission, Agreement States or Licensing States as appropriate.

Store the Fludeoxyglucose F 18 Injection vial upright in a lead shielded container at 25°C (77°F); excursions permitted to 15-30°C (59-86°F).

Store and dispose of Fludeoxyglucose F 18 Injection in accordance with the regulations and a general license, or its equivalent, of an Agreement State or a Licensing State.

The expiration date and time are provided on the container label. Use Fludeoxyglucose F 18 Injection within 12 hours from the EOS time.

17 PATIENT COUNSELING INFORMATION

Instruct patients in procedures that increase renal clearance of radioactivity.

Encourage patients to:

- drink water or other fluids (as tolerated) in the 4 hours before their PET study.
- void as soon as the imaging study is completed and as often as possible thereafter for at least one hour.

Manufactured by: PETNET Solutions Inc.
810 Innovation Drive
Knoxville, TN 37932

Distributed by: PETNET Solutions Inc.
810 Innovation Drive
Knoxville, TN 37932

PETNET Solutions

PN0002262 Rev. A

March 1, 2011

Indications

Fludeoxyglucose F^{18} Injection is indicated for positron emission tomography (PET) imaging in the following settings:

- **Oncology:** For assessment of abnormal glucose metabolism to assist in the evaluation of malignancy in patients with known or suspected abnormalities found by other testing modalities, or in patients with an existing diagnosis of cancer.
- **Cardiology:** For the identification of left ventricular myocardium with residual glucose metabolism and reversible loss of systolic function in patients with coronary artery disease and left ventricular dysfunction, when used together with myocardial perfusion imaging.
- **Neurology:** For the identification of regions of abnormal glucose metabolism associated with foci of epileptic seizures.

Important Safety Information

- **Radiation Risks:** Radiationemitting products, including Fludeoxyglucose F^{18} Injection, may increase the risk for cancer, especially in pediatric patients. Use the smallest dose necessary for imaging and ensure safe handling to protect the patient and healthcare worker.
- **Blood Glucose Abnormalities:** In the oncology and neurology setting, suboptimal imaging may occur in patients with inadequately regulated blood glucose levels. In these patients, consider medical therapy and laboratory testing to assure at least two days of normoglycemia prior to Fludeoxyglucose F^{18} Injection administration.
- **Adverse Reactions:** Hypersensitivity reactions with pruritus, edema and rash have been reported; have emergency resuscitation equipment and personnel immediately available.

Cardio-pulmonary MRI for Diagnosis and Monitoring of Chronic Thromboembolic Pulmonary Hypertension (CTEPH)

Christian Schoenfeld, M.D.[1,2]; Andreas Voskrebenzev, Ph.D.[1,2]; Jens Vogel-Claussen, M.D.[1,2]

[1] Diagnostic and Interventional Radiology, Hannover Medical School, Hannover, Germany
[2] Biomedical Research in Endstage and Obstructive Lung Disease Hannover (BREATH), Member of the German Center for Lung Research (DZL), Hannover, Germany

Introduction

Chronic Thromboembolic Pulmonary Hypertension (CTEPH) is a disease causing shortness of breath that could ultimately be life threatening but is potentially curable [1, 2]. Mean survival is less than 2 years in untreated CTEPH patients who have mean pulmonary artery pressure (mPAP) higher than 30 mmHg at diagnosis [3].

Currently there is a diagnostic algorithm for CTEPH diagnosis according to the 2015 ESC/ERS Guidelines for the diagnosis and treatment of pulmonary hypertension [4]. The diagnosis of pulmonary hypertension (PH) requires a clinical suspicion based on symptoms, physical examination and review of a comprehensive set of investigations to confirm that hemodynamic criteria are met and to describe the etiology, the functional and hemodynamic severity of the condition. The interpretation of these investigations requires, at the very least, expertise in cardiology, imaging and respiratory medicine and may best be discussed at a multidisciplinary team meeting [4]. Echocardiography is initially used to confirm a general diagnosis of PH. Then ventilation/perfusion scanning (V/Q- SPECT) is the recommended clinical standard to confirm or rule out CTEPH diagnosis. This should be followed by right heart catheterization (RHC) which is the gold standard for PH diagnosis. RHC is ideally coupled with conventional pulmonary angiography, the technique for confirming the location and extent of disease that is mandatory for treatment planning [4]. Further workup of CTEPH patients may include pulmonary angiography computed tomography or cardio-pulmonary MRI.

Within the last decade cardio-pulmonary MRI has been introduced into the clinic and its acceptance as a tool to diagnose CTEPH and monitor treatment of patients with CTEPH is rapidly increasing [5, 6]. As a non-invasive imaging technique that does not involve ionizing radiation, it is the standard of reference for biventricular functional evaluation that can provide comprehensive functional-, perfusion- and hemodynamic-evaluation of the cardio-pulmonary unit in the setting of CTEPH.

MRI-derived cardiac function and volumetry in CTEPH

Cine cardiac MR acquisitions have been established as the non-invasive gold standard for assessment of biventricular structure and function due to their inherent spatial resolution and freedom from acoustic window compared to echocardiography [7]. In CTEPH patients cardio-pulmonary MRI should include stacks of cine short axis and long axis images of both ventricles. These acquisitions allow reproducible and accurate biventricular size, function, volume and mass quantification. This is of particular importance in patients with pulmonary artery hypertension where right ventricular (RV) function is related to patient survival [8].

Typical signs for PH-related right heart strain are right RV dilatation, hypertrophy, right atrial dilatation and septal bowing [9]. RV hypertrophy is a remodeling mechanism in response to increased pulmonary pressure, which becomes insufficient to compensate increased afterload in the long term. It has been shown that in PH RV mass, wall thickness, and the ventricular mass index (VMI = ratio of RV mass to left ventricular (LV) mass) measured

Key Points

Chronic Thromboembolic Pulmonary Hypertension (CTEPH) is a disease causing shortness of breath that could ultimately be life threatening. Within the last decade cardio-pulmonary MRI has been introduced into the clinic and its acceptance as a non-invasive, radiation-free tool to diagnose and monitor treatment of patients with CTEPH is rapidly increasing. It is the standard of reference for biventricular functional evaluation that can provide a comprehensive assessment of the cardio-pulmonary unit. In this article, we provide an overview of diagnosis and management of CTEPH patients by MRI-derived assessment of the cardiopulmonary unit.

by cardio-pulmonary MRI are increased and correlate to increased afterload [10]. In addition, VMI has a high diagnostic accuracy for the detection of PH demonstrated by Swift et al. in the ASPIRE study [11]. Impaired RV diastolic function results in increased diastolic RV pressures and tricuspid regurgitation, inducing elevated right atrial pressures and dilatation Increased right atrial pressure is related to PH patient outcome [8]. The interventricular septum forms a functional unit between both ventricles. Under normal circumstances the septum has a rightward convexity that maintains during the cardiac cycle. In PH patients increased RV pressure shifts the septum toward the left, affecting LV filling that is generally reflected by low LV end-diastolic volumes in PH patients [12]. Eccentricity index and interventricular septal angle are parameters to quantify septal deformation [13, 14]. This septal bowing demonstrates strong correlation with the degree of pulmonary hypertension and is associated with worse prognosis in PH patients [15, 16].

Pulmonary vessels and perfusion

Two different approaches are available for MR angiography (MRA) acquisition: A high spatial resolution contrast enhanced GRE MRA (CMRA) acquiring a single 3D data set, or a time resolved 3D MRA (DCE-MRI) using e.g. TWIST sequences [17]. Using CMRA, a classic pattern of peripheral vascular pruning with central pulmonary artery dilatation is observed in PH patients. This central pulmonary artery dilatation can be used as an imaging marker for PH detection [18]. Additionally, in CTEPH patients, typical findings observed on CMRA are: intraluminal webs and bands, vessel cut-offs and organized pulmonary artery wall-adherent thrombus that can be assessed up to the segmental vessels. In the setting of acute pulmonary embolism, CMRA demonstrated only a sensitivity of 79% (50 of 63) for detecting pulmonary embolism in a main or lobar pulmonary artery, shown in the PIOPED III study [19]. In the setting of chronic thromboembolism DCE-MRA allows identification and localization of regional hypoperfused lung parenchyma and thus differentiation between CTEPH and other forms of PH [20, 21]. It is usually performed after contrast bolus injection with use of parallel imaging techniques that allows a temporal resolution of 1 second covering the whole lung. Using this method Rajaram et al. showed in a single center registry study with 132 patients with a clinical suspicion for CTEPH from July 2013 that DCE-MRI has at least a similar sensitivity (97%), specificity (92%)

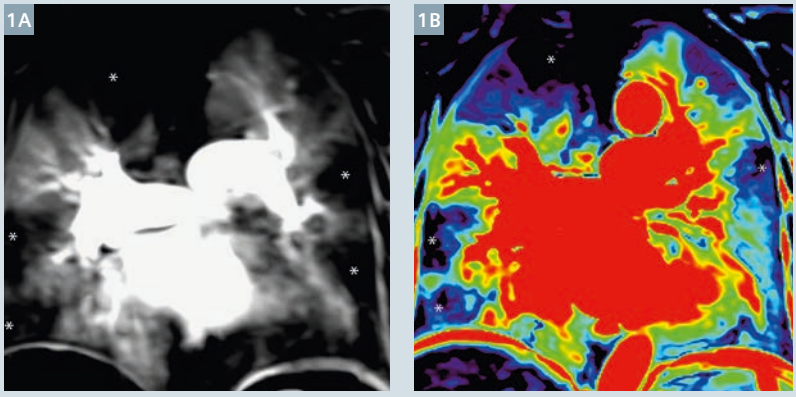

1 Corresponding lung maps of a patient with chronic thromboembolic pulmonary hypertension (CTEPH) by 4D dynamic contrast enhanced (DCE) MRI at phase of maximum pulmonary parenchymal contrast **(1A)** and quantified by model independent deconvolution (pulmonary parenchymal blood flow (PBF)) **(1B)**. CTEPH characteristic wedge shaped areas of hypoperfusion (*) can be seen bipulmonal both in the DCE- and the PBF-maps.

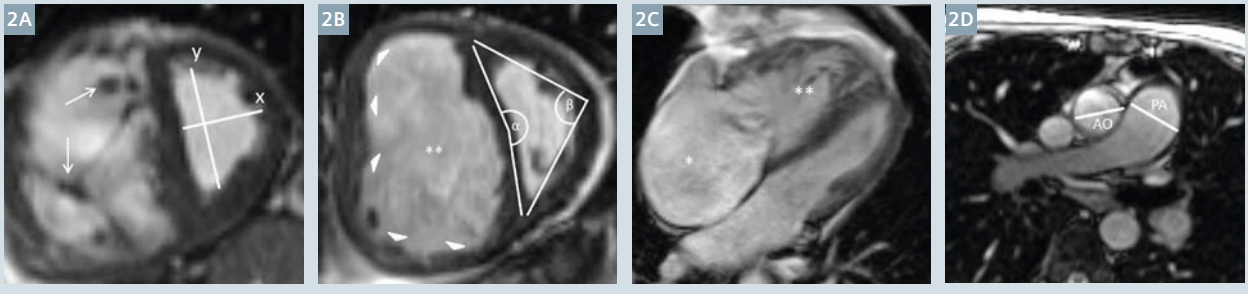

2 Cine true fast imaging with steady state precession (TrueFISP) sequences in short axis view **(2A, B)** and four-chamber-view **(2C)** as well as TrueFISP sequence of ascending aorta (AO) and main pulmonary artery (PA) of a patient with chronic thromboembolic pulmonary hypertension (CTEPH). Pulmonary hypertension (PH) causes right heart strain and dilatation of pulmonary vessels **(2D)**. MRI signs for PH are hypertrabeculation (arrows), right ventricular hypertrophy (arrowheads), dilated right ventricle (**) and dilated right atrium (*). Septal defomation due to elevated right sided volume and pressure can be quantified by the eccentricity index (y/x>1.5 = pathological) or by interventricular septal angle measurements (2B).

and accuracy (94%) compared to scintigraphy (96% / 90% / 94%) to diagnose CTEPH with conventional angiography as the reference standard [20]. An in-place diagnostic multicenter study to proof the equality of cardio-pulmonary MRI to diagnose CTEPH compared to VQ-SPECT is currently on its way (www.change-mri.de).

In addition, DCE-MRI is capable of absolute quantification of regional parenchymal blood flow. Using pixel-by-pixel deconvolution analysis of the first pass bolus Pulmonary parenchymal Blood Flow (PBF)-, Pulmonary Blood Volume-, and Mean Transit Time (MTT)-maps can be calculated from the dynamic MRI data [22]. Pulmonary PBF correlates with mPAP and pulmonary vascular resistance as well as MTT in patients with CTEPH and PH [23, 24]. Additionally, DCE-MRI can assess the gravity dependent distribution, usually seen in healthy persons [25], which is reduced in CTEPH patients and normalizes after PEA as a result of improved hemodynamics [23].

One challenge in the evaluation of CTEPH is the differentiation between lung parenchymal changes and CTEPH related hypoperfusion. Multiple etiologies, such as atelectasis or emphysema, are able to potentially mimic CTEPH like hypoperfusion [26]. However, there are clinically established sequences for evaluation of parenchymal and thoracic changes like T2 half Fourier acquisition single shot turbo spin echo (HASTE) and true fast imaging with steady state precession (TrueFISP) sequences, which may increase specificity when evaluated together with the DCE-MRI for CTEPH diagnosis [17, 20]. Recently, 3-dimensional ultrashort echo-time (UTE) sequences with high spatial resolution have been established, which improve lung tissue evaluation with close to lung CT quality [27].

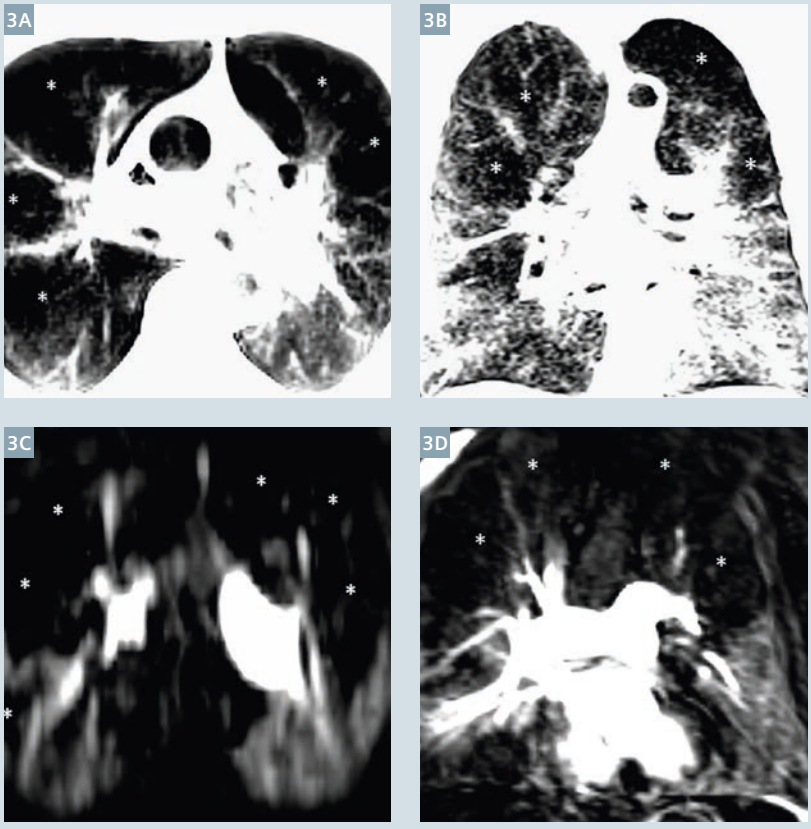

3 Anatomical images **(3A, B)** and dynamic contrast enhanced perfusion images **(3C, D)** in axial (3A, C) and coronal plane (3B, D) of a patient with chronic obstructive pulmonary disease negative for chronic thromboembolic pulmonary hypertension (CTEPH). Anatomical images (3A, B: T2 half Fourier acquisition single shot turbo spin echo) support discrimination between etiologies of hypoperfusion. In this patient areas of hypoperfusion (* in 3C, D) match with areas of emphysema (* in 3A, B) and in addition are not wedge shaped.

Encouraging expectations

One very promising development in MR evaluation of the lung is non-contrast-enhanced, proton-based lung ventilation and perfusion MRI. This approach, known as Fourier decomposition (FD) MRI, utilizes routine TrueFISP or fast low-angle shot gradient-echo (FLASH) sequences for acquisition of lung images with subsequent compensation for respiratory motion by using non rigid image registration. Spectral analysis of the dynamic image series allows identification of peaks at the respiratory and cardiac frequencies. The amplitude of these peaks is related to regional proton density changes caused by deformation of lung parenchyma and pulmonary blood flow. Further image post-processing produces ventilation- and perfusion-weighted maps for regional assessment of lung ventilation and perfusion from a single acquisition series [28].

FD-MRI derived lung perfusion and ventilation correlated well to V/Q-SPECT findings in a porcine model [29]. Furthermore FD-MRI showed promising results in humans to detect the presence or absence of chronic pulmonary embolism on a per patient basis [21]. Thus the FD-MRI-method could be a possible future alternative to V/Q-SPECT for CTEPH diagnosis in free-breathing without exposure to ionizing radiation.

4 Time-resolved 3D MRA (DCE-MRI) **(4A)** and high spatial resolution contrast enhanced GRE MRA (CMRA) **(4B)**. CMRA provides detection of intraluminal webs and bands, vessel cut-offs and organized central thrombus (*) causing hypoperfusion of associated pulmonary parenchyma (arrow).

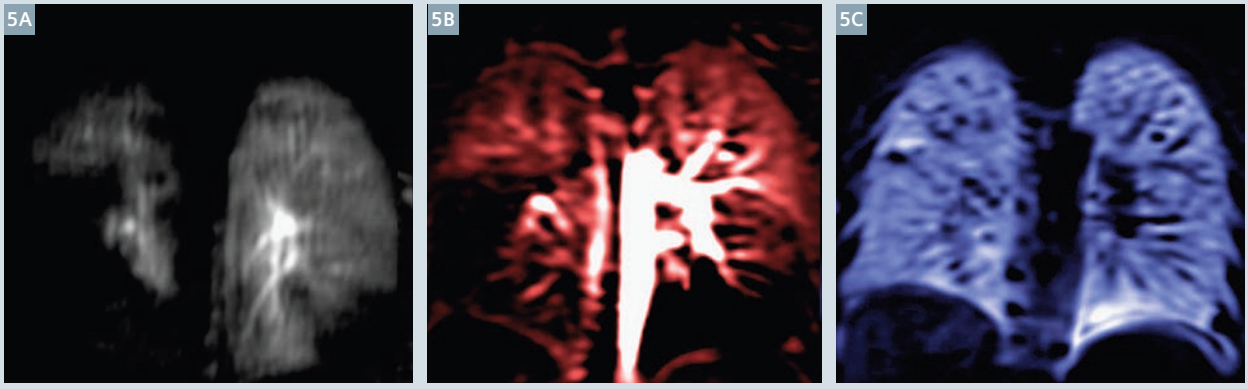

5 Corresponding Time-resolved 3D MRA (DCE-MRI) **(5A)**, perfusion-weighted (pw) Fourier Decomposition (FD) map **(5B)** and ventilation-weighted (vw) Fourier Decomposition (FD) map **(5C)** of a patient with chronic thromboembolic pulmonary hypertension (CTEPH). Hypoperfusion is proven in both lower lobes on the DCE-MRI and in the pw-FD-map. Ventilation/perfusion mismatch predominantly in the lower lobes is typical for CTEPH patients.

Conclusion

A comprehensive one-stop-shop cardio-pulmonary MRI exam has a promising future for detection and monitoring of CTEPH patients. Ventilation and perfusion weighted FD imaging of the lung is an especially promising technique of an MRI V/Q scan without contrast agent or radiation.

[1] WIP, the product is currently under development and is not for sale in the US and in other countries. Its future availability cannot be ensured.

References

1 Hoeper, M.M., et al., Chronic thromboembolic pulmonary hypertension. Lancet Respir Med, 2014. 2(7): p. 573-82.
2 Kim, N.H., et al., Chronic thromboembolic pulmonary hypertension. J Am Coll Cardiol, 2013. 62(25 Suppl): p. D92-9.
3 Lewczuk, J., et al., Prognostic factors in medically treated patients with chronic pulmonary embolism. Chest, 2001. 119(3): p. 818-23.
4 Galie, N., et al., 2015 ESC/ERS Guidelines for the diagnosis and treatment of pulmonary hypertension: The Joint Task Force for the Diagnosis and Treatment of Pulmonary Hypertension of the European Society of Cardiology (ESC) and the European Respiratory Society (ERS): Endorsed by: Association for European Paediatric and Congenital Cardiology (AEPC), International Society for Heart and Lung Transplantation (ISHLT). Eur Heart J, 2016. 37(1): p. 67-119.
5 Peacock, A.J. and A. Vonk Noordegraaf, Cardiac magnetic resonance imaging in pulmonary arterial hypertension. Eur Respir Rev, 2013. 22(130): p. 526-34.
6 Jenkins, D., et al., State-of-the-art chronic thromboembolic pulmonary hypertension diagnosis and management. Eur Respir Rev, 2012. 21(123): p. 32-9.
7 Berman, M., et al., Right ventricular reverse remodeling after pulmonary endarterectomy: magnetic resonance imaging and clinical and right heart catheterization assessment. Pulm Circ, 2014. 4(1): p. 36-44.

8 D'Alonzo, G.E., et al., Survival in patients with primary pulmonary hypertension. Results from a national prospective registry. Ann Intern Med, 1991. 115(5): p. 343-9.
9 Mertens, L.L. and M.K. Friedberg, Imaging the right ventricle--current state of the art. Nat Rev Cardiol, 2010. 7(10): p. 551-63.
10 Saba, T.S., et al., Ventricular mass index using magnetic resonance imaging accurately estimates pulmonary artery pressure. Eur Respir J, 2002. 20(6): p. 1519-24.
11 Swift, A.J., et al., Diagnostic accuracy of cardiovascular magnetic resonance imaging of right ventricular morphology and function in the assessment of suspected pulmonary hypertension results from the ASPIRE registry. J Cardiovasc Magn Reson, 2012. 14: p. 40.
12 Shehata, M.L., et al., Regional and global biventricular function in pulmonary arterial hypertension: a cardiac MR imaging study. Radiology, 2013. 266(1): p. 114-22.
13 Badagliacca, R., et al., Right ventricular dyssynchrony in idiopathic pulmonary arterial hypertension: determinants and impact on pump function. J Heart Lung Transplant, 2015. 34(3): p. 381-9.
14 Swift, A.J., et al., Noninvasive estimation of PA pressure, flow, and resistance with CMR imaging: derivation and prospective validation study from the ASPIRE registry. JACC Cardiovasc Imaging, 2013. 6(10): p. 1036-47.
15 Roeleveld, R.J., et al., Interventricular septal configuration at mr imaging and pulmonary arterial pressure in pulmonary hypertension. Radiology, 2005. 234(3): p. 710-7.
16 Dellegrottaglie, S., et al., Pulmonary hypertension: accuracy of detection with left ventricular septal-to-free wall curvature ratio measured at cardiac MR. Radiology, 2007. 243(1): p. 63-9.
17 Biederer, J., et al., MRI of the lung (2/3). Why ... when ... how? Insights Imaging, 2012. 3(4): p. 355-71.
18 Truong, Q.A., et al., Reference values for normal pulmonary artery dimensions by noncontrast cardiac computed tomography: the Framingham Heart Study. Circ Cardiovasc Imaging, 2012. 5(1): p. 147-54.
19 Stein, P.D., et al., Gadolinium-enhanced magnetic resonance angiography for pulmonary embolism: a multicenter prospective study (PIOPED III). Ann Intern Med, 2010. 152(7): p. 434-43, W142-3.
20 Rajaram, S., et al., 3D contrast-enhanced lung perfusion MRI is an effective screening tool for chronic thromboembolic pulmonary hypertension: results from the ASPIRE Registry. Thorax, 2013. 68(7): p. 677-8.
21 Schonfeld, C., et al., Performance of perfusion-weighted Fourier decomposition MRI for detection of chronic pulmonary emboli. J Magn Reson Imaging, 2015. 42(1): p. 72-9.
22 Ohno, Y., et al., Quantitative assessment of regional pulmonary perfusion in the entire lung using three-dimensional ultrafast dynamic contrast-enhanced magnetic resonance imaging: Preliminary experience in 40 subjects. J Magn Reson Imaging, 2004. 20(3): p. 353-65.
23 Schoenfeld, C., et al., MR Imaging-derived Regional Pulmonary Parenchymal Perfusion and Cardiac Function for Monitoring Patients with Chronic Thromboembolic Pulmonary Hypertension before and after Pulmonary Endarterectomy. Radiology, 2016. 279(3): p. 925-34.
24 Ohno, Y., et al., Primary pulmonary hypertension: 3D dynamic perfusion MRI for quantitative analysis of regional pulmonary perfusion. AJR Am J Roentgenol, 2007. 188(1): p. 48-56.
25 Anthonisen, N.R. and J. Milic-Emili, Distribution of pulmonary perfusion in erect man. J Appl Physiol, 1966. 21(3): p. 760-6.
26 Sandek, K., et al., Relationship between lung function, ventilation-perfusion inequality and extent of emphysema as assessed by high-resolution computed tomography. Respir Med, 2002. 96(11): p. 934-43.
27 Ohno, Y., et al., Pulmonary high-resolution ultrashort TE MR imaging: Comparison with thin-section standard- and low-dose computed tomography for the assessment of pulmonary parenchyma diseases. J Magn Reson Imaging, 2016. 43(2): p. 512-32.
28 Bauman, G., et al., Non-contrast-enhanced perfusion and ventilation assessment of the human lung by means of fourier decomposition in proton MRI. Magn Reson Med, 2009. 62(3): p. 656-64.
29 Bauman, G., et al., Pulmonary functional imaging: qualitative comparison of Fourier decomposition MR imaging with SPECT/CT in porcine lung. Radiology, 2011. 260(2): p. 551-9.

Contact

Jens Vogel-Claussen, M.D.
Institute for Diagnostic and Interventional Radiology
Hannover Medical School
OE 8220
Carl-Neuberg-Str. 1
30625 Hannover
Germany
Phone: +49 (511) 532 3421
Fax: +49 (511) 532 9421
vogel-claussen.jens@mh-hannover.de

Jens Vogel-Claussen

Christian Schoenfeld

Andreas Voskrebenzev

For further information, protocols, articles, and keynotes on MRI of the Thorax please visit **www.siemens.com/lung-mri**

Free-breathing Late Enhancement Imaging: Phase Sensitive Inversion Recovery (PSIR) with Respiratory Motion Corrected (MOCO) Averaging

Peter Kellman; Hui Xue; Michael S. Hansen

National Heart, Lung, and Blood Institute, National Institutes of Health, DHHS, Bethesda, MD, USA

Introduction

Late gadolinium enhancement (LGE) has become a gold standard in myocardial viability assessment [1, 2] providing excellent depiction of myocardial infarction (MI) and macroscopic scarring. The use of late enhancement in the diagnosis of ischemic heart disease and in guiding revascularization therapy has gained wide acceptance. More recently, late enhancement has been playing a broader role in characterizing fibrosis in non-ischemic cardiomyopathies [3,4], and in measurement of scar resulting from treatment of cardiac arrhythmias using radiofrequency ablation [5]. As the use of late enhancement imaging has matured and as the span of applications has widened, clinicians are examining late enhancement images for more subtle indication of fibrosis and the demands on image quality have grown [6].

Breath-held (BH), segmented FLASH has been the gold standard for LGE for many years [7] and is widely used with great success when patients are cooperative and can hold their breath. In instances where poor breath-holding results in ghost artifacts, single shot SSFP imaging has been used as an alternative. However, while single shot imaging mitigates ghosting artifacts, it generally has compromised spatial resolution and image quality compared to BH FLASH. Therefore, the single shot approaches are less sensitive to detection of subtle LGE and to detection of small lesions [8]. The development of PSIR LGE with respiratory motion corrected (MOCO) averaging[1] [6, 9, 10] has led to a free-breathing (FB) approach which achieves the robustness of single shot approaches and the resolution and image quality of BH segmented FLASH. In addition to elimination of ghosting artifacts due to poor breath-holds (Fig. 1), the PSIR MOCO LGE is inherently less sensitive to arrhythmias.

In addition to being easier on the patients, free-breathing PSIR MOCO LGE eliminates pauses between BH slices and is therefore faster to acquire than a BH stack. Free-breathing, MOCO LGE greatly simplifies the clinical workflow, particularly since LGE is typically at the end of the study where patient compliance is frequently a problem. PSIR MOCO LGE has been demonstrated to improve the image quality in both pediatric[2] [11] and adult populations [12]. It has been shown to make a significant improvement in the most vulnerable population of sick patients [12].

[1] The product is still under development and not commercially available yet. Its future availability cannot be ensured.

[2] MR scanning has not been established as safe for imaging fetuses and infants less than two years of age. The responsible physician must evaluate the benefits of the MR examination compared to those of other imaging procedures.

1

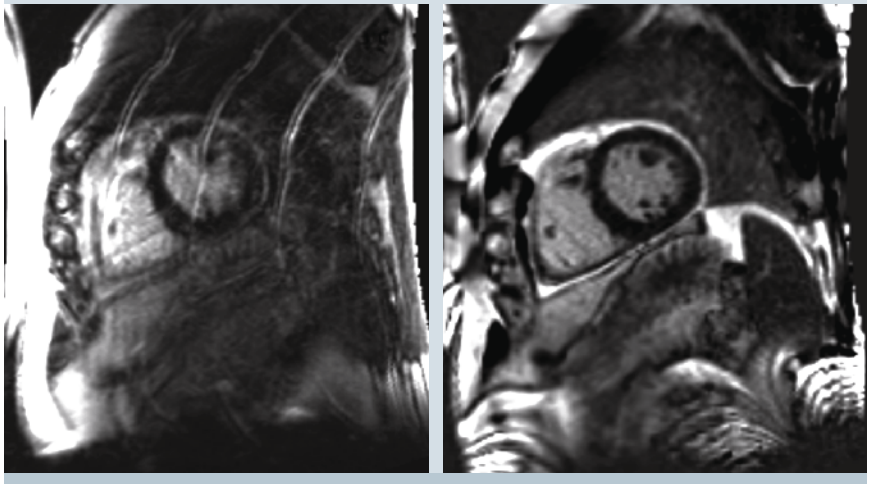

1 Free-breathing, MOCO PSIR LGE images eliminate ghosting artifacts and achieve high SNR by means of respiratory motion corrected averaging [6].

In a study of 390 consecutive patients [12], it was concluded that: "Myocardial infarction detection and quantification are similar between MOCO-LGE and BH-LGE when BH-LGE can be acquired well, but BH-LGE quality deteriorates with patient vulnerability. Acquisition time, image quality, diagnostic confidence, and the number of successfully scanned patients are superior with MOCO-LGE, which extends LGE-based risk stratification to include patients with vulnerability confirmed by outcomes." A number of sites have adopted PSIR MOCO LGE as their sole means of LGE imaging and combined they have been performing over 10,000 studies annually for the past several years.

Respiratory MOCO averaging can offer SNR improvements well beyond what is possible using BH FLASH by further increasing the number of averages. Therefore, with PSIR MOCO LGE, higher spatial resolution or thinner slices are achievable in clinical practice. Furthermore, PSIR MOCO LGE has been integrated with dark blood PSIR to provide improved contrast of subendocardial MI with the adjacent bright blood pool.

Key points/implications:

- Free-breathing imaging is easier for the patient
- Improves clinical workflow
- Free-breathing imaging reduces artifacts
- Improves diagnostic quality
- Is highly effective for the most vulnerable population

Free-breathing approach

Motion correction may be used to correct respiratory motion [9, 10] in the case of free-breathing acquisition, or diaphragmatic drift in the case of breath-holding. The SNR for individual single shot PSIR-SSFP images is slightly worse than segmented PSIR-FLASH due to the increase in bandwidth, despite the increase in flip angle. However, the SNR of single shot PSIR-SSFP may be significantly improved by averaging multiple repeated measurements (Fig. 2). Typically, using 8 PSIR images acquired in 16 heartbeats provides an SNR comparable or better than the FLASH protocol for approximately the same duration and may be extended to a larger number of averages since the acquisition is not breath-held. Parallel imaging at higher acceleration factors may be used to reduce the imaging duration in diastole to achieve higher spatial resolution or reduce motion blur at higher heart rates. Use of non-rigid motion correction provides correction over the full FOV in a fully automated fashion. Selective averaging may be used to discard images that do not meet similarity criteria due to through plane motion [10]. This retrospective image based navigator strategy is robust and simple to use, thereby eliminating the complexity and unreliability of prospective navigators.

2

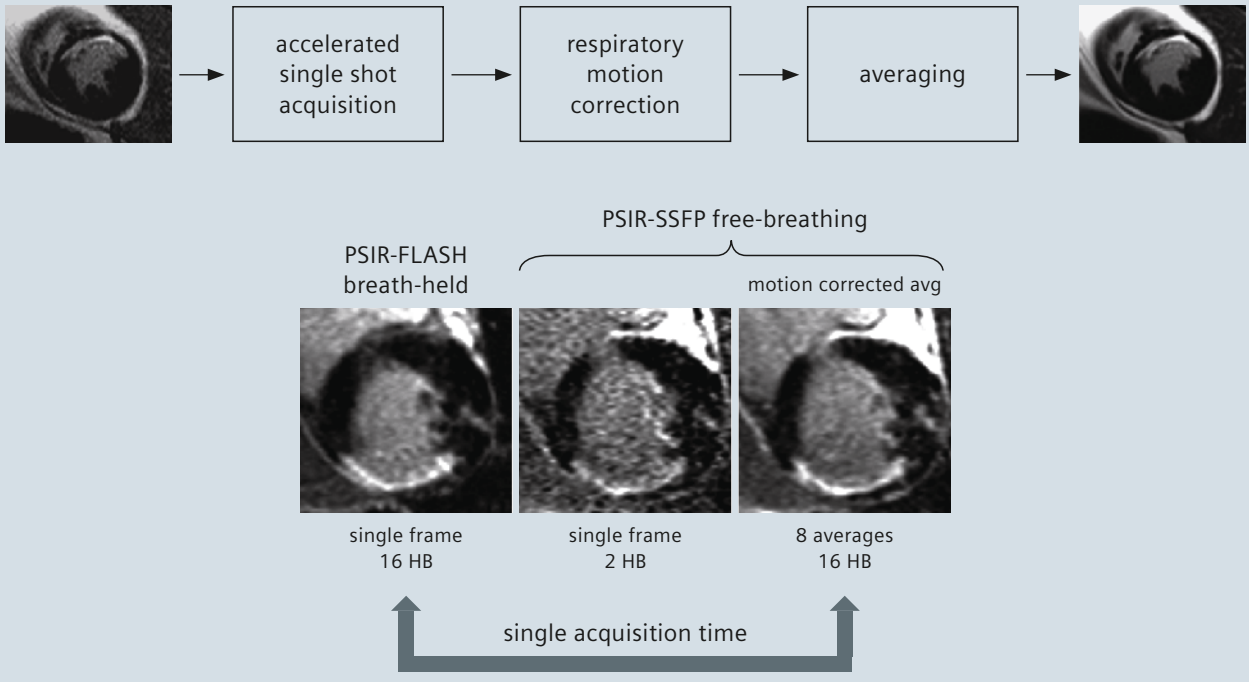

2 Respiratory motion corrected averaging strategy using accelerated single shot imaging to mitigate artifacts and motion corrected averaging to increase SNR [6].

Imaging protocols

PSIR MOCO LGE has been integrated with a number of imaging protocols to include SSFP, FLASH, and multi-echo GRE for water fat separated LGE, and dark blood (DB) PSIR LGE (Fig. 3). Typical parameters for these protocols are listed in Table 1. Additionally, early gadolinium enhancement (EGE) protocols use reduced averaging for more rapid multi-slice coverage, and higher spatial resolution protocols (e.g. 256 x 224 or 320 x 244) use higher parallel imaging acceleration (PAT) factors and increased averaging.

3

3 Simplified diagram of sequence for PSIR LGE with interleaved acquisition of IR and PD images on alternate heartbeats (top) and dark blood (DB) PSIR LGE using IR-T2 RF preparation. Readout may be single-shot SSFP, FLASH, or multi-echo GRE for water fat separated PSIR LGE imaging.

	Bright Blood (BB)		Dark Blood (DB)	Fat Water (FW)
Preparation	Inversion Preparation		Inversion Preparation & T2 preparation	Inversion Preparation
Readout (single shot)	SSFP FA_{IR} = 50° FA_{PD} = 8°	FLASH FA_{IR} = 10° FA_{PD} = 5°	SSFP FA_{IR} = 50° FA_{PD} = 8°	3-echo GRE (FA_{IR} = 25°, FA_{PD} = 5°) monopolar readout
Typical FOV / resolution	360 x 270 mm² 1.4 x 1.9 x 8 mm³			360 x 270 mm² 1.4 x 2.2 x 8 mm³
Matrix size	256 x 144 (parallel imaging factor 2)			256 x 123 (parallel imaging factor 3)
Number of acquired measurements	8		16	9
T2 prep TE	n/a		10 - 40 ms	n/a
TE / TR	1.2/2.8 ms	1.25/3.1 ms	1.2/2.8 ms	(1.5,3.8, 6.1)/7.2 ms
ECG triggering	Inversions every 2 RR (HR < 90 bpm) Inversions every 3 RR (HR > 90 bpm)			

Table 1: Typical imaging parameters for various PSIR LGE MOCO protocols.

PSIR motion corrected averaging

Non-rigid image registration is used to correct respiratory motion between repeated measurements acquired during normal free-breathing PSIR LGE imaging [6, 9, 10]. The motion correction (MOCO) is done independently for the IR and proton density (PD) images and the MOCO averaged complex images are co-registered prior to the PSIR demodulation step (Fig. 4, current implementation). The non-rigid image registration corrects in-plane motion and through-plane motion is dealt with by discarding 50% of the acquired measurements which are most dissimilar. The selection of the reference frame used for image registration as well as which frames to be discarded is based on the similarity of frames as estimated from a global mean square difference metric [10]. In this way, the retrospective image-based strategy averages the most frequent respiratory phase which is typically at end-expiration. The co-registered MOCO PD image is used for both PSIR demodulation, which preserves the sign of the IR signal by removing the background phase, as well as for correcting the surface coil intensity roll-off (Fig. 5). To improve the reliability of IR/PD co-registration which is critical for both PSIR demodulation and surface coil intensity correction, a volume preserving non-rigid co-registration is used to deal with the challenge of different contrasts between IR and PD images.

In dark blood imaging protocols SNR is typically lower due to T2 weighting and more averages are needed compared to the bright blood PSIR MOCO protocol. Likewise, for higher spatial resolution with higher PAT factors and smaller voxels, the loss in SNR in raw images may be compensated for by increased averaging.

Implementation

The PSIR MOCO implementation has evolved over the last several years and has achieved high quality and reliability used at a large number of sites in their clinical workflow. Initial off-line implementations [9, 10] were quickly

4

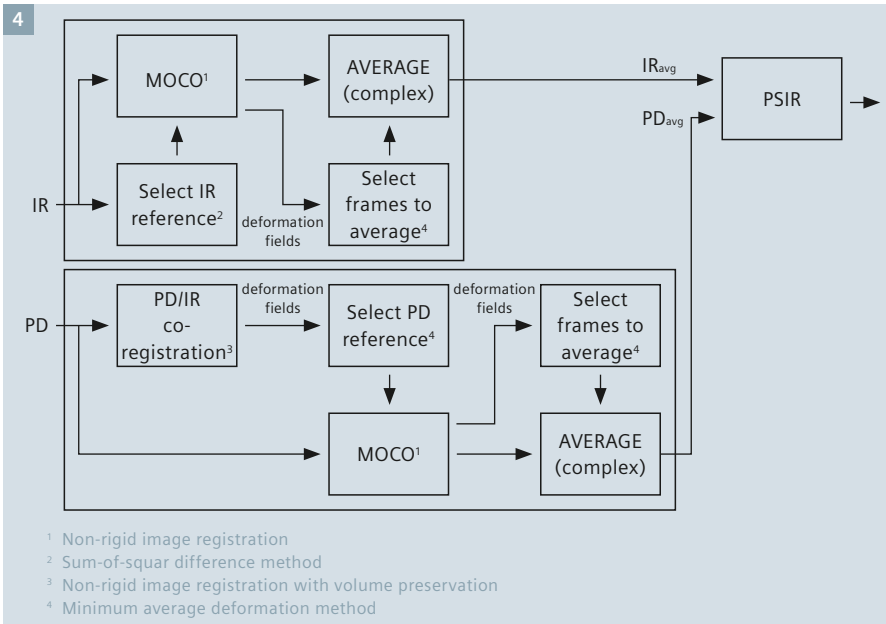

[1] Non-rigid image registration
[2] Sum-of-squar difference method
[3] Non-rigid image registration with volume preservation
[4] Minimum average deformation method

4 Current strategy for free-breathing, respiratory motion corrected averaging and PSIR demodulation.

5

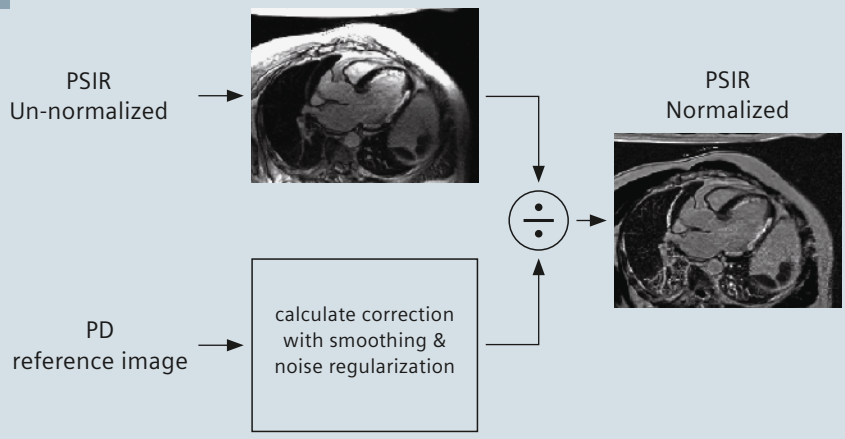

5 Correction of surface coil intensity roll-off used the proton density (PD) magnitude image after MOCO averaging.

moved to the scanner as works-in-progress (WIP) packages as part of co-development between NIH and Siemens under a cooperative research and development agreement (CRADA). Initial WIPs began in 2007 with WIP 373 (*syngo* MR B13A) for MAGNETOM Avanto and Espree, and were re-released with various improvements over the ensuing years.

Initial implementations applied respiratory MOCO and averaging directly to the individual single shot SSFP images, and significant through plane motion was dealt with by discarding frames as described above. Subsequent development applied MOCO averaging independently to the IR and PD, and performed the PSIR between IR and PD after motion corrected averaging. This mitigated artifacts arising due to respiratory motion between IR and PD. Early versions would output a number of intermediate series to include the raw images, MOCO images, as well the averages. As the development matured, the final versions output only the MOCO average.

A recent development has been the implementation of the PSIR MOCO reconstruction using the Gadgetron image reconstruction framework [13]. The Gadgetron framework provides increased speed and 'on-the-fly' reconstruction for multi-slice acquisitions. On-the-fly reconstruction immediately starts the computation when the image acquisition of the first slice is completed. For a scan covering multiple slices, this scheme allows image display during the acquisition of a stack of slices. Gadgetron software may be installed on the *syngo* MR E11 platforms (1.5T MAGNETOM Aera, 3T MAGNETOM Skyra and Prisma) to run on the scanner's image reconstruction computer (MARS) or may be run on an external computer connected over the network (currently a C2P with NIH research collaboration partners). Using on-the-fly reconstruction, the time to complete the full stack of slices (9 slices/8 measurements) is approximately 6 or 8 seconds after completion of the acquisition, when performed on a 24 core external Linux PC or 16 core MARS, respectively. For on-the-fly reconstruction, all measurements for a given slice are acquired consecutively (inner loop).

PSIR MOCO LGE

Free-breathing PSIR MOCO LGE protocols are now widely used at a number of clinical research sites. At many of these sites, the free-breathing protocol is used exclusively since it saves time and provides excellent quality. Examples of late enhancement for a wide range of patterns (Fig. 6) in both ischemic and non-ischemic heart disease illustrate that PSIR MOCO provides excellent image quality and high spatial resolution to detect small focal enhancement as well as more subtle enhancement.

The typical acquisition of a SAX stack of 9-slices (Fig. 7) is acquired in 9 slices × 8 measurements × 2 RR = 144 heart beats = 2:24 min at 60 bpm. The reconstruction is performed 'on-the-fly' and is completed within 10 seconds of the end of scan. Long axis views may be prescribed individually or as multi-slice. When prescribing long axis views off of free-breathing SAX images, the long axis may be at a different respiratory position and possibly not optimal. Some sites find it simpler to prescribe a parallel stack of 3 long axis slices for each view (Fig. 8) to ensure acquisition of the best position.

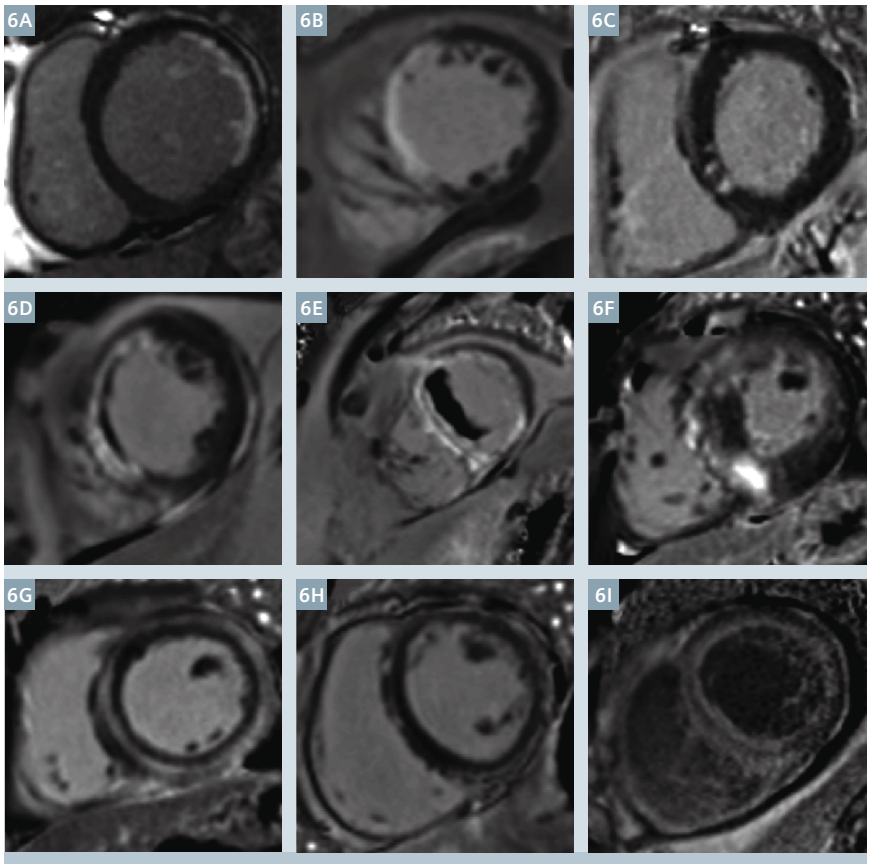

6 Examples of free-breathing PSIR MOCO LGE images illustrating the a variety of late enhancement patterns: (**6A**) sub-endocardial chronic MI, (**6B**) transmural chronic MI, (**6C**) small focal scar, (**6D**) acute MI with dark core due to microvascular obstruction (MVO), (**6E**) MI with thrombus, (**6F**) heterogeneous focal enhancement in a patient with HCM, (**6G**) mid-wall enhancement in patient with myocarditis, (**6H**) sub-epicardial enhancement in patient with myocarditis, and (**6I**) subendocardial fibrosis in patient with amyloidosis.

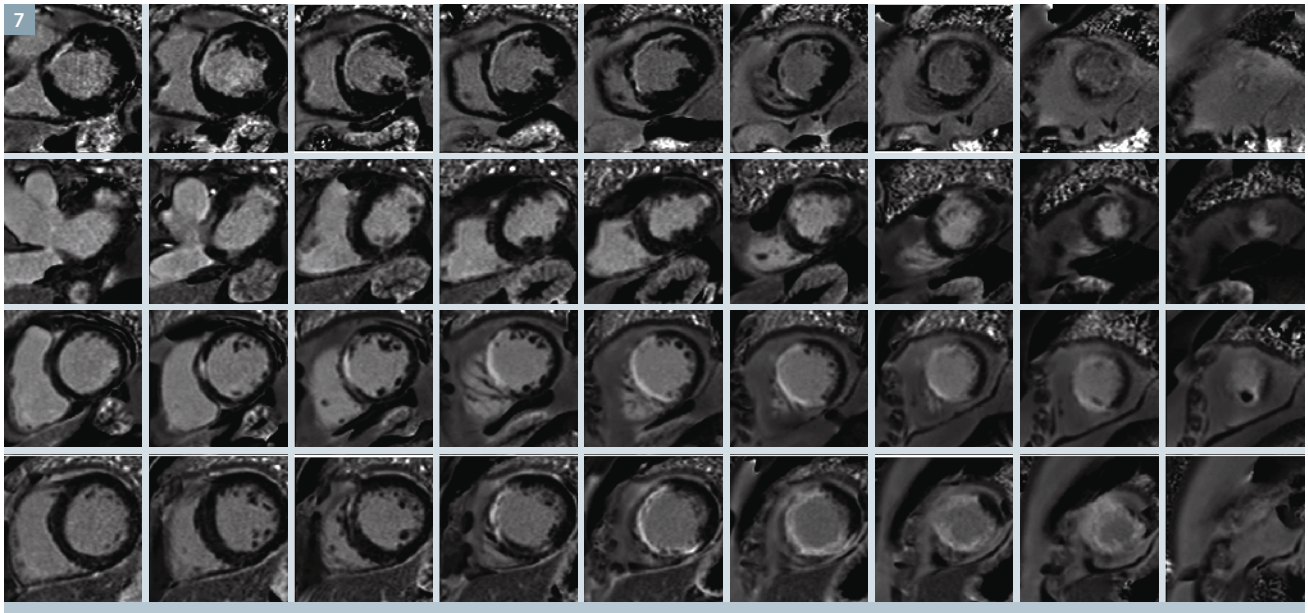

7 Examples of free-breathing acquisition of stacks of 9 short axis slices using PSIR MOCO LGE acquired and reconstructed on-the-fly in approximately 2.5 min, depending on heart rate.

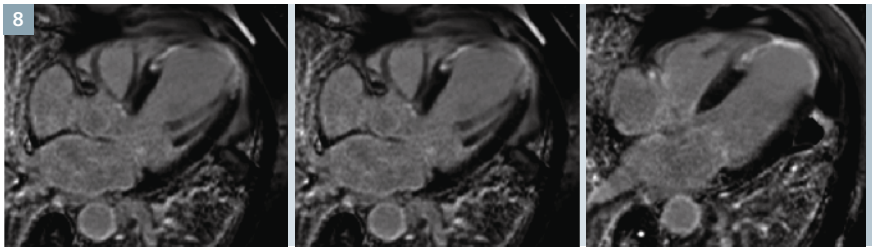

8 Example of free-breathing acquisition of a stack of 3 parallel long axis slices to ensure that the 4-chamber view is correctly obtained when prescribed off images that are potentially at a different respiratory position.

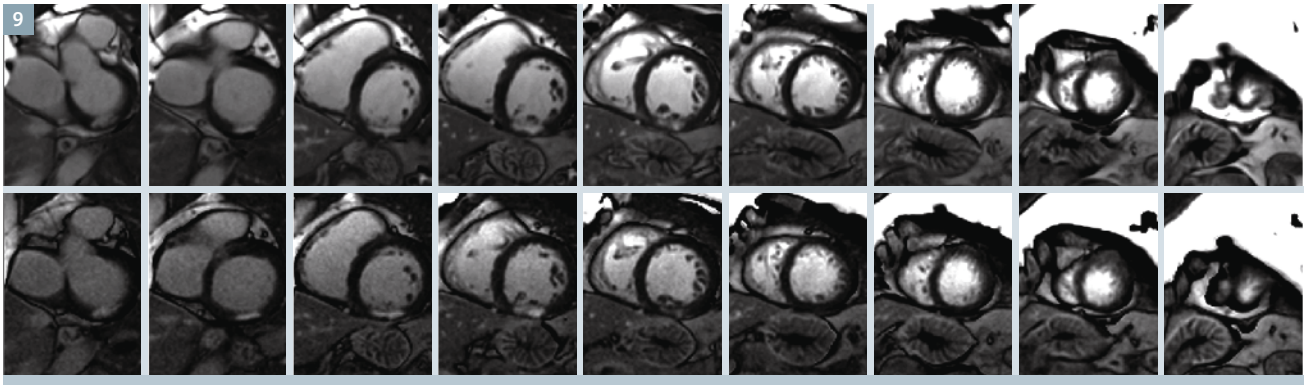

9 Comparison of 9 slice short axis stack acquired at 3T using the free-breathing PSIR MOCO LGE with SSFP (top) and FLASH (bottom) readouts, respectively.

The PSIR MOCO protocol most frequently used is the SSFP based protocol. A FLASH based protocol has also been tested, and is beneficial in situations with large off-resonance variations that are difficult to shim. There is a reduction in SNR that may be compensated by increased averaging. A comparison of SSFP and FLASH protocols at 3T is shown in Fig. 9 using the same averaging (protocols in Table 1).

Early enhancement imaging

Early gadolinium enhancement (EGE) during the phase between 1-5 minutes following gadolinium administration is often more sensitive to detection of edema, thrombus, or microvascular obstruction (MVO). MVO may be less apparent for LGE when the gadolinium may reach the MI core. Furthermore, in the case of acute MI, the early enhancement may show the area at risk since the edematous tissue will experience a more rapid early enhancement than the central core. Similarly the edematous region in acute myocarditis is more conspicuous in early phase.

The free-breathing PSIR MOCO LGE protocol may be used for EGE without tiring the patient. The EGE may use the same LGE protocol, or may use a reduced number of averages, e.g. 4, in order that a full SAX stack can be acquired in just over minute, in cases where better time resolution is desired.

Dark Blood PSIR LGE

Late-enhancement imaging typically achieves excellent contrast between infarcted and normal myocardium. However, the contrast between the MI and the blood pool is frequently suboptimal. A large fraction of infarctions caused by coronary artery disease are sub-endocardial and thus adjacent to the blood pool. The contrast between the blood and MI in the inversion recovery (IR) image depends on variables such as contrast agent dosage, time from gadolinium administration, clearance rate, and imaging parameters. Blood velocity may also have a role in the contrast, even though non-slice-selective IR is used. Therefore, as a result of mechanisms that are not fully characterized or controlled, it is not infrequent that sub-endocardial MIs are difficult to detect or clearly delineate.

A dark blood (DB) LGE may be achieved by combining a T2 preparation [14–16] with IR. In these schemes, the myocardial signal is reduced relative to the blood signal thereby reducing the inversion times to null the myocardium. In this way, it is possible to null both the myocardium and the blood at the same time. The order of the T2 and IR preparations may be applied as T2-IR [16] or IR-T2 [14]. Both of these previously reported schemes used a FLASH readout. We combined an IR-T2 with a single shot SSFP readout and respiratory motion corrected averaging to achieve the acceptable SNR while maintaining the desired spatial and temporal resolution. In this manner, imaging is conducted free-breathing which has benefits for image quality, patient comfort, and clinical workflow. Furthermore, by using a PSIR reconstruction [17] the blood signal may be made darker than the myocardium (i.e. negative signal values) thereby providing contrast between the blood and both the MI and remote myocardium [15].

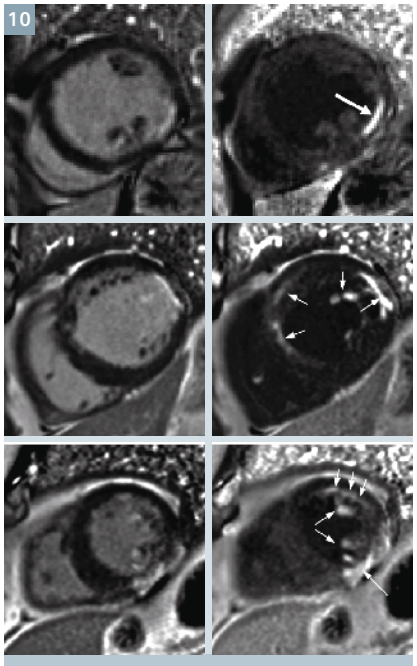

10 Examples of bright blood (left) and dark blood (DB) (right) PSIR MOCO LGE illustrating improved contrast between subendocardial MI and blood pool. The areas of scar indicated by LGE are more conspicuous on the DB PSIR images (see arrows) and in some cases might have been missed entirely in the bright blood PSIR images.

Dark blood LGE schemes provide contrast between the MI and the blood pool at the expense of SNR. However, the SNR cost of the proposed DB may be recovered by increased averaging. The DB PSIR MOCO LGE protocol in Table 1 achieves comparable contrast-to-noise ratio (CNR) between the MI and myocardium as the conventional bright blood protocol.

Free-breathing, dark blood PSIR LGE imaging has been demonstrated to improve the visualization of subendocardial MI and fibrosis in cases with low contrast with adjacent blood pool (Fig. 10). The proposed method also improves visualization of thin walled fibrous structures such as atrial walls and valves, as well as papillary muscles.

Fat water separated late enhancement

Lipomatous metaplasia is prevalent in chronic myocardial infarction (MI) [18] and other nonischemic cardiomyopathies. Using conventional late enhancement imaging, it is difficult to discriminate between fibrosis and intramyocardial fat since both have low T1 and appear bright. Furthermore, the presence of fat may create image artifacts due to the chemical shift of fat or the bright epicardial fat signal may obscure the subepicardium. Using fat-water separated late-enhancement imaging it is possible to distinguish the fibrosis from fat with improved sensitivity and to avoid erroneous tissue classification [19]. Detecting the presence of fibrofatty

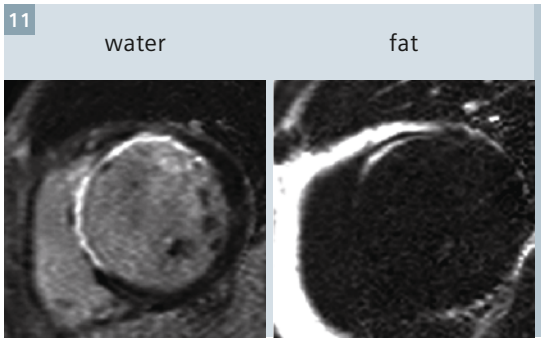

11 Patient with chronic MI in anteroseptal region with lipomatous metaplasia seen in fat-water separated PSIR MOCO LGE [19].

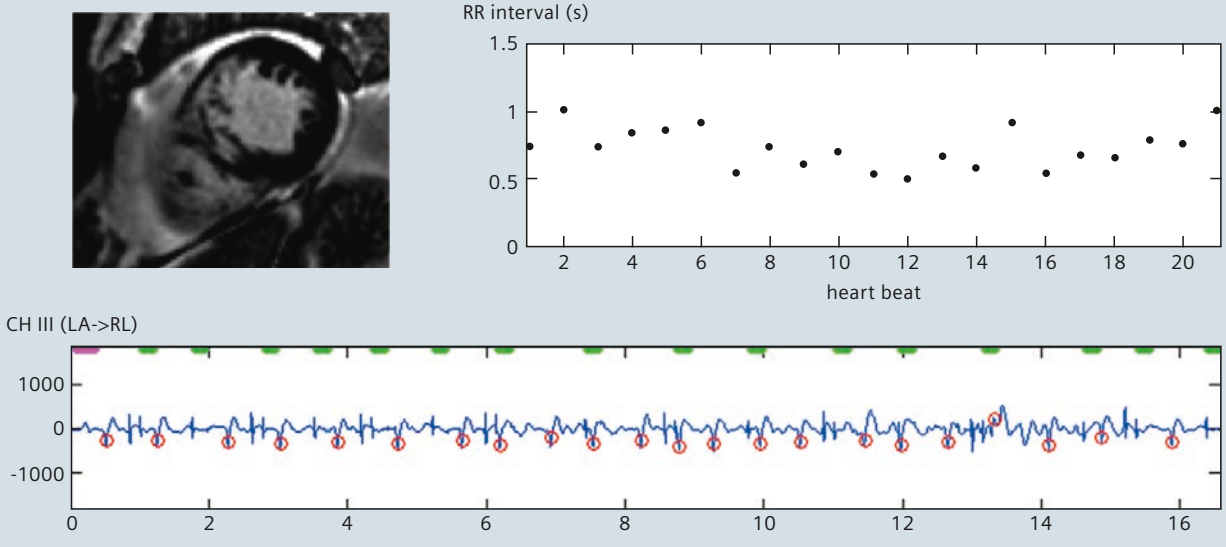

12 Free-breathing, PSIR MOCO LGE in patient with chronic MI in atrial fibrillation (shown at SCMR 2014 Annual Scientific Meeting, Real-time imaging: in case of atrial fibrillation, Kellman P).

infiltration or other intramyocardial fat may have diagnostic value. The presence of intramyocardial fat may form a substrate for arrhythmias due to the lower electrical conductivity of fat. It has been shown that fibrofatty infiltration of the myocardium is associated with sudden death, and therefore noninvasive detection could have prognostic value. Fat water separated imaging may be performed free-breathing [20] with multi-echo PSIR MOCO LGE (Table 1). An example of lipomatous metaplasia in chronic MI is shown in Fig. 11. It is also used to improve visualization of pericardial disease and in general mass characterization.

Insensitive to arrhythmias

The free-breathing PSIR MOCO LGE imaging based on single shot imaging is inherently insensitive to arrhythmias since it is free from ghosting artifacts experienced with breath-held segmented acquisitions. In patients with arrhythmias during scanning, there may be some variation in the cardiac phase of repeated measurements depending on the precise nature of the variation. It is possible to retrospectively discard heart beats outside of specified criteria, however in practice the MOCO average has been found to be relatively insensitive to a large variation in RR intervals and is even robust in subjects with atrial fibrillation (Fig. 12). Furthermore, some patients experience arrhythmias that are brought on or worsened by breath-holding, and are in sinus rhythm during normal free-breathing.

Discussion

The free-breathing approach to LGE using PSIR MOCO performs reliably with excellent image quality. The image is often better than breath-held LGE in the most vulnerable population that cannot breath-hold [12] and for pediatric subjects[3] [11]. The paradigm shift to free-breathing CMR has benefits to the clinical workflow in terms of speed, ease of use, and patient comfort. A number of other free-breathing protocols that incorporate retrospective MOCO have been recently developed and allow for a complete free-breathing CMR study to include real-time cine function [21, 22], T2-SSFP [23], T2* mapping [24], and myocardial perfusion mapping [25]. These afford a significant reduction in overall exam time when combined. The PSIR MOCO LGE has been adopted at a number of sites as the new standard and is widely used.

[3] MR scanning has not been established as safe for imaging fetuses and infants less than two years of age. The responsible physician must evaluate the benefits of the MR examination compared to those of other imaging procedures.

Acknowledgements

We would like to acknowledge our colleagues at Siemens, in particular Xiaoming Bi and Randall Kroeker, for their role in development of the PSIR MOCO LGE WIP, and to our numerous clinical collaborators for their insights and clinical examples: Andrew E. Arai, W. Patricia Bandettini, Erik B. Schelbert, James C. Moon, Marianna Fontana, Martin Ugander, Patricia Feuchter, Cavan McGurk, Sofie Olsson, Jenny Rasck, Sarah Anderson, and Christine Mancini.

Supported by the National Heart, Lung and Blood Institute, National Institutes of Health by the Division of Intramural Research.

References

1 Fieno DS, Kim RJ, Chen E, Lomasney JW, Klocke FJ, Judd RM. Contrast-Enhanced Magnetic Resonance Imaging of Myocardium at Risk Distinction Between Reversible and. 2000;36:1985–91.
2 Kim RJ, Fieno DS, Parrish TB, Harris K, Chen E-L, Simonetti O, et al. Relationship of MRI Delayed Contrast Enhancement to Irreversible Injury, Infarct Age, and Contractile Function. Circulation. 1999;100:1992–2002.
3 Bohl S, Wassmuth R, Abdel-Aty H, Rudolph A, Messroghli D, Dietz R, et al. Delayed enhancement cardiac magnetic resonance imaging reveals typical patterns of myocardial injury in patients with various forms of non-ischemic heart disease. Int. J. Cardiovasc. Imaging. 2008;24:597–607.
4 Hunold P, Schlosser T, Vogt FM, Eggebrecht H, Schmermund A, Bruder O, et al. Myocardial Late Enhancement in Contrast-Enhanced Cardiac MRI: Distinction Between Infarction and Non-Infarction-Related Disease. AJR. Am. J. Roentgenol. 2005;184:1420–6.
5 Vergara GR, Marrouche NF. Tailored management of atrial fibrillation using a LGE-MRI based model: from the clinic to the electrophysiology laboratory. J. Cardiovasc. Electrophysiol. 2011;22:481–7.
6 Kellman P, Arai AE. Cardiac imaging techniques for physicians: Late enhancement. J. Magn. Reson. Imaging. 2012;36:529–42.
7 Kim RJ, Shah DJ, Judd RM. How We Perform Delayed Enhancement Imaging. J. Cardiovasc. Magn. Reson. 2003;5:505–14.
8 Lee D, Wu E, Chung Y, Simonetti O, Elliot M, Holly T, et al. Comparison Between Single Shot TrueFISP and Segmented TurboFLASH for the Detection of Myocardial Infarction. J. Cardiovasc. Magn. Reson. 2003;5:79–80.
9 Kellman P, Larson AC, Hsu L-Y, Chung Y-C, Simonetti OP, McVeigh ER, et al. Motion-corrected free-breathing delayed enhancement imaging of myocardial infarction. Magn. Reson. Med. 2005;53:194–200.
10 Ledesma-Carbayo MJ, Kellman P, Hsu L-Y, Arai AE, McVeigh ER. Motion corrected free-breathing delayed-enhancement imaging of myocardial infarction using nonrigid registration. J. Magn. Reson. Imaging. 2007;26:184–90.
11 Olivieri L, Cross R, O'Brien KJ, Xue H, Kellman P, Hansen MS. Free-breathing motion-corrected late-gadolinium-enhancement imaging improves image quality in children. Pediatr. Radiol. Pediatric Radiology; 2016;46:983–90.
12 Piehler KM, Wong TC, Puntil KS, Zareba KM, Lin K, Harris DM, et al. Free-Breathing, Motion-Corrected Late Gadolinium Enhancement Is Robust and Extends Risk Stratification to Vulnerable Patients. Circ. Cardiovasc. Imaging. 2013;6:423–32.
13 Hansen MS, Sørensen TS. Gadgetron: an open source framework for medical image reconstruction. Magn. Reson. Med. 2013;69:1768–76.
14 Basha T, Roujol S, Kissinger K V, Goddu B, Manning WJ, Nezafat R. Black blood late gadolinium enhancement using combined T2 magnetization preparation and inversion recovery. J. Cardiovasc. Magn. Reson. BioMed Central Ltd; 2015;17:O14.
15 Kellman P, Xue H, Olivieri LJ, Cross RR, Grant EK, Fontana M, Ugander M, Moon JC, Hansen MS. Dark blood Late Enhancement Imaging. J. Cardiovasc. Magn. Reson. 2016; In press.
16 Liu C-Y, Wieben O, Brittain JH, Reeder SB. Improved delayed enhanced myocardial imaging with T2-Prep inversion recovery magnetization preparation. J. Magn. Reson. Imaging. 2008;28:1280–6.
17 Kellman P, Arai AE, Mcveigh ER, Aletras AH. Phase-Sensitive Inversion Recovery for Detecting Myocardial Infarction Using Gadolinium-Delayed Hyperenhancement. Magn. Reson. Med. 2002;383:372–83.

18 Mordi I, Radjenovic A, Stanton T, Gardner RS, McPhaden A, Carrick D, et al. Prevalence and Prognostic Significance of Lipomatous Metaplasia in Patients With Prior Myocardial Infarction. JACC. Cardiovasc. Imaging. American College of Cardiology Foundation; 2014;1–2.
19 Kellman P, Hernando D, Arai AE. Myocardial Fat Imaging. Curr. Cardiovasc. Imaging Rep. 2010;3:83–91.
20 Kellman P, Hernando D, Shah S, Chefdhotel C, Liang Z-P, Arai A. Free-breathing, single shot fat-water separated cardiac imaging with motion corrected averaging. ISMRM 2010 Sci. Meet. 2010;18:3662.
21 Kellman P, Chefd'hotel C, Lorenz CH, Mancini C, Arai AE, McVeigh ER. Fully automatic, retrospective enhancement of real-time acquired cardiac cine MR images using image-based navigators and respiratory motion-corrected averaging. Magn. Reson. Med. 2008;59:771–8.
22 Xue H, Kellman P, LaRocca G, Arai AE, Hansen MS. High spatial and temporal resolution retrospective cine cardiovascular magnetic resonance from shortened free breathing real-time acquisitions. J. Cardiovasc. Magn. Reson. 2013;15:102.
23 Kellman P, Aletras AH, Mancini C, McVeigh ER, Arai AE. T2-prepared SSFP improves diagnostic confidence in edema imaging in acute myocardial infarction compared to turbo spin echo. Magn. Reson. Med. 2007;57:891–7.
24 Kellman P, Xue H, Spottiswoode BS, Sandino CM, Hansen MS, Abdel-Gadir A, et al. Free-breathing T2* mapping using respiratory motion corrected averaging. J. Cardiovasc. Magn. Reson. 2015;17:3.
25 Xue H, Hansen MS, Nielles-vallespin S, Arai AE, Kellman P. Inline quantitative myocardial perfusion flow mapping. JCMR/ISMRM Workshop. 2016;18:4–6.

Contact

Peter Kellman
National Heart, Lung, and Blood Institute
National Institutes of Health, DHHS
10 Center Drive MSC-1061
Bethesda, MD 20892
USA
kellman@nih.gov

Siemens' global MRI community offers peer-to-peer support and information. Radiologists, physicists, cardiologists, and technologists, have all contributed with publications, presentations, training documents, case studies, and more – all freely available to you via this unique network.

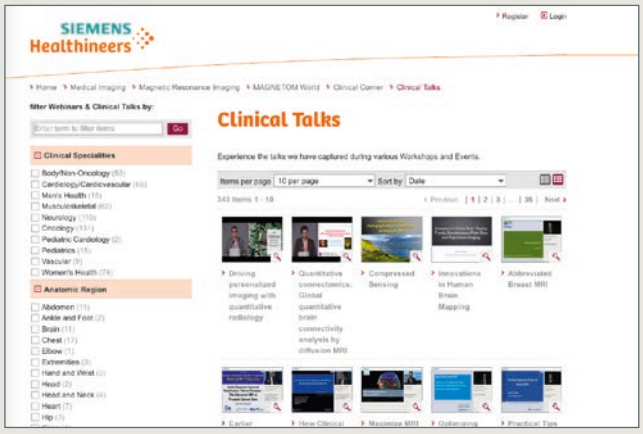

Don't miss the >300 lectures and presentations by international and renowned experts in the field on all aspects of MR imaging that will allow you to be exposed to new ideas and alternative approaches.

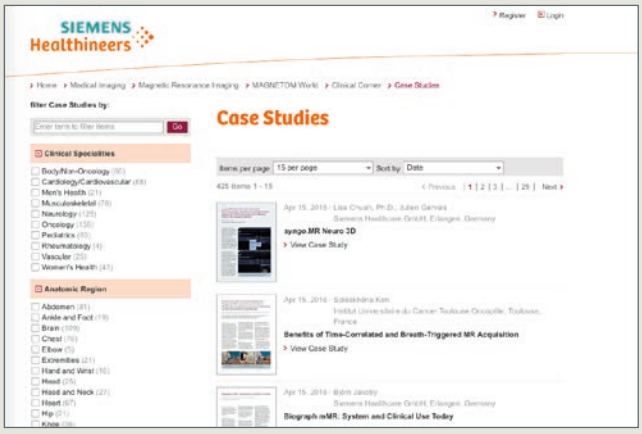

The centerpiece of the MAGNETOM World Internet platform consists of MAGNETOM users' results. Here you will find case reports, articles and application tips allowing you to optimize your daily work.

Put the advantages of the MAGNETOM World to work for you!

www.siemens.com/magnetom-world

4D Flow MRI – an Update

Michael Markl, Ph.D.[1,2]; James Carr, M.D.[1]; Michael Rose, B.S.[3]; Cynthia K. Rigsby, M.D.[1,3,4]; Julia Geiger, M.D.[1]

[1] Department of Radiology, Feinberg School of Medicine, Northwestern University, Chicago, USA
[2] Department Biomedical Engineering, McCormick School of Engineering, Northwestern University, Chicago, USA
[3] Department of Medical Imaging, Ann & Robert H. Lurie Children's Hospital of Chicago, Chicago, USA
[4] Department of Pediatrics, Feinberg School of Medicine, Northwestern University, Chicago, USA

Introduction

MRI techniques provide non-invasive and non-ionizing methods for the accurate anatomic depiction of the cardiovascular system. In addition, the intrinsic sensitivity of MRI to motion offers the unique ability to acquire blood flow simultaneously with anatomical data within a single measurement (phase contrast (PC) principle). The characterization of the dynamic components of blood flow with MRI has achieved considerable progress in recent years including new methodological advances such as 4D Flow MRI for the comprehensive *in-vivo* analysis of complex time-resolved 3D blood flow characteristics [1-7].

Standard clinically employed 2D CINE PC MRI takes advantage of the direct relationship between blood flow velocity and the MR signal to measure blood flow velocity along a single direction, similar to Doppler echocardiography [8]. Typical clinical imaging protocols measure blood flow in 2D imaging slices positioned orthogonal to the vessel which usually includes single-direction velocity measurement (through-plane encoding) and is performed during a 10-15 second breath-hold period. The resulting images are used to quantify flow parameters such as peak velocity, net flow, or regurgitant fraction at the site of the imaging plane.

In 4D Flow MRI[1], velocity is encoded along all three spatial dimensions throughout the cardiac cycle, thus providing a time-resolved 3D velocity field. As a result, 4D Flow MRI can provide full volumetric coverage of the vessel of interest and thus give more comprehensive spatial and temporal (4D = 3D + time) coverage. In this article, we describe the latest technical progress and data analysis protocols of the 4D Flow MRI for the Siemens platform, and we present different examples for clinical cardiothoracic and intracranial applications.

Technical advances

4D Flow data acquisition

Initial limitations for including 4D Flow MRI into clinical daily routine standard MRI protocols were related to long scan times of up to 20 minutes. Methodological improvements based on k-t parallel imaging or Compressed Sensing have been successfully employed to achieve significant imaging acceleration and reduced times [9, 10]. Combination with advanced respiration control [11, 12] for cardiothoracic and abdominal applications today allows the acquisition of 4D Flow MRI data within clinically acceptable scan times on the order of 5-10 minutes.

Continued developments based on alterative data sampling strategies such as radial or spiral data readout have high potential to further reduce scan times. For example, a recent study showed that the combination of highly efficient spiral sampling with dynamic compressed sensing can achieve major acceleration, which allowed for the acquisition of abdominal 4D Flow MRI data during a single breath-hold [10]. Ongoing methodological improvements focus on the acquisition of dual-venc acquisitions [13-15] which are expected to be of great benefit for the simultaneous assessment of low and fast flow velocities, e.g. in the brain or in congenital heart disease (CHD), where a high dynamic range is critical

[1] The product is still under development and not commercially available yet. Its future availability cannot be ensured.

	venc	respiration gating, R_{eff}	acceleration factor R	spatial resolution	temporal resolution	total scan time
aorta/PA	150-400 cm/s	60-80%	5	$(2.2\text{-}2.8\ mm)^3$	35-45 ms	5-8 min
whole heart	150-400 cm/s	60-80%	5	$(2.8\text{-}3.2\ mm)^3$	35-45 ms	8-12 min
head	80-120 cm/s	N/A	5	$(1.0\text{-}1.2\ mm)^3$	35-45 ms	8-10 min
abdomen	60-120 cm/s	60-80%	5	$(2.5\text{-}3.0\ mm)^3$	35-45 ms	10-15 min

Table 1: 4D Flow MR imaging scenarios for different application areas based on adult subjects with heart rates on the order of 60-70 bpm. For cardiothoracic and abdominal applications, respiratory navigator gating is typically used to minimize breathing artifacts. The combination with advanced data acquisition strategies (respiratory driven phase encoding) allows for high scan efficiencies (R_{eff}) on the order of 60-80%. The selection of the lower end of the velocity sensitivity (venc) is based on the expected maximal normal blood flow velocities in each vascular territory which will have to be adapted to higher velocities in patients with cardiovascular disease such as aortic valve stenosis. PA = pulmonary artery.

to cover the wide arterial and venous flow velocity spectrum.

A summary of imaging protocols for different application areas is provided in Table 1 and illustrates currently achievable spatio-temporal resolution and scan times based on recently described k-t accelerated 4D Flow MRI methods with high acceleration factors of R = 4 – 6 [16-18].

4D Flow data analysis workflow

For the visualization of cardiovascular flow patterns, commonly used techniques are 3D streamlines and time-resolved 3D pathlines to depict changes in hemodynamics associated with disease. Figure 1 illustrates the use of 3D streamlines to depict systolic 3D flow patterns in the thoracic aorta of a patient with a bicuspid aortic valve. Time-resolved 3D pathlines utilize the full 4D (3D and time) information and can be used to visualize the spatio-temporal dynamics of pulsatile 3D blood flow patterns.

An example of aortic 4D Flow MRI and comparison of the resulting imaging findings with standard MRI techniques is shown in Figure 1. A benefit compared to traditional 2D PC-MR imaging is related to the possibility for retrospective and flexible quantification and visualization of cardiovascular blood flow without being limited to 2D planes as in standard 2D CINE PC MRI. 4D Flow MRI offers a single and easy to prescribe data acquisition (3D volume covering cardiovascular region of interest) instead of multiple 2D planes for flow analysis with standard 2D CINE PC MRI that may be difficult to position in cases with complex vascular architecture (e.g. congenital heart disease, liver vasculature). As a result, 4D Flow MRI may help to avoid missing regions of interest for flow quantification where 2D CINE PC MRI may not have been acquired or planes were misplaced. Recent studies have confirmed that volumetric analysis based on 4D Flow MRI allows for improved assessment of aortic and pulmonary peak velocities which may be underestimated by 2D CINE PC MRI [19, 20].

The anatomic and velocity information of the 4D Flow data can additionally be used to calculate a 3D phase contrast angiogram (3D PC-MRA) which can be combined with 3D blood flow visualization to guide anatomic orientation (see Figs. 1-3). In addition, the 3D PC-MRA data serve as a basis for the 3D segmentation of vessels to improve 3D visualization or to provide the ability to mask the underlying velocity data to calculate systolic 3D velocity maximum intensity projections (MIP). As shown in Figure 2C, systolic velocity MIPs are an easy to use tool to give an overview over the 3D velocity distribution as well as automated quantification of peak velocities v_{peak} and thus estimate pressure gradients Δp using the simplified Bernoulli equation ($\Delta p = 4v_{peak}^2$). The increased complexity of 4D Flow data (3D + time + 3-directional velocities) offers the opportunity to derive new physiologic and pathophysiologic hemodynamic parameters, such as wall shear stress (WSS), pulse wave velocity, 3D pressure difference maps, or turbulent kinetic energy. These advanced hemodynamic measures can provide quantitative information on the impact of vascular pathologies on cardio- or cerebrovascular blood flow patterns beyond currently available techniques.
For example, methods have been developed to compute volumetric

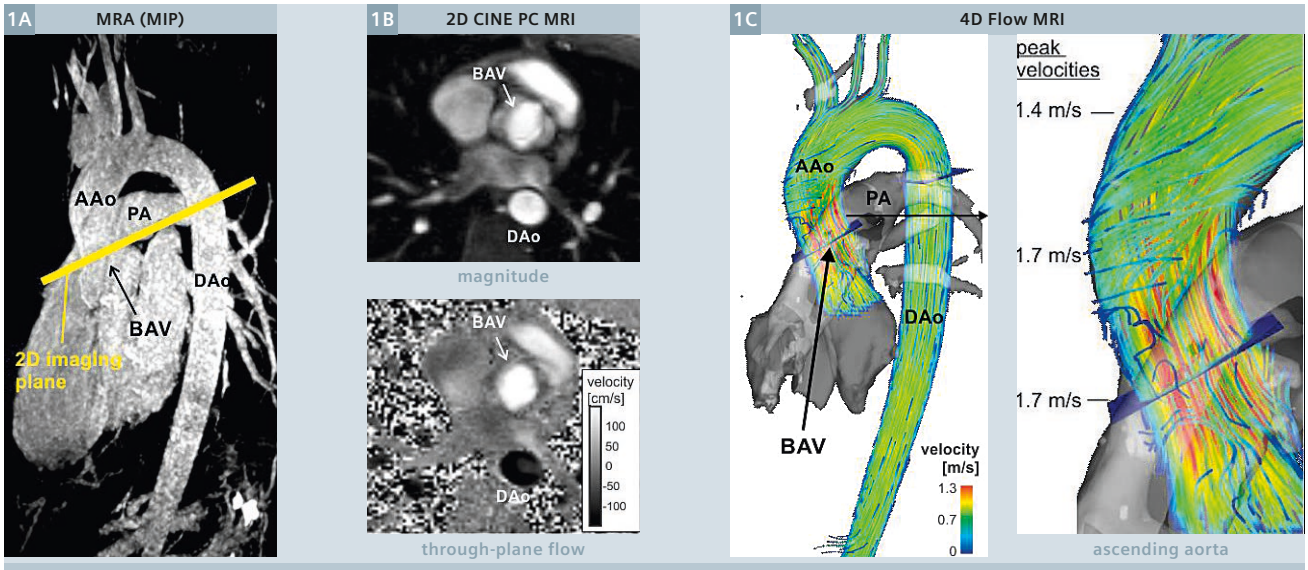

1 MR angiography (MRA, depicted as a maximum intensity projection, MIP) and 2D CINE PC-MRI in a patient with bicuspid aortic valve (BAV) disease. The patient underwent standard MR angiography **(1A)** as well as 2D CINE PC-MRI **(1B)** for the assessment of valve morphology and flow quantification at the level of the aortic valve in the ascending aorta (AAo). 1B shows the maximum aortic valve opening and blood flow during peak systole. The yellow line in 1A shows the imaging plane for 2D CINE PC-MRI acquisitions in 1B. **(1C)** 3D streamline visualization of systolic blood flow in the thoracic aorta as assessed by 4D Flow MRI. Note that 4D Flow MRI provides full volumetric coverage of the thoracic aorta and flexible retrospective quantification of peak systolic velocities at multiple locations in the thoracic aorta which revealed a peak velocity of 1.7 m/s distal to the BAV.
DAo = descending aorta, PA = pulmonary artery

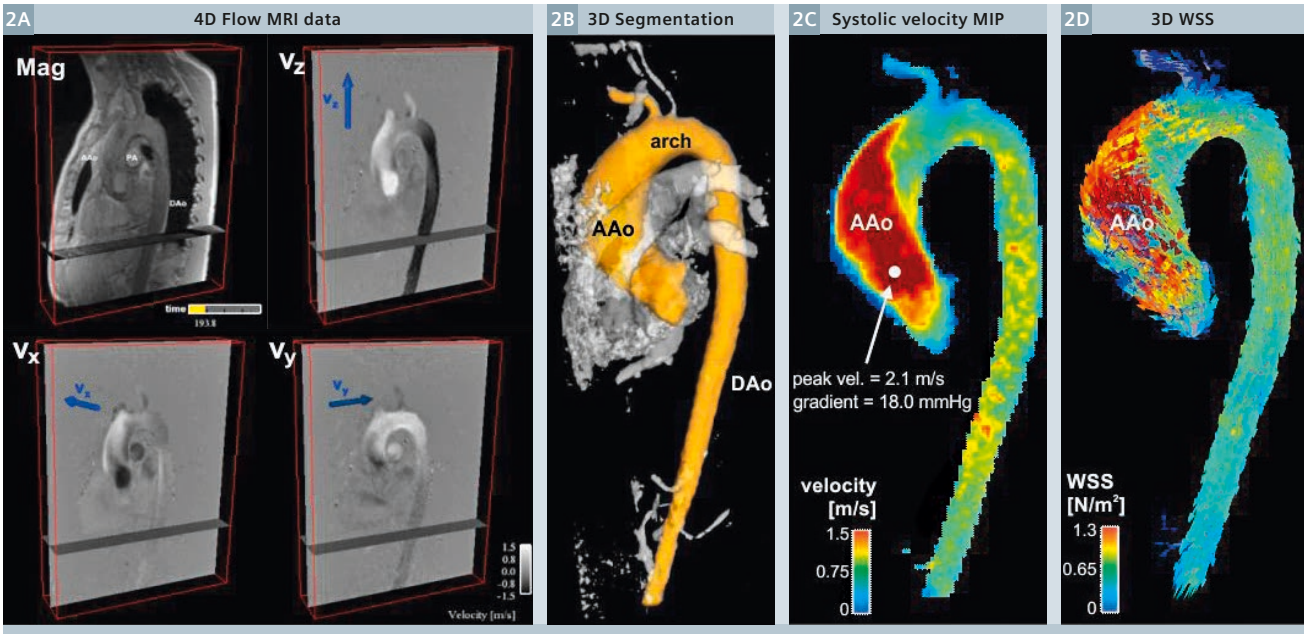

2 Data analysis workflow for the assessment of aortic velocity distribution and 3D WSS in a patient with bicuspid aortic valve (BAV) and ascending aortic (AAo) dilatation. **(2A)** 4D Flow MRI data with full volumetric coverage of the thoracic aorta including anatomical and 3-directional flow data. **(2B)** 3D segmentation based on 3D PC-MRA data (gray shaded iso-surface) is used to isolate the aortic lumen. **(2C)** The 3D segmentation is used to mask the measured time-resolved 3D velocity data and calculate a systolic velocity maximum intensity projection (MIP). The velocity MIP data can be used to automatically extract the peak systolic velocity and pressure gradient (estimated via the simplified Bernoulli equation) without the need for manual analysis plane placement. Results indicate mild BAV stenosis causing mildly elevated pressure gradient. **(2D)** Advanced hemodynamic analysis can be employed to map peak systolic wall shear stress (WSS) vectors onto the aortic surface which indicate substantially elevated WSS (red color) along the outer curvature of the ascending aorta.
DAo = descending aorta.

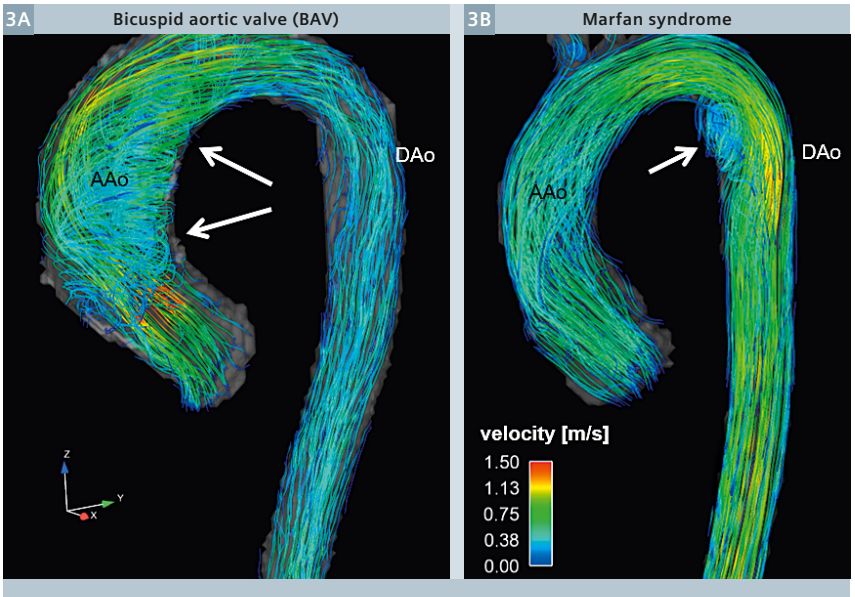

3 Systolic 3D streamline visualization in two patients with different aortic disease. **(3A)** 56-year-old patient with bicuspid aortic valve (BAV) demonstrates pronounced helix flow in the dilated ascending aorta (AAo) while blood flow in the descending aorta (DAo) is normal. **(3B)** In contrast, this 22-year-old patient with Marfan syndrome who has no marked aortic ectasia shows physiological flow in the AAo but an abnormal localized vortex flow pattern in the proximal DAo.

3D WSS, a known pathophysiological parameter implicated in vascular remolding, along the segmented surface of the entire aorta (Fig. 2D) [21, 22]. The application of this technique in patients with aortic disease demonstrated that a 3D WSS mapping technique allows for compact visualization and regional quantification of hemodynamic parameters assessed across multiple subjects [23].

For a detailed overview of 4D Flow MRI developments and its use for 3D flow visualization and quantification throughout the human circulatory systems the reader is referred to a number of recently published review articles [1-7] and 4D Flow MRI consensus statement [24].

Clinical applications

In recent years, 4D Flow MRI has been increasingly applied in various vessel territories and diseases ranging from aortic pathologies to complex CHD,

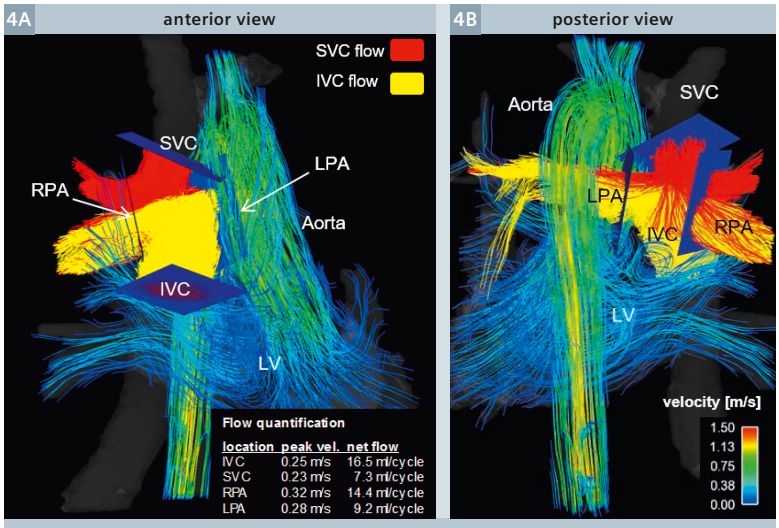

4 **(4A)** Blood flow visualization based on 3D streamlines in a 16-year-old patient with tricuspid atresia and palliative surgical repair with connection of the upper and lower caval veins directly to the right pulmonary artery (RPA) with detour of the right heart in the so called Fontan procedure. **(4B)** Color coded streamlines illustrate the distribution of venous flow originating in the superior caval vein (SVC, red) and inferior caval vein (IVC, yellow) towards the RPA and left pulmonary artery (LPA). Retrospective flow quantification allows for the assessment of peak velocities and flow volumes in the vessels of interest **(4A)**. Blood flow in the left ventricle and aorta is color-coded to local flow velocity in this example.

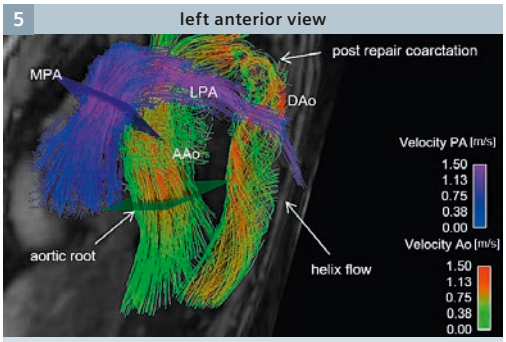

Flow quantification

location	peak vel.	net flow
aortic root	1.10 m/s	105 ml/cycle
MPA	2.26 m/s	99 ml/cycle

5 3D flow pattern in a 15-year-old patient with d-transposition of the great arteries (d-TGA) after arterial switch procedure depicting the typical postoperative anatomy of the main and branch pulmonary arteries without relevant postsurgical obstruction shown for main and left pulmonary artery (MPA, LPA). Color-coded streamlines according to vessel origin and velocity reveal the flow distribution in the pulmonary arteries (blue-purple) and the aorta (green-red) during systole. Note the marked helix flow in the DAo as a result after associated coarctation repair.

abdominal indications and intracranial applications.

Thoracic aorta

A number of studies indicate the important role of 4D Flow MRI for the comprehensive analysis of the impact of focal aortic abnormalities (aortic valve abnormality, coarctation, aortic dilatation) or genetic disorders (e.g. Marfan syndrome) on changes in 3D blood flow affecting the entire aorta [25-28]. Changes in flow patterns due to aortic valve stenosis or congenitally abnormal valves such as bicuspid aortic valve (BAV) affect predominantly the ascending aorta but can also expand into the aortic arch and descending aorta. In addition, the application of 4D Flow MRI in patients with aortic coarctation provides an overview of the hemodynamic changes which are not limited to the coarctation site and might be overlooked or misjudged by 2D CINE PC MRI. In addition, flow derived parameters such as WSS have shown high potential to derive better understanding of the underlying pathophysiology for aortic disease progression. Figure 3 depicts flow alterations in two representative patients with focal (BAV) and global (Marfan) aortic disease.

Complex congenital heart disease

Whole heart 4D Flow MRI techniques allow for a non-invasive comprehensive assessment of cardiovascular hemodynamics in the heart and its surrounding great vessels. While scan times are still long due to full volumetric coverage of the entire heart (8-12 minutes depending on heart rate and respiration control efficiency), it facilitates the systematic assessment of blood flow in multiple vessels and enables the retrospective analysis of any region of interest within the imaging volume. The examination of the pulmonary arteries and the right heart commonly has priority in CHD, and postsurgical assessment of the pulmonary blood flow is crucial to rule out potential re-stenoses or postsurgical sequelae which need re-intervention such as in patients with tetralogy of Fallot, transposition of the great arteries, or in subjects with functional single ventricle (see Figs. 4 and 5). Correct plane placement and flow assessment by 2D CINE PC MRI is particularly challenging in these cases. Previous studies have shown that the 4D Flow technique can reliably identify altered 3D flow characteristics related to the post-interventional status in patients with CHD. In addition, 4D Flow MRI based flow quantification has been shown to be equivalent or even improved when compared to 2D techniques, while needing less imaging time than time needed for positioning and acquisition of multiple planes [29-33].

Cerebrovascular disease

In clinical practice, transcranial Doppler ultrasound is routinely used for cerebrovascular flow measure-

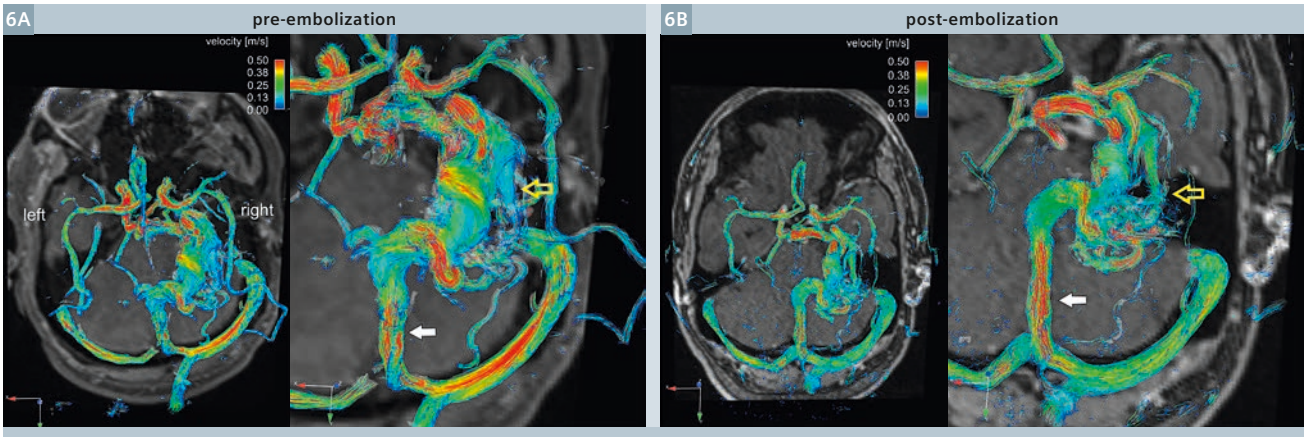

6 Intracranial 4D Flow MRI for the assessment of arterial and venous cerebrovascular hemodynamics. 3D blood flow visualization using time-integrated 3D pathlines in a 29-year old male patient with a large unruptured AVM centered in the right mesial temporal lobe with compact nidus prior to treatment **(6A)** and following invasive staged embolization therapy (**6B:** DSA guided endovascular superselective occlusion of AVM feeding arteries with nidal penetration). Complex arterial feeding and convoluted hemodynamics as well as differences in pre- and post-embolization vascularization and hemodynamics are clearly visible. Staged embolization resulted in compaction of the AVM with reduced blood flow velocities (yellow arrows) and reduced flow velocities for venous drainage (white arrow).

ments. However, the technique is operator-dependent and significantly limited by the available acoustic windows of the head, mainly in adults. 2D PC-MRI can provide flow measurements in large intracranial arteries and veins. However, small and tortuous vessels, complex vascular anatomy and the need for the manual placement of 2D imaging planes in multiple vessel segments represent challenges [34]. In contrast, 4D Flow MRI offers 3D blood flow visualization and retrospective flow quantification with full coverage of cerebral arteries and veins. Emerging applications include the hemodynamic evaluation of intra-cranial aneurysms, arteriovenous malformations (AVM), and intracranial atherosclerotic disease (ICAD), as well as venous flow. Figure 6 demonstrates the potential of 4D Flow MRI for the evaluation of global and regional AVM flow characteristics and treatment-induced changes in cerebrovascular flow distribution [35, 36]. In patients with cerebral AVMs, the pathological vascularization (direct shunting of blood from arterial to the venous sides without an intervening capillary bed) leads to abnormal hemodynamics. Flow information is potentially valuable for a better understanding of the impact of a focal AVM on the flow redistribution in the brain and/or in treatment planning by attempting to identify the feeding arteries with highest flow, enabling efficient and targeted embolization treatment.

Conclusion

A large number of studies have provided evidence that 4D Flow MRI can help to better understand altered hemodynamics in patients with cardiovascular diseases and may lead to improved patient management and monitoring of therapeutic responses. The novel hemodynamic insights obtained are also likely to provide new risk stratification metrics in patients that have prognostic significance and can also impact individualized treatment decisions to optimize patient outcome. Future research efforts will improve the clinical applicability of 4D Flow MRI and provide results in larger cohort studies.

References

1 Ebbers T. Flow imaging: cardiac applications of 3D cine phase-contrast MRI. Current Cardiovascular Imaging Reports. 2011;4:127-133.
2 Markl M, Kilner PJ, Ebbers T. Comprehensive 4D velocity mapping of the heart and great vessels by cardiovascular magnetic resonance. J Cardiovasc Magn Reson. 2011;13:7.
3 Frydrychowicz A, Francois CJ, Turski PA. Four-dimensional phase contrast magnetic resonance angiography: Potential clinical applications. Eur J Radiol. 2011.
4 Markl M, Frydrychowicz A, Kozerke S, Hope M, Wieben O. 4D flow MRI. J Magn Reson Imaging. 2012;36:1015-1036.
5 Hope MD, Sedlic T, Dyverfeldt P. Cardiothoracic magnetic resonance flow imaging. J Thorac Imaging. 2013;28:217-230.
6 Stankovic Z, Allen BD, Garcia J, Jarvis KB, Markl M. 4D flow imaging with MRI. Cardiovasc Diagn Ther. 2014;4:173-192.
7 Vasanawala SS, Hanneman K, Alley MT, Hsiao A. Congenital heart disease assessment with 4D flow MRI. J Magn Reson Imaging. 2015;42:870-886.
8 Nayak KS, Nielsen JF, Bernstein MA, Markl M, P DG, R MB, Saloner D, Lorenz C, Wen H, B SH, Epstein FH, J NO, Raman SV. Cardiovascular magnetic resonance phase contrast imaging. J Cardiovasc Magn Reson. 2015;17:71.
9 Schnell S, Markl M, Entezari P, Mahadewia RJ, Semaan E, Stankovic Z, Collins J, Carr J, Jung B. k-t GRAPPA accelerated four-dimensional flow MRI in the aorta: Effect on scan time, image quality, and quantification of flow and wall shear stress. Magn Reson Med. 2014;72:522-533.
10 Dyvorne H, Knight-Greenfield A, Jajamovich G, Besa C, Cui Y, Stalder A, Markl M, Taouli B. Abdominal 4D Flow MR Imaging in a Breath Hold: Combination of Spiral Sampling and Dynamic Compressed Sensing for Highly Accelerated Acquisition. Radiology. 2015;275:245-254.
11 Uribe S, Beerbaum P, Sorensen TS, Rasmusson A, Razavi R, Schaeffter T. Four-dimensional (4D) flow of the whole heart and great vessels using real-time respiratory self-gating. Magnetic resonance in medicine. 2009;62:984-992.
12 van Ooij P, Semaan E, Schnell S, Giri S, Stankovic Z, Carr J, Barker AJ, Markl M. Improved respiratory navigator gating for

thoracic 4D flow MRI. Magn Reson Imaging. 2015;33:992-999.
13 Ha H, Kim GB, Kweon J, Kim YH, Kim N, Yang DH, Lee SJ. Multi-VENC acquisition of four-dimensional phase-contrast MRI to improve precision of velocity field measurement. Magnetic resonance in medicine. 2016;75:1909-1919.
14 Binter C, Knobloch V, Manka R, Sigfridsson A, Kozerke S. Bayesian multipoint velocity encoding for concurrent flow and turbulence mapping. Magn Reson Med. 2013;69:1337-1345.
15 Macgowan CK, Liu GK, van Amerom JF, Sussman MS, Wright GA. Self-gated Fourier velocity encoding. Magn Reson Imaging. 2010;28:95-102.
16 Griswold MA, Jakob PM, Heidemann RM, Nittka M, Jellus V, Wang J, Kiefer B, Haase A. Generalized autocalibrating partially parallel acquisitions (GRAPPA). Magn Reson Med. 2002;47:1202-1210.
17 Baltes C, Kozerke S, Hansen MS, Pruessmann KP, Tsao J, Boesiger P. Accelerating cine phase-contrast flow measurements using k-t BLAST and k-t SENSE. Magn Reson Med. 2005;54:1430-1438.
18 Jung B, Stalder AF, Bauer S, Markl M. On the undersampling strategies to accelerate time-resolved 3D imaging using k-t-GRAPPA. Magn Reson Med. 2011;66:966-975.
19 Nordmeyer S, Riesenkampff E, Messroghli D, Kropf S, Nordmeyer J, Berger F, Kuehne T. Four-dimensional velocity-encoded magnetic resonance imaging improves blood flow quantification in patients with complex accelerated flow. Journal of magnetic resonance imaging : JMRI. 2013;37:208-216.
20 Rose MJ, Jarvis K, Chowdhary V, Barker AJ, Allen BD, Robinson JD, Markl M, Rigsby CK, Schnell S. Efficient method for volumetric assessment of peak blood flow velocity using 4D flow MRI. J Magn Reson Imaging. 2016, published online.
21 Potters WV, van Ooij P, Marquering H, Vanbavel E, Nederveen AJ. Volumetric arterial wall shear stress calculation based on cine phase contrast MRI. Journal of magnetic resonance imaging : JMRI. 2014:1-12.
22 van Ooij P, Potters WV, Nederveen AJ, Allen BD, Collins J, Carr J, Malaisrie SC, Markl M, Barker AJ. A methodology to detect abnormal relative wall shear stress on the full surface of the thoracic aorta using four-dimensional flow MRI. Magn Reson Med. 2015;73:1216-1227.
23 Guzzardi DG, Barker AJ, van Ooij P, Malaisrie SC, Puthumana JJ, Belke DD, Mewhort HE, Svystonyuk DA, Kang S, Verma S, Collins J, Carr J, Bonow RO, Markl M, Thomas JD, McCarthy PM, Fedak PW. Valve-Related Hemodynamics Mediate Human Bicuspid Aortopathy: Insights From Wall Shear Stress Mapping. J Am Coll Cardiol. 2015;66:892-900.
24 Dyverfeldt P, Bissell M, Barker AJ, Bolger AF, Carlhall CJ, Ebbers T, Francios CJ, Frydrychowicz A, Geiger J, Giese D, Hope MD, Kilner PJ, Kozerke S, Myerson S, Neubauer S, Wieben O, Markl M. 4D flow cardiovascular magnetic resonance consensus statement. J Cardiovasc Magn Reson. 2015;17:72.
25 Barker AJ, Markl M, Burk J, Lorenz R, Bock J, Bauer S, Schulz-Menger J, von Knobelsdorff-Brenkenhoff F. Bicuspid aortic valve is associated with altered wall shear stress in the ascending aorta. Circ Cardiovasc Imaging. 2012;5:457-466.
26 Allen BD, van Ooij P, Barker AJ, Carr M, Gabbour M, Schnell S, Jarvis KB, Carr JC, Markl M, Rigsby C, Robinson JD. Thoracic aorta 3D hemodynamics in pediatric and young adult patients with bicuspid aortic valve. J Magn Reson Imaging. 2015;42:954-963.
27 Frydrychowicz A, Markl M, Hirtler D, Harloff A, Schlensak C, Geiger J, Stiller B, Arnold R. Aortic Hemodynamics in Patients With and Without Repair of Aortic Coarctation: In Vivo Analysis by 4D Flow-Sensitive Magnetic Resonance Imaging. Invest Radiol. 2011;46:317-325.
28 Geiger J, Markl M, Herzer L, Hirtler D, Loeffelbein F, Stiller B, Langer M, Arnold R. Aortic flow patterns in patients with Marfan syndrome assessed by flow-sensitive four-dimensional MRI. J Magn Reson Imaging. 2012;35:594-600.
29 Nordmeyer S, Riesenkampff E, Crelier G, Khasheei A, Schnackenburg B, Berger F, Kuehne T. Flow-sensitive four-dimensional cine magnetic resonance imaging for offline blood flow quantification in multiple vessels: a validation study. J Magn Reson Imaging. 2010;32:677-683.
30 van der Hulst AE, Westenberg JJ, Kroft LJ, Bax JJ, Blom NA, de Roos A, Roest AA. Tetralogy of fallot: 3D velocity-encoded MR imaging for evaluation of right ventricular valve flow and diastolic function in patients after correction. Radiology. 2010;256:724-734.
31 Hsiao A, Alley MT, Massaband P, Herfkens RJ, Chan FP, Vasanawala SS. Improved cardiovascular flow quantification with time-resolved volumetric phase-contrast MRI. Pediatric radiology. 2011;41:711-720.
32 Valverde I, Nordmeyer S, Uribe S, Greil G, Berger F, Kuehne T, Beerbaum P. Systemic-to-pulmonary collateral flow in patients with palliated univentricular heart physiology: measurement using cardiovascular magnetic resonance 4D velocity acquisition. J Cardiovasc Magn Reson. 2012;14:25.
33 Gabbour M, Schnell S, Jarvis K, Robinson JD, Markl M, Rigsby CK. 4-D flow magnetic resonance imaging: blood flow quantification compared to 2-D phase-contrast magnetic resonance imaging and Doppler echocardiography. Pediatr Radiol. 2015;45:804-813.
34 Schubert T, Bieri O, Pansini M, Stippich C, Santini F. Peak velocity measurements in tortuous arteries with phase contrast magnetic resonance imaging: the effect of multidirectional velocity encoding. Invest Radiol. 2014;49:189-194.
35 Ansari SA, Schnell S, Carroll T, Vakil P, Hurley MC, Wu C, Carr J, Bendok BR, Batjer H, Markl M. Intracranial 4D Flow MRI: Toward Individualized Assessment of Arteriovenous Malformation Hemodynamics and Treatment-Induced Changes. AJNR Am J Neuroradiol. 2013;34:1922-1928.
36 Wu C, Ansari SA, Honarmand AR, Vakil P, Hurley MC, Bendok BR, Carr J, Carroll TJ, Markl M. Evaluation of 4D Vascular Flow and Tissue Perfusion in Cerebral Arteriovenous Malformations: Influence of Spetzler-Martin Grade, Clinical Presentation, and AVM Risk Factors. Am J Neuroradiol. 2015;36:1142-1149.

Contact

Michael Markl, Ph.D.
Department of Radiology
Northwestern University
737 N. Michigan Avenue Suite 1600
Chicago, Illinois 60611,
USA
Phone: +1 312-695-1799
Fax: +1 312-926-5991
mmarkl@northwestern.edu

James Carr

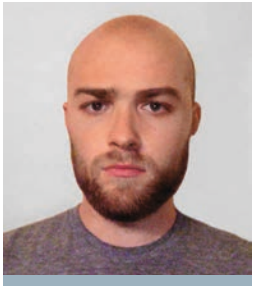
Michael Rose

Cindy Rigsby

Julia Geiger

Michael Markl

Imaging of Vascular Calcification Using PETRA and StarVIBE

Marcos P. Botelho[1,2]; Shivraman Giri[3]; Ioannis Koktzoglou[1,4]; Robert R. Edelman[1,2]; James Carr[1]

[1] Northwestern Memorial Hospital, Chicago, IL, USA
[2] NorthShore University HealthSystem, Evanston, IL, USA
[3] Siemens Healthineers, Chicago, IL, USA
[4] University of Chicago Pritzker School of Medicine, Chicago, IL, USA

New horizons for MRI of vascular calcifications

The presence of dense peripheral vascular calcifications has negative prognostic implications in patients with peripheral arterial disease (PAD). In addition, the presence of dense calcifications may alter the choice of access site for patients undergoing percutaneous revascularization or TAVR (transcatheter aortic valve replacement) procedures. Peripheral MR angiography is commonly used as an alternative to CT angiography for the evaluation of patients with PAD. While peripheral vascular calcifications are readily depicted with CT angiography, they are inapparent with MR angiography (MRA).

In this work, we present an approach that combines nonenhanced MRA with tailored 3D imaging of vascular calcifications. While QISS[1] is used for nonenhanced MRA, we propose two options for imaging of vascular calcifications:

1. PETRA, which relies on the use of an ultra-short echo time.
2. StarVIBE – as part of FREEZEit – which acquires data using a stack-of-stars *k*-space trajectory. Briefly, we adjust the echo time such that fat and water signals are in-phase, and apply a very small flip angle for the RF excitation which minimizes the impact of T1 relaxation time differences among tissues. This approach generates a homogenous signal level across most tissues, except for calcifications appear dark due to a very short T2* relaxation time. The use of StarVIBE is also helpful in minimizing motion sensitivity in the abdominal and pelvic regions compared with a fully Cartesian 3D acquisition.

[1] Requires QISS license on the scanner.

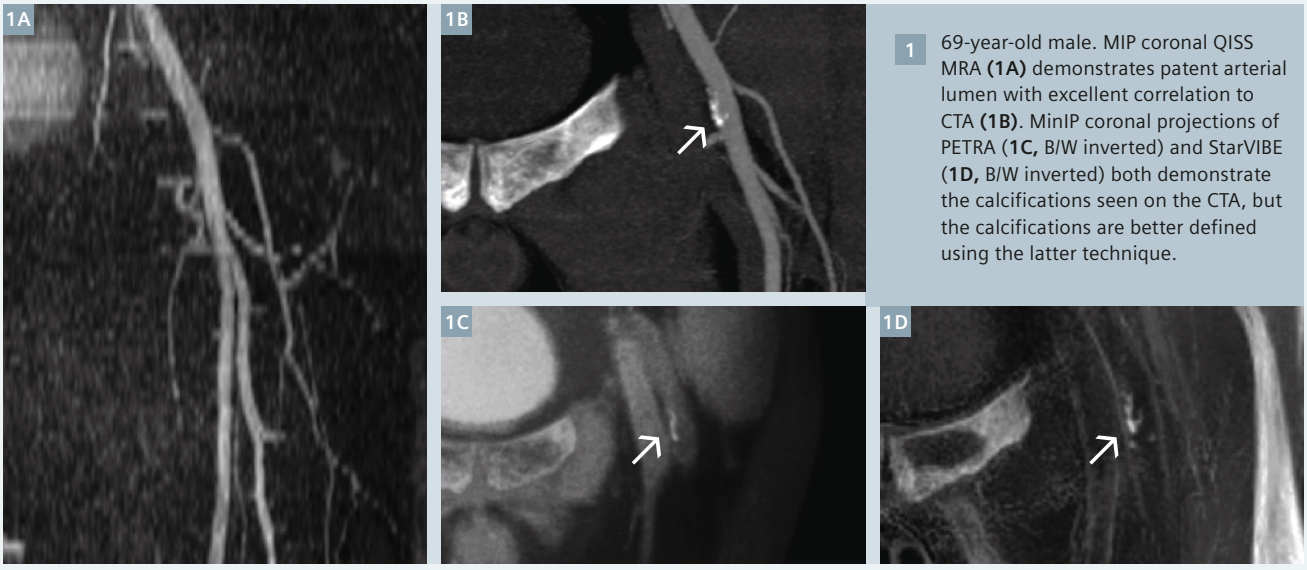

1 69-year-old male. MIP coronal QISS MRA **(1A)** demonstrates patent arterial lumen with excellent correlation to CTA **(1B)**. MinIP coronal projections of PETRA (**1C,** B/W inverted) and StarVIBE (**1D,** B/W inverted) both demonstrate the calcifications seen on the CTA, but the calcifications are better defined using the latter technique.

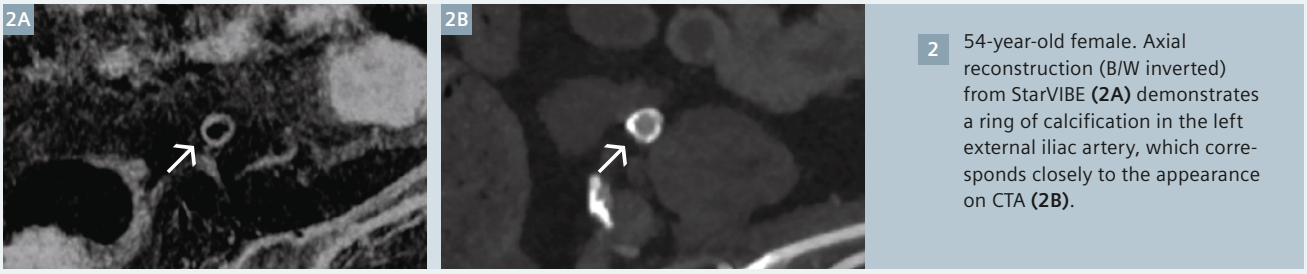

2 54-year-old female. Axial reconstruction (B/W inverted) from StarVIBE **(2A)** demonstrates a ring of calcification in the left external iliac artery, which corresponds closely to the appearance on CTA **(2B)**.

How to build your protocol on *syngo*.MR E11A 1.5T MAGNETOM Aera-XQ system?

1. PETRA approach:
One can start with the default PETRA protocol that can be found in the following location:

Default →
→ Sequence Region →
→ Siemens Seq→
→ Default.

The parameters to be updated are as follows:

Parameter name	Tab combination	Value
Orientation	Routine	Coronal
TR	Contrast/Common	4.7
TE	Contrast/Common	0.07
Flip angle	Contrast/Common	5
Table position mode	System/Miscellaneous	ISO
Radial views	Resolution/Common	60000
FOV read	Resolution/Common	400
Base resolution	Resolution/Common	384
Bandwidth	Sequence/Part1	338

Table 1: Protocol adaptations required for PETRA sequence to image calcification. Please start with the default protocol that can be found on scanner at: Default → Sequence Region → Siemens Seq → Default

2. StarVIBE approach (requires FREEZEit license):
One can start with any of the StarVIBE sequences. We started with the one in following location:

SIEMENS →
→ abdomen →
→ library → 3D

The parameters to be updated are as follows:

Please make sure that fat-suppression and centric ordering are turned off.

Parameter name	Tab combination	Value
Orientation	Routine	Coronal
Slice thickness	Routine	1.0
Slice Oversampling	Routine	25.0
Slices per slab	Routine	128
TR	Contrast/Common	7.61
TE	Contrast/Common	4.77
Flip angle	Contrast/Common	3.5
Fat suppr.	Contrast/Common	None
Table position mode	System/Miscellaneous	ISO
Radial views	Resolution/Common	600
FOV read	Resolution/Common	416
Base resolution	Resolution/Common	416
Slice resolution	Resolution/Common	75%
Optimization	Sequence/Part1	In phase
Bandwidth	Sequence/Part1	300
Incr. Gradient spoiling	Sequence/Part2	Yes

Table 2: Protocol adaptations required for StarVIBE sequence to image vascular calcification. Please start with the protocol that can be found on scanner at: SIEMENS → abdomen → library → 3D

PETRA	StarVIBE
Sensitive to motion	Insensitive to motion
Available on all *syngo*.MR E11 systems	Part of the FREEZEit option

Coils: Body matrix coils were used in our studies.

Suggestions for 3T imaging

1. For PETRA: No change required.
2. For StarVIBE: Please use the above values from MAGNETOM Aera-XQ, and then change the following TE = 2.46 ms, Flip angle = 2.5°, TR = 4.8 ms.

Post-processing to generate CT-like images

Both MR sequences generate images that make calcifications appear dark. This can be changed by going to the 'Image' menu, choosing the 'Color Lookup Table' option, and then selecting 'Inverted Gray Scale'. Now the calcifications appear bright – just like in CT. Use of a minimum intensity projection (MinIP) can improve display of the vascular calcifications.

Discussion

We have shown that angiography and calcification imaging can be accomplished using nonenhanced MR approaches during a single scan session. We presented two approaches for imaging of vascular calcification, one based on PETRA and the other on StarVIBE. In our experience so far, the StarVIBE outperforms PETRA due to its insensitivity to motion and overall image sharpness. A more detailed analysis, including 3T results, can be found in our recently published article "MR Imaging of Iliofemoral Peripheral Vascular Calcifications using Proton Density-Weighted, In-Phase Three-Dimensional Stack-of-Stars Gradient Echo" by Edelman et al. in *Magnetic Resonance in Medicine, 2016*.

Contact

Marcos P. Botelho, M.D.
Northwestern University
Department of Radiology
Evanston, IL, USA
marcos.botelho@fsm.northwestern.edu

Case Report: Hypertrophic Cardiomyopathy in a Pediatric Patient; Usefulness of T1 Mapping Synthetic Inversion Recovery Imaging

Giuseppe Muscogiuri, M.D.; Aurelio Secinaro, M.D.

Department of Imaging, Bambino Gesù - Children's Hospital IRCCS, Rome, Italy

Patient history

A 13-year-old patient with a family history of hypertrophic cardiomyopathy (HCM) underwent cardiac magnetic resonance (CMR) imaging in our MAGNETOM Aera 1.5T (Siemens Healthcare, Erlangen, Germany). The CMR examination focused on the evaluation of left ventricle outflow tract, biventricular architecture, myocardial thickness, systolic biventricular function, atrial dimensions and tissue characterization.

Sequence details

Steady state free precession cine images were acquired in long axis (4-, 2- and 3-chambers) and short axis, in order to measure atrial dimensions, maximum myocardial thickness in end diastolic phase and to evaluate presence of systolic anterior movement of the mitral valve and ventricular architecture. Systolic biventricular function was calculated using short axis cine images analysed on an off-line workstation.

Native T1 mapping (MOLLI 5(3)3) was acquired in long axis and short axis planes.

10-15 minutes after administration of gadolinium-based contrast agent (0.2 mmol/kg), the presence of late gadolinium enhancement (LGE) areas were assessed acquiring, on long axis and short axis, conventional 2D segmented magnitude inversion recovery and phase sensitive inversion recovery; followed by the acquisition of post T1 mapping (MOLLI 4(1)3(1)2) in the same cardiac planes of conventional LGE.

The extent of LGE was evaluated both on conventional and T1 mapping-derived (synthetic LGE)[1] sequences (Fig. 1).

The patient showed asymmetric HCM involving the basal antero-septum (23 mm of maximum wall thickness, Z score = 5 standard deviation), with associated mild dilatation of left atrium and absence of systolic anterior movement of the mitral valve. Biventricular systolic function was preserved.

A wide area of late enhancement (18% calculated using five standard deviation as cut-off compared to normal myocardium) was observed in hypertrophic segments of both conventional and synthetic LGE sequences (Fig. 2).

[1] Synthetic PSIR reconstruction from the T1 Mapping data is WIP. The product is currently under development and is not for sale in the US and in other countries. Its future availability cannot be ensured.

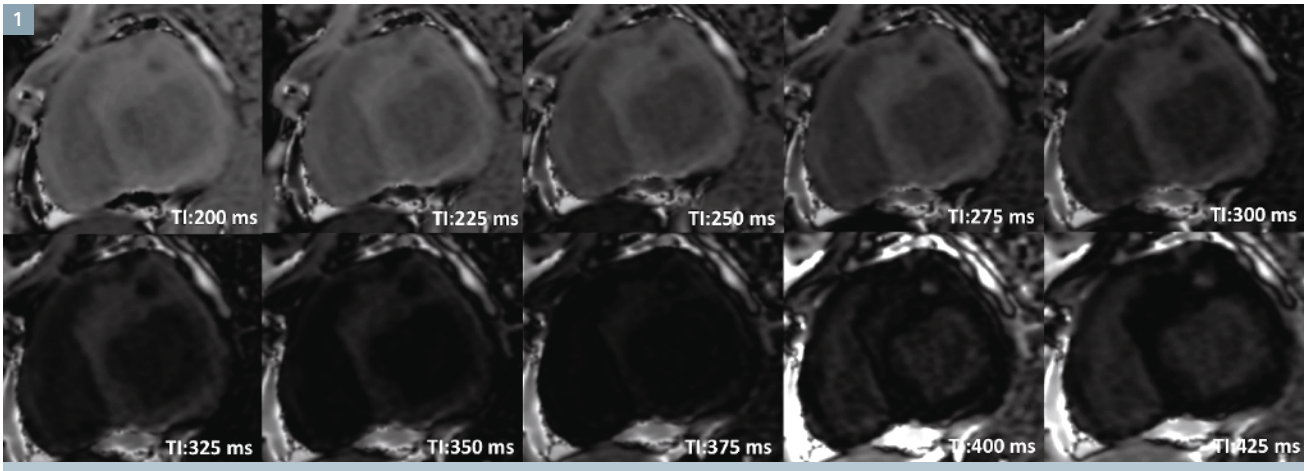

1 Synthetic LGE magnitude reconstructed, derived from post T1-mapping acquisition. Images are reconstructed with an inversion time included between 200 and 425 ms with an increment of 25 ms.

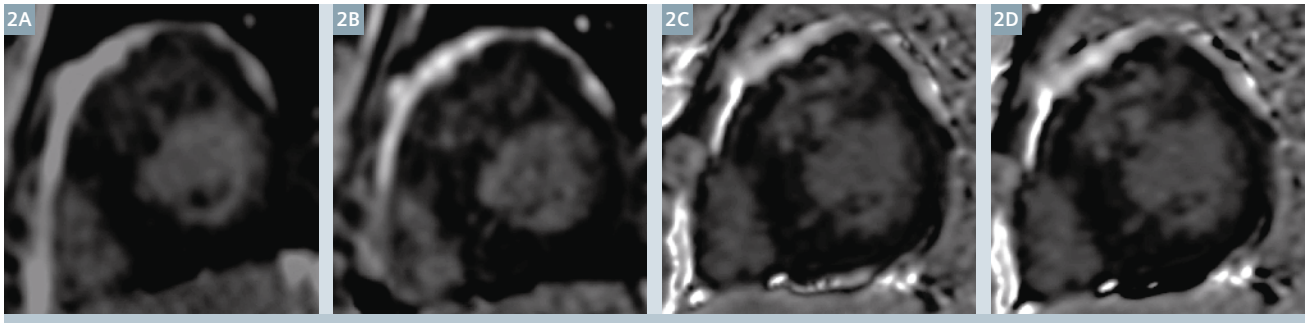

2 Images **(2A+B)** show conventional LGE acquired in short axis, reconstructed with magnitude inversion recovery **(2A)** and phase sensitive inversion recovery **(2B)**. LGE images **(2D+D)** are derived from T1 mapping. Synthetic magnitude LGE is shown in **(2C)** while synthetic phase sensitive LGE is in **(2D)**. The extent of LGE is similar for both conventional and synthetic LGE.

Comments

Nowadays CMR is crucial in the diagnosis and risk stratification of patients with HCM [1]. Indeed CMR in HCM allows the assessment of diffuse and focal fibrosis; the latter associated with a poor outcome [2].

The depiction of focal fibrosis in CMR is commonly available acquiring conventional LGE sequences 10-15 minutes after the injection of contrast agent. However, the acquisition of LGE sequences in children[2] can sometimes be challenging, particularly due to fast heart rate and small size of ventricle [3]. In our institution, the CMR protocol for cardiomyopathies includes the acquisition of T1 mapping, before and after contrast, in order to calculate the extracellular volume and to evaluate synthetic LGE derived from T1 mapping inversion recovery imaging. Indeed, Varga-Szemes et al. showed that the amount of LGE calculated with synthetic LGE is similar to that acquired with conventional sequences in patients with myocardial infarction [4].

Therefore, the possibility to acquire synthetic LGE, despite the lower spatial resolution compared to conventional segmented LGE sequences, can be useful in pediatric cases where the standard LGE approach might show presence of artefacts, and the evidence of LGE is pivotal in clinical management.

[2] MR scanning has not been established as safe for imaging fetuses and infants under two years of age. The responsible physician must evaluate the benefit of the MRI examination in comparison to other imaging procedures.

References

1 Bogaert J, Olivotto I. MR Imaging in Hypertrophic Cardiomyopathy: From Magnet to Bedside. Radiology. 2014;273(2):329-48. doi:10.1148/radiol.14131626.

2 Chan RH, Maron BJ, Olivotto I, Pencina MJ, Assenza GE, Haas T et al. Prognostic value of quantitative contrast-enhanced cardiovascular magnetic resonance for the evaluation of sudden death risk in patients with hypertrophic cardiomyopathy. Circulation. 2014;130(6):484-95. doi:10.1161/CIRCULATIONAHA.113.007094.

3 Fratz S, Chung T, Greil GF, Samyn MM, Taylor AM, Valsangiacomo Buechel ER et al. Guidelines and protocols for cardiovascular magnetic resonance in children and adults with congenital heart disease: SCMR expert consensus group on congenital heart disease. J Cardiovasc Magn Reson. 2013;15:51. doi:10.1186/1532-429X-15-51.

4 Varga-Szemes A, van der Geest RJ, Spottiswoode BS, Suranyi P, Ruzsics B, De Cecco CN et al. Myocardial Late Gadolinium Enhancement: Accuracy of T1 Mapping-based Synthetic Inversion-Recovery Imaging. Radiology. 2016;278(2):374-82. doi:10.1148/radiol.2015150162.

Giuseppe Muscogiuri

Aurelio Secinaro

Contact

Aurelio Secinaro, M.D.
Bambino Gesù –
Children's Hospital IRCCS
Department of Imaging
Piazza Sant'Onofrio 4
00146 Rome
Italy
Phone: +39 06 68592790
Fax: +39 06 68594561
aurelio.secinaro@opbg.net

Case Series: Utilization of the Pediatric 16 Coil for 1.5T and 3T Systems

Bac Nguyen, RT (R) (MR)

Oslo University Hospital, Rikshospitalet, Oslo, Norway

Introduction

At our institution we have a high rate of pediatric cases which can be both difficult and challenging. As a University Hospital, we perform pediatric imaging[1] for a wide range of indications including the brain, spine, heart, abdomen, pelvis and whole-body and the imaging of children can involve either general anesthesia or the feed and wrap technique. In all cases, fast and robust workflows for high-resolution imaging are required. In this article, we would like to share our experiences with the Pediatric 16 coil on both 1.5T and 3T to demonstrate what it can help achieve. We had acquired the coils in December 2015 for our 1.5T MAGNETOM Aera and 3T MAGNETOM Skyra. This gives us the opportunity to easily setup our program either with anesthesia or as feed and wrap. It simplifies the setup of our busy daily program and helps us to avoid any dead- or delay time that may arise from these cases.

The Pediatric 16 is a 16-channel receive coil with 16 integrated preamplifiers for head and neck imaging of new-borns and infants up to 18 months of age[1]. There are 13 channels for head imaging and 3 channels for the neck, and these channels can be used independently. The coil is equipped with DirectConnect technology and it connects directly into the scanner table with no connecting cables. Other special features include a recess in the anterior coil for easy positioning of intubation tubes, and a 4 cm aperture at the top of the coil for better ventilation. As a Tim4G Matrix coil, the Pediatric 16 can be combined flexibly with other coils including the Spine, Body, Flex and Special Purpose coils for whole CNS and whole-body imaging and this opens many opportunities for the imaging of infants and small children[1].

While this coil is intended for infants from 0-18 months, we have experienced a few cases where children did not fit. For instance, a 1-year-old infant with hydrocephalus may not fit due to the size of the head. Conversely, a 20-month-old infant may fit perfectly. Obviously, infants vary in size and this needs to be checked in each case.

In our experience, compared to the Head/Neck 20 this dedicated pediatric coil provides much better performance at the same scan times due to the fact that the coil fits more closely to the heads of small infants. Cases 1-4 illustrate the fast and high-resolution imaging we can achieve with this coil across infants of varying ages.

Along with Pediatric 16 comes a cradle with two straps and cushions to help with fixation. This cradle was designed to enable the preparation of infants away from the scanner and to provide safe and efficient transport of the infant to the scanner. This cradle has proven itself to be a true workflow enhancer at our institution, especially for our feed and wrap examinations. Firstly, we can plan our exam in good time with other departments so the patient can come to us in a position ready for examination. We do not lose time preparing the baby at the scanner, and we find that most babies lie much more still when everything is ready. All we need to do at our department is a final check for safety aspects (puls oximetry, ECG etc.). For children requiring only brain or brain and spine scans, the cradle can be slid easily into the Pediatric 16 coil (without the need to remove the anterior part) and the patient can be put into the scanner without further coil management. If the baby requires whole-body imaging, the Body coil can be easily placed on the child. This cradle has high edges, which means that coils can be put directly on these edges for stabilization, rather than laying them directly on top of the child. There are also cases where smaller coils would be needed, such as the small Flex coil. We can position this inside the edges along with cushions. This is much easier compared to the situation where the patient is lying directly on the table with positioning sandbags along the sides. Our use of the cradle has enabled faster, robust and more comfortable examinations for the child so much so that we use the cradle even for patients requiring only body or cardiac imaging.

Cases 5 and 6 are illustrations of our patients who have undergone liver and cardiac examinations where the cradle has helped with the workflow.

[1] MR scanning has not been established as safe for imaging fetuses and infants under two years of age. The responsible physician must evaluate the benefit of the MRI examination over other imaging procedures.

Case 1

10-day-old infant[1] with left-sided seizure and suspicion of cerebral infarct. The patient weight was approximately 3 kg. Imaging was performed on a 3T MAGNETOM Skyra with the Pediatric 16 coil, as a feed and wrap procedure. There were no findings.

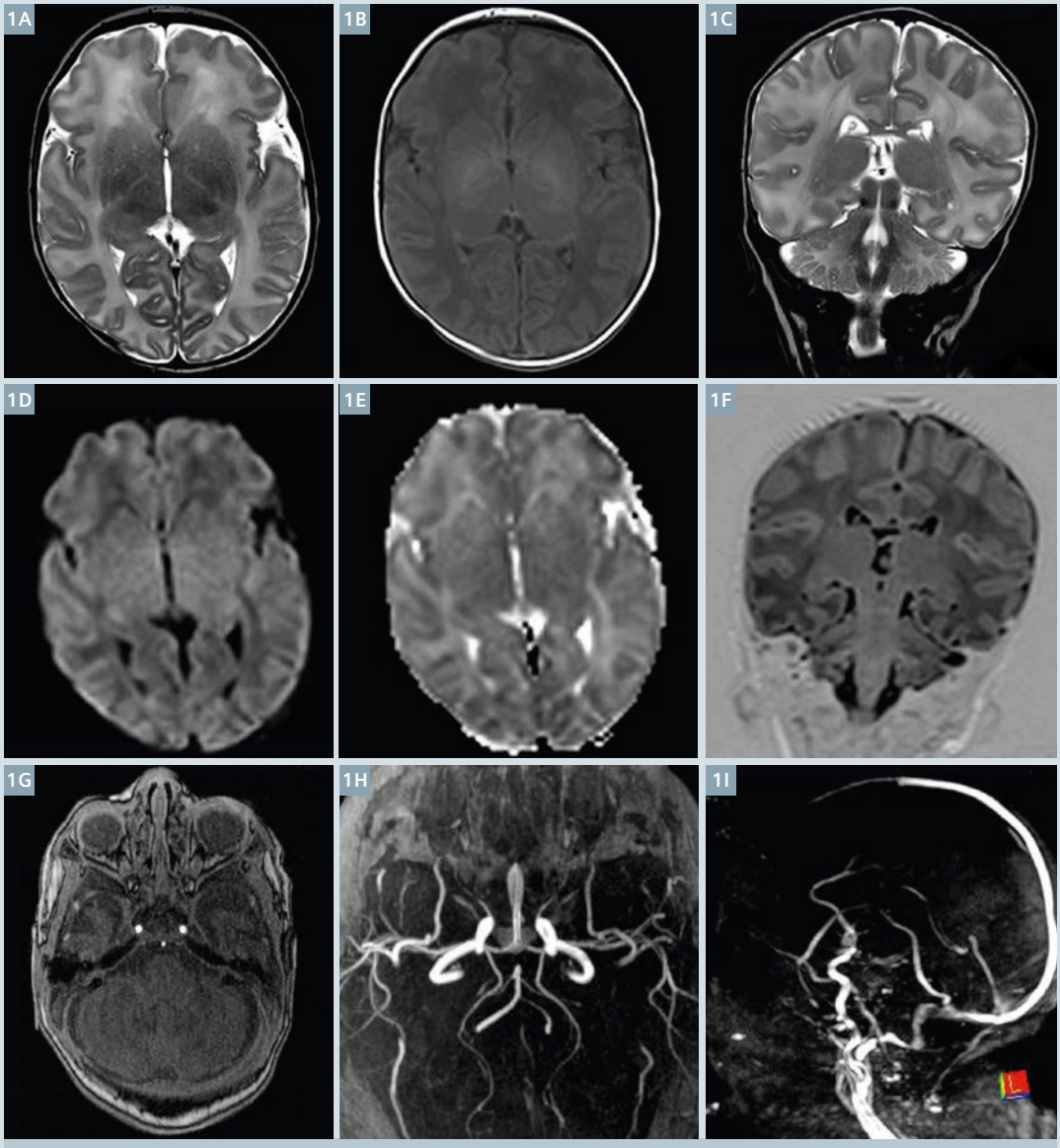

1 **(1A)** T2w TSE transversal, voxel 0.49 x 0.49 x 3 mm, TA: 2 min 12 sec.

(1B) T1w TSE transversal, voxel 0.74 x 0.74 x 3 mm, TA: 2 min 32 sec.

(1C) T2w TSE coronal, voxel 0.49 x 0.49 x 3 mm, TA: 2 min 12 sec.

(1D) Diffusion-weighted imaging (DWI) RESOLVE, b-value 1000 (acquired b0, b500 and b1000), voxel 1.5 x 1.5 x 4 mm, TA: 2 min 30 sec.

(1E) DWI apparent diffusion coefficient (ADC) map.

(1F) T1w SPACE IR coronal, voxel 1.17 x 1.17 x 0.9 mm, TA: 2 min 16 sec.

(1G) Time-of-flight (TOF) transversal, voxel 0.5 x 0.5 x 0.5 mm, TA: 3 min 42 sec.

(1H) TOF maximum intensity projection (MIP).

(1I) Phase contrast (PC) MIP sagittal, voxel 1.3 x 1 x 1 mm, TA: 4 min 37 sec.

Case 2

1-year-old male infant[1] with increasing frequency of epileptic seizures, hemiparesis, fever and a cold. The patient's weight is approximately 10 kg. Imaging was performed on a 3T MAGNETOM Skyra with the Pediatric 16 in combination with the Spine 32. The exam was performed under general anesthesia. The report for this patient indicated slight hypomyelination with a possible small syrinx in the distal medulla.

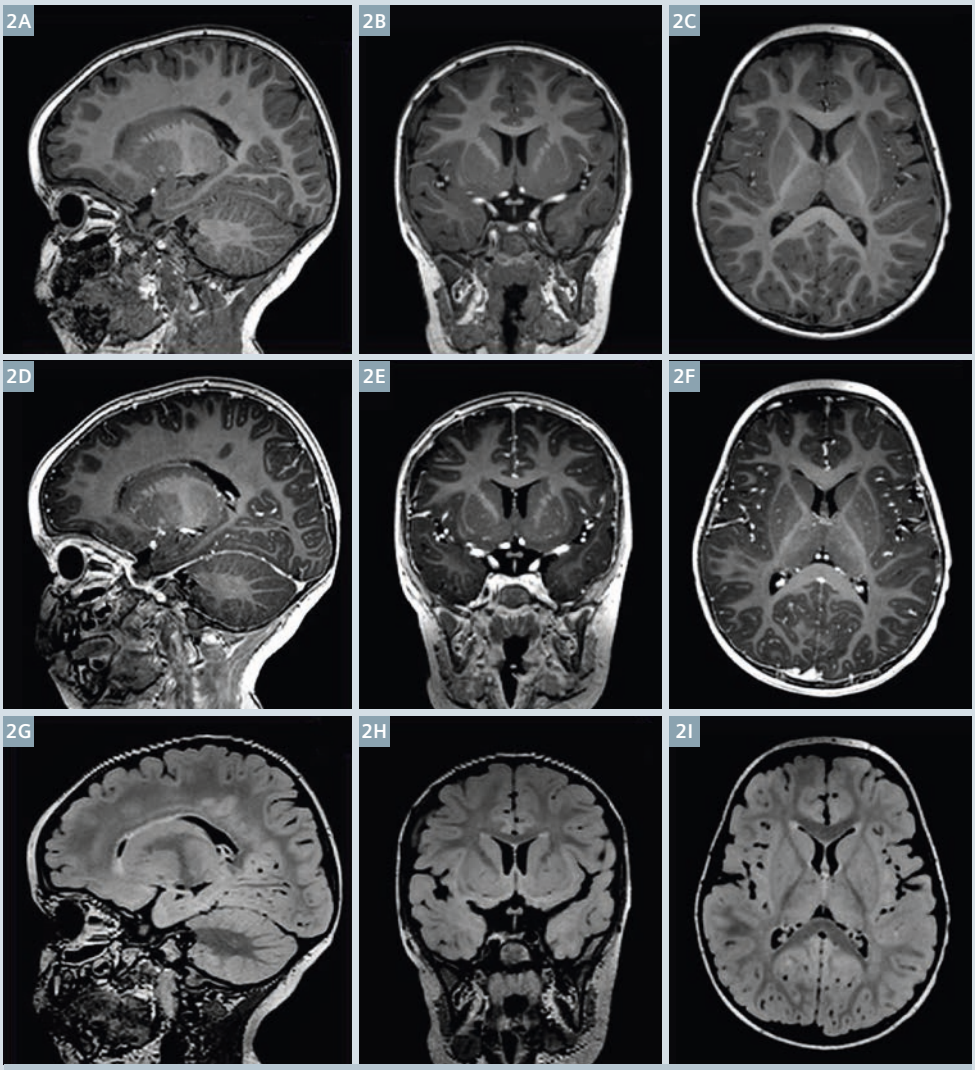

2 **(2A)** T1w 3D MPRAGE acquired in sagittal plane without contrast medium, voxel 1 x 1 x 1 mm, TA: 5 min 5 sec.

(2B) T1w 3D MPRAGE 1 mm coronal multi-planar reconstruction (MPR) without contrast.

(2C) T1w 3D MPRAGE 1 mm transversal MPR without contrast.

(2D) T1w 3D MPRAGE 1 mm acquired in sagittal plane with contrast medium, voxel 1 x 1 x 1 mm, TA: 5 min 5 sec.

(2E) T1w 3D MPRAGE 1 mm coronal MPR with contrast medium.

(2F) T1w 3D MPRAGE 1 mm transversal MPR with contrast medium.

(2G) T2w 3D SPACE FLAIR acquired in sagittal plane, voxel 1 x 1 x 1 mm, TA: 5 min 24 sec.

(2H) T2w 3D SPACE FLAIR 1 mm coronal MPR.

(2I) T2w 3D SPACE FLAIR 1 mm transversal MPR.

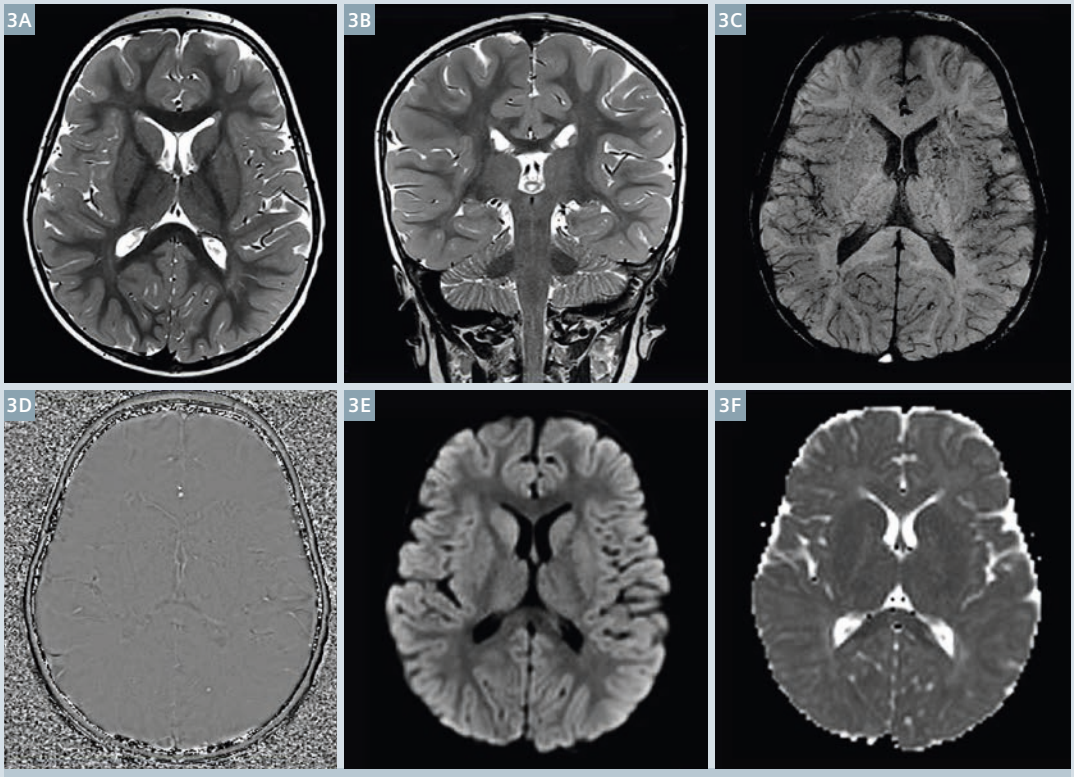

3 **(3A)** T2w TSE transversal, voxel 0.2 x 0.2 x 2 mm, TA: 4 min 32 sec.
(3B) T2w TSE coronal, voxel 0.2 x 0.2 x 2 mm, TA: 4 min 32 sec.
(3C) Susceptibility-weighted imaging (SWI) transversal minIP image, voxel 0.6 x 0.5 x 1.4 mm, TA: 5 min.
(3D) SWI Phase image.
(3E) DWI RESOLVE, b-value 1000 (acquired b0, b500 and b1000), voxel 1.5 x 1.5 x 4 mm, TA: 4 min 21 sec.
(3F) DWI ADC map.

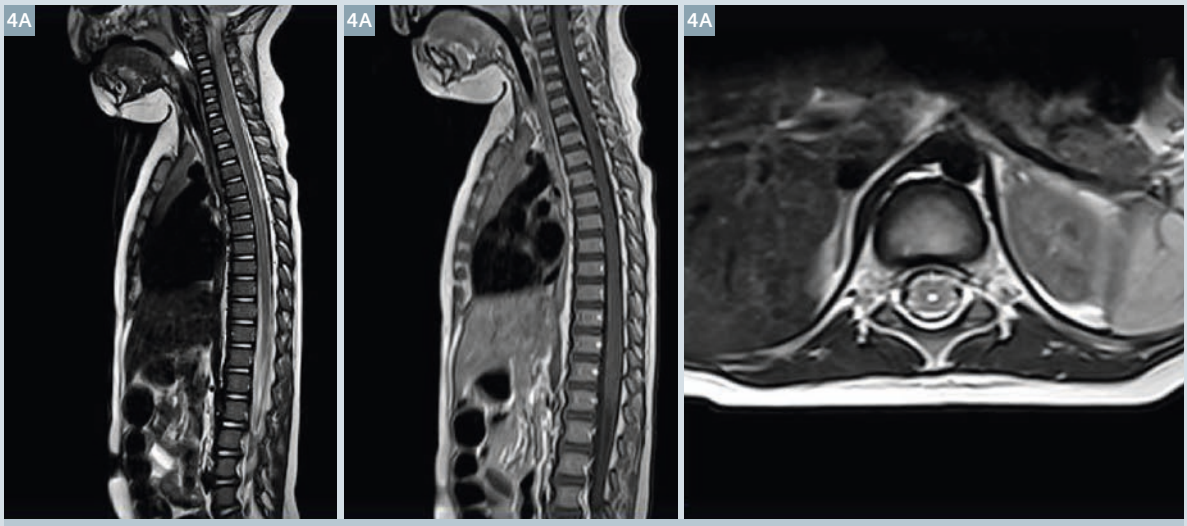

4 **(4A)** T2w TSE sagittal, voxel 0.9 x 0.8 x 2 mm, TA: 2 min 58 sec.
(4B) T1w TSE sagittal, voxel 1 x 0.9 x 2 mm, TA: 3 min 42 sec.
(4C) T2w TSE transversal, voxel 0.8 x 0.6 x 3 mm, TA: 3 min 10 sec

Case 3

A 2-week-old infant[1] with increased head circumference with suspicion of hydrocephalus. The patient's weight is approximately 4.8 kg. Imaging was performed on the 1.5T MAGNETOM Aera with the Pediatric 16, as a feed and wrap procedure. The report indicated that this infant might have BESS (benign enlargement of the subarachnoid spaces in infancy).

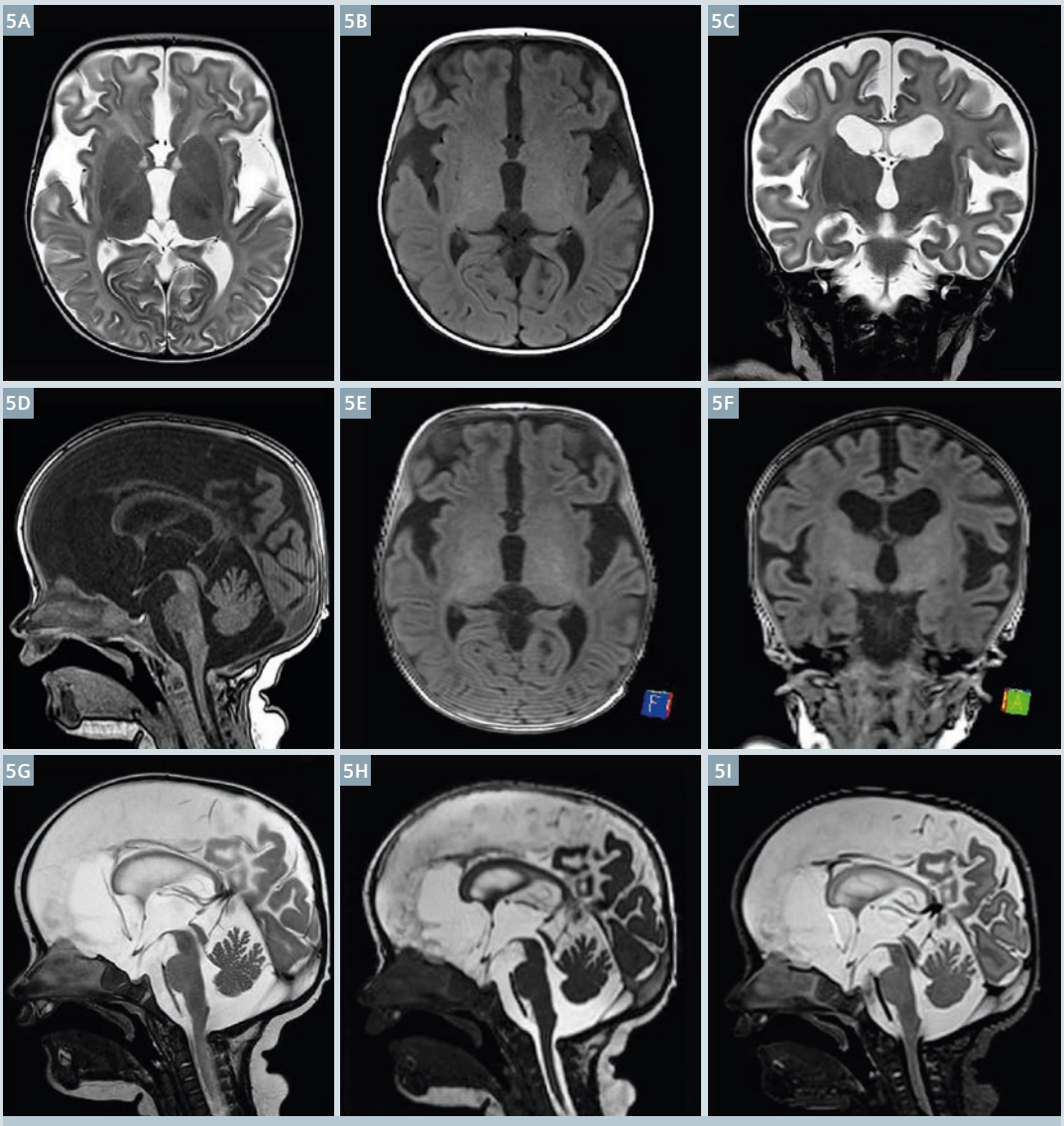

5 **(5A)** T2w TSE transversal, voxel 0.4 x 0.4 x 4 mm, TA: 4 min 32 sec.
(5B) T1w TSE transversal, voxel 0.7 x 0.7 x 4 mm, TA: 3 min 48 sec.
(5C) T2w TSE coronal, voxel 0.4 x 0.4 x 4 mm, TA: 4 min 32 sec.
(5D) T1w 3D MPRAGE, voxel 1 x 1 x 1 mm, TA: 4 min 23 sec.
(5E) T1w 3D MPRAGE 1 mm transversal MPR.
(5F) T1w 3D MPRAGE 1 mm coronal MPR.
(5G) T2w TSE sagittal, voxel 0.5 x 0.4 x 3 mm, TA: 4 min 19 sec.
(5H) CISS sagittal, voxel 0.9 x 0.9 x 0.7 mm, TA: 4 min 8 sec.
(5I) T2w 3D SPACE, voxel 1 x 1 x 1 mm, TA: 4 min 3 sec.

Case 4

2-year-old-child[1] with neuroblastoma of the neck. The patient has been imaged previously with both ultrasound and MR, but has not yet been treated. The patient's weight was approximately 6.8 kg. Imaging was performed on a 3T MAGNETOM Skyra with the Pediatric 16 in combination with Spine 32. The examination was performed under general anesthesia. The report indicated that central parts of the tumor show less contrast-enhancement compared to an earlier MRI exam, and tumor measurements remain the same.

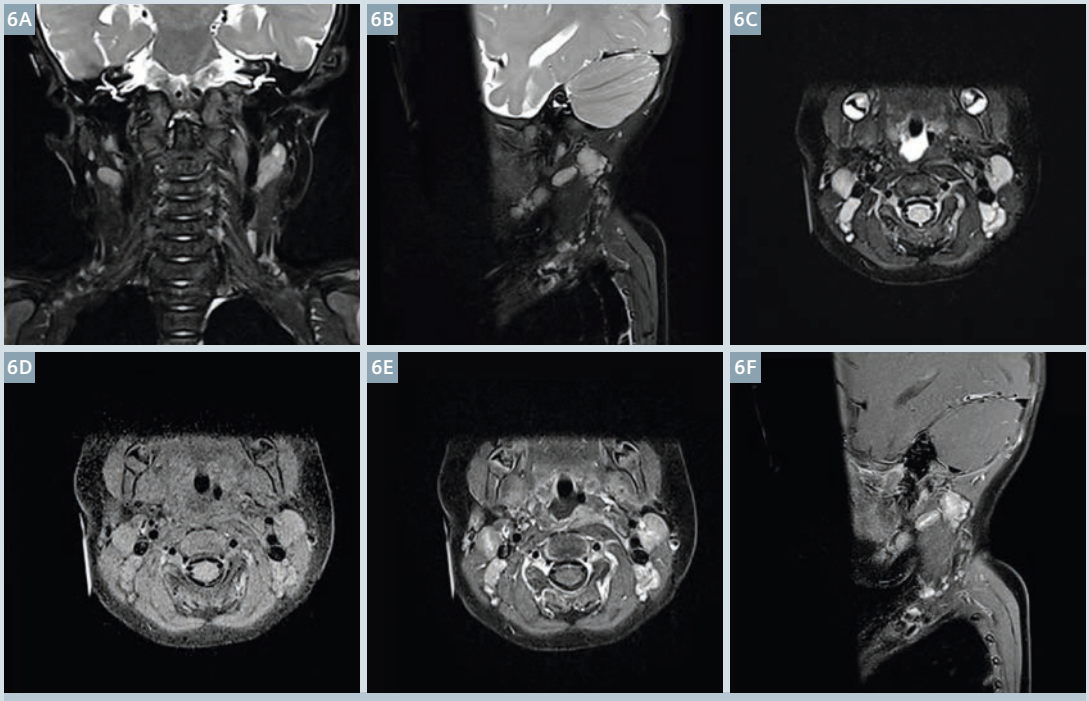

6 **(6A)** T2w TSE Dixon water only, voxel 0.7 x 0.7 x 2.5 mm, TA: 3 min 6 sec.
(6B) T2w TSE Dixon water only, voxel 0.7 x 0.7 x 2.5 mm, TA: 3 min 9 sec.
(6C) T2w TSE Dixon water only, voxel 0.7 x 0.7 x 2.5 mm, TA: 3 min 9 sec.
(6D) T1w TSE Dixon water only, voxel 0.5 x 0.5 x 2.5 mm, TA: 4 min 40 sec precontrast.
(6E) T1w TSE Dixon water only, voxel 0.5 x 0.5 x 2.5 mm, TA: 4 min 40 sec postcontrast.
(6F) T1w TSE Dixon water only, voxel 0.5 x 0.5 x 2.5 mm, TA: 4 min 23 sec postcontrast.

Conclusion

If your site does many pediatric cases, I can definitely recommend this coil. For the head imaging of neonates and small children, the size of the coil provides higher signal-to-noise ratio (SNR) which allows us to achieve better imaging in short scan times. After we started using this coil, we had many more successful feed and wrap exams thanks to the cradle itself. Given the complexity and sensitivity of an MR examination for small infants and children, it makes clinical sense to use a coil that is dedicated to their care. With the significant number of such exams that we perform at our site, the workflow benefits are, for us, innumerous.

Acknowledgements

I would like to thank my good friend and MR mentor Rolf Svendsmark. My fellow colleagues at work, and my friend Lisa Chuah.

Continued on page 90.

References / further reading

1 Siemens Healthineers: https://www.healthcare.siemens.com/magnetic-resonance-imaging/options-and-upgrades/coils/pediatric-16
2 Chavhan, G., et al. Diffusion-weighted Imaging in Pediatric Body Imaging: Principles, Technique, and Emerging Applications. Radiographics 2014; 34:E73-E88.
3 Verschuuren, S., et al. Susceptibility-Weighted Imaging of the Pediatric Brain. AJR 2012;198:W440-W449.
4 Mitchell, C., et al. An Approach to Pediatric Liver MRI. AJR 2011; 196:W519-W526.
5 Panigrahy, A., et al. Basic Principles and Concepts Underlaying Recent Advances In MRI of the Developing Brain. Semin Perinatol. 2010 Feb;32(1):3-19.
6 Tong, K.A., et al. Susceptibility- Weighted MR Imaging: A Review of Clinical Applications in Children. AJR 2008.

Case 5

A 3-week-old infant[1] with Trisomy 21 with a focal lesion seen on the left liver lobe with ultrasound and suspicion of malignancy. The patient's weight was approximately 5 kg. The examination was performed on a 1.5T MAGNETOM Aera with the Spine 32 in combination with the Flex 4 Small. The cradle of the Pediatric 16 coil was used for the preparation, transport and positioning of the patient for imaging. The examination was performed as a feed and wrap procedure. The report indicated the presence of a hypervascular tumor in the left liver lobe that could be a hemangioma.

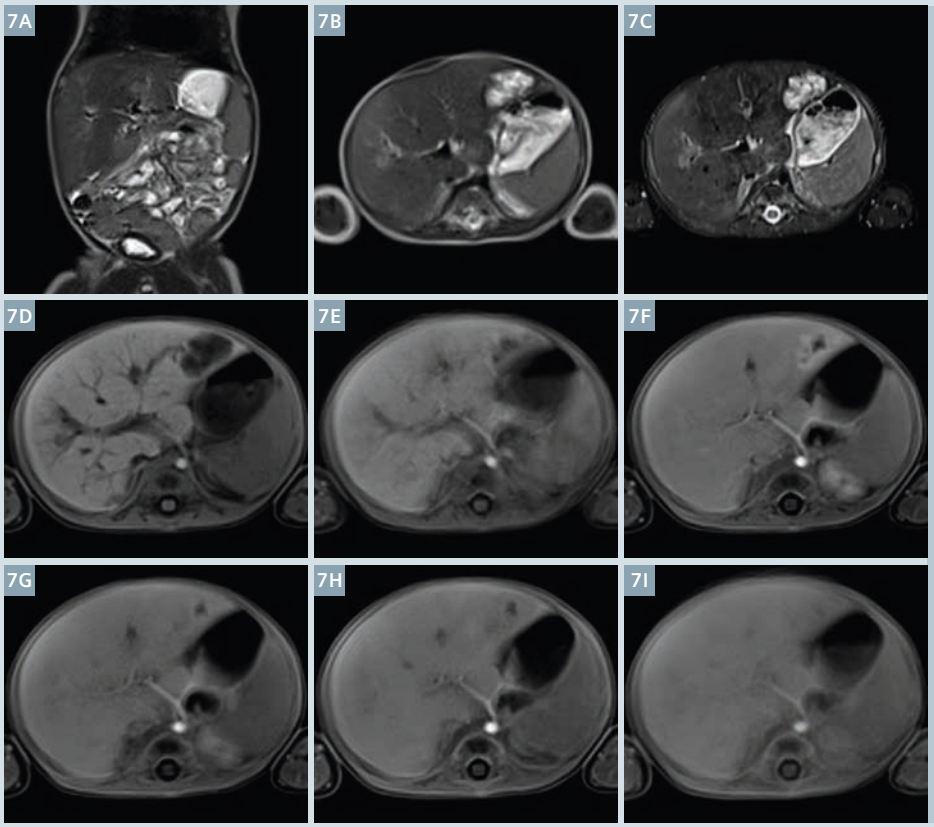

7 **(7A)** T2w HASTE coronal respiratory triggering, voxel 1.3 x 1.3 x 3.5 mm, TA: 44 sec.

(7B) T2w HASTE transversal respiratory triggering, voxel 1.3 x 1.3 x 3.5 mm, TA: 58 sec.

(7C) T2w 3D SPACE with SPAIR fatsat and respiratory triggering, voxel 1 x 1 x 1 mm, TA: approx. 5 min 20 sec.

(7D) T1w StarVIBE precontrast, voxel 1 x 1 x 3 mm, TA: 2 min 20 sec.

(7E-I) Multiple T1w StarVIBE images captured continuously after injection of contrast medium.

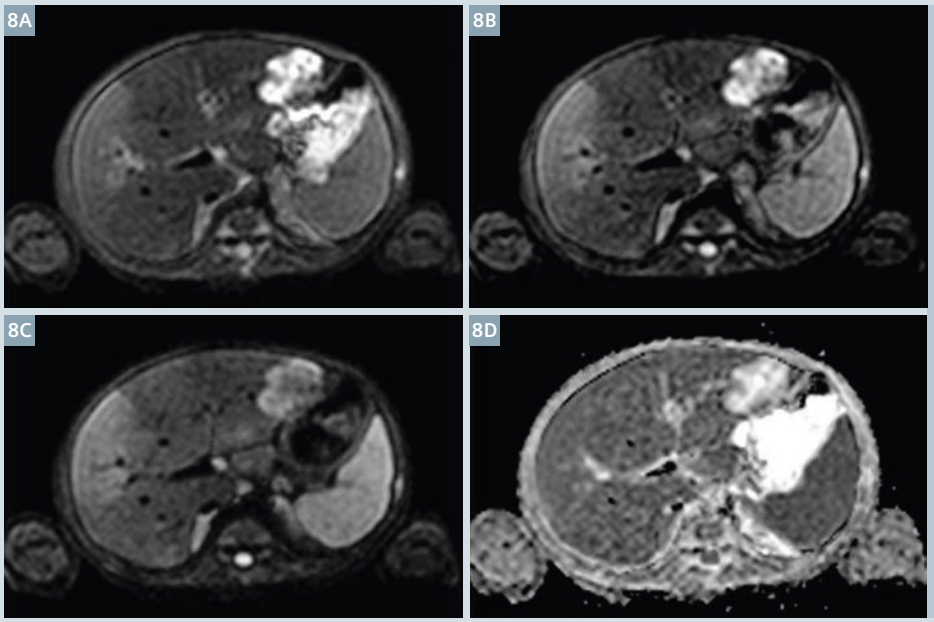

8 DWI free-breathing

(8A) b50

(8B) b400

(8C) b800

(8D) ADC map

voxel 2 x 2 x 3 mm, TA: 3 min.

Case 6

A 2-year-old child[1] with congenital heart disease. The patient has DORV (double outlet right ventricle) and TGA (transposition of the great arteries). The patient was referred with the question of possible hypertrophy and for pre-operative imaging. The patient's weight was approximately 10 kg. The examination was performed on a 1.5T MAGNETOM Aera with the Spine 32 in combination with the Flex 4 Small. The cradle of the Pediatric 16 coil was used for the preparation, transport and positioning of the patient for imaging. The examination was performed under general anesthesia. The report confirmed the known clinical conditions with no change to anatomy. No hypertrophy was found.

[1] MR scanning has not been established as safe for imaging fetuses and infants under two years of age. The responsible physician must evaluate the benefit of the MRI examination over other imaging procedures.

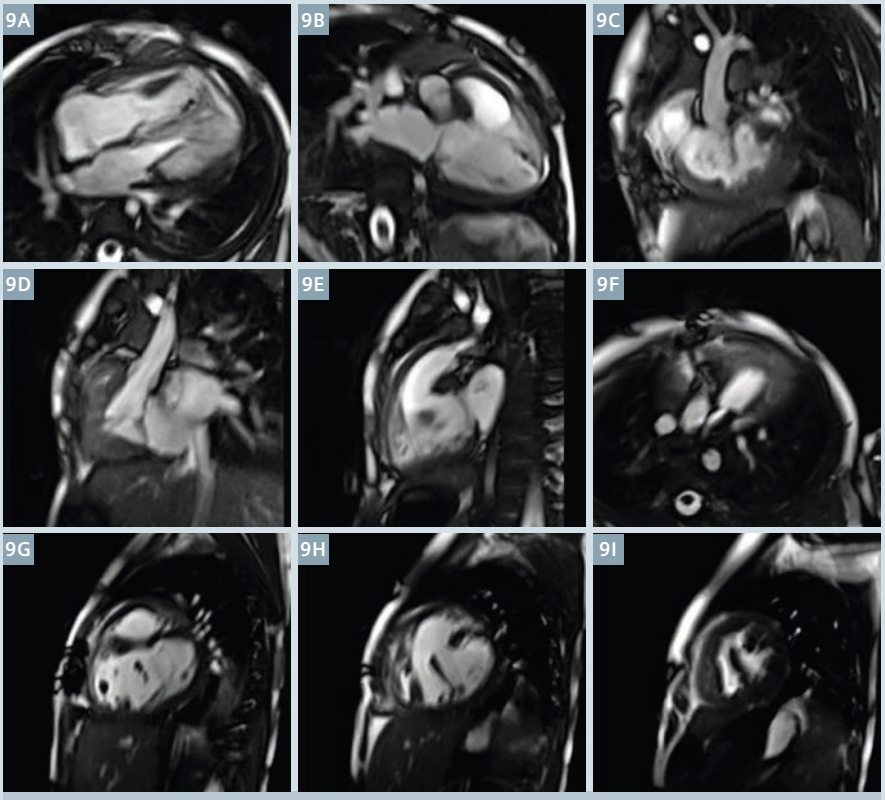

9 All images are CINE TrueFISP done as free-breathing, voxel 1.2 x 1 x 5 mm, TA: 30 sec.

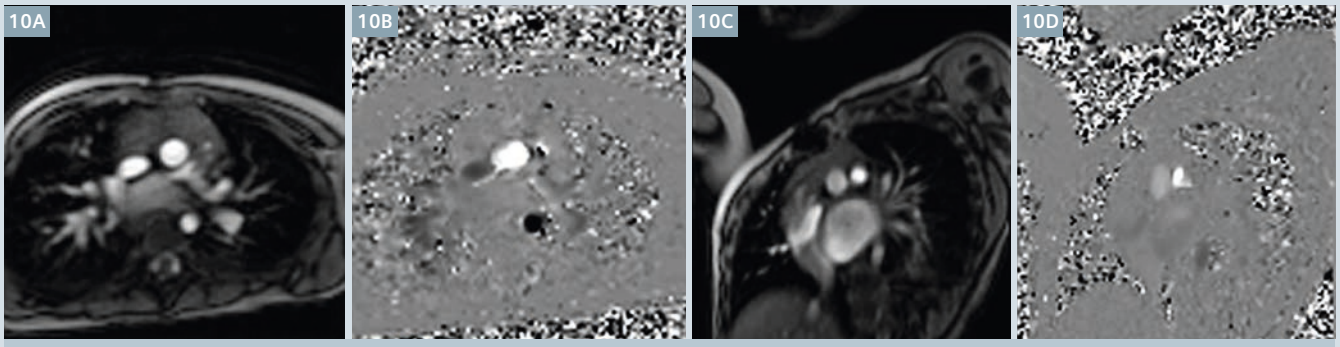

10 **(10A, B)** Flow aorta free-breathing (magnitude and phase images) VENC 120 cm/sec, voxel 1.7 x 1.5 x 5 mm, TA: 40 sec.
(10C, D) Flow pulmonary free-breathing (magnitude and phase images) VENC 400 cm/sec, voxel 1.7 x 1.5 x 5 mm, TA: 40 sec.

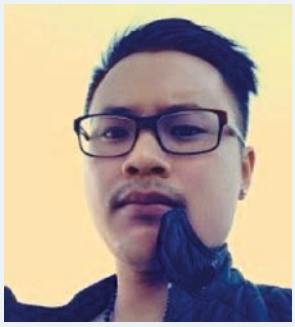

Contact

Bac Nguyen, RT (R) (MR)
Senior MR Radiographer
Oslo University Hospital, Rikshospitalet
Sognsvannsveien 20
0372 Oslo, Norway
Phone: +47 97702111
og_23@hotmail.com

FREEZEit StarVIBE: Freezing the Moving Head and Neck at a Sub-millimetric Scale

Marco Ravanelli; Davide Farina; Roberto Maroldi

Università degli Studi di Brescia, Radiologia 2, Spedali Civili Brescia, Italy

Introduction

3D sub-millimetric imaging is crucial for assessing complex anatomy and fine structures in the head and neck. That is why postcontrast 3D fat-saturated VIBE with isotropic spatial resolution of 0.5-0.8 mm has been included in all our Department's MRI protocols for head and neck lesions for around 15 years already. However, motion due to swallowing and breathing affects a high number of head and neck MR studies, and VIBE sequences are particularly prone to motion artifacts due to their long acquisition time and the underlying cartesian *k*-space filling scheme.

FREEZEit technology

FREEZEit with the StarVIBE sequence has been recently introduced by Siemens with the aim of reducing motion artifacts without sacrificing sub-millimetric isotropic resolution. The sequence employs an inplane stack-of-stars technique to reduce the effects of motion during phase-encoding. This has the added advantage that the center of *k*-space is sampled with every line, providing excellent contrast-agent sensitivity in contrast-enhanced scans. Our preliminary experience with FREEZEit in head and neck imaging demonstrates the strengths and clinical impact of this technique in selected patients.

Clinical impact

In Figure 1, the oral floor of a volunteer instructed to swallow every 20 seconds has been imaged with both conventional VIBE and StarVIBE. StarVIBE dramatically reduces motion artifacts, whilst key anatomic structures such as mandible, lingual septum, sub-lingual spaces are clearly better depicted and circumscribed. Furthermore, fat saturation is improved by reducing motion artifacts. Compared to conventional VIBE, the signal-to-noise ratio (SNR) is slightly reduced, which has been counterbalanced by using a lower matrix, slightly thicker slices and lower slice resolution, a parameter affecting the quality of multiplanar reconstructions (Table 1). An alternative strategy might be to increase the number of spikes, resulting in a longer acquisition time but uncompromised SNR.

This is why conventional cartesian VIBE is still used in our institution as the standard approach for cooperative patients. In our clinical experience of dealing with uncooperative patients, StarVIBE was effective in reducing

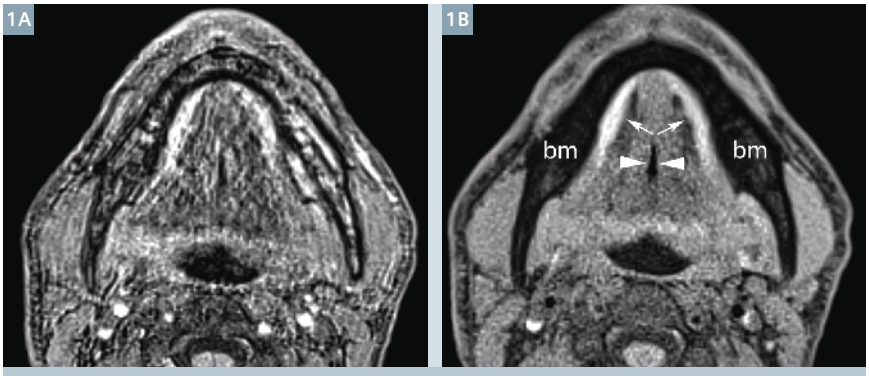

1 Conventional cartesian VIBE **(1A)** and StarVIBE **(1B)** in comparison in a moving volunteer. In the StarVIBE image, key structures of the oral cavity are well depicted despite movement: lingual septum (opposite arrowheads), extrinsic muscles, sublingual spaces (small arrows), mandible with optimal suppression of fatty bone marrow (bm). The same structures are blurred and not assessable with a sufficient diagnostic quality in the conventional VIBE image.

	Oral cavity		Larynx (surface coils)	
	StarVIBE	conventional VIBE	StarVIBE	conventional VIBE
FOV (mm)	205 x 205	270 x 186	190 x 190	190 x 154
thickness (mm)	0.8	0.7	0.7	0.6
in-plane resolution	0.8 x 0.8	0.7 x 0.7	0.74 x 0.74	0.6 x 0.6
matrix	256 x 256	384 x 384	256 x 256	320 x 320
slice resolution	50%	72%	65%	50%
slices	176	192	88	112
phase partial Fourier	off	6/8	off	6/8
slice partial Fourier	5/8	7/8	5/8	7/8

Table 1: Sequence parameters

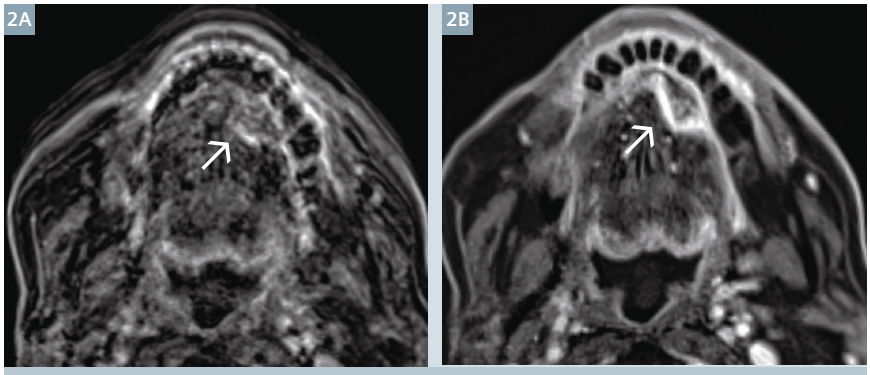

2 Conventional cartesian VIBE **(2A)** and StarVIBE **(2B)** in a patient followed for previously treated carcinoma of the right cheek. StarVIBE clearly depicted a metachronous lesion in the left anterior oral floor, which might have been missed with conventional VIBE due to motion artefact.

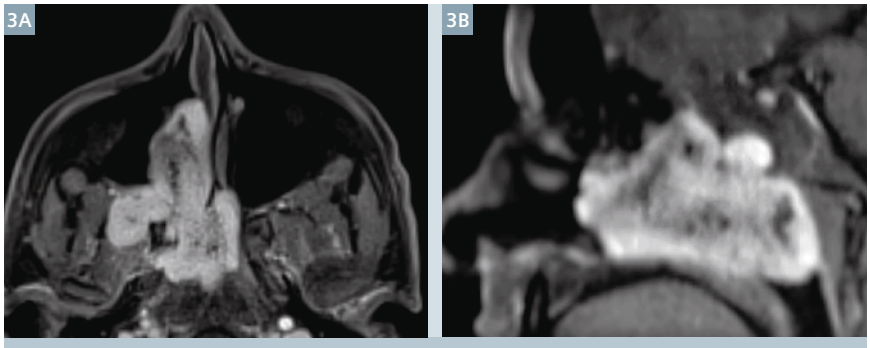

3 StarVIBE in a young uncooperative patient[1] with juvenile angiofibroma. The sequence has been acquired on axial plane and reconstructed on sagittal plane. A lack of quality in sagittal reconstruction is visible compared to axial images due to low spatial resolution along the slice selection direction (slice resolution 50%). However, both native and reconstructed images are free from motion artefacts. StarVIBE was the unique option for volumetric sequence to be acquired in such a patient.

motion artifacts in the oral cavity. A striking example is reported in Figure 2: A tumor of the anterior left oral floor was incidentally found with StarVIBE during a follow-up study for a different primary head and neck cancer. As shown in the example it is evident how the lesion conspicuity is improved with StarVIBE compared to conventional VIBE due to the substantial reduction of motion artifacts.

In the sinonasal tract and the skull base, motion artifacts are usually fewer than in anatomical areas closer to the pharynx and larynx, and therefore conventional VIBE is usually effective. However, in very uncooperative patients, StarVIBE represents the unique volumetric sequence to produce images with sufficient diagnostic quality, as in a young patient[1] affected by juvenile angiofibroma and post-neonatal ischemic encephalopathy (Fig. 3).

Moving down from the skull base into the infrahyoid neck, the larynx is one of the regions which benefits the most from the use of StarVIBE. It is a subtle anatomical area which is subject to breathing and swallowing movements but ideally should be

[1] MR scanning has not been established as safe for imaging fetuses and infants less than two years of age. The responsible physician must evaluate the benefits of the MR examination compared to those of other imaging procedures.

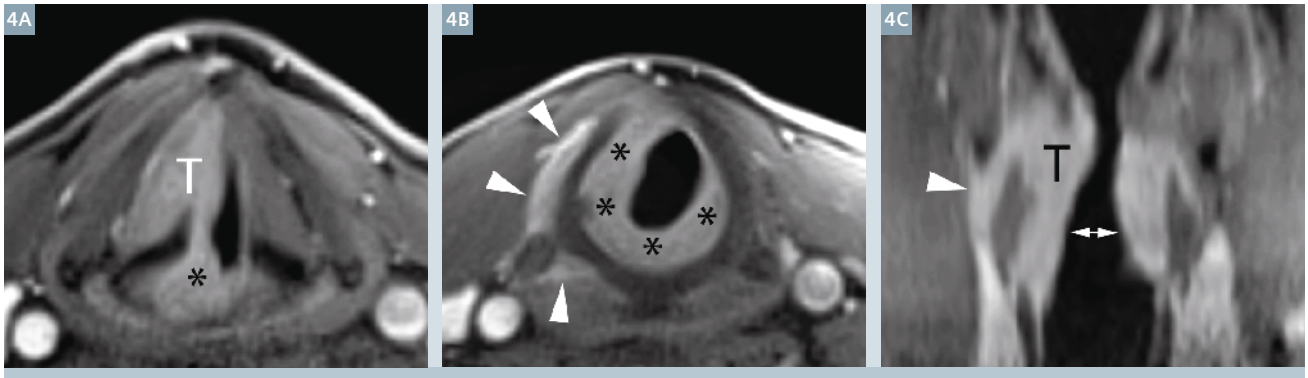

4 StarVIBE with surface coils in an uncooperative patient with T4a glottic-subglottic cancer. The sequence has been acquired on axial plane. Tumor (T) extends to posterior commissure (asterisk in **4A**) surrounding right arytenoid cartilage, Tumor circumferentially infiltrates subglottic region (asterisks in **4B**, opposite small arrows in the coronal reconstruction) and extends outside the larynx through the right inferior paraglottic space (arrowhead on **4C**) infiltrating lateral and posterior cricoarytenoid muscles (arowheads in **4B**).

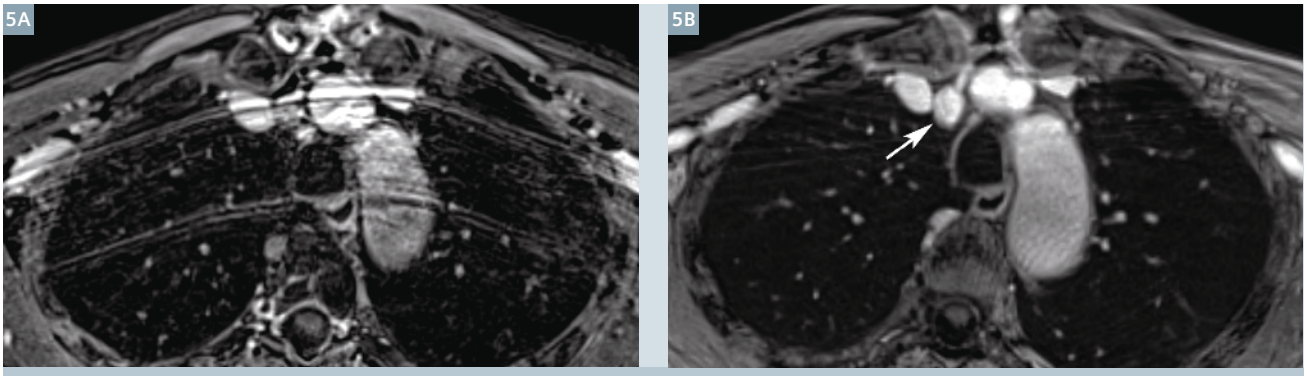

5 Conventional cartesian VIBE **(5A)** and StarVIBE **(5B)** in a patient with recurrent thyroid cancer. On the conventional VIBE image, breathing artefacts make a pathological lymph node in the upper mediastinum (arrow) not easily visible. Artifacts are almost completely suppressed with StarVIBE and the same lesion is clearly visible.

imaged with very high spatial resolution. We therefore apply small loop surface coils to image the larynx and hypopharynx. In this region and with these coils, StarVIBE has enough SNR to increase spatial resolution compared to e.g. the oral cavity, where we reduce the field-of-view (FOV) and slice thickness and increase the resolution. With the introduction of StarVIBE we are now able to image this particular region with sufficient suppression of motion artifacts while gaining excellent SNR to apply very high spatial resolution. For this reason, in our experience StarVIBE is not only indicated in uncooperative patients but provides some advantages also in compliant patients. Therefore, StarVIBE is replacing conventional cartesian VIBE in our standard imaging protocol for imaging of the larynx and hypopharynx (Fig. 4). Furthermore, given the relatively high slice thickness, which negatively impacts 3D reconstruction capabilities, we typically acquire a second StarVIBE dataset in coronal or sagittal orientation, when postcontrast sections along these planes are clinically indicated.

Moving further down to the lower limit of the neck, StarVIBE was very effective in imaging superior mediastinal lymphadenopathies from a recurrent Tx cancer (Fig. 5), reducing breathing artifacts at the pulmonary apices.

Conclusion

StarVIBE is a helpful tool in uncooperative head and neck patients, especially when oral cavity and infrahyoid neck are studied. In compliant patients, conventional VIBE is generally preferable because of the adoption of a more efficient "SNR per acquisition time" ratio. When studying the larynx with surface coils, the surplus in SNR can be spent to increase respective resolution parameters, obtaining a spatial resolution similar to conventional VIBE, with significantly less motion artifacts. As we have demonstrated in this case series, StarVIBE can help to detect pathologies which might be mimicked in conventional scans due to severe artifacts and hence is considered to provide additional value to our daily clinical practice.

Contact

Marco Ravanelli
Università degli Studi di Brescia
Radiologia 2
Spedali Civili Brescia
Italy
Phone: +39 3270877836
marcoravanelli@hotmail.it

New Protocol for the MR Imaging of Pituitary Adenomas. Multiphase, Dynamic and Volumetric Imaging on MAGNETOM Skyra

The Importance of StarVIBE and CAIPIRINHA Sequences

Denis Gardeur, M.D.

Centre RMX, Paris, France

Introduction

The detection of pituitary microadenomas can be a diagnostic challenge even with MRI. Higher spatial resolution enabled by higher field strengths (3T) has been reported to improve the detection of small adenomas, especially those known to be most difficult to detect, for example, the adrenocorticotropic hormone (ACTH) and growth hormone (GH) producing pituitary adenomas. Stobo et al. reported a sensitivity improvement from 54% to 85% when going from 1.5T to 3T [1]. Dynamic contrast-enhanced (DCE) MRI has also been shown to improve diagnostic performance [2, 3].

Some pituitary microadenomas can be detected without contrast media injection, seen as T2 hyperintensities in the coronal plane. However, many microadenomas are depicted in MRI only after injection of gadolinium due to different pharmacokinetics of contrast enhancement as compared to a healthy pituitary. Microadenomas typically show a delayed peak of enhancement which is often less intense compared to the normal anterior pituitary (90 to 120 ms vs 60 to 80 ms). This makes them appear relatively hypointense in the series of scans performed a few seconds after the injection of gadolinium chelate (see Figure 1 for mean curves of relative enhancement of normal anterior pituitary and microadenomas).

However, not all pituitary microadenomas have the same pharmacokinetics of enhancement. Not all of them are vascularized by the hypophyseal portal system with a delay of interstitial diffusion of contrast medium compared to a normal pituitary gland. Some of them are partially or totally vascularized by pituitary arteries and may enhance earlier than the normal anterior pituitary. Others, conversely, have necrotic or hemorrhagic components which are sometimes predominant and enhance later and less intensively.

1

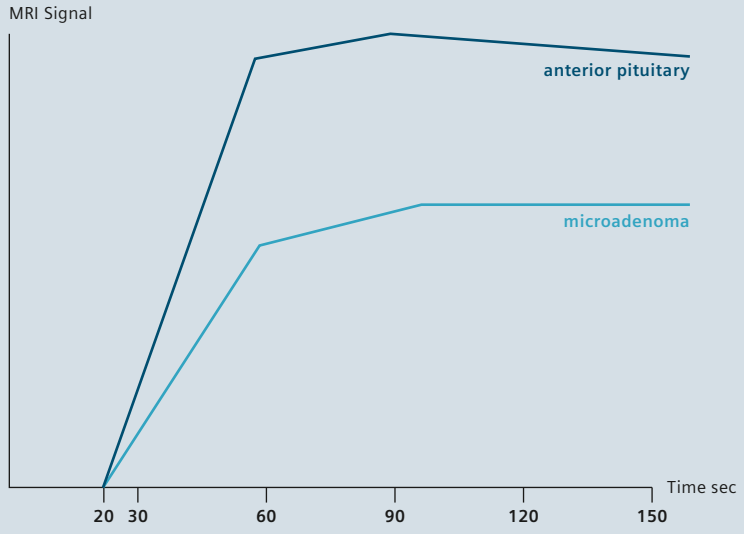

1 Pituitary microadenoma pharmacokinetic.

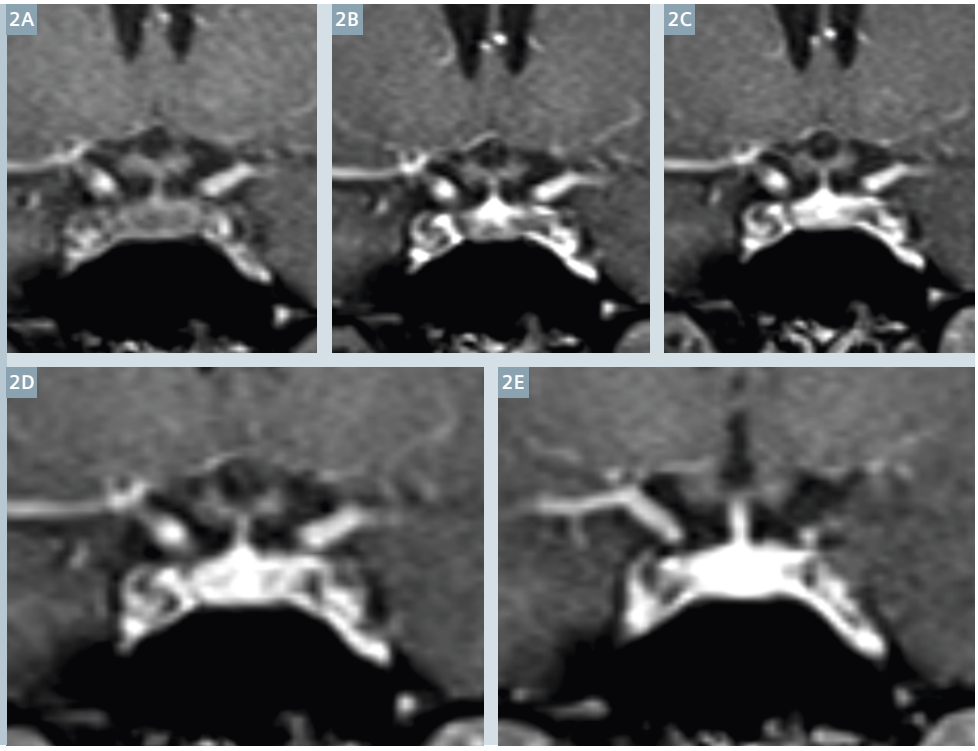

2 Normal pituitary MRI of an 18-year-old woman. Dynamic study after injection of gadolinium chelate. 3D StarVIBE series with 6 repetitions for an overall acquisition time of 150 seconds. First stage **(2A)** arrival of the bolus in the carotid. Next step: arteriolar opacification of the posterior pituitary **(2B)**. Next step: opacification of the pituitary stalk and of the hypophyseal portal venous system **(2C)**. Then, progressive opacification of the anterior pituitary **(2D, E)**.

In the case of a recent hemorrhagic conversion, parametric imaging and subtracted images are useful because these microadenomas might have a T1 hypersignal before the injection and become isointense compared to normal pituitary gland after injection. Some microadenomas could be cystic and difficult to differentiate compared to simple non-tumor cysts of the pars intermedia and Rathke's pouch. Here, again, dynamic studies are useful because simple cysts have no enhancement and a flat kinetic curve. ACTH microadenomas often have an enhancement kinetics that are closer to that of the anterior pituitary and are, therefore, more difficult to detect than prolactin and GH microadenomas [7].

New sequences, such as FREEZEit StarVIBE and CAIPIRINHA VIBE, enable high-resolution, temporal and spatial, 3D dynamic studies [4, 5, 8]. The 3D acquisitions allow multiplanar reformats for better detection of very small (even sub-millimeter) lesions while the high temporal resolution imaging provides better sensitivity to detect pharmacokinetic differences.

We have developed a new MRI examination for pituitary microadenomas on our 3T MAGNETOM Skyra scanner which combines high-resolution volumetric as well as a multiphase, dynamic imaging.

This examination starts with a native series of sagittal T1-weighted, coronal T2-weighted and coronal T1-weighted TSE images with thin slices (1.5 to 2 mm). We then inject contrast with a 'half dose' (7 cc at a rate of 2 cc/sec) which has been shown to be sufficient for the detection of microadenomas. We then run a dynamic series – CAIPIRINHA VIBE – with 12 slices of 2 mm thickness in 6 repetitions with a total acquisition time of 2 min 30 sec. With this acquisition, we see several stages of enhancement:

a) early stage with arterial opacification blush of post pituitary then of pituitary stalk, then

b) intermediate stage with opacification of the hypophyseal portal venous system, then

c) progressive opacification of anterior pituitary supported by the portal system.

Microadenomas usually enhance later (and often less intensely) than other portions of the anterior pituitary and appear relatively hypointense during this early opacification stage of the anterior pituitary. The dynamic multi-slice protocol provides many different parameters: wash-in, wash-out, time-to-peak (TTP), area under the curve (AUC), etc. These parameters improve the detectability of microadenomas, especially wash-in and AUC. In addition, this dynamic multi-slice series provides other diagnostic elements such as hypothalamic-pituitary pharmacokinetics, mass effect on pituitary stalk, diagnostic with other hypervascular intrasellar process, aneurism, intrasellar artery or vein. Some microadenomas could be hypervascular in the arterial phase and are only visible in a dynamic study [6]. In a CT dynamic study, Bonneville *et al.* reported that 34% of microadenomas had a partial or complete early opacification before the portal opacification stage, demonstrating a direct arterial vascularization and not only a pituitary portal as mostly observed in anterior pituitary microadenomas. It seems that such hyper-arterialized microadenomas, opacified at early time, are less often observed in MRI, but they could be visualized by these new 3D dynamic protocols with multiparametric imaging.

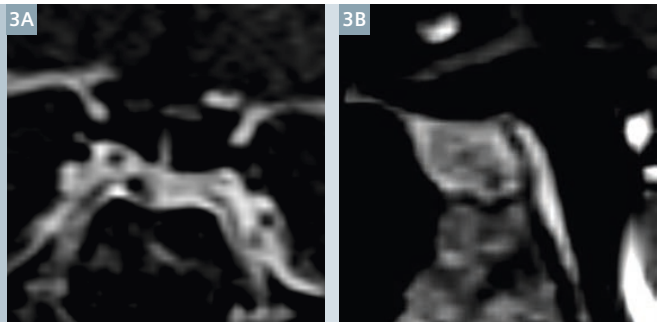

3 Prolactin microadenomas of a 29-year-old woman. Despite its small size of 1.4 mm diameter, this microadenoma – initially isointense on T1 without injection – is marked out in the dynamic VIBE series. It is relatively hypointense compared to the normal anterior pituitary, and the contrast is optimal during the phase of 75 seconds after injection of chelate gadolinium. On a second high-resolution volume series CAIPIRINHA with re-injection, the microadenoma is visualized in the 3 space plans, illustrated by this parasagittal reformation.

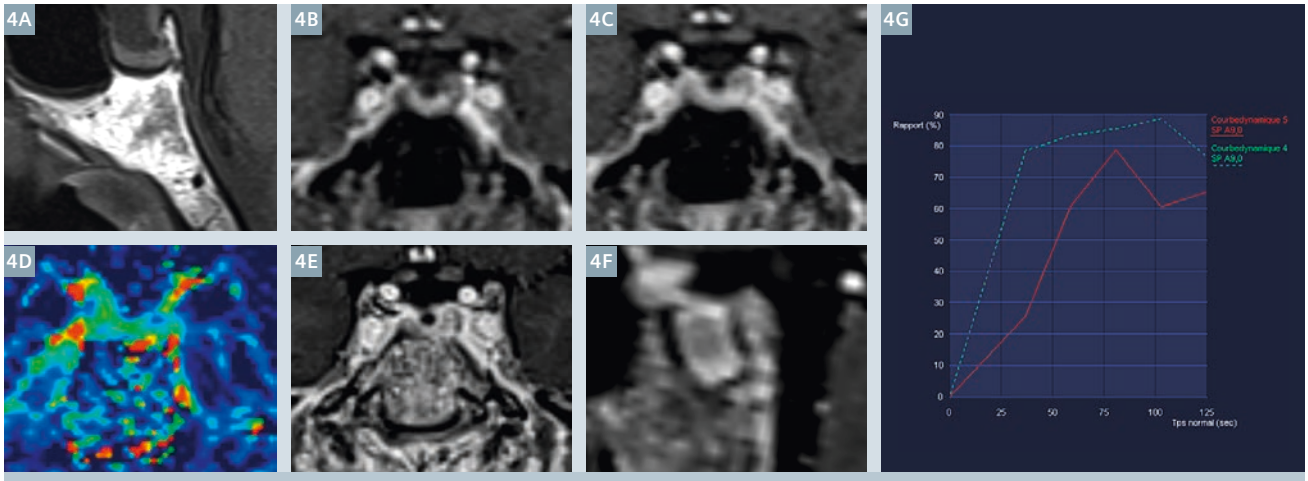

4 Hyperprolactinaemia of a 53-year-old man. Pituitary MRI without injection shows an 'empty' sella turcica with pituitary residue pressed against the sellar floor **(4A)**. VIBE multiphase dynamic series shows a lateralized lesion in left wing pituitary **(4B, C)** with a delay of relative opacification on wash-in parametric imaging **(4D)**. On a CAIPIRINHA volumetric series with re-injection, this left side microadenomas with empty sella turcica is visualized in the 3 space plans **(4E, F)**. Detection of microadenomas on empty sella turcica is difficult with 2D TSE pituitary classic protocols. **(4G)** The comparative analysis of the pharmacokinetic curve of microadenoma opacification (red curve) and of the normal anterior pituitary (green curve) show both the delay and the lowest relative microadenoma opacification. The relative contrast (hypointensity of microadenoma) predominates between 50 and 80 seconds following the injection of contrast medium.

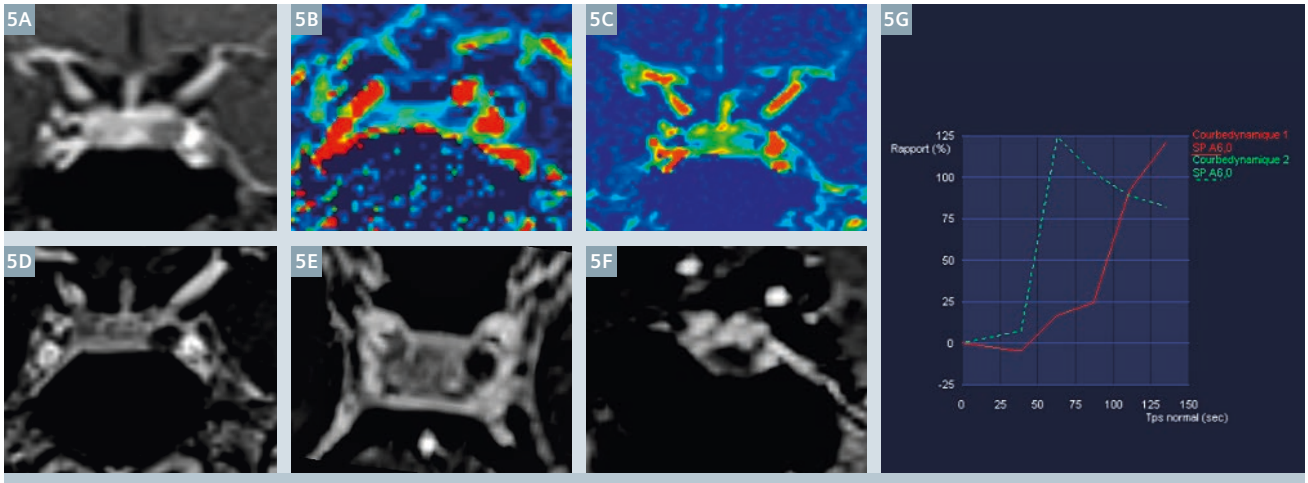

5 Prolactin microadenomas of a 57-year-old woman. Dynamic MRI StarVIBE. Opacification stage of the anterior pituitary **(5A)**, the microadenoma is hypointense compared to the rest of the anterior pituitary. Thanks to the 6 stages of this dynamic series, parametric imaging can be visualized, wash-in **(5B)** and time-to-peak **(5C)** showing the lesion of the left side portion of the pituitary gland and its relative opacification delay. In a second volume series **(5D-F)** CAIPIRINHA enables microadenomas reformations in the 3 space plans. The comparative analysis of the pharmacokinetic curve of microadenoma opacification (red curve) and of the normal anterior pituitary (green curve) show both the delay and the lowest initial microadenoma opacification. The relative contrast (hypointensity of microadenoma) predominates between 60 and 90 seconds following the injection of contrast medium **(5G)**.

However, the spatial resolution in these dynamic studies (which favors temporal resolution and series multiplication) is lower than on the conventional series (even with these new fast 3D sequences). We find it clinically useful to continue with one (or several) high-resolution scans, but there is a risk of making these scans at a pharmacokinetic stage when progressive opacification of adenoma meets or even exceeds that of the healthy pituitary, which decreases the detectability of microadenomas.

The new FREEZEit StarVIBE sequence has an advantage over the T1 TSE sequence as it enables a high-resolution submillimetric and isotropic volume acquisition in one acquisition (48 sections of 0.8 mm in 3 min 50 sec in our protocol) together with the ability to perform 3D multiplanar reformats. As dynamic imaging has been performed with a half dose, we inject a further half dose at a lower rate (0.5 cc/sec) for a total injected dose of 15 cc. This biphasic protocol enables us to make a volume acquisition with submillimeter slices while maintaining the best relative pharmacokinetic detectability of adenomas vs healthy anterior pituitary. Thanks to this high spatial resolution volume acquisition, (sub)millimeter microadenomas – relatively hypointense – can be detected and visualized in 3D space. Even in the most difficult diagnostic circumstances, such as microadenomas on empty sella turcica, we are able to better detect microadenomas.

In conclusion, this protocol combines the advantages of dynamic and anatomic studies in high resolution while using a standard gadolinium injection dose and in an exploration time substantially similar to the one of a classic protocol (with 2D TSE series). The combination of images 3D dynamic studies with high spatial and temporal resolution improves the visualization of microadenomas and contributes to better differential diagnostics, which in turn optimizes the diagnostic sensitivity and specificity of MRI for pituitary tumors.

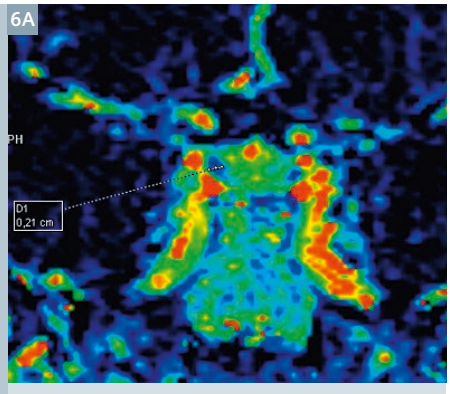

6 Prolactin microadenoma of a 27-year-old woman. It can only be visualized with a dynamic study and mainly with parametric imaging wash-in due to its delay in opacification compared to a healthy pituitary gland. It is visible at the right side next to the cavernous sinus and has a size of 2 mm. On the same coronal wash-in image the early vascularization of the hypophyseal portal system and of the pituitary stalk are visualized, shown red in the superomedian part of the pituitary gland. A comparative study of enhancement kinetics between the microadenoma (red curve) and the lateral left part of the anterior pituitary (green curve) shows the delay in opacification of the microadenoma. But in the second minute after the injection, it becomes isointense and therefore it is impossible to detect without re-injecting contrast medium.

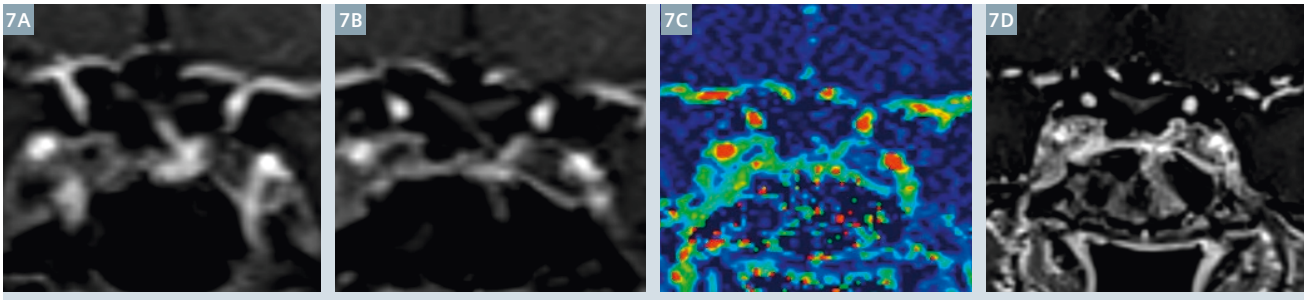

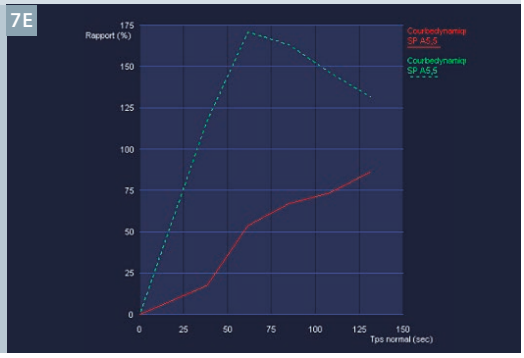

7 40-year-old woman operated 6 years ago for an ACTH pituitary adenoma and referred 2 years later to focal radiotherapy due to an invasive recurrence. Follow-up non-contrast pituitary MRI shows partial empty sella and inhomogeneous tissue adjacent to the left cavernous sinus. Dynamic contrast-enhanced MRI shows pituitary stalk deviation to the left and pituitary portal blush. The pituitary adenoma recurrence is well delineated between the portal blush and the left cavernous sinus. A delayed series **(7D)** demonstrates progressive enhancement of the adenoma. Pharmacokinetic curves **(7E)** demonstrate delayed but progressive enhancement of the adenoma. So it is not a post radiotherapy cyst or radiation necrosis (with a plateau curve) but a solid recurrence.

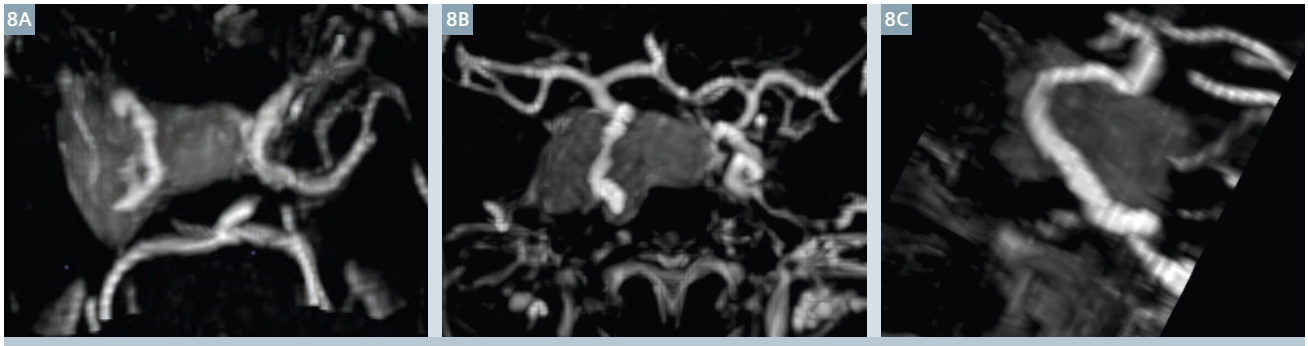

8 Invasive pituitary macroadenoma which infiltrates widely the right cavernous sinus. The dynamic MRI after injection of gadolinium does not aim at detecting the voluminous adenoma, but at characterizing its kinetics of opacification (similar to the normal pituitary gland) and at detecting the areas of hyperperfusion or necrosis. The main interest is the possibility of multiplanar reconstruction of the adenoma thanks to the 3D acquisition and mostly to carry out an angioMRI analysis of the stretched, infiltrated and irregular carotid artery as the adenoma covers completely the endo-cavernous carotid.

Contact

Denis Gardeur, M.D.
Centre RMX
80 Avenue F Faure
75015 Paris
France
dgimag@aol.com

References

1 Stobo DB et al. Initial experience of 3T versus conventional field strength MRI of small functioning pituitary tumors. Clin Endocrinology. 2011. 75:673-7.
2 Rand T et al. Evaluation of pituitary microadenomas with dynamic MRI. EUR J Radiol 2002 41:131-5.
3 Sakamoto Y et al. Normal and abnormal pituitary glands: gadopentate-enhanced MR imaging. Radiology 1991. 178:441-5.
4 Rossi Espagnet MC et al. High resolution DCE MRI of the pituitary gland using radial k space acquisition with compressed sending reconstruction. AJNR. 2015. 10.3174:1-6.
5 Fushimi Y et al. 3D dynamic pituitary MRI with CAIPIRINHA.EUR. J Radiology. 2014-83:1900-6.
6 Bonneville JF et al. Pituitary microadenomas: early enhancement with dynamic CT, implications of arterial blood supply and potential importance. Radiology. 1993. 187:857-61.
7 Kim B. Comparison of CAIPIRINHA VIBE, radial VIBE and conventional VIBE sequences for DCE MRI. Magnetic Resonance Imaging. 2016.38:638-644.

For details on Dr. Gardeur's protocols please visit

www.siemens.com/magnetom-world

> Clinical Corner > Protocols

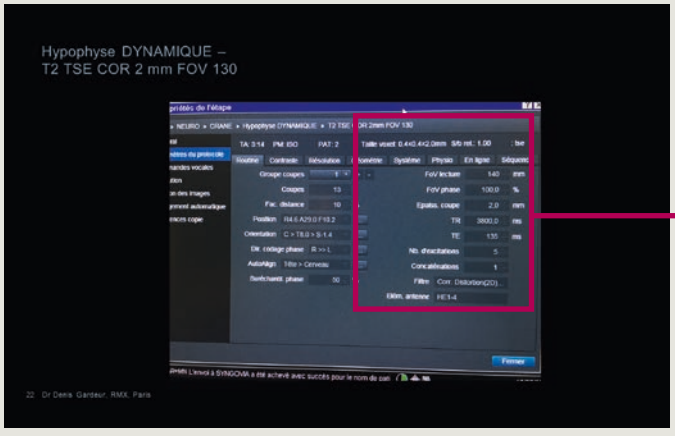

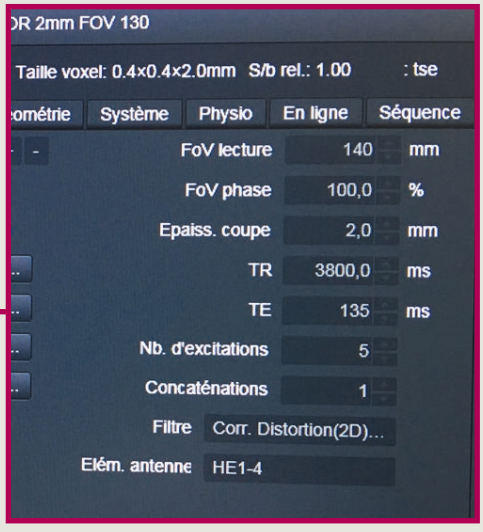

Case Study: Magnetic Resonance Fingerprinting (MRF) Imaging of the Brain

Elisabeth Springer, M.D.; Wolfgang Bogner, Ph.D.; Pavol Szomolanyi, Ph.D.; Siegfried Trattnig, M.D.

MR Center of Excellence (MRCE), Department of Biomedical Imaging and Image-Guided Therapy,
Medical University Vienna, Austria

Introduction

Because of its ability to probe numerous tissue properties, including those reflective of many common disease states, Magnetic Resonance Imaging (MRI) is widely used as a diagnostic tool in medicine. Whenever a patient is referred to MRI, for example due to neurological disorders of unknown origin, a (more or less standardized) set of qualitative images with different contrast is acquired. Each contrast reflects a different 'weighting' of tissues. The radiologist is trained to identify and describe areas which are 'hyperintense' or 'hypointense' compared to surrounding, normal-appearing areas. Reading all contrasts in conjunction and mentally comparing them to typical disease patterns, the radiologist will come to a diagnosis which is potentially accompanied by one or more differential diagnoses. Although successfully practiced around the world every day in thousands of cases, this approach has various disadvantages. Conventional MR imaging does not provide a quantitative indication of the contrast differences which are described, and the absolute signal intensity in the images has no direct meaning or implication for diagnosis. Furthermore, some diseases and early disease states may cause very subtle changes of tissue parameters which may not be reflected in visibly discernable contrast differences.

MR Fingerprinting (MRF)[1] is a new approach for MR data acquisition, post-processing and visualization [1]. Instead of acquiring images with different contrast, signals from different body locations are acquired using a pseudo-randomized acquisition scheme. As a result, each voxel appears to have a unique signal evolution or 'fingerprint' which reflects the multiple tissues and tissue properties present in the respective location. During post-processing, a pattern recognition algorithm matches the fingerprints to a previously acquired dictionary of signal evolutions, providing knowledge about the materials, their properties and concentration.

Finally, the information can be translated into quantitative maps of the magnetic parameters of interest but also into synthetic, 'classically weighted' images.

Theoretically, MRF could be applied in almost all cases where conventional, qualitative MRI is used today, including the imaging of the body stem [2]. In this case study we present two cases of frequent neurologic disorders and their representation in MRF images and maps.

Imaging details

Conventional MR imaging and MRF of the neurocranium was performed using a 1.5T MR scanner (MAGNETOM Aera, Siemens Healthcare, Erlangen, Germany). The MRF sequence prototype was based on a FISP (fast imaging with steady-state precession) acquisition scheme as described in Jiang *et al.* [3], consisting of an initial inversion pulse followed by a rapidly acquired series of 3000 undersampled spiral images with varying TR (14-17 ms) and flip angle (0-75°). Slices with 20% slice gap and 5 mm slice thickness covered the pathological region of interest. The spatial resolution of the acquired images was a 256 x 256 matrix with <1.2 mm isotropic resolution. The scan time requirements for MRF was ~48 sec per acquired slice.

Based on the MRF data, different conventional contrasts were generated. Images were processed by manually placing regions-of-interest (ROIs) in different locations and plotting the derived T1 and T2 values against each other.

Conclusion

As the cases presented here demonstrate, MRF is able to characterize tissues in terms of their quantitative instead of qualitative attributes.

With the prospect of acquiring tissue fingerprints with music-like gradient schemes [4] in the future, MRF may eventually overcome the common patient impression of MRI being a loud and frightening technology.

Acknowledgement

The authors thank Mark Griswold (Case Western Reserve University) and Vikas Gulani (University Hospitals Case Medical Center, Cleveland, OH, USA) for sharing the C2P version of MR Fingerprinting.

[1] WIP, MR Fingerprinting is currently under development and is not for sale in the US and in other countries. Its future availability cannot be ensured.

Case 1

Patient with a Glioblastoma multiforme, WHO grade IV. The patient presented with subjective visual deterioration persisting for one week. The neurologic and ophthalmologic examination showed a complete postchiasmal left hemispheric lesion of the visual pathway.

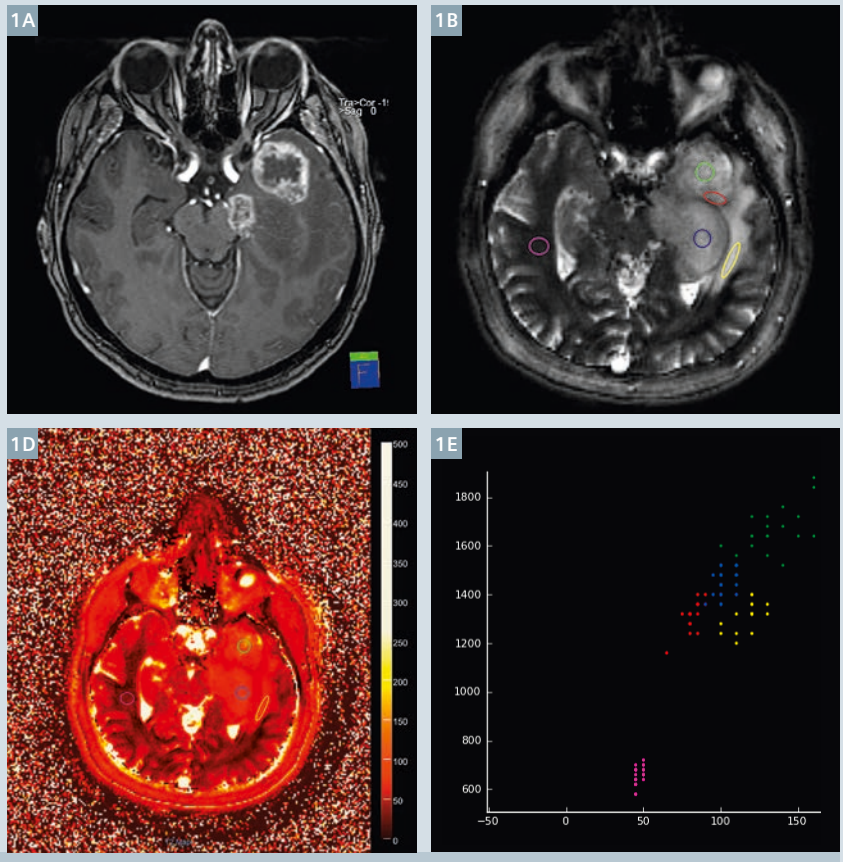

1 **(1A)** Contrast-enhanced T1-weighted MPRAGE images show one central necrotic lesion in the left temporal lobe, with contrast media uptake at its margin. A solid part of the lesion is visible at its dorsal margin. Another equally appearing lesion is located in the left cerebral peduncle. Dorso-laterally adjacent, this part of the tumor migrates into another solid part of the tumor that ranges along the hippocampus towards dorsal. This part shows little contrast media uptake, only in the lateral portion, and no central necrosis. Spectroscopic assessment of the central necrotic lesion (not shown here) revealed Choline / NAA disproportion and a lipid peak, while the more dorso-laterally located lesion also showed Choline / NAA disproportion, but to a lesser extent and no lipid peak. Consequently, in comparison to the central necrotic and strongly enhancing high grade part (Glioblastoma WHO IV) of the tumor, a lower grade part of the tumor has to be considered here. **(1B-D)** Corresponding calculated T2 image, T1 map and T2 map, derived from MRF data. ROIs were placed in the solid part of the tumor (red), the central necrosis (green), the lower grade part of tumor (blue), and in the surrounding edema respectively area of suspected tumor infiltration (yellow), as well as in normal appearing, contralateral white matter (pink). **(1E)** The scatterplot of T1 over T2 shows visible differences between the solid part of the centrally necrotic lesion (red), the central necrosis (green), the lower grade part of the tumor (blue), the surrounding edema / potential infiltration (yellow) and a clear distinction from normal appearing white matter (pink).

Case 2

Patient with low grade glioma (WHO grade I), histologically differential diagnosis included pilocytic astrocytoma (WHO grade I) and ganglioglioma (WHO grade I). The patient presented with a history of repeated headaches and dizziness over the course of the last year and had one singular seizure about six months ago, manifesting with clonic muscle spasms of the left upper extremity spreading to the right upper extremity.

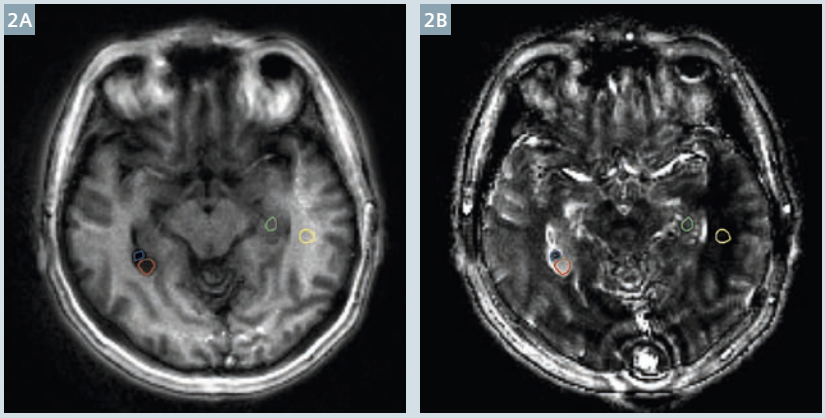

T1-FLAIR (calculated) T2-FLAIR (calculated)

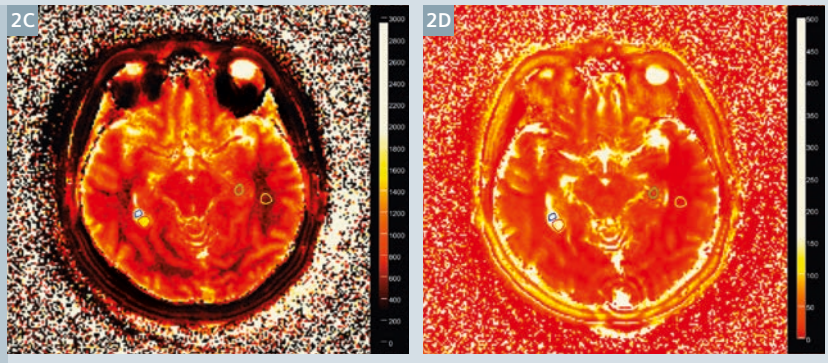

T1 Map T2 Map

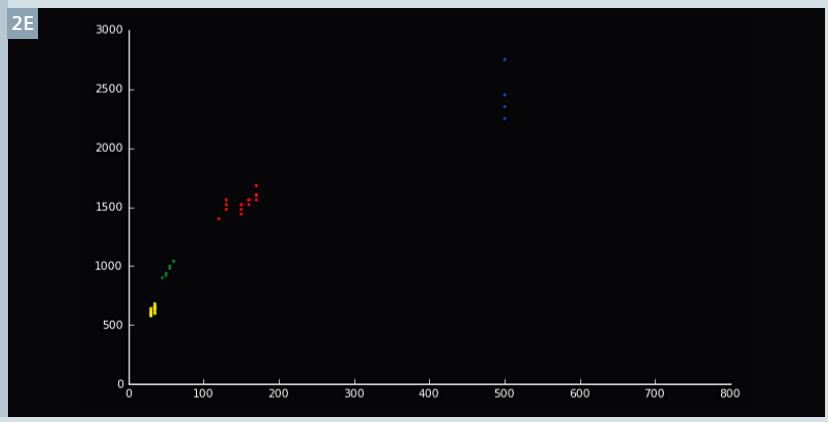

2 **(2A, B)** Calculated T1w and T2w FLAIR images. A lesion in the right temporal lobe located beneath the lateral ventricle is visible. It consists of a dorsal solid part and a rostral cystic part. In contrast-enhanced imaging (not shown here) the solid part showed uptake of contrast media, the cystic part did not. In spectroscopy (not shown here), the solid part of the tumor showed a mildly abnormal choline / NAA concentration and minimal expression of lactate.
(2C-E) ROI placement revealed different characteristics in the scatterplot representation, with the following assignments: solid part of the tumor (red), cystic part of the tumor (blue), normal appearing white matter (yellow) and gray matter (green).

Contact

Professor Siegfried Trattnig, M.D.
Medical University of Vienna
Department of Biomedical Imaging and Image-Guided Therapy
MR Center of Excellence (MRCE),
Lazarettgasse 14
1090 Vienna
Austria
siegfried.trattnig@akhwien.at

References

1 Ma D, Gulani V, Seiberlich N, Liu K, Sunshine JL, Duerk JL, Griswold MA. Magnetic Resonance Fingerprinting. Nature. 2013 Mar 14;495(7440):187-92.
2 Chen Y, Jiang Y, Pahwa S, Ma D, Lu L, Twieg MD, Wright KL, Seiberlich N, Griswold MA, Gulani V. MR Fingerprinting for Rapid Quantitative Abdominal Imaging. Radiology. 2016 Apr;279(1):278-86.
3 Jiang, Y., et al., MR fingerprinting using fast imaging with steady state precession (FISP) with spiral readout. Magn Reson Med, 2015. 74(6):1621-31.
4 Ma D, Pierre EY, Jiang Y, Schluchter MD, Setsompop K, Gulani V, Griswold MA. Music-based magnetic resonance fingerprinting to improve patient comfort during MRI examinations. Magn Reson Med. 2016 Jun;75(6):2303-14. doi: 10.1002/mrm.25818. Epub 2015 Jul 16.

Clinical Neuroimaging at 7T Compared to Lower Field: a Photo Essay

Stephen E. Jones, Ph.D., M.D.[1]; Emmanuel Obusez, M.D.[1]; Sehong Oh, Ph.D.[1]; Irene Wang, Ph.D.[2]; Mark Lowe, Ph.D.[1]

Imaging Institute (1), Epilepsy Center (2), Cleveland Clinic, Cleveland, OH, USA

Introduction

The recent introduction of a clinical 7T human MRI scanner continues the progress of increasing field strength, ever since the invention of MRI. While research is understandably emphasized as the initial application when a new higher field MRI system is commercially introduced, inevitably clinical applications become the majority appliation. Similarly, such 7T scanners as are currently available are used mainly for research. However, with anticipated FDA approval in the next few years, 7T MRI will become clinically available. While the research utility of 7T is already clear, especially in functional brain imaging using BOLD fMRI [1-4], the clinical utility is uncertain at this time.

The main advantage of using higher magentic field is an increased signal from precessing magnetic moments, which scales as the field strength increases [5]. The increased signal improves images in several ways: Images with the same voxel size but higher signal-to-noise ratio (SNR), images with smaller voxels but the same SNR, or images with the same SNR but scanned faster (for example less averaging would be needed). It is likely that the second advantage yielding higher spatial resolution will be the principle clinical advantage of 7T.

The goal of this paper is to illustrate the potential advantages of 7T in clinical neuroimaging, by imaging a variety of neurological diseases at 7T and directly comparing them to lower field imaging (typically 3T) in the same patient.

Amytrophic lateral sclerosis	14
Dementia	1
Epilepsy	66
Multiple Sclerosis	18
Parkinsons disease	2
Traumatic brain injury	22
Tumors (brain)	6
Tumors (eye)	3
Vasculitis	2
Total	134

Sequences	$TR/TE_1/TE_2$ (ms)	FOV (mm^2)	Matrix	Slice thickness (mm)
Coronal FLAIR	8360/111	170	320 x 320	4
Axial FLAIR	8360/117	201	224 x 192	4
Axial 3D GRE	9.8/4.76	256	256 x 256	1
Coronal 3D GRE	11/4.92	230	224 x 256	1.25
Axial MPRAGE	1800/3.12	256	256 x 256	1
SWI	49/40	220	224 x 204	3

Table 1: 1.5T sequence parameters

Sequences	$TR/TE_1/TE_2$ (ms)	FOV (mm^2)	Matrix	Slice thickness (mm)
Coronal FLAIR	8100/115	180	240 x 192	3
Axial FLAIR	8640/128	180	256 x 204	3
Axial 3D GRE	4000/112	180	320 x 320	3
Coronal 3D GRE	10/4.6	256	256 x 256	1
Axial MPRAGE	1900/2.54	256	256 x 256	1
SWI	27/20	210	256 x 256	2.5

Table 2: 3T sequence parameters.

MRI technique

Currently the 7T system[1] is not FDA approved, and this study was approved by our institutional IRB for the strict purpose of comparing imaging features of neuropathology at 7T to imaging features obtained previously at lower field on an FDA approved clinical scanner. Exclusion criteria included implants not validated as safe at 7T, body weight less than 30 kg, inability to lay motionless while in MRI, claustrophobia, and a normal MRI at lower field.

The 7 tesla whole-body MRI system used at Cleveland Clinic is a Siemens MAGNETOM with an Agilent 830AS magnet. For all the studies presented here, a head-only CP transmit/32-channel phased-array receive coil (Nova Medical, Wilmington, MA, USA) was used. Sequences used in the following figures were: FLAIR, MP2RAGE, SWI, and GRE, as well as TSE T2 in the lower field scans. In order to focus on the qualitative features of the differences in imaging results, we list the complete scan protocols here and in individual figures highlight spatial resolution differences between the different field strength images. Although slight variations in clinical scan prescriptions exist across the scanner installations at Cleveland Clinic, the basic scan protocol for each at 1.5T and 3T are shown in Tables 1 and 2, respectively.

For 7T the scan protocols are:

Coronal and transverse 2D FLAIR TSE sequence
- TR/TE = 9000/124 ms
- FOV = 192 x 192 mm^2
- slice number = 45
- slice thickness = 2 mm
- In-plane resolution = 0.75 x 0.75 mm^2
- TI = 2600 ms
- matrix = 256 x 256
- GRAPPA 3
- bandwidth 244 Hz/pixel
- scan time = 3:02 min

Axial and/or sagittal T1-weighted MP2RAGE
- TR/TE = 6000/2.99 ms
- FOV = 240 x 240 mm^2
- slice number = 192
- resolution = 0.75 mm^3 isotropic voxel
- flip angle = 4° and 5°
- TI1/TI2 = 700/2600 ms
- Matrix = 320 x 320 6/8 partial Fourier in k_y and k_z
- GRAPPA 3
- bandwidth 240 Hz/pixel
- scan time = 9:48 min

T2*-weighted GRE
- TR/TE = 2290/17.8 ms
- FOV = 192 x 192 mm^2
- slice number = 60
- slice thickness = 1.5 mm
- In-plane resolution = 0.38 x 0.38 mm^2
- flip angle = 250
- matrix = 512 x 512
- GRAPPA 2
- bandwidth 40 Hz/pixel
- scan time =10:08 min

Transverse 3D SWI sequence
- TR/TE = 23/15 ms
- FOV = 220 x 220 mm^2
- slice number = 144
- resolution = 0.49 x 0.49 x 0.8 mm^3
- flip angle =20°

[1] MAGNETOM 7T is ongoing research. All data shown are acquired using a non-commercial system under institutional review board permission. MAGNETOM 7T is still under development and not commercially available yet. Its future availability cannot be ensured.

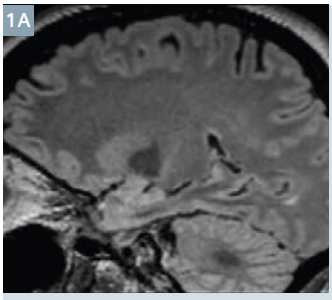

3T 5000/393/1800 [TR/TE/TI]

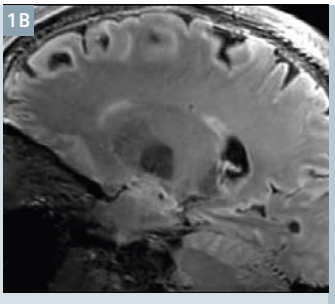

7T 7000/380/2100

1 Example of increased SNR in a FLAIR sequence from a 7T image **(1B)** compared to a 3T image **(1A)** in different patients. For comparison purposes, similar sequences were used that had the same voxel size (1 x 1 x 1 mm). In the flat region of anterior white matter, the SNR was 32.3 for 7T and 16.0 for 3T. While the increased SNR at 7T is apparent as a 'flatter' appearance of the white matter, this may not yield additional clinical benefit for most neurological disease, which would benefit more from using the increased SNR to enable smaller voxels and higher spatial resolution with the same SNR [5, 6].

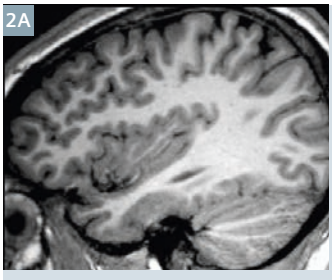

3T 1 x 1 x 1.2 mm
2300/2.98/900

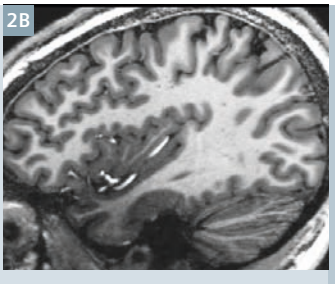

7T 0.75 x 0.75 x 0.75 mm
6000/2.99

2 Example of increased contrast-to-noise ratio (CNR) in a T1-weighted sequence, with 7T MP2RAGE **(2B)** and a 3T MPRAGE **(2A)**. The CNR of signal in white matter to gray matter is 18.3 (7T) and 9.9 (3T). This increased distinction between the gray-white interface is very important in the evaluation of a class of lesions causing epilepsy. In addition, any lesion embedded within white matter that follows gray matter signal characteristics will have increased conspicuity [7, 8].

3 Example of increased in-plane resolution, with 7T MP2RAGE **(3B)** and 3T MPRAGE **(3A)**. The in-plane voxel size is 0.75 x 0.75 mm (7T) and 1.0 x 1.0 mm (3T). Although the decrease in linear size is only 25%, this small change can noticeably improve image quality, as seen in the improved detail of the cerebellar folia. Also contributing to visual improvement at 7T is a thinner slice, being 0.75 mm compared with 1.2 mm for 3T, which provides less volume averaging and thereby sharper images [7-9].

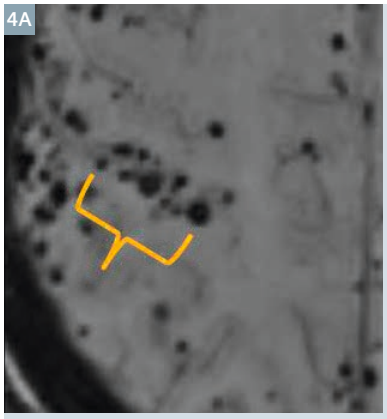

3T SWI 0.82 x 0.82 x 2.5 mm

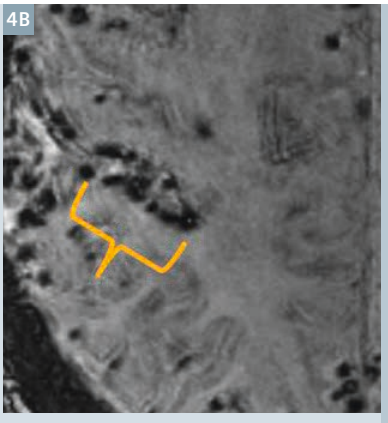

7T SWI 0.49 x 0.49 x 0.80 mm

4 Example of combination of increased spatial resolution and lesion conspicuity, enabling improved colocalization of small lesions on underlying anatomy. While this 64-year-old female already had a known diagnosis of cerebral amyloid angiopathy, manifest with innurable microhemorrhages (CMH) throughout the brain, the high spatial resolution of 7T revealed a strong colocalization of the CMH with the cortical ribbon. At lower field, this association could not be appriciated on the SWI sequence. Similar studies have shown the utility of 7T in the localization of microhemorrhages to the cortex in patients with cebebral amyloid angiopathy [10-12].

3T T2-TSE 0.55 x 0.55 x 4 mm thick

7T T2*-GRE 0.375 x 0.375 x 1.5 mm thick

5 Example of clinical utility in a multiple sclerosis patient. This 23-year-old female has a four-year history of progressive MS, whose diagnosis is not in question. This image examplifies a characteristic of MS well visualized with the high resolution of 7T, namely the central vein coursing through the middle of the MS plaque [14, 15]. The arrows point to the same plaque on a 3T T2-weighted sequence **(5A)**, and a 7T T2* GRE sequence **(5B)**. This imaging feature can be very useful in patients with lesser disease, where the diagnosis of MS is uncertain.

3T T2w 0.43 x 0.43 x 4 mm thick

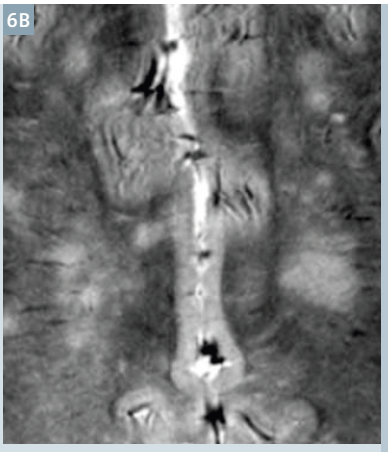

7T T2* GRE 0.375 x 0.375 x 1.5 mm thick

6 Counter-example to the previous patient of Figure 5 who had established MS. This 63-year-old female with cognitive issues has a heavy burden of white matter disease, and was referred to our mutiple sclerosis clinic for possible MS due to a 3T MRI. Images show a heavy burden of white matter disease, from a 3T T2-weighted sequence on the left **(6A)**, and a 7T T2* GRE sequence on the right **(6B)**. In distinction to the MS patient of Figure 5, no definitive central vein is seen at either field strength, and the diagnosis of MS was lowered, while the diagnosis of non-specific vasculopathy was raised [16]. A subseqent paratid biopsy revealed underlying Sjogren's disease, whose chronic small vessel disease likely caused the findings.

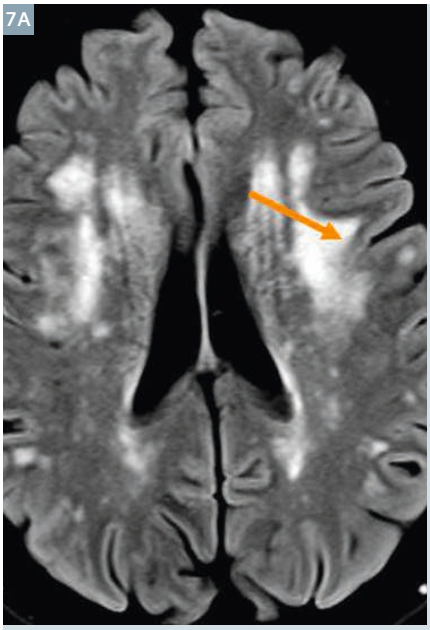

3T FLAIR 0.69 x 0.69 x 4 mm thick

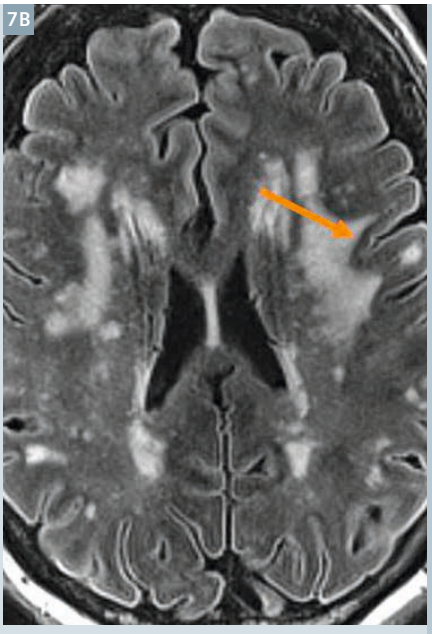

7T FLAIR 0.75 x 0.75 x 2 mm thick

7 Example of another discriminator of MS vs vasculopathy, using the same patient as in Figure 6. The subcortical U-fibers have a dual arterial blood supply (from both the adjacent capillary plexus occupying the gray matter ribbon, and from deep arterial penetrators coursing through the gray matter). This redundant supply of blood make this tissue more resiliant to ischemic injury, unlike deeper white matter. However, this tissue still remains as vulnerable to demyelinating disease as deeper white matter. Thus, careful delination of a preserved subcortical U-fibers can help discrimiate vasculopathy from demyelinating disease. In this case, the arrows point to a segment of subcortical U-fibers, which is better defined throughout (compare the segment just inferior to the arrows) with the high spatial resolution of 7T.

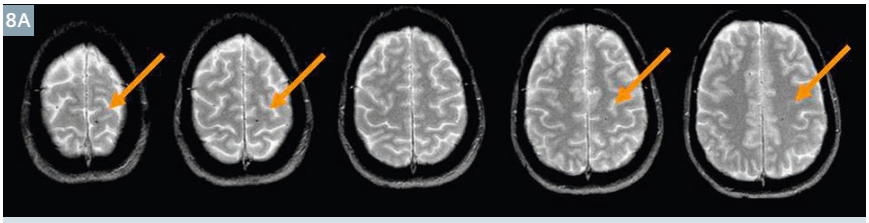

1.5T GRE 0.875 x 0.875 mm x 4 mm thick

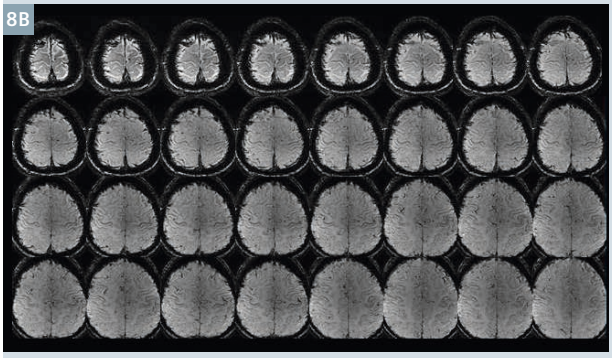

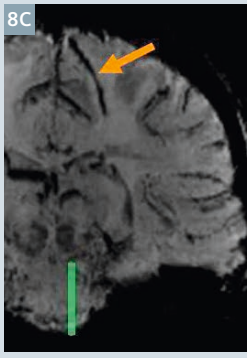

7T SWI 0.49 x 0.49 x 0.8 mm thick

8 Example of clinical value of small voxels and thin slices. A 43-year-old female presents six months after falling from a horse with headaches and presumed post-concussive syndrome. Several continuous slices from a 1.5T GRE sequence are shown in the top panel **(8A)**, with arrows pointing to small foci of susceptibility effect felt to be microhemorrhages. A 7T MRI was then obtained, bottom two panels **(8B, C)**. The lower panel shows an axial SWI sequence, whose 24 slices span the same axial distance as the 5 axial GRE slices at 1.5T. An advantage of the smaller voxels is that a high resolution MPR image was obtained in a coronal oblique direction **(8C)**, clearly revealing the dots of presumed microhemorrhage to be a linear morphology, and most likely a benign developmental venous anomaly, which is not related to traumatic brain injury (TBI). The patient has since been treated for chronic migraine headache, rather than post concussive syndrome. One similar study showed increased detection of developmental venous anomalies at 7T compared to 3T in patients with cavernous malformations [13].

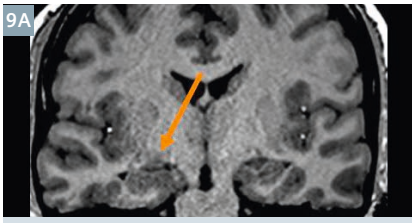

3T 0.41 x 0.41 x 1 mm

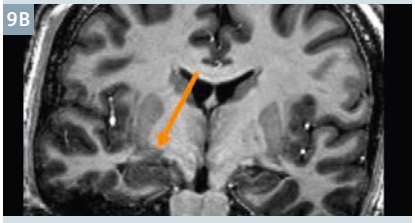

7T 0.75 x 0.75 x 0.75 mm

9 Example of a subtle heterotopia, never before appreciated at lower field MRI. The patient is a 30-year-old female, suffering from seizures since birth. A 7T T1 MP2RAGE **(9B)** revealed a previously unnoticed periventricular gray matter focus (arrow), lying adjacent to the right amygdala and hippocampus, which also appeared mildly enlarged. In addition, 7T revealed extensive periventricular heterotopias filling bilateral occipital horns (not shown). The patient recently underwent a right temporal lobectomy, and currently remains seizure free.

3T MPRAGE post gadolinium
0.45 x 0.45 x 2 mm thick

7T MP2RAGE post gadolinium
0.75 x 0.75 x 0.75 mm thick

10 Example of imaging recurrent tumor. This 65-year-old male has a known anaplastic oligodendroglioma, status post prior resection and radiation treatment. These post-gadolinium images (**10A**: 3T T1 MPRAGE; **10B**: 7T T1 MP2RAGE) show a thin segment of enhancement along the periventricular margin (shown by the bracket), indicative of tumor recurrence. While this 7T did not alter any clinical management, the high resolution and increased tissue contrast characteristics show better detail of the recurrence and adjacent tissue. This capability could potentially help patients because recurrence can be detected at a smaller level, earlier in the disease. Similarly, other studies have also shown increased tumor detection using different sequences at 7T compared to 3T [17-19].

3T SWI
0.43 x 0.43 mm x 2 mm thick

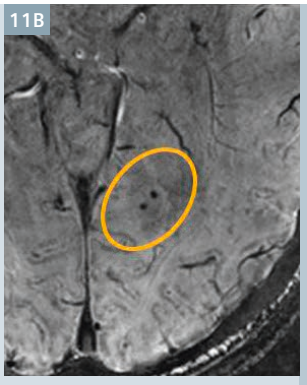

7T SWI
0.49 x 0.49 x 0.80 mm thick

11 Example of microhemorrhages not reported at lower field. This 54-year-old male experienced a motor vehicle accident 18 months earlier, and presents with persistant chronic headache. It is unclear if the headache is post-concussive syndrome, or a seperate headache syndrome. His 3T clinical MRI **(11A)** was reported as normal, however the 7T MRI **(11B)** showed several microhemorrhages with increased conspicuity. In retrospect, those microhemorrhages were visible with lower conspicuity at 3T. This example shows the practical importance of improved conspicuity of lesions, which is just as important as 7T revealing new lesions: if lesions with low conspicuity are present but not detected by the radiologist, they are effectively not present. On review of literature, one study has also shown 7T SWI improves identification of small hemorrhagic diffuse axonal injury compared to 3T [20].

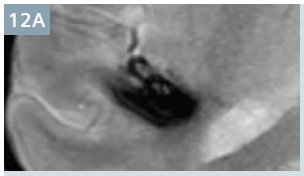

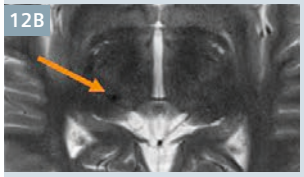

3T GRE 0.66 x 0.66 mm x 3 mm
and 3T T2-TSE
0.55 x 0.55 x 3 mm thick

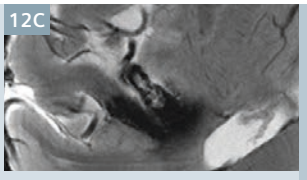

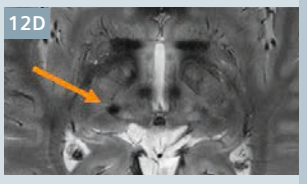

7T T2*-GRE
0.375 x 0375 x 2.00 mm thick

12 Another example of increased lesion conspicuity showing additional lesions. This 47-year-old male with a known cavernous malformation (shown on **12A, B** at 3T) had a 7T scan shown on **12C, D**. While the known large cavernous malformation in the posterior right insula shows increased detail at 7T, a second cavernous malformation not previously appreciated was seen in the right thalamus. In retrospect, this focus was present before but its marginal conspicuity was insufficient for a radiologist's detection. This lesion is now known and being followed. Prior earlier 7T studies using SWI have shown increased detection of a significant number of cavernous malformations and better definition of cavernous angioma angioarchitecture compared to lower fields [13, 21].

3T 0.28 x 0.28 x 3 mm

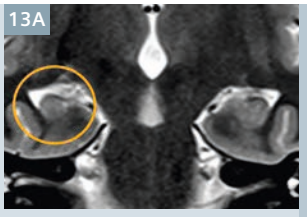

7T 0.375 x 0.375 x 1.50 mm

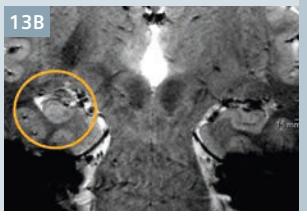

13 Example of high resolution confirming a diagnosis of mesial temporal sclerosis (MTS) in epilepsy. The patient is a 26-year-old male, who had a 3T MRI **(13A)** showing a rounded right hippocampal head (circled), slightly hyperintense, with indistinct internal architecture (compare those features with the patient's normal left hippocampus). 7T image **(13B)** provides superior definition of the rounded morphology and hyperintensity. This hippocampus was subsequently resected and the patient has now been seizure-free for over 2 years. While 7T did not change the diagnosis in this case, this example illustrates its potential to improve the diagnosis of MTS due to its superior resolution. Similarly, one study of 6 patients using 7T T2*-weighted sequence to evaluate hippocampal sclerosis showed greater anatomic detail than 1.5T [25].

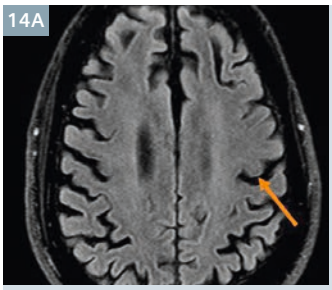

3T FLAIR
0.66 x 0.66 x 3 mm thick

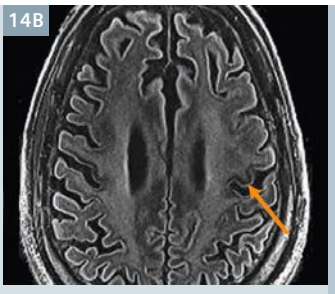

7T FLAIR
0.75 x 0.75 x 2 mm thick

14 Example of 7T applied to amytrophic lateral sclerosis (ALS), also known as Lou Gehrig's disease. The patient is a 68-year-old with ALS diagnosed 3 months earlier. **14A** is a 3T axial FLAIR, and **14B** a 7T axial FLAIR. The arrow points to the 'hand knob' of the motor strip in the left precentral gyrus. Note the gyriform decreased signal seen in the 7T, which is not well apparent at 3T. While this finding did not alter diagnosis or medical management, it has the potential to affect patients earlier in their disease when diagnosis may be ambiguous, as shown in other 7T studies [22-24].

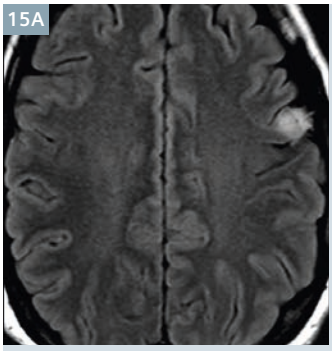

3T FLAIR
0.35 x 0.35 x 3 mm thick

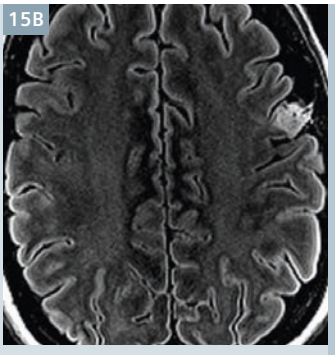

7T FLAIR
0.75 x 0.75 x 2.0 mm thick

15 Example left frontal lesion suspicious for a mass. This 31-year-old female presents with her first seizure in 25 years, after a history of childhood seizures. Images at 3T **(15A)** showed a left frontal lesion thought to be a low grade tumor, and was referred for possible resection. A 7T image **(15B)** provided sufficient detail to suggest the lesion is actually a post-traumatic lepto-meningeal cyst with subjacent scarring. The patient subsequently reported a prior history of head trauma at age 3 years. Surgery has been postponed and her seizures will be managed medically. This example shows increased lesion detail was able to alter the diagnosis of a tumor to a post-traumatic scar.

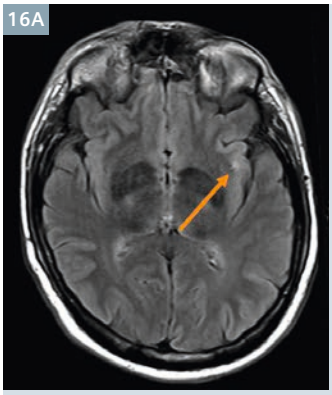

3T FLAIR
0.36 x 0.36 x 4 mm thick

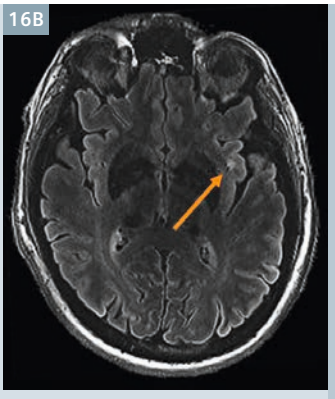

7T FLAIR
0.75 x 0.75 x 2.0 mm thick

16 Example of a lesion thought to be epilepstogenic, but determined to be benign with high resolution images. The patient is a 56-year-old male with epilepsy for 32 years, now medically refractory and being evaluated for surgery. A 3T FLAIR **(16A)** showed left subcortical gray-white indistinction of the insular cortex, suspicious for a focal cortical dysplasia. While this location was inconsistant with EEG findings, the patient was scheduled for an invasive neurosurgical evaluation to explore the lesion and other possible areas for seizure generation. A 7T FLAIR **(16B)** was obtained whose high resolution revealed the lesion to be a vascular abnormality causing adjacent scar that mimiced the appearance of a dysplasia. The patient's surgical plan was altered to not include the left insula.

3T FLAIR
0.35 x 0.35 x 3 mm thick

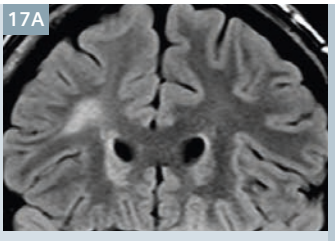

7T FLAIR
0.375 x 0.375 x 2 mm thick

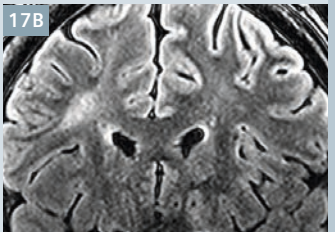

17 Example of ambiguous white matter lesion. The patient is a 24-year-old male with18 years of epilepsy. His 3T MRI image **(17A)** shows an unusual lesion in the right frontal lobe suggestive of a form of malformation of cortical development called a transmantle dysplasia. It was unclear if the lesion was related to his epilepsy because all his other tests pointed to posteriorly to this region. Higher detail due to smaller voxels from a 7T image **(17B)** verified that the lesion has no frank connection to the cortex, the adjacent cortex is normal with no gray-white indistinction, and the abnormality is most likely a vascular lesion. These features could be best appreciated by scrolling through the thin 7T sections. This suggestion was confirmed at 3T, and altered the patient's surgical plan to focus on other areas of the brain.

3T MPRAGE
0.41 x 0.41 x 1 mm

7T MP2RAGE
0.75 x 0.75 x 0.75 mm

18 Example of malformation of cortical development (MCD), not appreciated on imaging. The patient is a 37-year-old male with a 5-year history of epilepsy. His previous MRIs (typically 3T) only revealed a right thalamus cyst, which was known to be not epileptic. A 7T T1 MP2RAGE image **(18B)** showed an abnormal projection of gray matter signal extending into the white matter, compatible with a subcortical heterotopia (a form of MCD). In retrospect, guided by the 7T finding, subtle correlates could be found on 3T MRI **(18A)**. This identification of a subtle lesion started at 7T, and confirmed at 3T, altered the patient's management by making him a surgical candidate. This patient is currently undergoing intracranial EEG to confirm the epileptogenicity of the lesion.

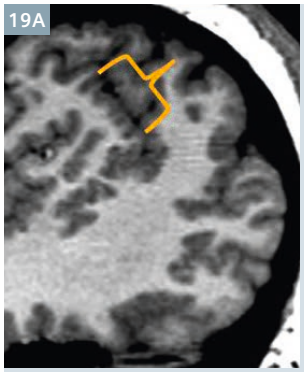

3T 0.46 x 0.46 x 0.94 mm

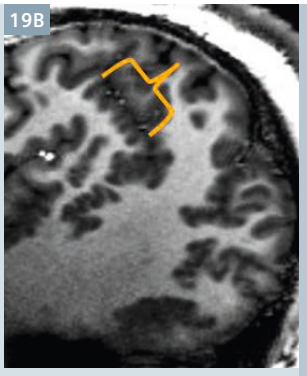

7T 0.75 x 0.75 x 0.75 mm

19 Example of improved conspicuity of Polymicrogyria (PMG). The patient is a 20-year-old male with a known congenital malformation of cortical development called PMG, manifest as abnormally small and tightly packed gyri (as an example, see cortex within interval of bracket). While the 3T sagittal MPGR image **(19A)** reveals the presence of PMG, the 7T MP2RAGE **(19B)** shows superior definition, due to combination of smaller voxels and increased CNR of gray to white matter. Occasionally regions of PMG are surgically removed, and accurate visualization of the extension is very important to clear surgical margins and potential cure. A study conducted by De Ciantis and colleagues also showed 7T provided additional details and greater involvement of cortical polymicrogyria compared to 3T, this was attributed to increased signal-to-noise and increased magnetic susceptibility [27].

3T T1-weighted
0.65 x 0.65 x 4 mm thick

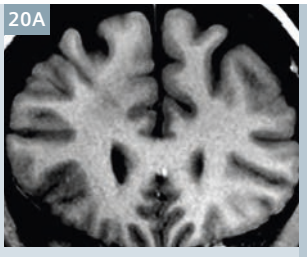

7T MP2RAGE
0.75 x 0.75 x 0.75 mm

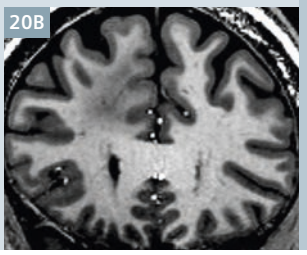

20 Example of low-grade brain tumor. The patient is a 50-year-old female, with a 15-year history of biopsy proven low grade astrocytoma, which had been grossly stable during that time. In addition, she had a 40-year history of epilepsy, well controlled until recently, and was now under consideration for surgery. A 3T coronal T1-weighted image **(20A)** shows subtle signal abnormality in the right frontal lobe white matter. The corresponding 7T image **(20B)** redemonstrates this finding with greater conspicuity. This detail improved visualization of the tumor's margins, which were more extensive than originally thought, and guided the decision to continue medical management rather than undergo a larger brain surgery. Another 7T study used a different approach and different set of sequences to evaluate 15 patients with astrocytomas (WHO grades II-IV) – greater susceptibility was used to detect tumor margins by observation of tumor vascularity which was only present at lower grade as diffusely infiltrating astrocytoma [18].

Discussion

One weakness of this method of using a gallery of side-by-side image comparisons of 7T to lower field to assess any clinical utility is that it only assesses the two-dimensional image. Our experience is that when actively viewing images on a DICOM viewer, with the ability to scroll up and down through lesions, and actively window, markedly increased lesion conspicuity, as opposed to simply viewing one static image. Thus, any conspicuity of images shown in this paper should be qualitatively considered a lower limit.

Another weakness is that the 7T protocols used in this study are not clincally optimized in terms of scanning time, as are the refined protocols on clinical MRIs at lower field. Imaging slots on the 7T do not face the same adminstrative pressures for patient throughput as clinical magnets, and are currently more liberal with scan times. Note this increased time is not unexpected at this early stage in the evolution of clinical sequence and protocol development at 7T. Thus, in the future, a more valid clinical comparison might involve using common sequences and protocols at 7T and lower field that require the same scan time.

Another limitation of the clinical utility of 7T is the increased B_1 inhomogeneities compared with lower field strength scanning. This presents a problem for interpretation of

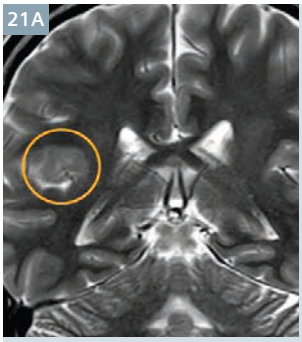

3T 0.28 x 0.28 x 3 mm

7T 0.375 x 0.375 x 2 mm

21 Example of subtle right peri-insular malformation of cortical development. This patient is a 26-year-old male who had intractable epilepsy for 19 years. EEG showed that seizures were originating from the left frontotemporal area. Coronal 3T T2-weighted image **(21A)** showed a suspicious lesion in the right posterior insular/parietal operculum region. 7T coronal GRE image **(21B)** delineated the lesion with much better conspicuity. The patient underwent surgery with complete resection of the subtle right peri-insular lesion and is now seizure free. Pathology confirmed a severe focal cortical dysplasia. A similar 7T study of patients with intractable focal epilepsy and unrevealing lesions, showed 26% improved detection of epileptogenic lesions not seen on 1.5T or 3T [26].

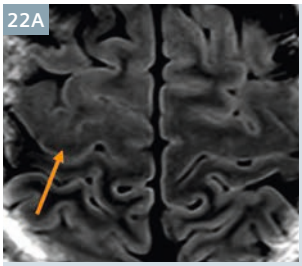

3T 0.82 x 0.82 x 4 mm

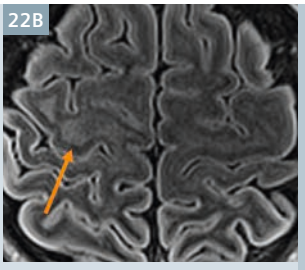

7T 0.75 x 0.75 x 2 mm

22 Example of subtle cortical dysplasia in epilepsy. The patient is an 18-year-old female with refractory focal epilepsy, with multiple prior 3T MRIs all read as normal. A 7T axial FLAIR image **(22B)** showed abnormally increased and asymmetric subcortical hyperintensity (arrow), which was also hypointense with indistinct gray-white margins on T1 MPRAGE sequence (not shown). In retrospect, a subtle abnormality could be seen at 3T **(22A)**, but with much less conspicuity and only on the exact same slice. The lesion was resected, with pathology confirming a focal cortical dysplasia. The patient remains seizure free.

whole-brain images, particularly in the lower parts of the temporal lobe, an important region for consideration of surgical intervention in epilepsy. Head coils incorporating multiple parallel transmission coil elements show considerable promise to improve the whole-brain B_1 homogeneity [28].

This paper presents a gallery of images of various neurological diseases, portrayed as a side-by-side comparison of 7T to lower field, each obtained in the same patient. This wide ranging comparison is made possible by an IRB permitting imaging of clinical patients at 7T for the expressed comparison of those imaging findings to those already obtained at lower field. Often this prompted a reappraisal of the earlier lower field findings and occassionally affected patient management.

The visualization of a lesion at 7T that was frankly not visible at lower field was infrequent, and typically the lesion was visible on the lower field image but less conspicuous. Sometimes this decerased conspicuity meant the lesion was not noticed at lower field by the radiolgoist. Therefore, in a busy clinical practice, there could be value for 7T imaging that increases lesion conspicuity that enables a radiolgist's detection, and this improvement is just as important as any de novo appearance of new lesions at 7T.

This series of cases includes clinical vignettes decribing how 7T findings influenced clinical management. While a few cases showed new, or de facto new lesions (such as Figure 8 microhemorrhages in TBI), the majority simply showed lesions visible at lower field, but with greater conspicuity. This increase is mainly due to smaller voxels providing higher spatial resolution, perhaps accentuated by intrinsically increased contrast-to-noise ratio of different tissue types. While the linear decrease in voxel size at 7T may seem modest (around 25%), this small increase nonetheless greatly aids lesion discrimiation to the radiologist's eye.

It is difficult to exactly predict the future clinical niche of 7T in neurological imaging. Some guidance of the extension from 3T to 7T may come from our prior experience from the extension from 1.5T to 3T [29-33]. Today 3T clincial image quality is superb but the initial MRIs suffered from inhomogenities. There were early concerns about differences of tissue contrast, gadolinium contrast, and poor coils [34, 35]. Today with over a decade of continued development and experience, 3T MRI addressed these issues and is now a mainstay of clinical imaging when high resolution and quality are required, for example in epilepsy. While the costs for 7T will be considerably more than 3T, there may likely evolve many clinical applications where 7T imaging will be specifically sought, especially after an analogous decade of continued developement and improvement [36].

Lastly, the role of 7T could borrow from an analogy in the technology of television, and its recent adoption of high-definition television (HDTV): 7T could viewed as 'high definition MRI'. In this analogy, whereas a television viewer can generally enjoy a program in both low-definition and high-definition TV, occassionally the extra detail makes a difference, for example when viewing the scores displayed during a sports broadcast. Similarly with MRI, both low-field and 7T can show important radiological features, but occassionally the extra resolution makes an important clinical difference.

Conclusion

The greatest clinical utility of 7T may be its improved spatial resolution, which can aid in the clinical diagnosis of pathologies that contain fine detail. A second utility may be its increased sensitivity to susceptibility effects. Finally, while 7T infrequently showed new lesions not frankly visible at lower field, it shows lesions better, and this can provide clinical significance.

References

1 Hua J, Qin Q, van Zijl PCM, et al. Whole-brain three-dimensional T2-weighted BOLD functional magnetic resonance imaging at 7 Tesla. Magn Reson Med 2014;72:1530–40.
2 Harmer J, Sanchez-Panchuelo RM, Bowtell R, et al. Spatial location and strength of BOLD activation in high-spatial-resolution fMRI of the motor cortex: a comparison of spin echo and gradient echo fMRI at 7 T. NMR Biomed 2012;25:717–25.
3 van der Zwaag W, Francis S, Head K, et al. fMRI at 1.5, 3 and 7 T: characterising BOLD signal changes. Neuroimage 2009;47:1425–34.
4 Olman CA, Yacoub E. High-field FMRI for human applications: an overview of spatial resolution and signal specificity. Open Neuroimag J 2011;5:74–89.
5 Vaughan JT, Garwood M, Collins CM, et al. 7T vs. 4T: RF power, homogeneity, and signal-to-noise comparison in head images. Magn Reson Med 2001;46:24–30.
6 Pohmann R, Speck O, Scheffler K. Signal-to-noise ratio and MR tissue parameters in human brain imaging at 3, 7, and 9.4 tesla using current receive coil arrays. Magn Reson Med 2016;75:801–9.
7 Shin W, Shin T, Oh S-H, et al. CNR improvement of MP2RAGE from slice encoding directional acceleration. Magn Reson Imaging 2016;34:779–84.
8 Seiger R, Hahn A, Hummer A, et al. Voxel-based morphometry at ultra-high fields. a comparison of 7T and 3T MRI data. Neuroimage 2015;113:207–16.
9 Fujimoto K, Polimeni JR, van der Kouwe AJW, et al. Quantitative comparison of cortical surface reconstructions from MP2RAGE and multi-echo MPRAGE data at 3 and 7 T. Neuroimage 2014;90:60–73.
10 Ni J, Auriel E, Martinez-Ramirez S, et al. Cortical localization of microbleeds in cerebral amyloid angiopathy: an ultra high-field 7T MRI study. J Alzheimers Dis 2015;43:1325–30.
11 van Veluw SJ, Biessels GJ, Klijn CJM, et al. Heterogeneous histopathology of cortical microbleeds in cerebral amyloid angiopathy. Neurology 2016;86:867–71.
12 De Reuck J, Deramecourt V, Cordonnier C, et al. Superficial siderosis of the central nervous system: a post-mortem 7.0-tesla magnetic resonance imaging study with neuropathological correlates. Cerebrovasc Dis 2013;36:412–7.
13 Frischer JM, Göd S, Gruber A, et al. Susceptibility-weighted imaging at 7 T: Improved diagnosis of cerebral cavernous malformations and associated developmental venous anomalies. NeuroImage Clin 2012;1:116–20.
14 Tallantyre EC, Morgan PS, Dixon JE, et al. 3 Tesla and 7 Tesla MRI of multiple sclerosis cortical lesions. J Magn Reson Imaging 2010;32:971–7.
15 Ge Y, Zohrabian VM, Grossman RI. Seven-Tesla magnetic resonance imaging: new vision of microvascular abnormalities in multiple sclerosis. Arch Neurol 2008;65:812–6.
16 Kilsdonk ID, Wattjes MP, Lopez-Soriano A, et al. Improved differentiation between MS and vascular brain lesions using FLAIR* at 7 Tesla. Eur Radiol 2014;24:841–9.
17 Noebauer-Huhmann I-M, Szomolanyi P, Kronnerwetter C, et al. Brain tumours at 7T MRI compared to 3T--contrast effect after half and full standard contrast agent dose: initial results. Eur Radiol 2015;25:106–12.
18 Moenninghoff C, Maderwald S, Theysohn JM, et al. Imaging of adult astrocytic brain tumours with 7 T MRI: preliminary results. Eur Radiol 2010;20:704–13.
19 Paek SL, Chung YS, Paek SH, et al. Early experience of pre- and post-contrast 7.0T MRI in brain tumors. J Korean Med Sci 2013;28:1362–72.
20 Moenninghoff C, Kraff O, Maderwald S, et al. Diffuse axonal injury at ultra-high field MRI. PLoS One 2015;10:e0122329.
21 Dammann P, Wrede K, Zhu Y, et al. Correlation of the venous angioarchitecture of multiple cerebral cavernous malformations with familial or sporadic disease: a susceptibility-weighted imaging study with 7-Tesla MRI. J Neurosurg http://doi.org/10.3171/2016.2.JNS152322.
22 Cosottini M, Donatelli G, Costagli M, et al. High-Resolution 7T MR Imaging of the Motor Cortex in Amyotrophic Lateral Sclerosis. AJNR Am J Neuroradiol 2016;37:455–61.
23 Versluis MJ, van der Grond J, van Buchem MA, et al. High-field imaging of neurodegenerative diseases. Neuroimaging Clin N Am 2012;22:159–71, ix.
24 Kwan JY, Jeong SY, Van Gelderen P, et al. Iron accumulation in deep cortical layers accounts for MRI signal abnormalities in ALS: correlating 7 tesla MRI and pathology. PLoS One 2012;7:e35241.
25 Breyer T, Wanke I, Maderwald S, et al. Imaging of patients with hippocampal sclerosis at 7 Tesla: initial results. Acad Radiol 2010;17:421–6.
26 De Ciantis A, Barba C, Tassi L, et al. 7T MRI in focal epilepsy with unrevealing conventional field strength imaging. Epilepsia 2016;57:445–54.
27 De Ciantis A, Barkovich AJ, Cosottini M, et al. Ultra-high-field MR imaging in polymicrogyria and epilepsy. AJNR Am J Neuroradiol 2015;36:309–16.
28 Zhu, Y: Parallel excitation with an array of transmit coils. Magnetic resonance in medicine, 51, 775-84, (2004).
29 Lin W, An H, Chen Y, et al. Practical consideration for 3T imaging. Magn Reson Imaging Clin N Am 2003;11:615–39, vi.
30 Frayne R, Goodyear BG, Dickhoff P, et al. Magnetic resonance imaging at 3.0 Tesla: challenges and advantages in clinical neurological imaging. Invest Radiol 2003;38:385–402.
31 Shapiro MD, Magee T, Williams D, et al. The time for 3T clinical imaging is now. AJNR Am J Neuroradiol 2004;25:1628–9; author reply 1629.
32 Pattany PM. 3T MR imaging: the pros and cons. AJNR Am J Neuroradiol 2004;25:1455–6.
33 Schmitz BL, Aschoff AJ, Hoffmann MHK, et al. Advantages and pitfalls in 3T MR brain imaging: a pictorial review. AJNR Am J Neuroradiol 2005;26:2229–37.
34 Runge VM, Case RS, Sonnier HL. Advances in clinical 3-tesla neuroimaging. Invest Radiol 2006;41:63–7.
35 Alvarez-Linera J. 3T MRI: advances in brain imaging. Eur J Radiol 2008;67:415–26.
36 Schmitt F, Grosu D, Mohr C, et al. [3 Tesla MRI: successful results with higher field strengths]. Radiologe 2004;44:31–47.

Contact

Stephen Jones, M.D., Ph.D.
Diagnostic Radiology
Cleveland Clinic Main Campus
Mail Code U15
9500 Euclid Avenue
Cleveland, OH 44195
USA
Phone: +1 216.444.4454
joness19@ccf.org

Rapid Estimation of Myelin for Diagnostic Imaging (REMyDI)

Tobias Granberg[1,2]; Marcel Warntjes[3,4]

[1] Karolinska Institutet, Department of Clinical Science, Intervention and Technology, Stockholm, Sweden
[2] Karolinska University Hospital, Department of Radiology, Stockholm, Sweden
[3] SyntheticMR, Linköping, Sweden
[4] Center for Medical Imaging Science and Visualization, CMIV, Linköping, Sweden

Introduction

Myelin plays an important part in the development of the nervous system where it acts as an insulator of nerve fibres and greatly improves the speed of signal transmission. Myelin wraps around axons and consists of sheaths of phospholipid membranes separated by thin layers of water [1, 2]. Disease and aging cause degradation of myelin, which impairs the signal transmission and may lead to axonal loss and consequently atrophy and brain dysfunction. Accurate *in vivo* myelin measurements could therefore be valuable for differential diagnostics of white matter changes, and to study treatment response in demyelinating and neurodegenerative disorders [3-7].

The water entrapped between the myelin sheaths has specific physical properties with rapid relaxation times (~10 ms), due to its strong magnetization exchange with the macromolecules in the myelin. It is therefore challenging to visualize the bound myelin water with conventional MRI methods. An established method for MRI-based myelin estimation is T2 relaxometry, where a multi-compartment model is applied to compare the fast relaxing myelin water fraction with the slower relaxing intra- and extracellular water [8-10]. This approach, however, is practically difficult and relatively time-consuming for whole-brain coverage, limiting its clinical feasibility.

Recently, a new MRI myelin detection model was proposed to measure the presence of myelin by its effect on the surrounding cellular water [11]. The observable relaxation rates of cellular water increase in the vicinity of myelin due to magnetization exchange with the fast relaxing myelin water. Meanwhile, the observable proton density decreases in the presence of myelin, since the myelin water decays faster than conventional imaging can detect. These effects can be used for myelin estimations using a multi-parametric MRI acquisition that quantifies R1 and R2 relaxation rates (the inverse of the corresponding relaxation times) and the proton density (PD). The concept of this method is incorporated in the REMyDI[1] feature of the SyMRI post-processing framework and its clinical applications are described below.

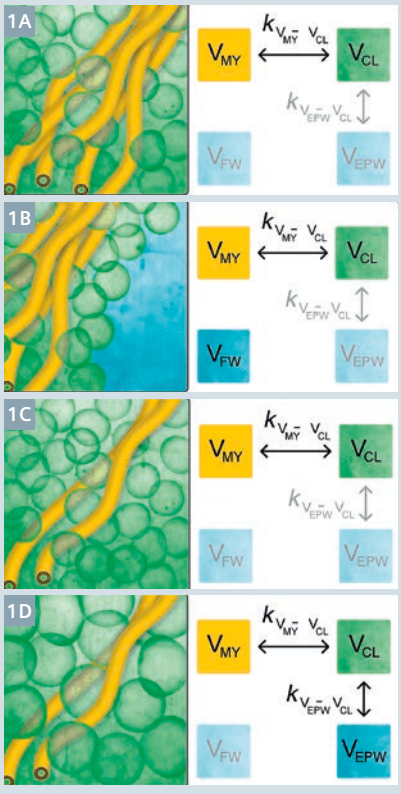

1 The used myelin model for the brain. Each voxel consists of a myelin partial volume V_{MY} and a cellular partial volume V_{CL}. Between V_{MY} and V_{CL}, there is a net magnetization exchange rate $k_{VMY\text{-}VCL}$ **(1A)**. At the interface with cerebrospinal fluid, a voxel also contains free water partial volume, V_{FW}, which has no magnetization exchange **(1B)**. In the pathological brain myelin loss may occur, resulting in a decrease of V_{MY}. Consequently, the total brain volume decreases **(1C)**. Alternatively, there can be edema, expressed as the presence of excess parenchymal water partial volume V_{EPW}. This will result in a relative decrease of V_{MY} per voxel and an increase in the total brain volume **(1D)**.

Myelin mapping with REMyDI

Figure 1 illustrates the myelin estimation in the normal and pathological brain where the signal is modelled as multiple partial volume compartments, contributing to the observable R1, R2 and PD of each acquisition voxel. In the normal brain, tissue contains myelin partial volume V_{MY}, consisting of both the myelin sheaths and myelin water. The myelin water exhibits very high R1 and R2 relaxation rates which are difficult to measure directly. The surrounding cellular partial volume V_{CL} does have

[1] REMyDI is currently under development at SyntheticMR and is not for sale in the US and in other countries. Its future availability cannot be ensured.

R1 and R2 relaxation rates that can be detected by MRI quantification sequences. The V_{CL} relaxation rates are, however, influenced by the presence of myelin due to magnetization exchange ($k_{Vmy\text{-}Vcl}$), see Figure 1A. The exchange will make the observable relaxation rates higher if there is more myelin in the voxel. In voxels with cerebrospinal fluid there is also a partial volume compartment of free water partial volume, V_{FW}, without magnetization exchange to any of the other compartments (Fig. 1B). Hence, observed R1, R2 and PD values of a voxel in the normal brain can be decomposed into a combination of V_{MY}, V_{CL} and V_{FW}. The properties of the three partial volume compartments have been calibrated with R1, R2 and PD measurements in 20 healthy volunteers.

In the pathological brain there may be demyelination, i.e. a decrease of V_{MY} (Fig. 1C). Since tissue is lost, this process will result in a brain volume reduction. There may also be an increase of water (edema), which is modelled as the appearance of excess parenchymal water partial volume V_{EPW}. The already present water in the cells and the excess parenchymal water are indistinguishable, and thus the exchange rate $k_{Vepw\text{-}Vcl}$ is infinitely high (Fig. 1D). The increase of water in the brain results in an increase of brain volume. Full application of the model therefore means that the observed R1, R2 and PD values of the brain are decomposed into a combination of V_{MY}, V_{CL}, V_{FW} and V_{EPW}. All possible combinations of the partial volumes lead to different R1 and R2 relaxation rates and PD value combinations and hence can be related to observable patient data.

MRI sequence

The sequence to obtain the R1, R2 and PD maps is described in detail in [12] and illustrated in Figure 2. A turbo spin echo sequence is performed with a 120° saturation pulse at every TR with different delay times, followed by a multi-echo acquisition. The acquisition results in a matrix of images, with multiple saturation delay times and multiple echo times; in total 8 complex

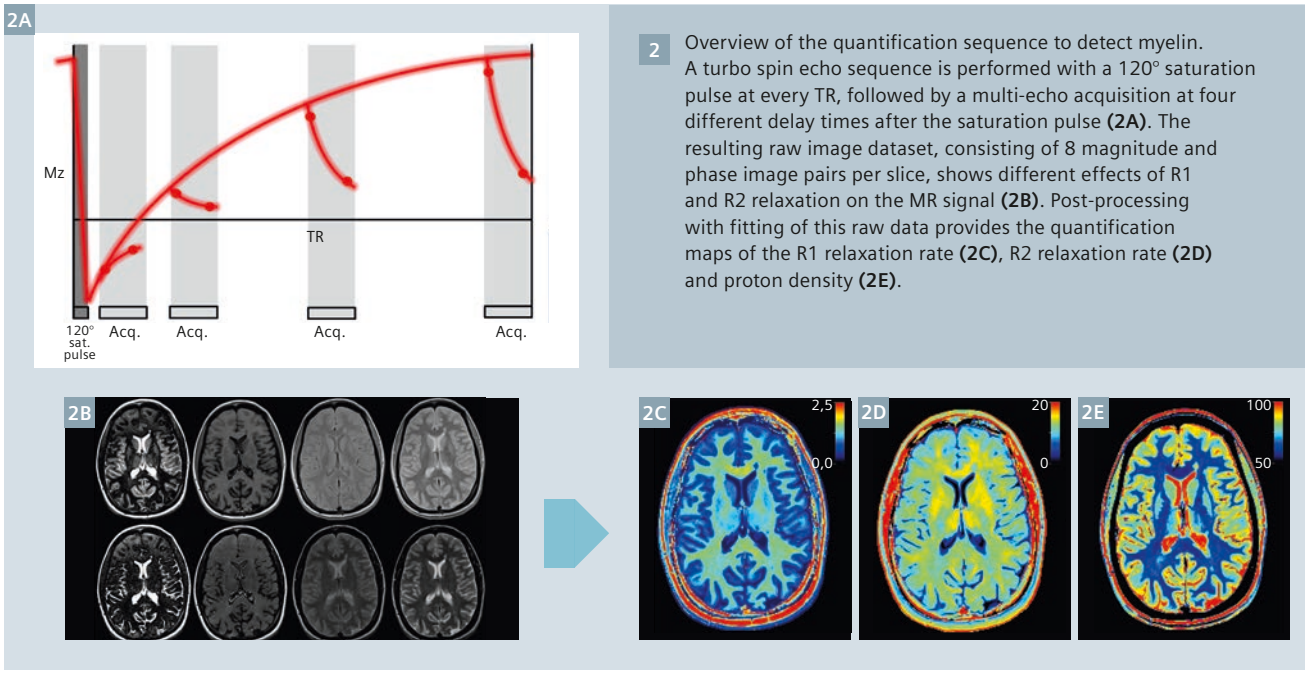

2 Overview of the quantification sequence to detect myelin. A turbo spin echo sequence is performed with a 120° saturation pulse at every TR, followed by a multi-echo acquisition at four different delay times after the saturation pulse **(2A)**. The resulting raw image dataset, consisting of 8 magnitude and phase image pairs per slice, shows different effects of R1 and R2 relaxation on the MR signal **(2B)**. Post-processing with fitting of this raw data provides the quantification maps of the R1 relaxation rate **(2C)**, R2 relaxation rate **(2D)** and proton density **(2E)**.

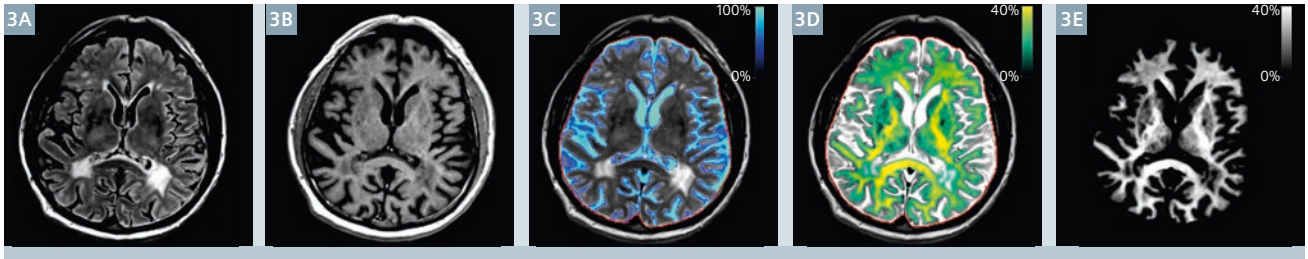

3 Example of the application of REMyDI in a patient diagnosed with HDLS. Based on the quantification maps conventional images such as FLAIR **(3A)** and T1w **(3B)** can be synthesized for visual aid. At first, the intracranial volume (red line) and CSF (blue) are segmented to segment the brain **(3C)**. Then, the brain is decomposed into the partial tissue volumes, including myelin **(3D)**. Summation of all myelin partial volume voxels provides the total myelin volume in the brain **(3E)**. This patient (58-year-old male) had a myelin volume of 153 ml, a brain volume of 1069 ml (myelin ratio 14.3%) and an ICV of 1409 ml (myelin ratio 10.9%). The brain to intracranial volume ratio (BPF) was 75.9%.

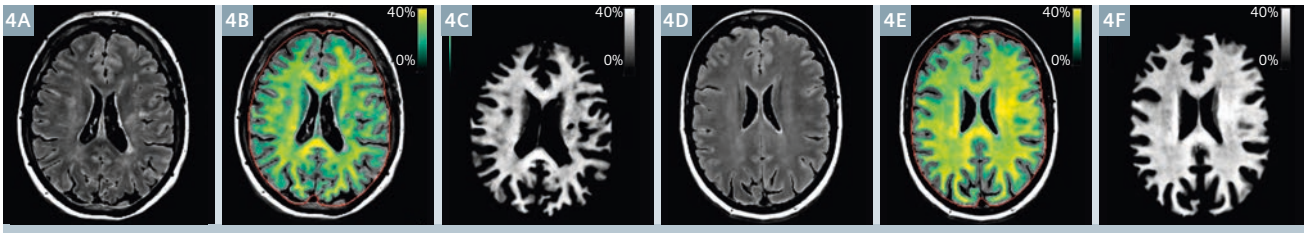

4 Example of the application of REMyDI in a patient diagnosed with Multiple Sclerosis (57-year-old female), showing a synthetic FLAIR **(4A)**, the myelin map as a color overlay **(4B)** and the myelin map only **(4C)**. The patient had a myelin volume of 126 ml, a brain volume of 931 ml (myelin ratio 13.5%) and an ICV of 1122 ml (myelin ratio 11.2%). The BPF was 83.0%. For comparison, a healthy (age and gender matched) control is shown in **4D-F**. The control had a myelin volume of 178 ml, a brain volume of 1108 ml (16.0%) and an ICV of 1252 ml (14.2%). The BPF was 88.5%.

images per slice. The maximum signal is proportional to the PD and after fitting the raw data provides quantitative maps of the R1 and R2 relaxation rates. Effects from B_1 inhomogeneity, imperfect RF pulse profiles, and spurious echoes are corrected for using a spin-model. The scan time of the sequence is around 6 minutes, with automatic post-processing completed in less than 10 seconds.

Practical workflow for REMyDI

Using the MRI acquisition described above, the R1, R2 and PD maps are measured. All combinations of R1, R2 and PD values that can be assigned to grey matter, white matter and CSF are put together in a contiguous volume to determine the intracranial cavity. The edge of the ICV is well-defined on PD = 50%, i.e. at the interface of CSF (PD = 100% PD) and bone (PD = 0%). Using the PD map rather than an arbitrary intensity scale of a conventional MR image makes this process very robust and repeatable [13-15]. Subsequently, CSF (V_{FW}) is segmented and removed to retrieve the brain. This procedure provides the Brain Parenchymal Fraction (BPF), the ratio of brain and intracranial volume. The BPF is a very suitable measure to monitor brain atrophy [16]. The repeatability error for brain volume was reported as low as 0.14% [17]. For comparison, the annual atrophy rate in MS is 0.6-1.2% [13]. Finally, each voxel that contains brain tissue is decomposed in the four partial volume compartments of the myelin model. Typically, the myelin partial volume in the brain is in the range of 0-40%. Summing the partial volumes of all voxels provides the total myelin volume of the patient. In Figure 3 the myelin quantification is exemplified in a patient with the demyelinating disorder Hereditary Diffuse Leukoencephalopathy with Spheroids (HDLS).

Clinical relevance

The advantage of retrieving a myelin measurement from a quantitative MR sequence is that a wealth of information is collected using a single, 6 minute long acquisition. The quantitative maps are on an absolute scale and the resulting measurements can therefore be compared between patients, even across scanners, since MR scanner imperfections are corrected for. The R1, R2 and PD values may provide more accurate description of MS lesions, tumors or other pathological processes and allow better statistics. Based on the quantitative maps, it is also possible to create conventional weighted images, a process called synthetic MRI. An advantage with this approach is that the synthesized echo time TE, repetition time TR and inversion delay time TI can be customized to produce optimal contrasts for any given pathology or to the preference of the reading radiologists, using the same input data [12, 18]. Coming from the same data source, all images are perfectly co-registered. Therefore, MR quantification may provide unprecedented time efficiency, since conventional contrast images such as T2-weighted, T1-weighted, FLAIR and any other combination of TE, TR and TI can be synthesized from the same acquisition that also provides brain volumetrics and myelin mapping. In Figure 4 another example is provided of a Multiple Sclerosis patient where a synthetic FLAIR image is placed next to the myelin map. Volumes are retrieved for ICV, brain and myelin, which can be compared to a gender and age matched healthy control.

Future perspectives

Currently, the REMyDI method is being further validated using post-mortem acquisitions and subsequent staining of slices of brain with Luxol Fast Blue (LFB), a light blue dye that specifically binds to myelin. Preliminary results are presented in Figure 5, where the registered slices of LFB optical density are compared to the quantitative MRI derived myelin maps.

Further evaluation is performed on large groups of MS patients and on pediatric patients[1] to monitor developmental myelination. Cerebral myelination starts at about 4 months of age and seems to follow a very specific developmental pattern. Although it remains a challenge to collect healthy pediatric reference data, precise measurements of myelin in development may become an important aid in pediatric patient monitoring, especially in development and metabolic disorders.

We hope, and expect, that many more projects will start soon. There has been an increasing focus and availability on MRI quantification for both research and routine clinic and REMyDI is an exciting step in that direction.

[1] MR scanning has not been established as safe for imaging fetuses and infants under two years of age. The responsible physician must evaluate the benefit of the MRI examination over other imaging procedures.

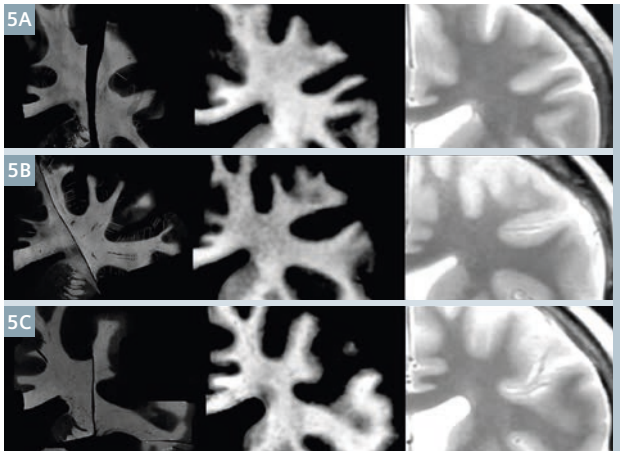

5 Post-mortem validation of REMyDI. The quantification sequence was performed on fresh, intact brains *in situ*. After a temperature correction of R1 relaxation rates the myelin maps were calculated (center). The brains were extracted, fixated, stained with Luxol Fast Blue and photographed. The optical density maps of the photographs (left column) were registered and correlated with quantitative MRI method. For comparison, a synthetic PD-weighted image is shown on the right.

References

1 Back SA, Riddle A, McClure MM. Maturation-dependent vulnerability of perinatal white matter in premature birth. Stroke (2007) 38:724-730.

2 Fields RD. White matter in learning, cognition and psychiatric disorders. Trends Neurosci (2008) 31:361-370.

3 Miller DH, Barkhof F, Frank JA, Parker GJ, Thompson AJ. Measurement of atrophy in multiple sclerosis: pathological basis, methodological aspects and clinical relevance. Brain (2002) 125:1676-1695.

4 Bakshi R, Thompson AJ, Rocca MA, et al. MRI in multiple sclerosis: current status and future prospects. Lancet Neurol (2008) 7:615-625.

5 Hinman JD, Abraham CR. What's behind the decline? The role of white matter in brain aging. Neurochem Res (2007) 32:2023-2031.

6 Peters A. The effects of normal aging on myelin and nerve fibers: a review. J Neurocytol (2002) 31:581-593.

7 Matsusue E, Sugihara S, Fujii S, Ohama E, Kinoshita T, Ogawa T. White matter changes in elderly people: MR-pathologic correlations. Magn Reson Med Sci (2006) 5:99-104.

8 Whittall KP, MacKay AL, Graeb DA, Nugent RA, Li DK, Paty DW: In vivo measurement of T2 distributions and water contents in normal human brain. Magn Reson Med (1997) 37:34-43.

9 MacKay A, Laule C, Vavasour I. Bjarnason T, Kolind S, Mädler B: Insights into brain microstructure from the T2 distribution. Magn Reson Imag (2006) 24:515-525.

10 Levesque IR, Pike GB. Characterizing healthy and diseased white matter using quantitative magnetization transfer and multicomponent T2 relaxometry: A unified view via a four-pool model. Magn Reson Med (2009) 62:1487-96.

11 Warntjes M, Engström M, Tisell A, Lundberg P. Modelling the presence of myelin and oedema in the brain based on multi-parametric quantitative MRI. Frontiers in Neurology (2016) doi 10.3389.

12 Warntjes M, Dahlqvist Leinhard O, West J and Lundberg P. Rapid Magnetic Resonance Quantification on the brain: Optimization for Clinical Usage. Magn Reson Med (2008) 60:320-329.

13 Vågberg M, Lindqvist T, Warntjes M, Sundström P, Birgander R and Svenningsson A. Automated Determination of Brain Parenchymal Fraction in Multiple Sclerosis. AJNR Am J Neuroradiol (2013) 34:498-504.

14 Ambarki K, Lindqvist T, Wåhlin A, Petterson E, Warntjes M, Vågberg M, Birgander R, Malm J and Eklund A. Evaluation of Automatic Measurement of the Intracranial Volume Based on Quantitative MR Imaging. AJNR Am J Neuroradiol (2012) 33:1951-1956.

15 Virhammar J, Warntjes M, Laurell K, Larsson EM. Quantitative MRI for Rapid and User-Independent Monitoring of Intracranial CSF Volume in hydrocephalus. AJNR Am J Neuroradiol (2016) 37:797-801.

16 Grassiot B, Desgranges B, Eustache F, et al. Quantification and clinical relevance of brain atrophy in multiple sclerosis: a review. J Neurol (2009) 256:1397–1412.

17 Granberg T, Uppman M, Hashim F, Cananau C, Nordin LE, Shams S, Berglund J, Forslin Y, Aspelin P, Fredrikson S, Kristoffersen-Wiberg M. Clinical Feasibility of Synthetic MRI in Multiple Sclerosis: A Diagnostic and Volumetric Validation Study. AJNR Am J Neuroradiol. (2016) 37:1023-1029.

18 Bobman SA, Riederer SJ, Lee JN, Suddarth SA, Wang BP, Drayer BP, MacFall JR. Cerebral magnetic resonance image synthesis. AJR Am J Neuroradiol (1985) 6:265–269.

Contact

Tobias Granberg, M.D., Ph.D.
Karolinska Institutet, Department of Clinical Science, Intervention and Technology
Karolinska University Hospital, Department of Radiology, 141 86 Stockholm, Sweden
tobias.granberg@ki.se

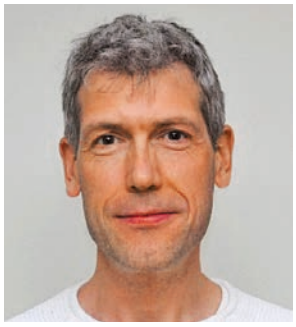

Contact

Marcel Warntjes, Ph.D.
SyntheticMR AB
Storgatan 11, 58224, Linköping, Sweden
Center for Medical Imaging Science and Visualization, CMIV
University Hospital, 58185, Linköping, Sweden
marcel.warntjes@syntheticmr.com

First Clinical Experiences with Simultaneous Multi-Slice Accelerated Diffusion-Weighted Imaging Throughout the Body

Valentin Tissot, M.D.[1]; Olivier Legeas, M.D.[1]; Isabelle Kergastel, M.D.[1]; Erwan Derrien[2]; Gregor Thörmer, Ph.D.[3]

[1] Morvan Hospital, Centre Hospitalier Regional Universitaire (CHRU), Brest, France
[2] Siemens Healthineers, La Chapelle-sur-Erdre, France
[3] Siemens Healthineers, Erlangen, Germany

Case 1

60-year-old female patient with multiple lesions at the cortico-medullary junction in the brain.

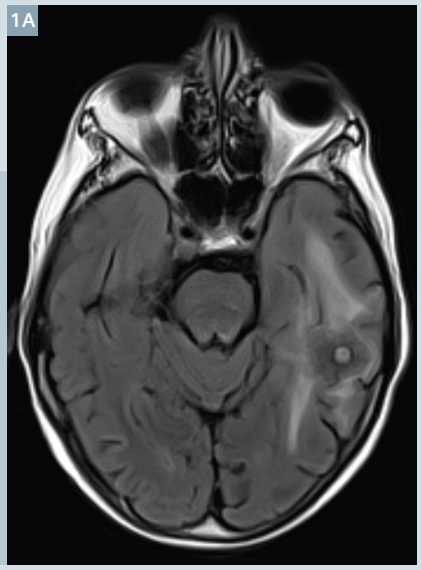

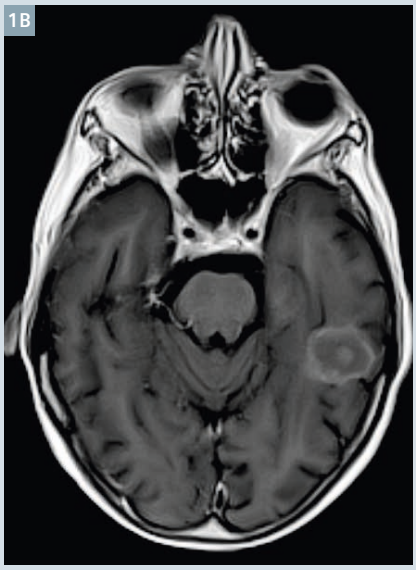

1A–B T2 FLAIR and T1w post-contrast image show a lesion in the left temporal lobe with surrounding edema and moderate mass effect. The central cavity of the lesion is hyperintense and surrounded by a thin capsule. In postcontrast images the lesion shows a 'target sign' with rim enhancement and central hyperintensity.

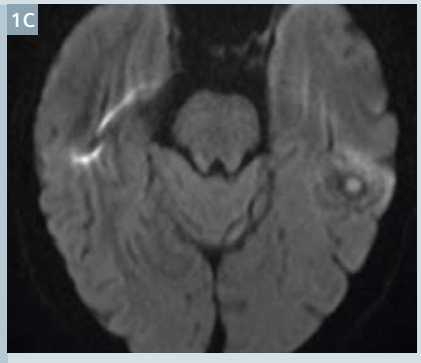

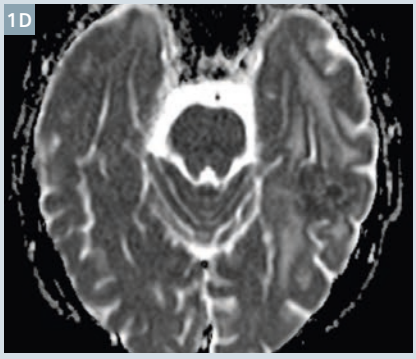

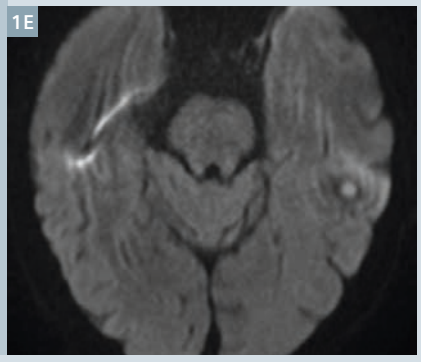

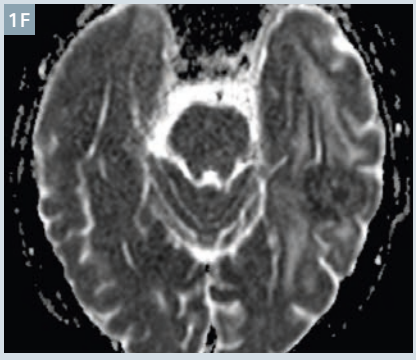

1C–F DWI at the same level demonstrates a target lesion, with high signal intensity in b1000 **(1C, E)** and corresponding lowered ADC **(1D, F)**, reflecting very strong diffusion restriction (mean ADC ~ 400 mm^2/s) in the central part of the lesion, consistent with a highly viscous abscess formation. While 1C and D were acquired with standard parameters (see Table 1), images 1E and F were acquired with an SMS factor of 2, which allowed to reduce the TR from 5600 ms to 2700 ms. Accordingly, the overall acquisition time was shortened from 1:54 min to 1:11 min without compromising image quality.

Introduction & Motivation

The service spectrum of our radiology department and medical imaging center at the Hôpital Morvan comprises multidisciplinary diagnostic and interventional activities, with a focus on visceral imaging, neuroradiology, vascular imaging as well as musculoskeletal imaging. To serve both in- and outpatient referrals of different medical disciplines we are, amongst others, equipped with two Magnetic Resonance Imaging (MRI) systems of which one is a MAGNETOM Avanto^{fit}, 1.5T scanner.

Running on *syngo* MR E11C software, this system facilitates a new method for advanced and accelerated diffusion-weighted imaging (DWI), namely Simultaneous Multi-Slice (SMS) imaging, which is of tremendous value for our daily clinical work. DWI has become an integral part not only of neuro imaging studies but also imaging of the head & neck region, breast, liver, prostate, rectum and so forth. Especially in body oncology, DWI can be used as a sensitive tool to identify potential areas of impeded diffusion on high b-value images and to improve lesion characterization in terms of cellular properties with the Apparent Diffusion Coefficient (ADC).

Case 2

72-year-old male patient with mass tumor in the right submandibular space.

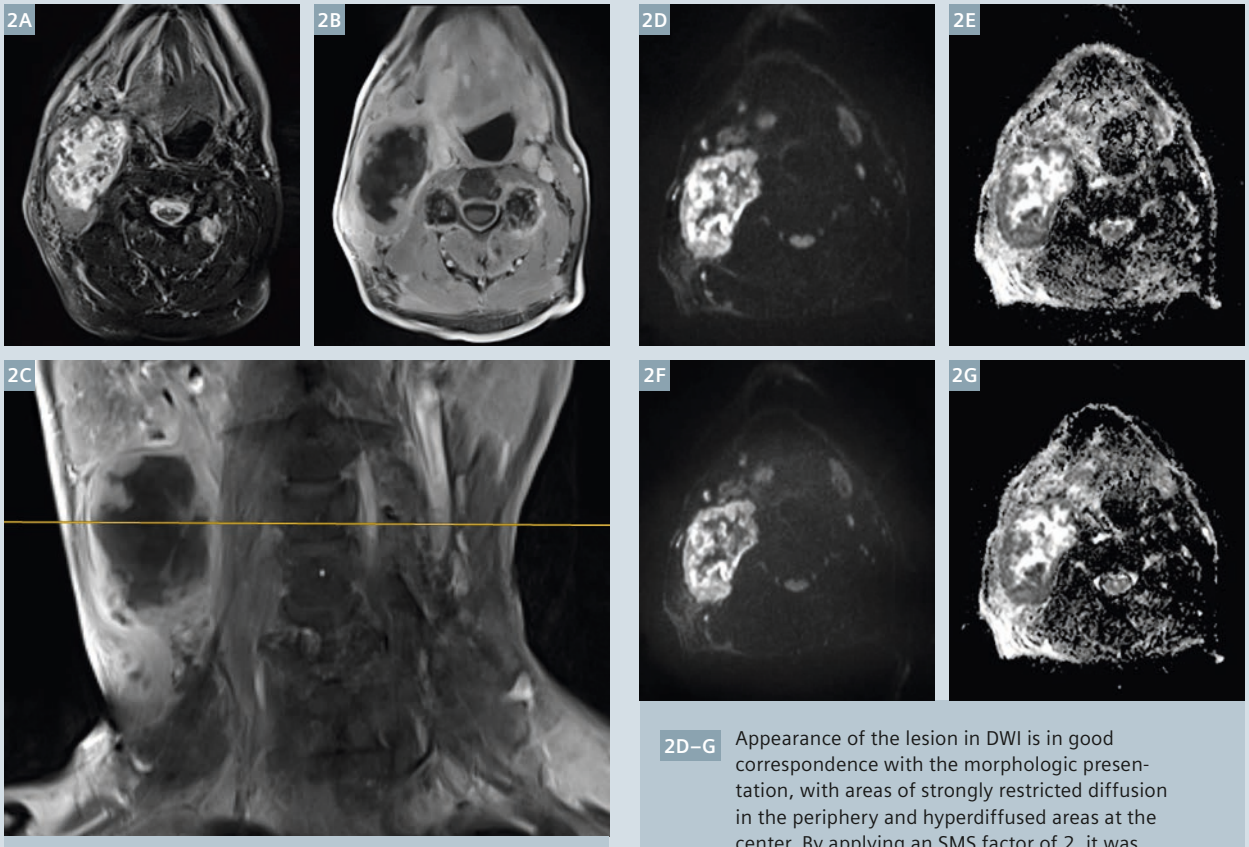

2A–C T2w and T1w postcontrast images show an extended, oval-shaped, inhomogeneous imposing mass in the right submandibular space, displacing the trachea and major cervical vessels towards medial. The tumor presents with solid, nodular appearing areas in the parietal part and shows T2w hyperintensity in the more centrally located aspects, consistent with fluid accumulation due to necrosis. T1w postcontrast images show rim like enhancement of the tumor and advanced infiltration of the musculus sternocleidomastoideus, lingual area, platysma and tongue are present.

2D–G Appearance of the lesion in DWI is in good correspondence with the morphologic presentation, with areas of strongly restricted diffusion in the periphery and hyperdiffused areas at the center. By applying an SMS factor of 2, it was possible to reduce the TR from 4300 to 2200 ms and the overall acquisition time from 4:18 min to 2:12 min (further parameters in Table1).

Case 3

33-year-old woman with invasive breast cancer of the left breast.

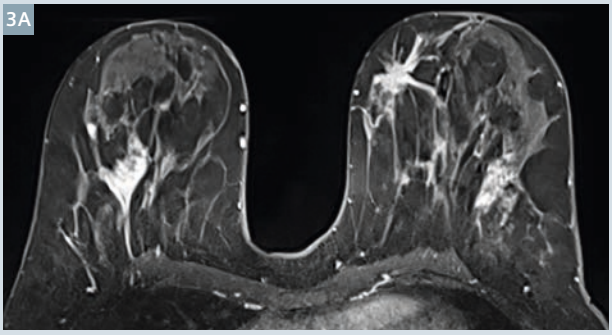

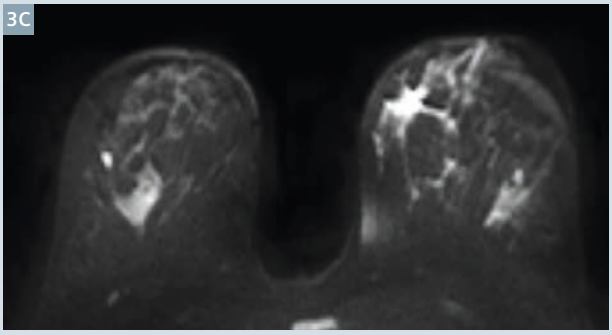

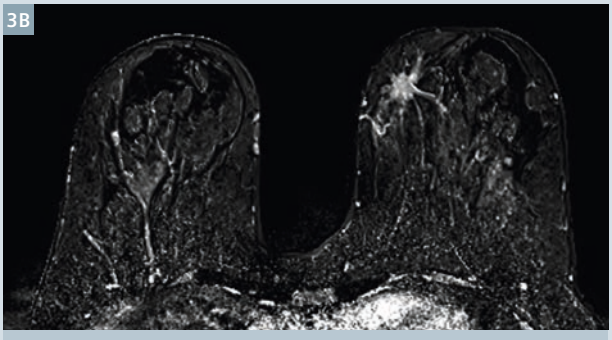

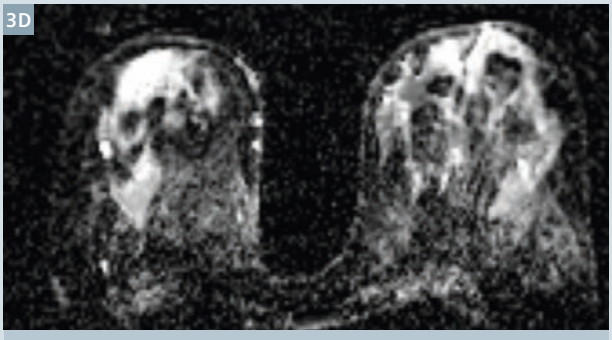

3A–B First postcontrast T1w image of the dynamic contrast-enhanced series and respective subtraction view clearly show a lesion in the left breast, demonstrating fast enhancement and subsequent washout. The mass is irregular shaped, spiculated and homogenously enhancing. In the right breast, wedge-shaped, moderate enhancement of the glandular tissue and a small lenticular lesion can be found.

3C–D SMS accelerated DWI at the same level shows a hyperintense area in the left breast in b1000 with corresponding ADC restriction and a mean ADC value of 865 x 10^{-3} mm^2. The small, round, well circumscribed lesion in the right breast manifests as a T2 shine-through effect in the high b-value image with corresponding high ADC value, most likely corresponding to a fibroadenoma. Acquisition parameters can be found in Table 1.

Region		Field-of-View [mm]	Matrix	Slice thickness [mm]	#slices	TR /TE [ms]	*b*-values [s/mm²]	PAT factor	SMS factor	Acquisiton time [min]
Brain	Conv	230x230	384x384i	4	26	5600 / 84	0, 1000	2	0	1:54
	SMS					2700 / 84		2	2	1:11
Head & Neck	Conv	230x230	384x384	4	24	4300 / 106	50, 800	2	0	4:18
	SMS					2200 / 106		2	2	2:12
Breast	SMS	203x339	108x180	4	26	2600 / 84	50, 800	2	2	3:08
Prostate	Conv	200x200	128x128	3.5	18	3400 / 72	50, 800	2	0	4:58
	SMS					2000 / 72		2	2	2:55
Rectum	SMS (axial)	200x200	128x128	4	24	2400 / 72	50, 400, 800	2	2	2:24
	SMS (sag)	200x200	128x128	4	20	2100 / 79	50, 800, 1600	2	2	3:30

Table 1: Acquisition parameters

Case 4

68-year-old man with prostate cancer.

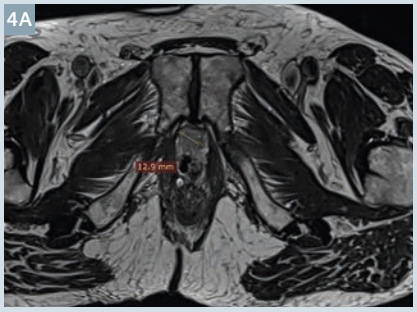

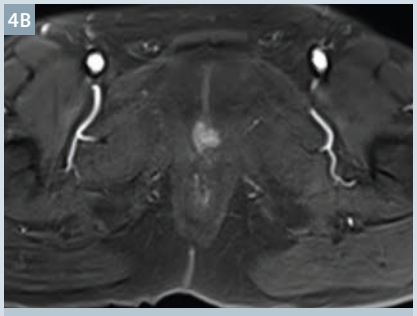

4A–B T2w images show a benign hyperplasia of the transition zone of the prostate in accordance with the patient's age. In the apex of the gland, however, a lenticular shaped, T2 hypointense lesion with irregular margins and a maximum diameter of ~13 mm is visible. Early phase T1w images after contrast application show a distinct, well circumscribed enhancement of contrast medium in the respective area.

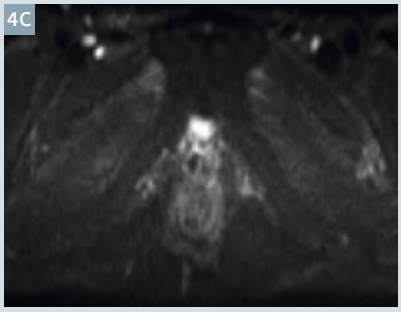

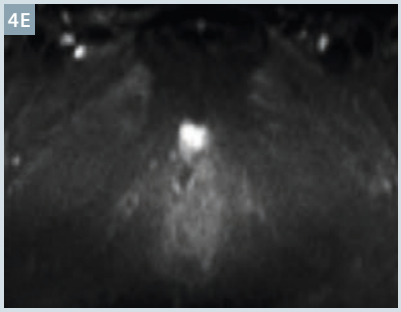

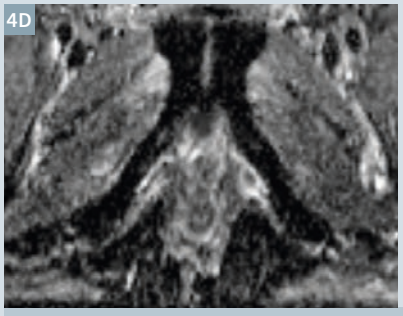

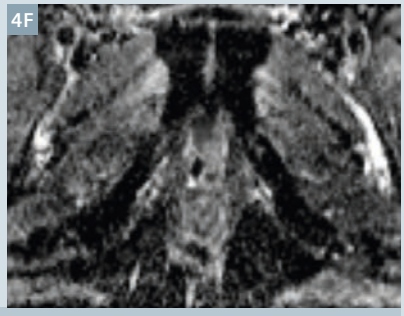

4C–F Conventional **(4C, D)** and SMS accelerated **(4E, F)** high b-value image and ADC map show an apical lesion with strongly restricted diffusion. Measured ADC values show a high inter-method reproducibility with values of 758 and 744 x10^{-3} mm^2/s, respectively. With Simultaneous Multi-Slice acceleration, acquisition time could be reduced from 4:58 min to 2:55 min (further parameters in Table 1).

4G–F Due to the unusual position of the lesion an additional DWI scan with a very high b-value of 1600 s/mm^2 was performed in the sagittal plane, which confirmed the suspicion and was rated PI-RADS 4.

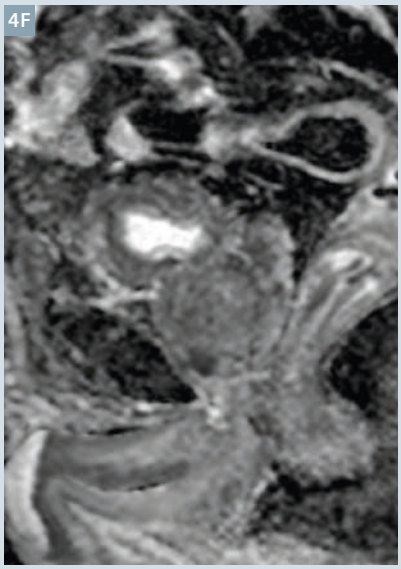

Case 5

65-year-old male patient with sigmoid carcinoma.

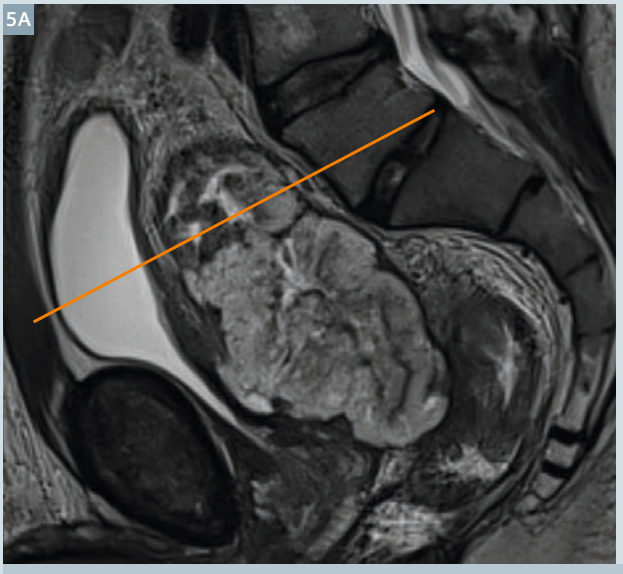

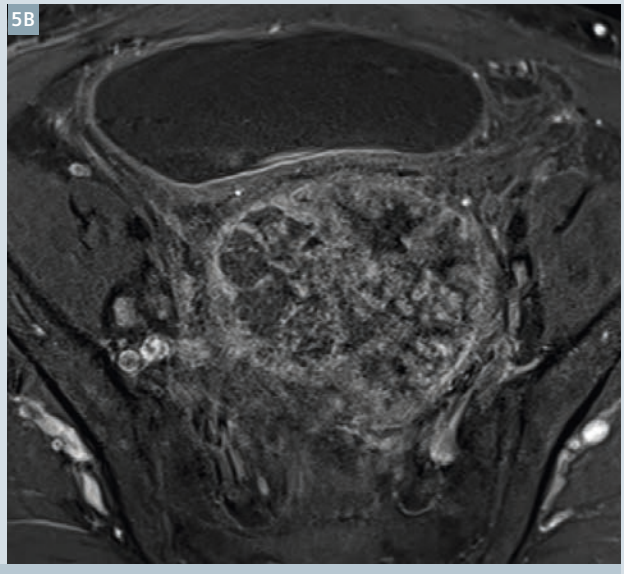

5A–B T2w images show a hyperintense, regularly structured mass in the pelvis, most probably originating from the sigma. Towards caudal, the tumor touches the seminal vesicles or potentially infiltrates these. Metastatis of lumbar vertebra 4 and iliac lymph nodes are likely to be present. In postcontrast T1 images, the tumor shows irregular, enhancement from parietal aspects towards the center.

5C–F Corresponding sagittal **(5C, D)** and axial **(5E, F)** diffusion-weighted images (b800) and ADC maps show a very inhomogeneous pattern in the tumor corresponding to the anatomical appearance and with aspects, especially towards cranial and in the center, showing strongly restricted diffusion.

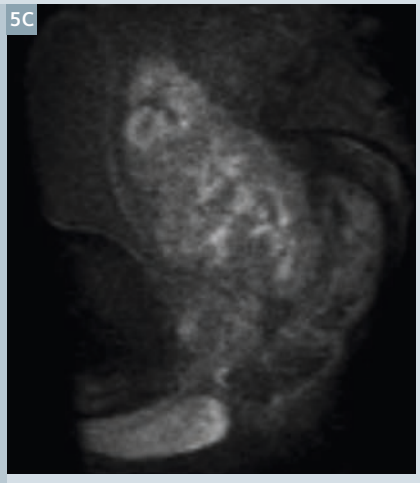

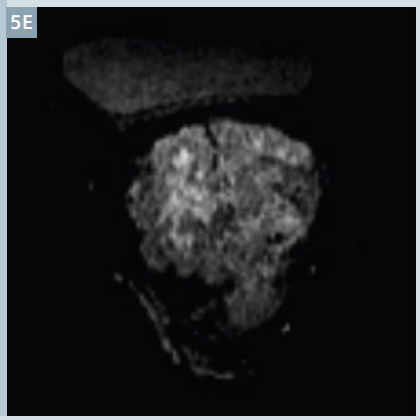

Technically, however, DWI is commonly based on a single-shot, 2D EPI sequence, which is a highly inefficient approach of image acquisition. Every imaging slice has to be excited individually, then the diffusion encoding gradients are played out and finally the image information is acquired with EPI encoding [1]. This process is repeated multiple times, once for each imaging slice, until the entire volume of interest is covered. This inefficient approach can be overcome with Simultaneous Multi-Slice. Instead of a successive excitation of slices, slices are exited simultaneously with a multiband pulse and blipped-CAIPIRINHA SMS-EPI ensures preservation of high SNR and low artifact levels [2].

Motivated by the promising results with Simultaneous Multi-Slice accelerated abdominal imaging presented by the NYU group [3], we decided to evaluated the benefits of Simultaneous Multi-Slice beyond neuro imaging and started to set up own protocols for imaging of various body regions with the support of our local application specialist.

6

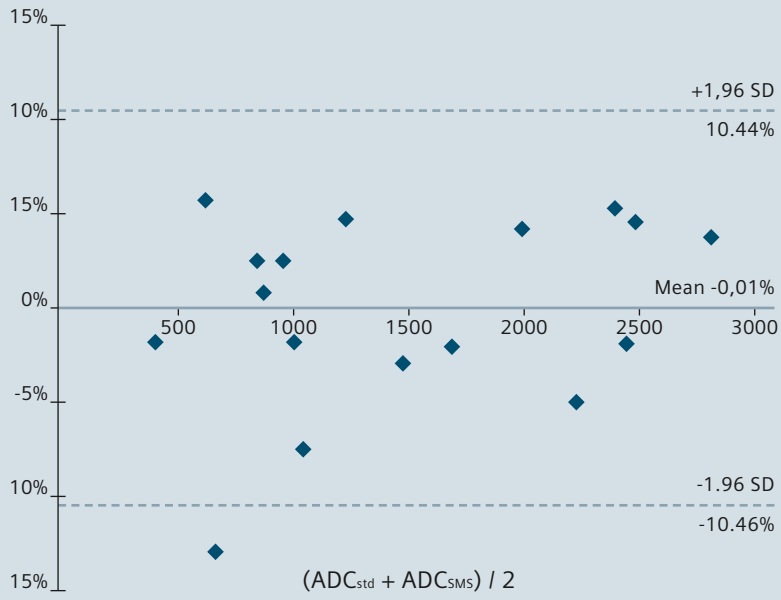

6 Bland-Altman-Diagram showing that ADC values are highly reproducible between the conventional and the accelerated technique.

Summary and Conclusion

As demonstrated with the cases presented here, Simultaneous Multi-Slice acceleration is a valuable technique for the acceleration of diffusion-weighted imaging in almost all clinical applications where DWI is commonly applied. Robust results and good image quality can be achieved with an SMS factor of 2, which allows to achieve near two-fold acceleration in DWI acquisitions. As shown in the Bland-Altman-Diagram (Fig. 6), ADC values are highly reproducible between the conventional and the accelerated technique.

In the meantime we have incorporated Simultaneous Multi-Slice Diffusion-weighted Imaging (SMS DWI) with 2-fold acceleration in our clinical protocol for various body regions, allowing shorter overall scan time, better slice coverage or improved resolution.

References

1 Setsompop K, et al. Advancing Diffusion MRI Using SMS EPI. MAGENTOM Flash 3(63): 2015; 16-22.
2 Breuer F, et al. CAIPIRINHA – Revisited. MAGENTOM Flash 3(63): 2015; 8-15.
3 Chandarana H, et al. Simultaneous Multi-Slice Accelerated Free-Breathing Diffusion-Weighted Imaging in Abdomen and Pelvis. MAGENTOM Flash 3(63): 2015; 32-35.

Contact

Valentin Tissot, M.D.
Morvan Hospital
Centre Hospitalier Regional Universitaire (CHRU)
2 Avenue Foch
29609 Brest cedex
France
Phone: +33 298223333
valentin.tissot@chu-brest.fr

Pelvic Congestion Syndrome: The Role of MRI

Gligor Milosevic, M.D.[1]; Bianka Freiwald, M.D.[1]; Manuela Birrer, M.D.[2]; Christoph L. Zollikofer, M.D.[1]; Rahel A. Kubik-Huch, M.D., M.P.H.[1]

[1] Institute of Radiology, Kantonsspital Baden, Baden, Switzerland
[2] Center for Vascular Diseases, Kantonsspital Baden, Baden, Switzerland

Clinical background

Chronic pelvic pain is a common condition occurring in women of childbearing age. Up to 38 out of 1,000 women annually present in primary care with intermittent or constant pain in the lower abdomen or pelvis, a rate comparable with that of Asthma and lower back pain (37 and 41 in 1000, respectively) [1]. Chronic pelvic pain associated with pelvic venous insufficiency has been termed 'Pelvic Congestion Syndrome' and recognized as an often overlooked cause of chronic pelvic pain [2].

The list of differential diagnoses is long and includes gynaecological, urological, gastrointestinal or musculoskeletal entities such as endometriosis, recurrent urinary tract infections, irritable bowel syndrome or pelvic floor myalgia [3].

The etiology of Pelvic Congestion Syndrome is probably multifactorial, with valvular insufficiency (e.g. congenital absence of ovarian vein valves), venous obstruction (e.g. nutcracker syndrome), hormonal factors/reproductive age and multiple pregnancies being widely acknowledged risk factors [4].

Presentation

Most women report noncyclic, intermittent or constant, dull pain or fullness, sometimes associated with nonspecific symptoms such as headache, nausea, vulvar swelling or feeling of leg fullness. They may also complain of sharp exacerbations of pain, dyspareunia, dysmenorrhea and urinary urgency. The symptoms are typically exacerbated by menstruation, coitus, pregnancy, prolonged standing, walking or activities that increase intraabdominal pressure. The pain is usually unilateral, but can also be bilateral. At presentation, the symptoms have often already persisted for more than six months. Possible clinical findings are varicose veins of the vulva, perineum, buttocks and lower extremities [3].

Imaging findings

It must be stressed that imaging studies alone cannot diagnose Pelvic Congestion Syndrome in the absence of according patient history or the clinical features listed above, since dilated pelvic veins can often be incidentally found in asymptomatic women [5].

Ovarian vein dilatation more commonly affects the left side, presumably due to the right angle formed when it joins the left renal vein, facilitating reflux [3, 6]. This is in contrast to septic puerperal ovarian vein thrombosis, which reportedly more often occurs on the right side [7].

Ultrasonography with color Doppler allows a dynamic examination of flow in the pelvic veins. Dilated peri-uterine and peri-ovarian veins can be identified in Pelvic Congestion Syndrome. The Valsalva maneuver or examining the patients in an upright position can be used to increase venous filling. Established diagnostic criteria are reversal of flow in the ovarian veins, tortuosity of the ovarian veins and pelvic varicosities > 6 mm [8].

Both CT and MRI allow a detailed depiction of anatomy including vascular structures and pelvic organs. Contrast-enhanced studies are preferred to visualize the pelvic venous system. MRI is widely being regarded as the modality of choice, as it has the advantage of not relying on ionising radiation and, based on its superior soft tissue contrast, being able to show signs of other pathological conditions, e.g. of the gynaecologic

Key points and implications for patient care

- Dilatation of ovarian and pelvic veins in the context of chronic pelvic pain is the imaging hallmark of Pelvic Congestion Syndrome, but can also be found in asymptomatic women.
- MRI is the imaging modality of choice, offering good spatial and temporal resolution, as well as the possibility to show other pathologic conditions causing chronic pelvic pain.
- In our experience, examinations of diagnostic quality are more reliably achieved using dynamic contrast-enhanced MR-angiography than with its time-resolved counterpart.

organs or the intestine, like endometriosis or inflammatory bowel disease. The findings of dilatation of the peri-uterine and peri-ovarian venous plexus and ovarian veins are the same as in ultrasonography (Figs. 1-4). Ovarian vein reflux can directly be shown using time-resolved MR-angiography [9], as well as be observed in dynamic contrast-enhanced MR-angiography in some cases (Figs. 2-4). Compared to ultrasound, different cut-off values for venous diameters in cross-sectional modalities have been proposed by Coakley et al.: Identification of four ipsilateral pelvic veins, at least one of which measuring > 4 mm, and an ovarian vein diameter > 8 mm are regarded as consistent with pelvic varices and, in the appropriate clinical setting, with Pelvic Congestion Syndrome [10].

Selective retrograde catheter venography of the ovarian veins using a femoral approach is regarded as the imaging gold standard, which can show retrograde flow in the ovarian and pelvic veins, incompetent pelvic veins and congestion of flow in the ovarian, pelvic, vulvovaginal or thigh veins [11]. Drawbacks are it being an invasive procedure and the use of ionising radiation. In our institution, percutaneous venography is accordingly performed with the intent of therapeutic intervention in the same session.

MRI protocol and post-processing

MRI is usually performed using a body phase-array coil. In our institution the examination includes axial T2*-weighted TrueFISP sequences covering the abdomen and pelvis from the upper pole of the left kidney to the proximal thighs, pre-contrast T1-weighted fast low angle shot (FLASH) in axial plane and T2-weighted turbo spin echo in axial and sagittal planes covering the pelvis. Five phases of dynamic contrast-enhanced angiography (Gd-DOTA [Dotarem®], 0.1 mmol/kg body weight) are performed in coronal plane. Contrast medium

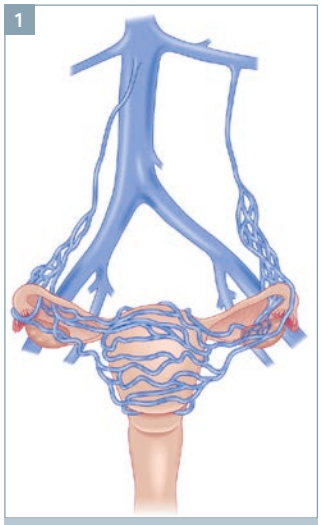

1 Illustration showing the uterine and ovarian venous plexus, the ovarian veins draining into the inferior Vena cava on the right and the left renal vein on the left.

Illustration by Wolfgang Herzig.

2 Arterial-predominant phase contrast-enhanced MR-angiography in a 37-year-old patient shows early filling of the dilated left ovarian vein indicating reflux as well as dilatation of ovarian and uterine venous plexus of the left side (arrowheads in cranio-caudal order, respectively).

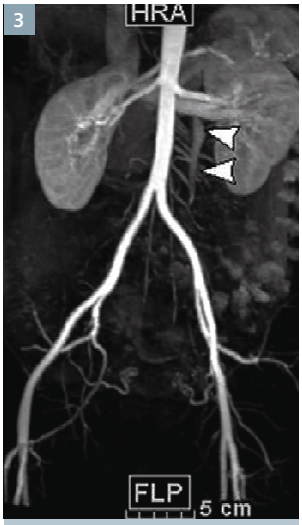

3 Arterial-predominant phase contrast-enhanced MR-angiography in a 33-year-old patient showing early filling of the left ovarian vein (arrowheads) indicating reflux.

4 Contrast-enhanced MR-angiography in the same patient as in Figure 3 shows progressive filling of the left ovarian vein (arrowheads) in a later phase.

Sequence	TR [ms]	TE [ms]	Flip angle	FOV [mm]	Slice thickness [mm]
localizer	5.5	2.45	20°	430	6
t2_trufi_tra_bh 2 blocks covering abdomen and pelvis	4.64	2.32	70°	360	6
t1_fl2d_tra_mbh pelvis	176	4.76	70°	360	6
t2_tse_sag pelvis	5100	90	150°	210	4
t2_tse_tra pelvis	3570	100	150°	210	4
test_bolus	34.61	1.29	30°	420	21
fl3d_cor abdomen and pelvis, injection of contrast media (Dotarem® 0,1 mmol/kg b.w.) after first phase	3.03	1.09	25°	360	0.94
t1_vibe_dixon_tra_caipi abdomen and pelvis	5.79	2.28	10°	320	3

Table 1: MRI Protocol used in our institution (MAGNETOM Aera 1.5T)

is injected after acquisition of the first phase, which is later used for subtraction. Finally a post-contrast 3D fat-suppressed T1-weighted sequence covering the abdomen and pelvis in axial plane acquisition is performed (CAIPIRINHA parallel imaging technique). The protocol is summarized in Table 1.

The contrast-enhanced angiography images are post-processed using maximum intensity projection (MIP) algorithms.

The whole examination is completed in approximately 20 minutes (Siemens MAGNETOM Aera 1.5T).

We employ dynamic contrast-enhanced MR-angiography due to the higher spatial resolution it provides compared to time-resolved angiography (TWIST technique). Before switching to gadoterate-based contrast media, we used a gadofosveset-based product (Ablavar® or formerly Vasovist®) prior to its withdrawal from the European market [12].

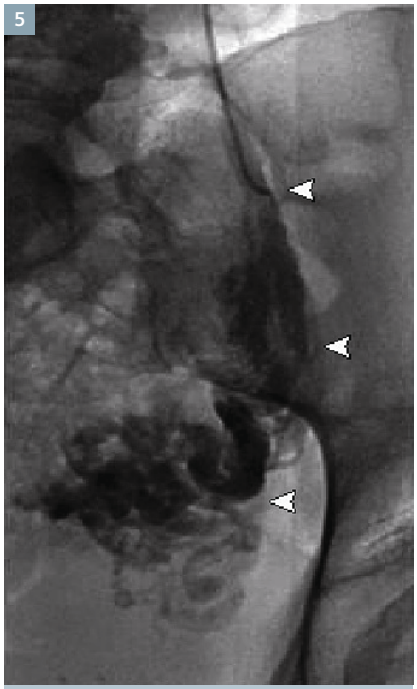

5 Percutaneous catheter-venography in the 37-year-old patient already shown in Fig. 2: the catheter tip lies in the distal left ovarian vein; ovarian and uterine plexus varicosities are shown with retrograde injection of contrast media (arrowheads in craniocaudal order, respectively).

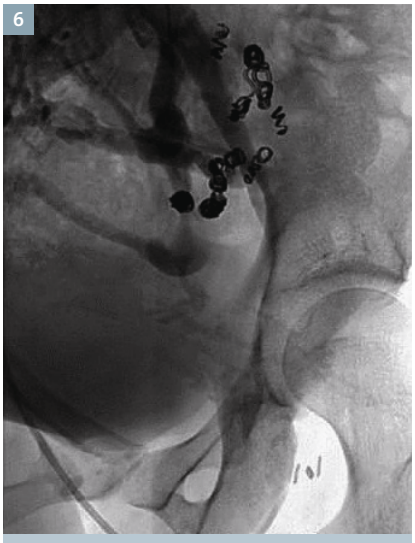

6 Catheter-venography in the same patient as in Figures 2 and 5 after placement of multiple coils in the left ovarian vein. The ovarian plexus is successfully excluded from retrograde flow. Contrast is seen in the internal iliac veins and its tributaries.

Treatment

Even if a causal relationship between pelvic varicosities, venous stasis and pelvic pain has not been proven, it is supported by limited data from numerous smaller studies. Conservative treatment with gonadotropin-releasing hormone agonists or synthetic progestins has been reported to have positive effects on patients' pain levels [1]. Nevertheless, ovarian and pelvic vein embolisation has now become the standard of treatment of Pelvic Congestion Syndrome. The procedure is commonly performed under analgosedation, using embolisation coils, sclerosants or a combination of both [13]. Success rates of up to 80% have been reported after a follow-up of 5 years [14]. An exemplary case is shown in Figures 5 and 6.

Conclusion

Pelvic Congestion Syndrome is an important cause of chronic pelvic pain, typically occurring in women of reproductive age. When clinically suspected, imaging can reliably confirm the diagnosis showing dilated ovarian and pelvic veins or retrograde venous flow. Notably, different cut-off values have been proposed for ultrasound and CT/MRI. MRI is considered the modality of choice and may better show other pathologic conditions causing the symptoms. Treatment by ovarian and pelvic vein embolisation can provide long-term benefit.

Acknowledgements

The help of Alexander Peters, Kantonsspital Baden, and Johan Post, Siemens Schweiz, for critically reviewing the technical MRI-related aspects, is gratefully acknowledged.

References

1 Champaneria R, Shah L, Moss J, Gupta JK, Birch J, Middleton LJ, et al. The relationship between pelvic vein incompetence and chronic pelvic pain in women: systematic reviews of diagnosis and treatment effectiveness. Health Technol Assess. 2016;20(5).

2 Cura M, Cura A. What is the significance of ovarian vein reflux detected by computed tomography in patients with pelvic pain? Clin Imaging. 2009 Jul-Aug;33(4).

3 Phillips D, Deipolyi AR, Hesketh RL, Midia M, Oklu R. Pelvic congestion syndrome: etiology of pain, diagnosis, and clinical management. J Vasc Interv Radiol. 2014 May;25(5).

4 Borghi C, Dell' Atti L. Pelvic congestion syndrome: the current state of the literature. Arch Gynecol Obstet. 2016 Feb;293(2).

5 Arnoldussen CWKP, de Wolf MAF, Wittens CHA. Diagnostic imaging of pelvic congestive syndrome. Phlebology. 2015; Vol. 30(1S).

6 Asciutto G, Asciutto KC, Mumme A, Geier B. Pelvic venous incompetence: reflux patterns and treatment results. Eur J Vasc Endovasc Surg. 2009 Sep;38(3).

7 Basili G, Romano N, Bimbi M, Lorenzetti L, Pietrasanta D, Goletti O. Postpartum ovarian vein thrombosis. JSLS. 2011 Apr-Jun;15(2).

8 Park SJ, Lim JW, Ko YT, Lee DH, Yoon Y, Oh JH, et al. Diagnosis of Pelvic Congestion Syndrome Using Transabdominal and Transvaginal Sonography. Am J Roentgenol. 2004;182.

9 Kim CY, Miller Jr. MJ, Merkle EM. Time-Resolved MR Angiography as a Useful Sequence for Assessment of Ovarian Vein Reflux. Am J Roentgenol. 2009;193.

10 Coakley FV, Varghese SL and Hricak H. CT and MRI of pelvic varices in women. J Comput Assist Tomogr. 1999;23.

11 Geier B, Barbera L, Mumme A, et al. Reflux patterns in the ovarian and hypogastric veins in patients with varicose veins and signs of pelvic venous incompetence. Chir Ital. 2007;59.

12 European Medicines Agency. Public statement on Ablavar (gadofosveset). 24.10.2011. EMA/854517/2011.

13 Black CM, Thorpe K, Venrbux A, Kim HS, Millward SF, Clark TW et al. Research reporting standards for endovascular treatment of pelvic venous insufficiency. J Vasc Interv Radiol. 2010 Jun;21(6).

14 Kim HS, Malhotra AD, Rowe PC, Lee JM, Venbrux AC. Embolotherapy for pelvic congestion syndrome: long-term results. J Vasc Interv Radiol. 2006 Feb;17(2 Pt 1).

Contact

Prof. Rahel A. Kubik-Huch, M.D., M.P.H.
Head of Department
Institute of Radiology
Kantonsspital Baden
Im Ergel 1
5404 Baden
Switzerland
rahel.kubik@ksb.ch

Contact

Gligor Milosevic, M.D.
Institute of Radiology
Kantonsspital Baden
Im Ergel 1
5404 Baden
Switzerland
gligor.milosevic@ksb.ch

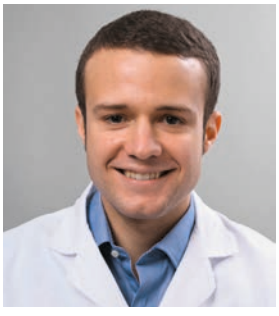

Simultaneous Multi-Slice RESOLVE for Optimized Diffusion-Weighted Imaging of the Breast at 3 Tesla

Lukas Filli, M.D.[1]; Soleen Ghafoor, M.D.[1]; David Kenkel, M.D.[1]; Wei Liu, Ph.D.[2]; Elisabeth Weiland, Ph.D.[3]; Gustav Andreisek, M.D., MBA[4]; Thomas Frauenfelder, M.D.[1]; Val M. Runge, M.D.[5]; Andreas Boss, M.D., Ph.D.[1]

[1] Institute of Diagnostic and Interventional Radiology, University Hospital Zurich, University of Zurich, Switzerland
[2] Siemens Shenzhen Magnetic Resonance Ltd., Shenzhen, China
[3] Siemens Healthineers, MR Application Development, Erlangen, Germany
[4] Kantonsspital Münsterlingen, Switzerland
[5] Inselspital Bern, Switzerland

Abstract

Simultaneous multi-slice (SMS) acquisition significantly reduces scan times in clinical MRI. Readout-segmented echo planar imaging (RESOLVE) is a recently developed sequence which produces sharp diffusion-weighted images with high spatial resolution. In this article, we describe our early experience with SMS RESOLVE[1] for optimized diffusion-weighted imaging of the breast. SMS RESOLVE combines the advantages of high image quality and greatly reduced scan times.

[1] The product is still under development and not commercially available yet. Its future availability cannot be ensured.

Introduction

Diffusion-weighted imaging improves diagnostic accuracy of breast MRI [1-3] and may be used for predicting treatment outcome in breast cancer [4, 5]. Traditionally, diffusion-weighted imaging is based on single-shot echo planar imaging (EPI). With this technique, the entire *k*-space is filled during a single T2* decay, which makes imaging prone to signal blurring and susceptibility artifacts. These technical obstacles can be overcome with readout-segmented EPI (RESOLVE), which divides the *k*-space trajectory into separate segments along the readout direction and allows short echo times [6]. Because the resulting images are very sharp and of high spatial resolution, RESOLVE has superior diagnostic performance compared to single-shot EPI in breast imaging [7].

Since every readout segment in the *k*-space is preceded by a separate radiofrequency pulse, RESOLVE is limited by relatively long acquisition times. An interesting method to compensate for this is simultaneous multi-slice (SMS) imaging, which is a three-dimensional parallel imaging method. In brief, SMS utilizes the different elements of a phased-array coil to acquire signal from multiple slices at once, thereby enabling accelerated image acquisition. The concept of SMS has been elucidated in detail in the MAGNETOM Flash (63) 3/2015 edition. That edition also includes an

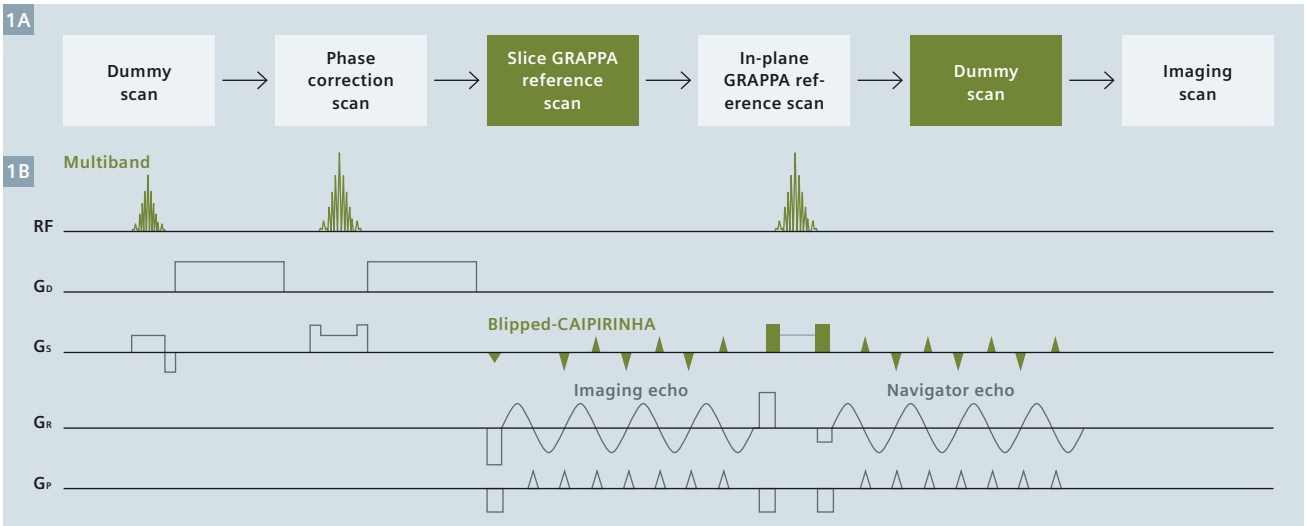

1 SMS RESOLVE sequence diagram for a complete acquisition **(1A)** and for a single readout segment **(1B)**. SMS modifications are colored green.

article by Frost et al., who developed SMS RESOLVE in 2014 [8]. Here, we present our initial experience with this novel pulse sequence for optimized diffusion-weighted imaging of the breast.

Image acquisition

We routinely perform breast MRI on a clinical 3 Tesla scanner (MAGNETOM Skyra with TimTX TrueShape) using an 18-channel breast coil (Siemens Healthcare). We can acquire SMS RESOLVE images of the breast with a dedicated work-in-progress package running on the *syngo* MR VE11A platform. The sequence applies a conventional phase-encoding direction blip for EPI readouts along with an additional blip in the slice direction ("blipped CAIPIRINHA") [9]. Furthermore, like the conventional RESOLVE sequence, it contains two-dimensional navigator correction [6] (Fig. 1).

Comparison between RESOLVE and SMS RESOLVE

In a recently published study, we compared the image quality of conventional RESOLVE with SMS RESOLVE (with twofold and threefold slice acceleration) for axial diffusion-weighted imaging of the breast [10]. All imaging parameters were kept constant except for the slice acceleration factor and resulting adjustments of repetition time (lowest possible value as determined by the scanner console) and echo time. Details of imaging parameters are provided in Table 1.

Parameter	RESOLVE (no slice acceleration) 4 min 21 sec	SMS RESOLVE (2-fold acceleration) 2 min 35 sec	SMS RESOLVE (3-fold acceleration) 1 min 44 sec
Repetition time [ms]	5410	2250	1450
Echo time [ms]	56	55	55
Slices	28	28	27 (28 not possible)
Distance factor	20%		
Voxel size [mm³]	1.2 x 1.2 x 5.0		
Readout segments	5		
Readout partial Fourier	5/8		
Field-of-view [mm²]	340 x 136		
Bandwidth [Hz/Pixel]	829		
Echo spacing [ms]	0.38		
iPAT (GRAPPA) factor	2		
Averages	b=50 (1), b=800 (4)		

Table 1: Imaging parameters of conventional RESOLVE and SMS RESOLVE at our institution.

With twofold and threefold slice acceleration, we found a slight decline in signal-to-noise ratio compared to conventional RESOLVE, which however was not statistically significant ($p = 0.83$). In other words, SMS RESOLVE offers a substantial gain in signal-to-noise ratio per unit of time. Mean ADC values in fibroglandular breast tissue were $1.62 \pm 0.29 \times 10^{-3}$ mm²/s, with almost no differences found among the sequences ($p = 0.99$) (Figs. 2, 3). Image quality was rated similarly high between RESOLVE and twofold accelerated SMS RESOLVE. With threefold accelerated SMS RESOLVE, we perceived more shading in the prepectoral region, which may be reduced by changing over from 5/8 to 6/8 readout partial Fourier acquisition in the future. The results of our study suggest that SMS can be applied to RESOLVE for optimized breast imaging, with an optimal slice acceleration factor of 2 or potentially 3.

2

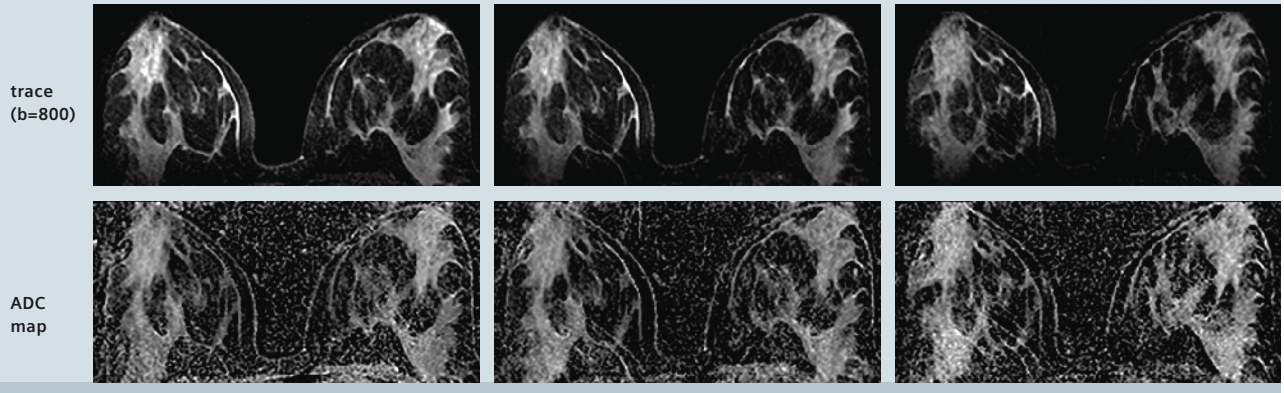

2 Example 3T diffusion-weighted images from a 26-year-old healthy volunteer with corresponding ADC maps. The in-plane resolution is 1.2 x 1.2 mm². There is almost no visible difference between RESOLVE and 2-fold accelerated SMS RESOLVE. With 3-fold acceleration, the image is still sharp and most parts of the breast can be depicted very well, whereas the prepectoral region is slightly affected by shading.

3

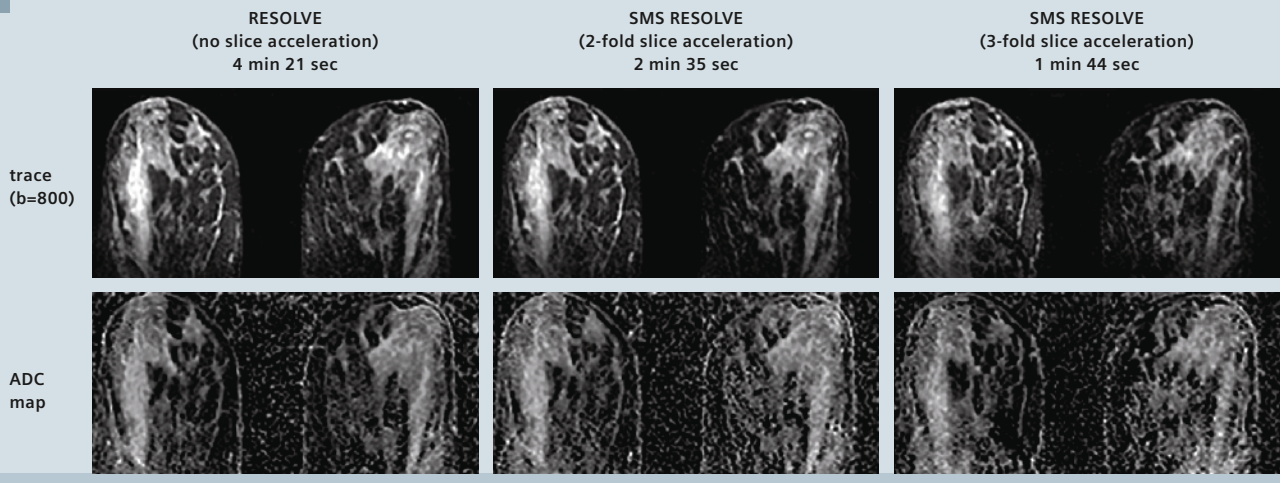

3 Example diffusion-weighted images from a 38-year-old healthy volunteer with large breasts. Except for the prepectoral shading artifact at 3-fold acceleration, there is almost no visible difference between the sequences despite substantial differences regarding acquisition time.

Discussion

In a recent study, RESOLVE showed many advantages over single-shot EPI for diffusion-weighted imaging of the breast. These included reduced blurring, reduced geometric distortions, better depiction of breast lesions, and improved discrimination between benign and malignant lesions [7]. SMS RESOLVE drives this image optimization one step forward: It reduces the acquisition time while maintaining similar image quality and ADC accuracy compared to conventional RESOLVE as long as a moderate acceleration factor is applied.

With regard to SMS RESOLVE of the breast, the main advantage of SMS acquisition lies in the reduction of acquisition time. Alternatively, depending on the application or body region, the gain in SNR efficiency offered by SMS may be reinvested in extended slice coverage or to increase spatial resolution while keeping the acquisition time constant.

In conclusion, SMS RESOLVE enables the acquisition of high-quality diffusion-weighted images at greatly reduced scan times. Our initial experience with SMS RESOLVE for breast imaging is very promising for the future.

References

1 Bickel H, Pinker-Domenig K, Bogner W, Spick C, Bago-Horvath Z, Weber M, et al. Quantitative apparent diffusion coefficient as a noninvasive imaging biomarker for the differentiation of invasive breast cancer and ductal carcinoma in situ. Invest Radiol. 2015;50(2):95-100.

2 Bogner W, Gruber S, Pinker K, Grabner G, Stadlbauer A, Weber M, et al. Diffusion-weighted MR for differentiation of breast lesions at 3.0 T: how does selection of diffusion protocols affect diagnosis? Radiology. 2009;253(2):341-51.

3 Pinker K, Bogner W, Baltzer P, Karanikas G, Magometschnigg H, Brader P, et al. Improved differentiation of benign and malignant breast tumors with multiparametric 18fluorodeoxyglucose positron emission tomography magnetic resonance imaging: a feasibility study. Clin Cancer Res. 2014;20(13):3540-9.

4 Iacconi C, Giannelli M, Marini C, Cilotti A, Moretti M, Viacava P, et al. The role of mean diffusivity (MD) as a predictive index of the response to chemotherapy in locally advanced breast cancer: a preliminary study. Eur Radiol. 2010;20(2):303-8.

5 Liu S, Ren R, Chen Z, Wang Y, Fan T, Li C, et al. Diffusion-weighted imaging in assessing pathological response of tumor in breast cancer subtype to neoadjuvant chemotherapy. Journal of magnetic resonance imaging : JMRI. 2015;42(3):779-87.

6 Porter DA, Heidemann RM. High resolution diffusion-weighted imaging using readout-segmented echo-planar imaging, parallel imaging and a two-dimensional navigator-based reacquisition. Magnetic resonance in medicine. 2009;62(2):468-75.

7 Bogner W, Pinker-Domenig K, Bickel H, Chmelik M, Weber M, Helbich TH, et al. Readout-segmented echo-planar imaging improves the diagnostic performance of diffusion-weighted MR breast examinations at 3.0 T. Radiology. 2012;263(1):64-76.

8 Frost R, Jezzard P, Douaud G, Clare S, Porter DA, Miller KL. Scan time reduction for readout-segmented EPI using simultaneous multislice acceleration: Diffusion-weighted imaging at 3 and 7 Tesla. Magnetic resonance in medicine. 2014.

9 Setsompop K, Gagoski BA, Polimeni JR, Witzel T, Wedeen VJ, Wald LL. Blipped-controlled aliasing in parallel imaging for simultaneous multislice echo planar imaging with reduced g-factor penalty. Magnetic resonance in medicine. 2012;67(5):1210-24.

10 Filli L, Ghafoor S, Kenkel D, Liu W, Weiland E, Andreisek G, et al. Simultaneous multi-slice readout-segmented echo planar imaging for accelerated diffusion-weighted imaging of the breast. Eur J Radiol. 2016;85(1):274-8.

Contact

Lukas Filli, M.D.
Institute of Diagnostic and Interventional Radiology
University Hospital Zurich, University of Zurich
Raemistrasse 100
CH-8091 Zurich
Switzerland
Phone: +41 44 225 11 11
lukas.filli@usz.ch

PI-RADS 2
Standardized Prostate MRI Reporting

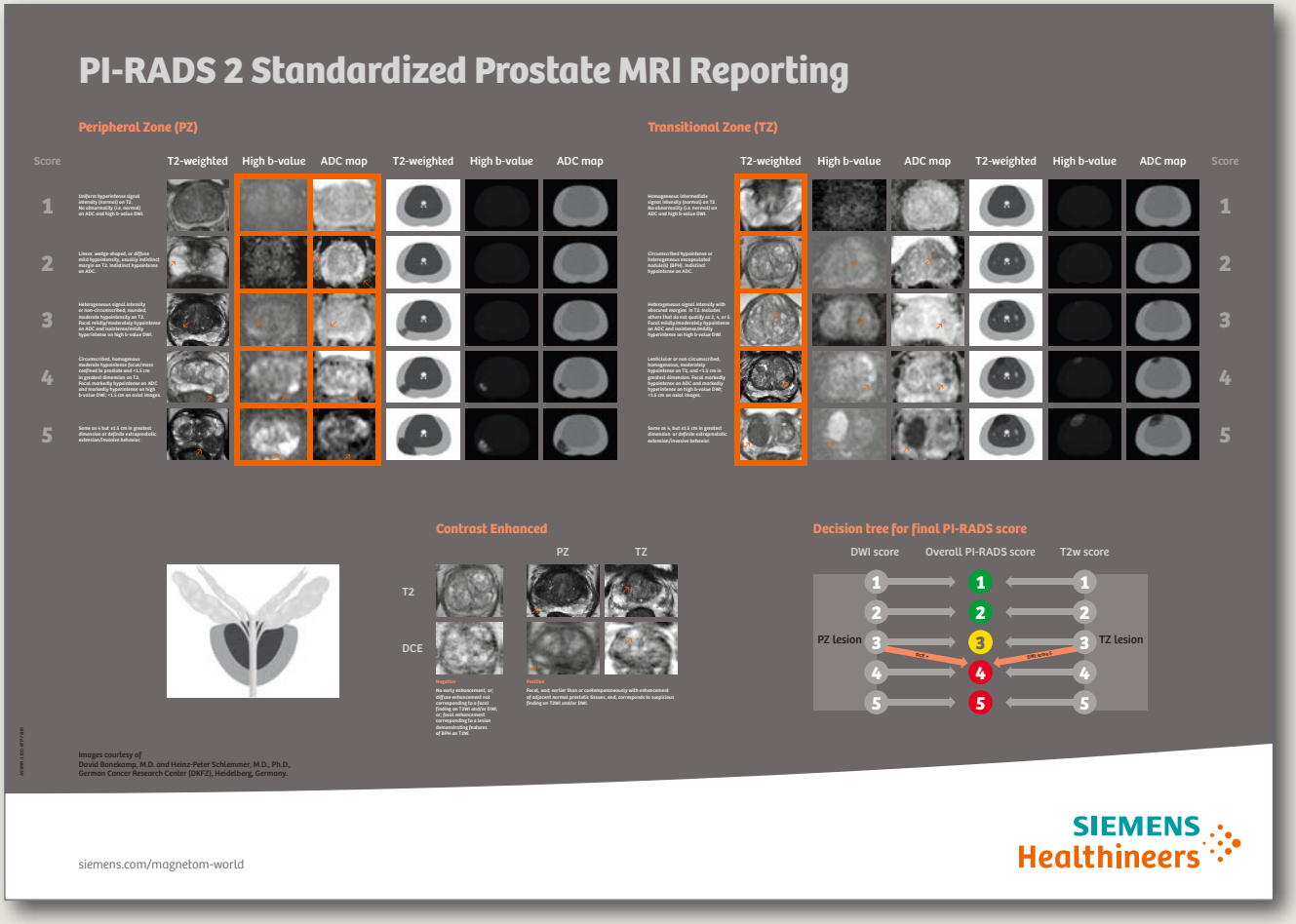

Visit us **at www.siemens.com/magnetom-world**

Go to > Publications > Subscriptions > **MRI Poster**

Get your free copy of the PI-RADS 2 poster

Transurethral MR-Thermometry Guided Ultrasound Ablation of the Prostate – The Heidelberg Experience During Phase I of the TULSA-PRO Device Trial

Maya Mueller-Wolf[1]; Matthias Röthke[1]; Boris Hadaschik[2]; Sascha Pahernik[2]; Joseph Chin[4]; James Relle[5]; Mathieu Burtnyk[6]; Simon Dubler[3]; Johann Motsch[3]; Markus Hohenfellner[2]; Hein-Peter Schlemmer[1]; David Bonekamp[1]

[1] Department of Radiology, German Cancer Research Center (DKFZ), Heidelberg, Germany
[2] Department of Urology, University Hospital Heidelberg, Heidelberg, Germany
[3] Department of Anesthesiology, University Hospital Heidelberg, Heidelberg, Germany
[4] Department of Urology, Western University, London Victoria Hospital, London Health Sciences Center, London, ON, Canada
[5] Department of Urology, Beaumont Health System, Royal Oak, MI, USA
[6] Department of Clinical Affairs, Profound Medical Inc., Toronto, ON, Canada

Background

Prostate cancer (PCa) is the malignancy most commonly diagnosed in men in the western hemisphere. Despite the substantial increase of predominantly low-grade and early stage PCa diagnosed since the appearance of prostate-specific antigen (PSA) screening, PCa remains the second most common cause of cancer-related death in men in the developed world [1], highlighting its aggressive potential and the need for screening and therapy.

The use of prostate-specific antigen (PSA) screening has decreased the average age at diagnosis and increased the proportion of men diagnosed with low-grade, small-volume, localized prostate cancer [2, 3]. Average age at diagnosis is 66 years. While PSA screening is sensitive for prostate cancer, its specificity is low. False positive PSA elevation may be related to benign changes such as prostate hyperplasia (BPH) or prostatitis. Also, PSA and gland size-adjusted parameters such as PSA-density (PSAD) have limited ability to differentiate between BPH and cancer, or between the aggressive life-threatening and low-grade slow-growing forms of the disease [4].

After detection of significant PCa by biopsy, conventional prostate cancer therapy typically consists of either surgical radical prostatectomy or radiation therapy. Due to persistent limitations to predict the aggressiveness of PCa, many patients still receive overtreatment of their disease and are exposed to the associated morbidity with potential long-term erectile dysfunction, urinary incontinence, and bowel complications that may significantly compromise quality of life [5]. It is well-known that low-risk PCa may carry only an insignificant mortality risk compared to men without PCa [6]. Accordingly, the concept of active surveillance (AS) was developed which consists of following patients with low-grade PCa by PSA testing and possibly magnetic resonance imaging (MRI) until significant PCa is detected. Recently, MRI has shown promise to increase detection of PCa compared to standard transrectal ultrasound-guided systematic (TRUS) biopsies [7], with preferential detection of intermediate and higher grade PCa. Negative MRI does currently not exclude significant PCa, although the risk of significant PCa was reported to be lower in patients with negative MRI [8]. The

1 Patient setup in the MRI suite with MR technologist, physicist and anesthesiologist featuring MR-compatible anesthesia machine and monitoring devices needed for general anesthesia on location at the DKFZ Heidelberg, Germany.

continued improvement of MRI detection, localization and grading of PCa and growing data on sensitivity and specificity of MR for PCa detection increase the foundation for evidence-based development of alternative, less invasive treatments of PCa by local therapy. This addresses an important need as intermediate therapeutic approaches between AS and radical therapy which provide good control of local disease are highly sought-after. With such therapies it would be possible, both, to tailor therapy to the intermediate-risk group and reduce permanent adverse side effects while also addressing the needs of the growing number of young men diagnosed with small low- to intermediate grade PCa and those of older patients who are not suitable candidates for surgery.

Minimally invasive ablative therapies have the potential to achieve good oncologic outcomes and low morbidity. Adding MR guidance to ablative therapies offers the advantage of direct monitoring of therapy without the need for intermodality co-registration. Furthermore, MR allows temperature monitoring in the form of MR thermometry which can be used to drive a feedback loop for optimal delivery of thermal energy to the target tissue. At the same time, MR-guidance is based on the principal and currently most promising imaging modality for the visualization of PCa. By combining these properties, a MR thermometry-guided ultrasound thermal ablation technique appears very promising to achieve precise lesion targeting and local tumor control. This report is based on our institutional experience during the recent prospective, multi-center, Phase I clinical trial of the TULSA-PRO (described below) device. Within this phase I trial, the TULSA-PRO device was used to heat and ablate prostate tissue in 30 men with localized prostate cancer. Of the 30 men included in the trial, 14 were treated at our site in Heidelberg. All procedures were performed within a 3T Siemens MAGNETOM Tim Trio MR system. Twelve-month follow-up results of the phase I trial have been analyzed and published [9]. The objective of the phase I trial was to determine the clinical safety and feasibility of the TULSA-PRO device for whole-gland prostate ablation in the primary treatment setting of patients with localized prostate cancer. As the precision of targeting was being evaluated during the trial, all treatments included a 3-mm safety margin to the prostate capsule with an expected 10% residual viable prostate tissue expected around the ablation margin.

TULSA overview

MRI Guided **T**ransurethral **UL**trasound **A**blation (TULSA) is a novel, minimally invasive technology that ablates the entire prostate gland, via the urethra. It combines quantitative image-based planning, monitoring, and treatment control with transurethral delivery of therapeutic ultrasound to ablate prostate tissue (both benign and malignant) through thermal coagulation [9, 10].

The procedure is conducted within an MRI scanner (Fig. 1), which provides high-resolution planning images that are registered to real-time quantitative thermometry images acquired during treatment. A closed-loop temperature feedback control algorithm modulates the intensity, frequency, and rotation rate of the ultrasound, shaping the ablation volume with high accuracy to individual prostate anatomy and reducing the risk of possible damage to peri-prostatic structures (rectum, urinary sphincter and neurovascular bundles) [11].

The MRI scanner provides real-time thermal dosimetric monitoring for feedback-controlled ultrasound ablation.

TULSA-PRO™ technical principle

During the phase I clinical trial, we used the TULSA-PRO device developed by Profound Medical Inc. (Toronto, Canada).

The TULSA-PRO System components are depicted in Figure 2. A rigid

2 TULSA-PRO System Components. The Ultrasound Applicator, Endorectal Cooling Device and Positioning System are inside the Scanning room on the MRI bed. The Treatment Delivery Console and System Electronics remain outside the Scanning room, in the Console and Equipment room, respectively. *Figure courtesy of Profound Medical Inc.*

Ultrasound Applicator (UA) is inserted into the urethra, making contact with and delivering ultrasound energy directly into the prostate gland. A linear array of 10 independent ultrasound transducer elements emits directional (but unfocused) high-intensity ultrasound energy directly into the adjacent prostate, quickly raising tissue temperatures to thermal coagulation. The configuration of the ultrasound beams enables treatment of a large volume of prostate tissue, resulting in shorter treatment times of typically less than 40 minutes. Fluid is circulated through the UA, providing 1-2 mm of urethral tissue preservation. A separate circuit flows water through the Endorectal Cooling Device (ECD) to provide thermal protection of rectal tissue during ultrasound ablation delivery. Figure 3 shows a conceptual illustration and a sagittal MR image of the UA and ECD in a patient.

The UA is held in situ with a Positioning System (PS) that provides remote robotic linear and rotational motion of the device within the prostate. During treatment, the UA is rotated continuously by the PS, ensuring a continuous pattern of thermal damage and preventing cold spots between ultrasound sonications. The System

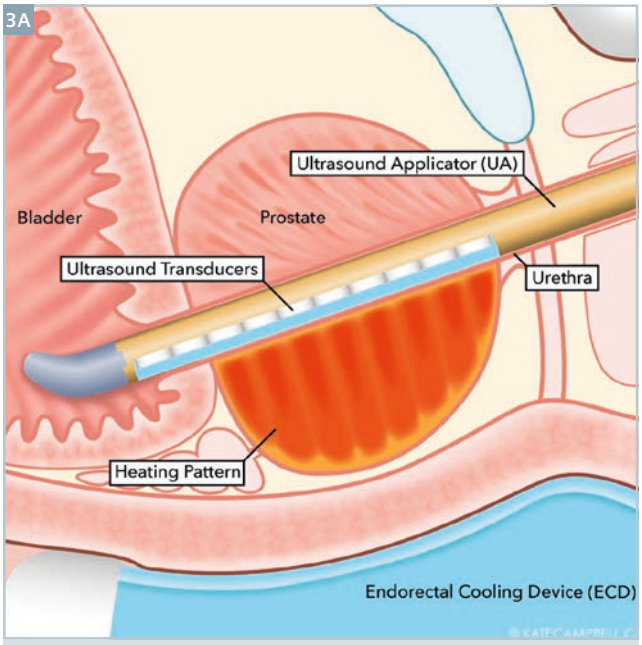

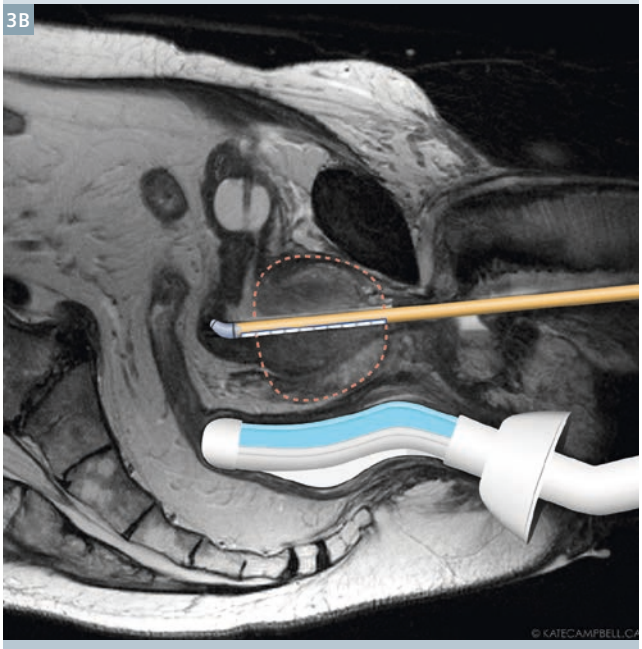

3 Conceptual illustration **(3A)** and sagittal MR image **(3B)** of the UA and ECD in a patient.
Figure courtesy of Profound Medical Inc.

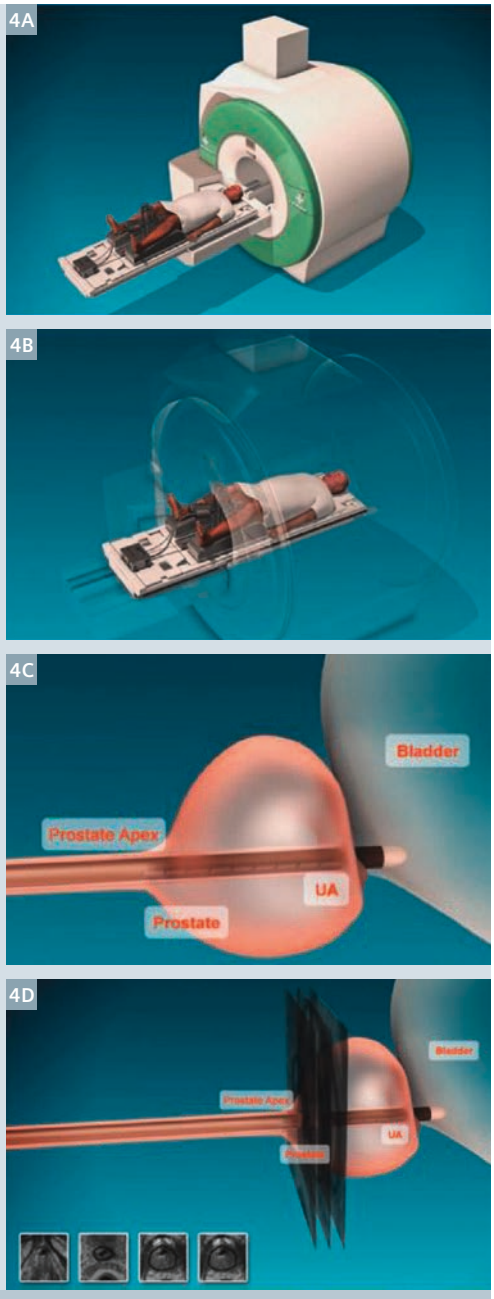

4 Conceptual illustration **(3A)** and sagittal MR image **(3B)** of the UA and ECD in a patient.
Figure courtesy of Profound Medical Inc.

Cart (SC) positioned in the MRI equipment room, houses the fluid circuits and the System Electronics (SE), which power the UA transducer elements and PS motors.

The treatment is conducted completely within an MRI, providing real-time temperature images of the heated region to be acquired as the ultrasound treatment is delivered. A custom software interface (Treatment Delivery Console, TDC) communicates with the MR scanner to display high-resolution images for device positioning and treatment planning, and temperature images for treatment monitoring and control. Using MRI thermometry during treatment, dynamic temperature feedback control over the intensity of the ultrasound beams and rotation of the UA can shape the pattern of thermal coagulation accurately and precisely in the prostate gland, thereby reducing the risk of possible damage to important surrounding anatomy, such as, the rectum, urinary sphincters and neurovascular bundles [11].

During the procedure, the software automatically adjusts ultrasound parameters (power, frequency, and device rotation rate) to achieve at least the target temperature (≥ 55°C) within the target boundary. Prostate tissue temperature feedback is provided from the MR scanner in real-time during the procedure and is displayed in the form of a temperature map (see Fig. 5).

The procedure

Patients undergo general anesthesia prior to insertion of suprapubic catheter and a transurethral guidewire. The patient is then moved onto the MR bed and the UA is inserted manually over the guidewire, followed by the ECD (Fig. 4A).

Under MR guidance and remote operation of the robotic PS, the UA is positioned precisely within the prostatic urethra (Figs. 4B and 4C). High-resolution prostate MR images are acquired for treatment planning (T2-weighted turbo spin echo, echo/repetition time 52/3000 ms, 26-cm field of view, 1 x 1 x 2.5 mm^3 voxels).

Using the TDC, the physician traces the outer prostate boundary on oblique-axial images acquired transverse to the UA and aligned with each transducer element (Fig. 4D).

The target prostate volume is defined from the outer prostate boundary drawn by the physicians, and heated to ≥55°C, the temperature critical to achieve acute thermal coagulation (Fig. 5). Treatment begins with high-intensity ultrasound energy delivered to the prostate in one complete rotation of the UA under active MRI thermometry feedback control (proton resonance frequency shift method, echo planar imaging, oblique-axial aligned with planning images, echo/repetition time 8/350 ms, 26-cm field of view, 2 x 2 x 4 mm^3 voxels, 0.8°C average precision *in vivo* human prostate). Real-time MRI thermometry images are acquired every 5.9 s, providing continuous assessment of a three-dimensional temperature volume during treatment. After treatment, contrast-enhanced (CE) MRI may be acquired to confirm non-perfused tissue volume.

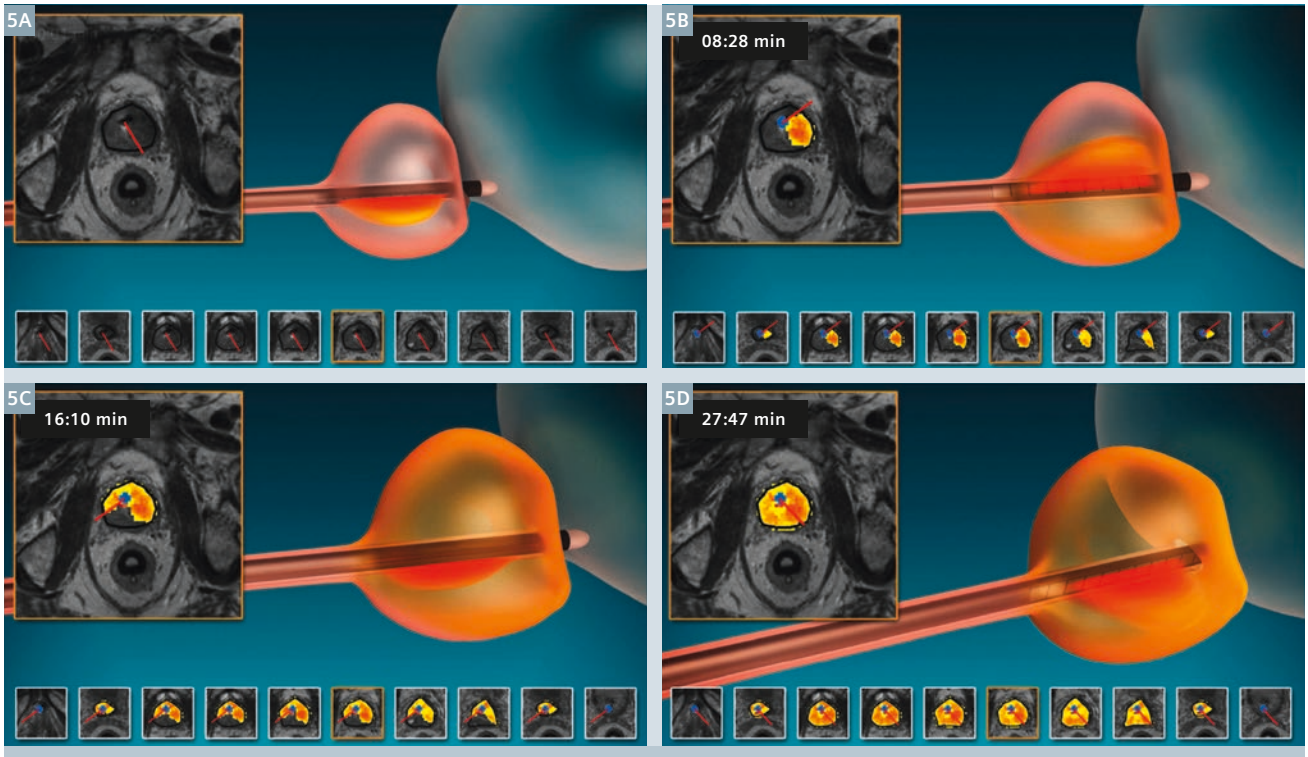

5 Temporal evolution of a MRI-guided TULSA treatment, completed in one full rotation of the UA.
Figure courtesy of Profound Medical Inc.

Case 1

A 70-year-old patient in good health, initially managed on active surveillance, was enrolled in the Phase I study and treated with the TULSA-PRO. In 2012, the patient presented with a PSA of 6.3 ng/ml, clinical stage T1c and initial biopsy showing 1/12 positive cores with Gleason Score 3+3. In 2013, the patient's PSA increased to 7.5 ng/ml and he subsequently underwent a second biopsy, this time with 6/26 positive cores with Gleason Score 3+3. The patient then enrolled in the TULSA-PRO study and was treated in October 2013.

The prostate volume was 33 cc, and the duration of the ultrasound treatment was 25 min. Figure 6A shows an example mid-gland MR thermometry image demonstrating the millimeter accuracy and precision of prostate ablation. Thermometry findings are confirmed on post-treatment CE-MRI with the hypointense region of non-perfused tissue concordant with the region of cytoablative thermal treatment (Fig. 6B). Figures 6C and D illustrate the prostate anatomical changes at 12 months, demonstrating an 85% decrease in gland volume.

Figure 7 illustrates the changes in PSA and patient quality of life following treatment with the TULSA-PRO. PSA reached a nadir of <0.10 ng/ml at 1 month and remained stable to 0.25 ng/ml at 24 months. The International Prostate Symptom Score (IPSS, range from 0 "no symptoms" to 35 "severe symptoms") initially increased at 1 month and returned to baseline at 3 months after treatment with the TULSA-PRO, further decreasing at 24 months. Internal Index of Erectile Function (IIEF) Item 2 (erection firmness sufficient for penetration, range from 0 "never or almost never" to 5 "always or almost always") remained unchanged after treatment with the TULSA-PRO through 24 months of follow-up. This patient presented with a total of one adverse event attributable to treatment with the TULSA-PRO, which was an asymptomatic urinary tract infection that was resolved with oral antibiotics. At 12 months, the patient's 12-core transrectal follow-up biopsy was negative for adenocarcinoma.

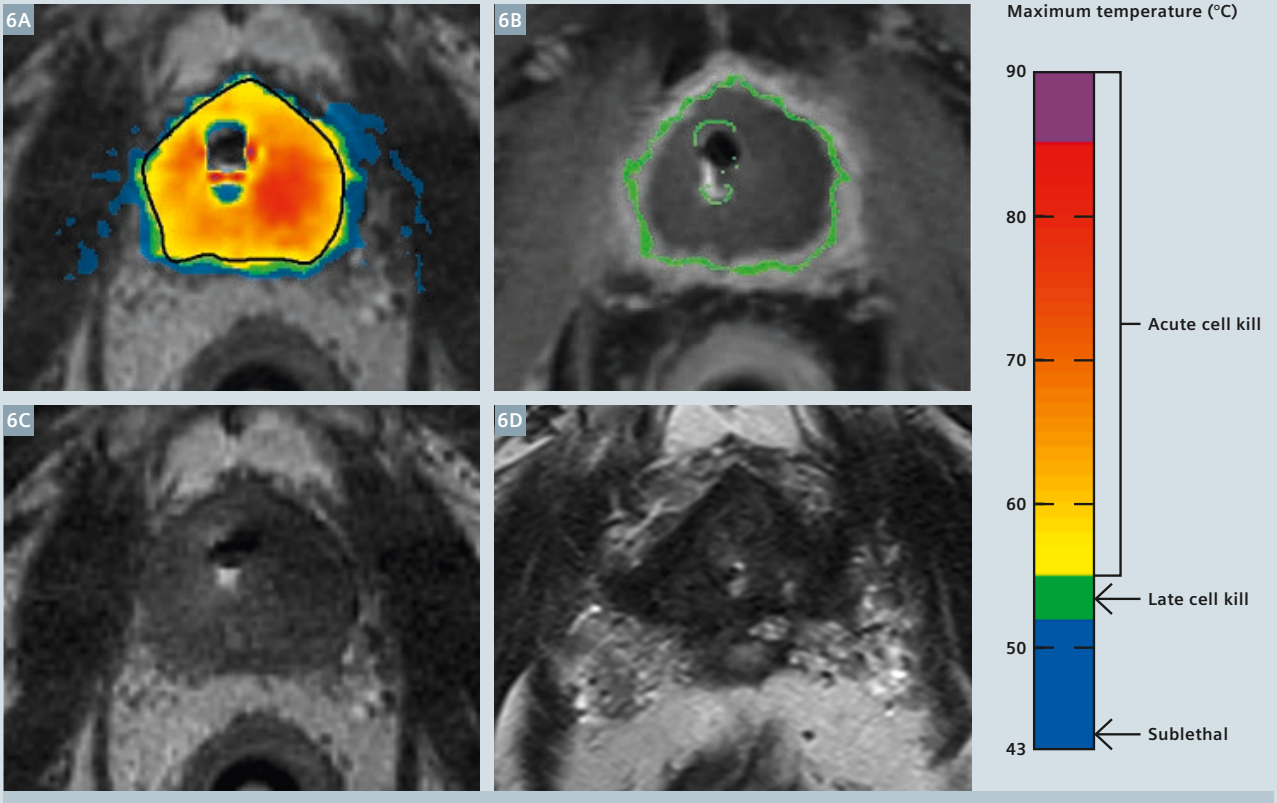

6 MRI findings of case study patient, with example images through the mid-gland. **6A** shows the maximum temperature reached in the prostate measured using real-time MR thermometry; the acute cell kill target temperature ≥ 55°C was shaped accurately and precisely to the treatment plan (black contour). **6B** shows the CE-MRI acquired immediately after treatment, demonstrating the hypointense region of non-perfused prostate tissue concordant with the ablative temperatures on MR thermometry. **6C** shows the corresponding treatment planning image (Day 0), which is compared to **6D** showing the same location at 12-month follow-up.

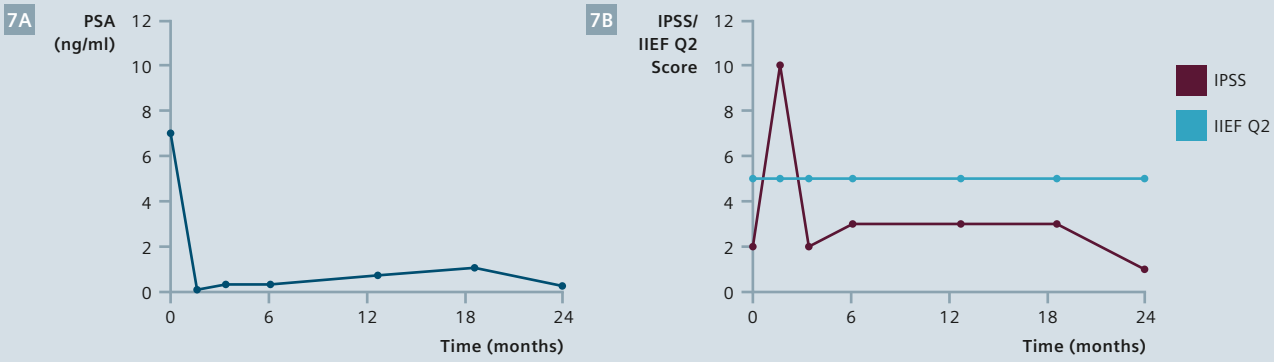

7 PSA and Quality of Life outcomes for case study patient (TULSA-PRO treatment at time 0). **7A** shows the PSA decreasing to <0.10 ng/ml at 1 month after treatment with the TULSA-PRO, and stable to 0.25 ng/ml at 24 months. **7B** shows the IPSS score [range 0 (no symptoms) to 35 (severe symptoms)] increase at 1 month and return to baseline at 3 months after treatment with the TULSA-PRO, further decreasing at 24 months. IIEF Q2 score (erection firmness sufficient for penetration) [range 0 (never or almost never) to 5 (always or almost always)] remains unchanged after treatment with the TULSA-PRO through 24 months of follow-up.

Case 2

A 68-year-old patient with an initial PSA of 9.1 ng/ml and a Gleason Score of 3+3 was treated with TULSA-PRO in March 2014. Prostate volume was 58 cc requiring a longer than average ultrasound treatment time of 58 min. Prior to treatment, the patient had IPSS of 20 (severe symptoms), which decreased to 11 and 9 (both moderately symptomatic) at 3 and 24 months, respectively. Baseline IIEF item 2 score was 2, and remained stable to 2 and 3, at 3 and 24 months, respectively. Side effects associated with the procedure were urinary tract infection, resolved with oral antibiotics, and obstructive micturition, requiring prolonged post-treatment catheterization from 2 weeks (per-protocol) to 5 weeks.

Following treatment the PSA value decreased to 1.0 ng/ml at 1 month, 0.9 ng/ml at 3 months, 0.7 ng/ml at 6 months, and remaining stable at 0.55 ng/ml at 24 months. Biopsy at 12 months was negative. Figure 8 shows this patient's treatment day and 12 months' mid-gland MR images.

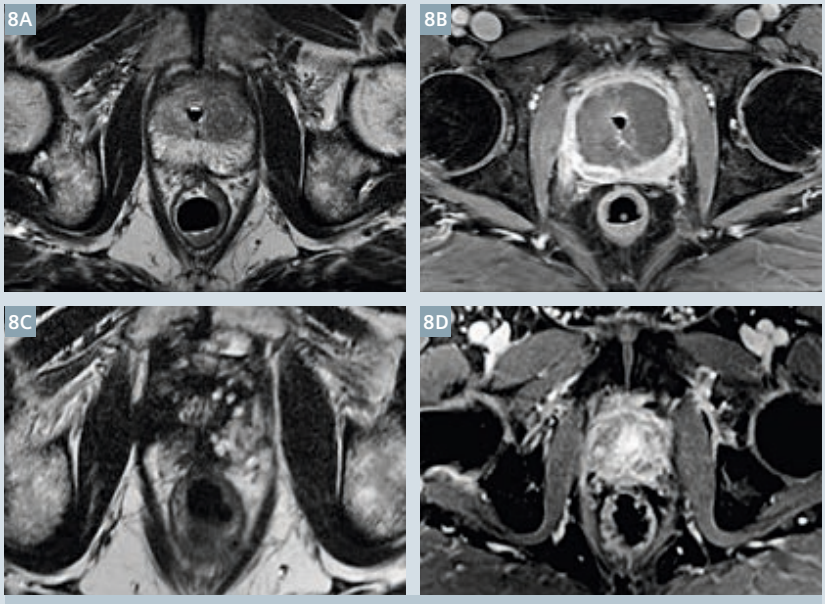

8 MRI findings of case study II patient. Example images through the mid-gland on treatment day **(8A, B)** and at 12 months **(8C, D)**. **8A** shows the axial T2-weighted treatment planning image, used to define the target boundaries for the real-time MR thermometry algorithm. **8B** shows the T1-weighted fatsat contrast-enhanced image acquired immediately following treatment. It demonstrates accurate ablation with the hypointense region of non-perfused prostate tissue and demonstrates the peripheral security margin of 3 mm used in the phase I trial, which will be reduced in the upcoming Pivotal trial. **8C** shows the axial T2-weighted image of the prostate gland at 12 months. Prostate volume is significantly reduced and T2 hypointense scarring is seen. **8D** demonstrates the low post-treatment prostate volume at the 12 month follow-up on a T1-weighted fatsat contrast-enhanced image with enhancement corresponding to a mixture of fibrotic tissue and remaining peripheral prostate tissue.

Parameter (n=30)		Average	Std Deviation	Median	IQR
Patient Age (years)		69.0	3.7	69	67-71
Prostate Volume (cc)		47.6	17.2	44	38-48
Ultrasound Treatment Time (min)		35.8	10.4	36	26-44
Thermal Ablation Accuracy (mm)		0.1	0.4	0.1	–0.3-0.4
Thermal Ablation Precision (mm)		1.3	0.4	1.3	1.0-1.5
Median Value (IQR)	**Baseline**	**1 month**	**3 months**	**6 months**	**12 months**
IPSS	8 (5-13)	14 (11-19)	6 (4-10)	5 (3-8)	5 (4-7)
IIEF item 2	13 (6-28)	7 (2-12)	11 (4-18)	11 (4-19)	13 (5-25)
Bowel Habits	100 (90-100)	100 (80-100)	100 (89-100)	100 (89-100)	100 (100-100)
PSA (ng/ml)	5.8 (3.8-8.0)	0.8 (0.5-1.1)	0.9 (0.4-1.7)	0.8 (0.4-1.1)	0.8 (0.6-1.1)

Table 1: Results summary of the prospective 12-month Phase I follow-up data.

Results summary of the TULSA-PRO prospective phase I study

An analysis of the prospective 12-month Phase I follow-up data showed that the TULSA-PRO is spatially accurate and precise to ablate prostate tissue, both malignant and benign, to millimeter accuracy, while providing a favourable safely profile and a low rate of erectile dysfunction [9].

Of the 30 study subjects, median (IQR) age was 69 (67-71) years, with 24 (80%) low-risk and 6 (20%) intermediate-risk cancers (D'Amico criteria). As summarized in Table 1, ultrasound treatment time was 36 (26–44) min and prostate volume 44 (38–48) cc. Spatial control of ablation was 0.1 ± 1.3 mm (spatial accuracy of 0.1 mm, precision of ± 1.3 mm). Adverse events (CTCAE v4) included haematuria Grade 1 (asymptomatic) in 13 patients (43%), and Grade 2 (symptomatic) in 2 patients (6.7%); urinary tract infections Grade 2 in 10 patients (33%); acute urinary retention Grade 1 (blocked suprapubic catheter) in 3 patients (10%), and Grade 2 (prolonged catheterization) in 5 patients (17%); and epididymitis Grade 3 (resolved with IV antibiotics) in 1 patient (3.3%). There were no rectal injuries or intraoperative complications.

Baseline IPSS of 8 (5-13) recovered to 6 (4-10) at 3 months, stable to 5 (4-7) at 12 months (n=29). The proportion of patients with erections sufficient for penetration (IIEF item 2 ≥ 2) remained unchanged from 21/30 (70%) at baseline to 20/29 (69%) at 12 months. Median PSA decreased 87% at 1 month, stable to 0.8 (0.6-1.1) ng/ml at 12 months (n=30). Positive biopsies at 12 months show 61% reduction in total cancer length, clinically significant disease in 9/29 patients (31%), and any disease in 16/29 patients (55%).

Conclusion

Here we report our initial experience with the TULSA-PRO device during a recently completed comprehensive prospective Phase I study, with Heidelberg being the center that has enrolled most of the patients into the trial. The TULSA-PRO device offers a novel, MRI-guided, minimally-invasive method to safely ablate target benign and malignant prostate tissue with millimeter accuracy and precision. Real-time MR thermometry performed during transurethral ultrasound delivery enables active feedback control of the thermal volume, with high success in the ablation of the target tissue. Furthermore, MRI-guidance allows acquisition of high-resolution images of the prostate for accurate treatment planning without the need for fusion algorithms. The TULSA-PRO device demonstrated conformal thermal ablation of target prostate volumes with a favorable side-effect profile and minor or no impact on urinary, erectile and bowel function, while maintaining a security margin of 3 mm to the prostate capsule during the phase I trial. In the upcoming Pivotal trial, and after assessment of millimeter accuracy during phase I, the security margin will be reduced further to allow treatment of the most peripheral portions of prostatic tissue.

TULSA-PRO has the potential to be an effective therapy option for clinicians and their patients diagnosed with localized prostate disease. The effectiveness of the device continues to be evaluated through the upcoming prospective pivotal study, with a 110-patient trial being established in over 10 institutions across Europe (Germany, The Netherlands, Spain), Canada and the United States.

References

1 Carlsson S and Vickers A, "Spotlight on prostate cancer: the latest evidence and current controversies," BMC Medicine 13:60 (2015).

2 Cooperberg M, Broering J, Kantoff P and Carroll P, "Contemporary trends in low risk prostate cancer: risk assessment and treatment," The Journal of Urology 178(3 Pt 2): S14-9 (2007).

3 Neutel C, Gao R, Blood P and Gaudette L, "The changing age distribution of prostate cancer in Canada," Canadian Journal of Public Health 98(1): 60-4 (2007).

4 Hammerer P, Kattan M, Mottet N and Prayer-Galetti T, "Using prostate-specific antigen screening and nomograms to assess risk and predict outcomes in the

management of prostate cancer," BJU International 98(1): 11-9 (2002).
5 Thompson I, Thrasher JB, Aus G, Burnett AL, Canby-Hagino ED, Cookson MS, D'Amico AV, Dmochowski RR, Eton DT, Forman JD, Goldenberg SL, Hernandez J, Higano CS, Kraus SR, Moul JW, Tangen CM; AUA Prostate Cancer Clinical Guideline Update Panel, "Guideline for the management of clinically localized prostate cancer: 2007 update," The Journal of Urology 177(6): 2106-31 (2007).
6 Rider JR, Sandin F, Andrén O, Wiklund P, Hugosson J, Stattin P. Long-term outcomes among noncuratively treated men according to prostate cancer risk category in a nationwide, population-based study. Eur Urol. 2013 Jan;63(1):88-96. doi: 10.1016/j.eururo.2012.08.001. Epub 2012 Aug 10. PMID: 22902040
7 Siddiqui MM, Rais-Bahrami S, Truong H, Stamatakis L, Vourganti S, Nix J, Hoang AN, Walton-Diaz A, Shuch B, Weintraub M, Kruecker J, Amalou H, Turkbey B, Merino MJ, Choyke PL, Wood BJ, Pinto PA. Magnetic resonance imaging/ultrasound-fusion biopsy significantly upgrades prostate cancer versus systematic 12-core transrectal ultrasound biopsy. Eur Urol. 2013 Nov;64(5):713-9. doi: 10.1016/j.eururo.2013.05.059. Epub 2013 Jun 12.
8 Dianat SS, Carter HB, Pienta KJ, Schaeffer EM, Landis PK, Epstein JI, Trock BJ, Macura KJ. Magnetic resonance-invisible versus magnetic resonance-visible prostate cancer in active surveillance: a preliminary report on disease outcomes. Urology. 2015 Jan;85(1):147-53. doi: 10.1016/j.urology.2014.06.085. Epub 2014 Oct 16.
9 Chin JL1, Billia M2, Relle J3, Roethke MC4, Popeneciu IV5, Kuru TH5, Hatiboglu G5, Mueller-Wolf MB4, Motsch J5, Romagnoli C2, Kassam Z2, Harle CC2, Hafron J3, Nandalur KR3, Chronik BA2, Burtnyk M6, Schlemmer HP4, Pahernik S5. Magnetic Resonance Imaging-Guided Transurethral Ultrasound Ablation of Prostate Tissue in Patients with Localized Prostate Cancer: A Prospective Phase 1 Clinical Trial. Eur Urol. 2016 Jan 6. pii: S0302-2838(15)01238-5. doi: 10.1016/j.eururo.2015.12.029. [Epub ahead of print]
10 Chopra R, Colquhoun A, Burtnyk M, N'djin WA, Kobelevskiy I, Boyes A, Siddiqui K, Foster H, Sugar L, Haider MA, Bronskill M and Klotz L, "MR imaging-controlled transurethral ultrasound therapy for conformal treatment of prostate tissue: initial feasibility in humans," Radiology 265(1): 303-13 (2012).
11 Burtnyk M, Chopra R and Bronskill M, "Simulation study on the heating of the surrounding anatomy during transurethral ultrasound prostate therapy: A 3D theoretical analysis of patient safety," Medical Physics 37(6): 2862-75 (2010).
12 Fütterer JJ, Briganti A, De Visschere P, Emberton M, Giannarini G, Kirkham A, Taneja SS, Thoeny H, Villeirs G and Villers A, "Can clinically significant prostate cancer be detected with multiparametric magnetic resonance imaging? A systematic review of the literature," European Urology 68(6): 1045-53 (2015).
13 American Cancer Society, http://www.cancer.org/cancer/prostatecancer

Contact

David Bonekamp, M.D.
Department of Radiology - E010
German Cancer Research Center (DKFZ)
Im Neuenheimer Feld 280
69120 Heidelberg
Germany
d.bonekamp@dkfz-heidelberg.de

Learn more

Don't miss the talks of experienced and renowned experts on all aspects of Prostate MR imaging at

www.siemens.com/magnetom-world

Prostate MR: Pearls, Pitfalls and Practical Tips

Leonardo K. Bittencourt,
Clínica de Diagnóstico Por Imagem (Rio de Janeiro, Brazil)

PET/MRI of Prostate Cancer: Current Experience and Clinical Integration

Matthias Röthke,
German Cancer Research Center (Heidelberg, Germany)

Economic Aspects and the Future Role of Prostate MRI

Jurgen Fütterer,
Radboud University Medical Center (Nijmegen, The Netherlands)

The entire editorial staff at Diagnostische Gemeinschaftspraxis Karlstrasse and at Siemens Healthineers extends their appreciation to all the radiologists, technologists, physicists, experts and scholars who donate their time and energy – without payment – in order to share their expertise with the readers of MAGNETOM Flash.

MAGNETOM Flash – Imprint

© 2016 by Siemens Healthcare GmbH, All Rights Reserved

Publisher:
Siemens Healthcare GmbH
Magnetic Resonance,
Karl-Schall-Straße 6, D-91052 Erlangen, Germany

Editor-in-chief:
Antje Hellwich
(antje.hellwich@siemens.com)

Guest Editor:
Prof. Dr. Henrik Michaely
Diagnostische Gemeinschaftspraxis Karlstrasse
Karlstrasse 104-106
76137 Karlsruhe
Germany

Editorial Board:
Reto Merges; Wellesley Were;
Sunil Kumar S.L., Ph.D.;
Gary R. McNeal, MS (BME);

Review Board:
Lisa Chuah, Ph.D.; Christoph Forman;
Berthold Kiefer, Ph.D; Heiko Meyer, Ph.D.;
Edgar Müller; Michaela Schmidt;
Gregor Thörmer, Ph.D.

Production:
Norbert Moser,
Siemens Healthcare GmbH

Layout:
Agentur Baumgärtner,
Friedrichstraße 4, D-90762 Fürth, Germany

Printer:
G. Peschke Druckerei GmbH,
Taxetstrasse 4,
D-85599 Parsdorf b. Munich, Germany

Note in accordance with § 33 Para.1 of the German Federal Data Protection Law: Despatch is made using an address file which is maintained with the aid of an automated data processing system.

MAGNETOM Flash is sent free of charge to Siemens MR customers, qualified physicians, technologists, physicists and radiology departments throughout the world. It includes reports in the English language on magnetic resonance: diagnostic and therapeutic methods and their application as well as results and experience gained with corresponding systems and solutions. It introduces from case to case new principles and procedures and discusses their clinical potential. The statements and views of the authors in the individual contributions do not necessarily reflect the opinion of the publisher.

The information presented in these articles and case reports is for illustration only and is not intended to be relied upon by the reader for instruction as to the practice of medicine. Any health care practitioner reading this information is reminded that they must use their own learning, training and expertise in dealing with their individual patients. This material does not substitute for that duty and is not intended by Siemens Healthcare to be used for any purpose in that regard. The drugs and doses mentioned herein are consistent with the approval labeling for uses and/or indications of the drug. The treating physician bears the sole responsibility for the diagnosis and treatment of patients, including drugs and doses prescribed in connection with such use. The Operating Instructions must always be strictly followed when operating the MR system. The sources for the technical data are the corresponding data sheets. Results may vary.

Partial reproduction in printed form of individual contributions is permitted, provided the customary bibliographical data such as author's name and title of the contribution as well as year, issue number and pages of MAGNETOM Flash are named, but the editors request that two copies be sent to them. The written consent of the authors and publisher is required for the complete reprinting of an article.

We welcome your questions and comments about the editorial content of MAGNETOM Flash. Please contact us at magnetomworld.med@siemens.com.

Manuscripts as well as suggestions, proposals and information are always welcome; they are carefully examined and submitted to the editorial board for attention. MAGNETOM Flash is not responsible for loss, damage, or any other injury to unsolicited manuscripts or other materials. We reserve the right to edit for clarity, accuracy, and space. Include your name, address, and phone number and send to the editors, address above.

MAGNETOM Flash is also available online:

www.siemens.com/magnetom-world

Siemens Healthineers Publications

Our publications offer the latest information and background for every healthcare field. From the hospital director to the radiological assistant – here, you can quickly find information relevant to your needs.

MAGNETOM Flash
Everything from the world of magnetic resonance imaging.

SOMATOM Sessions
Everything from the world of computed tomography.

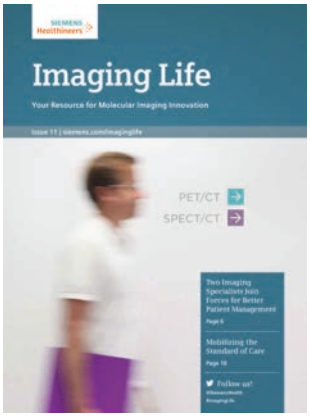

Imaging Life
Everything from the world of molecular imaging innovations.

AXIOM Innovations
Everything from the world of interventional radiology, cardiology, and surgery.

Heartbeat
Everything from the world of sustainable cardiovascular care.

Medical Solutions Online
Innovations and trends in healthcare.
The magazine is designed especially for members of hospital management, administration personnel, and heads of medical departments. Read online at:
siemens.com/medical-solutions

For current and past issues, and to order the magazines, please visit
siemens.com/healthcare-magazine

→Visit www.siemens.com/magnetom-world for case reports, clinical methods, application tips, talks and much more clinical information.

SUBSCRIBE NOW!

– and get your free copy of future MAGNETOM Flash! Interesting information from the world of magnetic resonance – gratis to your desk. Send us this postcard, or subscribe online at www.siemens.com/MAGNETOM-World

Siemens Healthcare GmbH
Antje Hellwich
HC DI MR CRM SCI
Karl-Schall-Straße 6
91052 Erlangen
Germany

MAGNETOM Flash

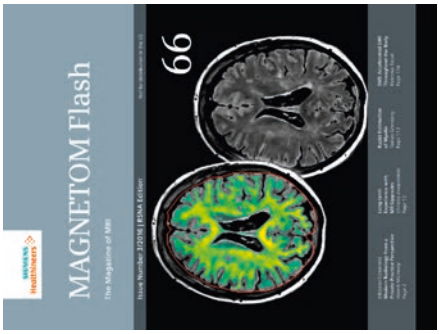

SIEMENS Healthineers

MAGNETOM Flash

The Magazine of MRI

Issue Number 3/2016 | RSNA Edition

Not for distribution in the US

Editorial Comment
Modern Radiology from a Private Practice Perspective
Henrik Michaely
Page 2

Long-term Experience with MR Upgrades
Christos Loupatatzis
Page 12

Rapid Estimation of Myelin
Tobias Granberg
Page 112

SMS Accelerated DWI Throughout the Body
Valentin Tissot
Page 116

Please enter your business address

Institution

Department

Function

Title

Name

Street

Postal Code

City

State

Country

MR system used

Please include me in your mailing list for the following Siemens Healthcare customer magazine(s):

☐ Medical Solutions

☐ MAGNETOM Flash

☐ SOMATOM Sessions

☐ AXIOM Innovations

Stay up to date with the latest information

Register for:

E-mail

☐ Yes, I consent to the above information being used for future contact regarding product updates and other important news from Siemens.

☐ unsubscribe from info service

Please print clearly!

On account of certain regional limitations of sales rights and service availability, we cannot guarantee that all products included in this brochure are available through the Siemens sales organization worldwide. Availability and packaging may vary by country and is subject to change without prior notice. Some/All of the features and products described herein may not be available in the United States.

The information in this document contains general technical descriptions of specifications and options as well as standard and optional features which do not always have to be present in individual cases, and which may not be commercially available in all countries. Due to regulatory reasons their future availability cannot be guaranteed. Please contact your local Siemens organization for further details.

Siemens reserves the right to modify the design, packaging, specifications, and options described herein without prior notice. Please contact your local Siemens sales representative for the most current information.

Note: Any technical data contained in this document may vary within defined tolerances. Original images always lose a certain amount of detail when reproduced.

Not for distribution in the US

Siemens Healthineers Headquarters
Siemens Healthcare GmbH
Henkestr. 127
91052 Erlangen
Germany
Phone: +49 9131 84-0
siemens.com/healthineers

Order No. A91MR-1000-122M-7600 | Printed in Germany | CC MR 3933 111610. | © Siemens Healthcare GmbH, 2016

siemens.com/magnetom-world